

NITROGEN ENRICHED NANOPOROUS POLYTRIAZINES FOR ENERGY AND ENVIRONMENTAL APPLICATIONS

Ph.D. THESIS

by

MONIKA CHAUDHARY



**DEPARTMENT OF CHEMISTRY
INDIAN INSTITUTE OF TECHNOLOGY ROORKEE
ROORKEE – 247 667 (INDIA)
JUNE, 2019**

NITROGEN ENRICHED NANOPOROUS POLYTRIAZINES FOR ENERGY AND ENVIRONMENTAL APPLICATIONS

A THESIS

*Submitted in partial fulfilment of the
requirements for the award of the degree*

of

DOCTOR OF PHILOSOPHY

in

CHEMISTRY

by

MONIKA CHAUDHARY



**DEPARTMENT OF CHEMISTRY
INDIAN INSTITUTE OF TECHNOLOGY ROORKEE
ROORKEE – 247 667 (INDIA)
JUNE, 2019**



**©INDIAN INSTITUTE OF TECHNOLOGY ROORKEE, ROORKEE-2019
ALL RIGHTS RESERVED**



*Dedicated to
my beloved parents and my loving husband,
the two pillars of strength behind my success*



INDIAN INSTITUTE OF TECHNOLOGY ROORKEE ROORKEE

CANDIDATE'S DECLARATION

I hereby certify that the work which is being presented in the thesis entitled "NITROGEN ENRICHED NANOPOROUS POLYTRIAZINES FOR ENERGY AND ENVIRONMENTAL APPLICATIONS" in partial fulfilment of the requirements for the award of the Degree of Doctor of Philosophy and submitted in the Department of Chemistry of the Indian Institute of Technology Roorkee, Roorkee is an authentic record of my own work carried out during a period from July, 2013 to June, 2019 under the supervision of Dr. Paritosh Mohanty, Associate Professor, Department of Chemistry, Indian Institute of Technology Roorkee, Roorkee.

The matter presented in this thesis has not been submitted by me for the award of any other degree of this or any other Institute.

Monika Ch.
03/Sep/19
(MONIKA CHAUDHARY)
Signature of the Candidate

This is to certify that the above statement made by the candidate is correct to the best of my knowledge.

Paritosh
03-09-2019
(PARITOSH MOHANTY)
Signature of Supervisor (s)

The Ph. D. Viva-Voce Examination of **Monika Chaudhary**, Research Scholar, has been held on **September 03, 2019**.

Amank
03/09/19
Chairman, SRC

Ashok Kumar Mishra
03/09/2019
Signature of External Examiner

This is to certify that the student has made all the corrections in the thesis.

Paritosh
03-09-2019
Signature of Supervisor (s)
Date: September 03, 2019

Amank
3/9/19
Head of the Department

ABSTRACT

The profound interest of the author in the areas of “energy and environment” led to carry out research during this doctoral work related to the development of high surface area polymeric materials for abatement of pollution in air and water as well as in the area of energy storage. Thorough literature studies indicated a strong relationship between the performance of the polymeric materials with the textural properties and presence of heteroatoms. Thus, in this research it is intended to synthesize nanoporous high surface area polymeric materials with hierarchical pore structure that are rich in nitrogen. For this, various synthetic approaches such as conventional heating, solvothermal, sonochemical and microwave assisted methods have been utilized for condensing two of the inexpensive precursors, melamine and cyanuric chloride, that are very rich in nitrogen. All the specimens have been investigated extensively using state of the art characterization techniques. Among these, the condensation is complete only in the specimens made by microwave assisted method. By optimizing the synthesis conditions, NENP-1, the best material, was made within 30 min at 140 °C with a microwave power of 400 W, when 1 mmol of each of the precursors were dissolved in 20 ml DMSO. The S_{ABET} of 840 m² g⁻¹ and hierarchical PSD centred 1.3 and 3.8 nm along with high N content of 50 wt% drove the NENP-1 to achieve large CO₂ capture capacity of 22.9 wt% at 0 °C and 1 bar. The H₂ and CH₄ storage capacities are 2.3 and 1.8 wt% at -196 °C and 0 °C, respectively, at 1 bar. Pre-carbonization at 350 °C further improved the CO₂ capture capacity to 33.8 wt% and H₂ storage capacity to 2.4 wt%. As an active electrode material for supercapacitor, the NENP-1 has shown high C_{sp} of 1256 F g⁻¹ @ 1 mV sec⁻¹. An asymmetric supercapacitor device fabricated using NENP-1 has high energy density of 102 Wh kg⁻¹ at 1.6 kW kg⁻¹, could lit 1.5 V red and green LEDs, and 3.0 V blue LED up to 11, 4 and 0.5 min, respectively, on charging for 30 s at 3.0 V. The NENP-1 as an organocatalyst efficiently catalyses the Knoevenagel reaction for C-C bond formation with high yield (~98%) in a short reaction time of 30 min at RT. Its uranium adsorption capacity of 489 mg g⁻¹ (97.8% efficiency) at 25 °C and *pH* of 7 and its ability to satisfy the WHO (0.015 mg l⁻¹) and USEPA (0.03 mg l⁻¹) permissible limits along with the adsorption of uranium from simulated seawater conditions made it an efficient adsorbent for uranium removal and enrichment. All these properties and applications made this research successful as planned and designed at the beginning of the research.

ACKNOWLEDGEMENTS

Though only my name appears on the cover of this dissertation, a great many people have contributed in completion of this work. I owe my gratitude to all those people who have made this dissertation possible and because of whom my graduate experience has been one that I will cherish forever.

It is my proud privilege to express my gratitude to my supervisor, Prof. Paritosh Mohanty, Associate Professor, Department of Chemistry, IIT Roorkee, for his guidance in contextualizing the research, starting from its early stages to thesis fruition. He has been actively interested in my work and has always been available to advise me. He has also provided insightful discussions about the research. His advices always guided me in the right direction. I have learned a lot from him. I am very grateful for his patience, motivation, enthusiasm, and immense knowledge that taken together make him a great mentor. I strongly believe that the experience of working with him will have a far-reaching influence in my future life. I would like to extend my sincere thanks to Mrs. Solvia Priyadarshini for her continued support and care.

I also appreciate the expert advice of the SRC members Prof. P. Jeevanandam (SRC chairman, Department of Chemistry), Prof. T. K. Mandal (Member, SRC, Department of Chemistry) and Prof. V. C. Srivastava (Member, SRC, Department of Chemical Engineering) for advice, suggestions and sharing their valuable experience relevant to my research work.

I owe a huge debt of thanks to Prof. K. R. Justin Thomas, HOD, Department of Chemistry, IIT Roorkee. I would also like to thank the faculty members of Department of Chemistry, IIT Roorkee for their co-operation and support during this research work. I gratefully acknowledged the support of Department of Chemistry, Department of Applied Science and Engineering and Institute Instrumentation Center towards providing the necessary research and characterization facilities. I also thank to all the support staffs of IIT Roorkee for their support throughout my research work.

I am indebted to all my friends and colleagues especially, Dr. Anushree, Dr. Amit, Dr. Pawan, Dr. Indu, Dr. Vivek, Dr. Raesh, Dr. Sunil, Dr. Ankushi, Deepa, Ruchi, Nisha, Sudiksha, Chandravati, Nishant, Jasasmita, Anuj and Shubham, for standing by my side in my good and bad times and also for providing a stimulating and funny environment to learn and grow. And at the last but not least, I offer my regards and blessings to all of those who supported me in any respect during the completion of the thesis.

I express my special thanks to my husband, Mr. Vinit Chaudhary, for tolerating my moods and inattention at times when the Ph.D. seemed like so demanding. His unconditional love, patience, and continued support on my academic endeavours have helped me a lot to complete this thesis.

Words cannot completely express my love and gratitude to my family who have supported and encouraged me through this journey. I would like to thank my parents, Sh. Rajveer Singh, Smt. Suhagvati Devi, Sh. Inderpal Singh and Smt. Kamlesh Devi, my caring brother and sister-in-law Ramavtar Singh and Sushma Chaudhary, and all my relatives for their everlasting love and sacrifices, which sustained my interest in research and motivated me towards the successful completion of this study. Thanks to my loving nephews Ankur, Shubham, Devansh, Goli and Ishu for creating a stress free environment.

I thank the Almighty God for providing me the passion, strength, diligence and the resources to complete this research.



(MONIKA CHAUDHARY)

CONTENTS

	Page No.
CERTIFICATE	i
ABSTRACT	ii
ACKNOWLEDGEMENTS	iii
ABBREVIATIONS	ix
LIST OF PUBLICATIONS	xi
CHAPTER I: INTRODUCTION	1-44
1. Introduction	1
1.1. Overview	1
1.2. Statement of the problem	1
1.3. Nanoporous polymers	5
1.4. Nitrogen enrichment in nanoporous polymers: polytriazines and triazine based polymers	6
1.5. Synthesis of polytriazines and triazine based polymers	8
1.5.1. Triazine based polymers made from the cyclotrimerization of nitriles	9
1.5.2. Triazine based polymers made by Schiff's base condensation	11
1.5.3. Triazine based polymers made by Friedal-Craft reaction	13
1.5.4. Triazine based polymers made by nucleophilic substitution reaction	14
1.6. Applications of nitrogen enriched nanoporous polytriazines and triazine based polymers	15
1.6.1. Gas sorption and storage	16
1.6.2. Supercapacitors	20
1.6.3. Organocatalysis using nanoporous polytriazines and triazine based polymers	24
1.6.4. Abatement of water pollution by nanoporous polytriazines and triazine based polymers	28
1.7. Motivation and objectives	31
1.8. Thesis outlines	32
References	34
CHAPTER II: MATERIALS AND METHODS	45-66
2.1. Introduction	45

2.2.	Experimental details	45
2.2.1.	Materials	45
2.3.	Synthesis of NENPs	45
2.3.1.	Conventional heating method	46
2.3.2.	Solvothermal method	47
2.3.3.	Sonochemical method	48
2.3.4.	Synthesis using microwave radiation	48
2.3.4.1.	Domestic microwave oven	50
2.3.4.2.	Microwave reactor	50
2.4.	NENPs as electrode materials for electrochemical supercapacitor	51
2.4.1.	Electrode fabrication for three electrodes system	51
2.4.2.	Electrode fabrication for two electrodes system	53
2.5.	Catalysis	53
2.6.	Uranium sorption experiments	53
2.6.1.	Sorption experiments in aqueous solution	54
2.6.2.	Sorption experiments in simulated sea water condition	54
2.7.	Characterization	54
2.7.1.	Fourier transform infrared (FTIR) spectroscopy	54
2.7.2.	Nuclear magnetic resonance (NMR) spectroscopy	55
2.7.3.	X-ray photo electron spectroscopy (XPS)	56
2.7.4.	X-ray diffraction (XRD)	56
2.7.5.	Field emission scanning electron microscopy (FESEM)	57
2.7.6.	Transmission electron microscopy (TEM)	57
2.7.7.	Thermal analysis	58
2.7.8.	Elemental analysis	58
2.7.8.1.	CHNS(O)	58
2.7.8.2.	Inductively coupled plasma-optical emission spectrometry (ICP-OES)	58
2.7.9.	Gas sorption	59
2.7.10.	Electrochemical workstation	61
2.7.11.	Gas chromatography-mass spectrometry (GC-MS)	61
	References	62
	CHAPTER III:	67-90

3.1.	Introduction	67
3.2.	Characterization of NENPs	67
3.2.1.	NENP-C-x synthesized by conventional heating method	67
3.2.2.	NENP-S-x synthesized by solvothermal method	74
3.2.3.	NENP-U synthesized by sonochemical method	76
3.2.4.	NENP-x synthesized by microwave assisted method	78
3.3.	Summary	87
	References	88
	CHAPTER IV:	91-114
4.1.	Introduction	91
4.2.	Textural analysis of specimens NENP-C-x (x =120, 140 and 160)	91
4.3.	Textural analysis of NENP-S-x (x = 140 and 160)	92
4.4.	Textural analysis of NENP-U	93
4.5.	Textural analysis of NENP-x (x = 1-9)	94
4.5.1.	Effect of reaction time on textural properties	95
4.5.2.	Effect of microwave power (MWP) on textural properties	96
4.5.3.	Effect of reaction temperature on textural properties	96
4.5.4.	Effect of solvent amount on textural properties	97
4.6.	CO ₂ sorption studies of NENP-C-x, NENP-S-x and NENP-U	98
4.7.	Gas sorption studies of NENP-x	100
4.8.	Summary	111
	References	112
	CHAPTER V:	115-126
5.1.	Introduction	115
5.2.	NENP-1 as an electrode material for supercapacitor application	115
5.3.	Summary	124
	References	124
	CHAPTER VI:	127-138
6.1.	Introduction	127
6.2.	Catalytic activity of NENP-1	127
6.3.	Summary	137
	References	137
	CHAPTER VII:	139-156

7.1.	Introduction	139
7.2.	Uranium sorption in aqueous solution	139
7.3.	Uranium batch adsorption studies	139
7.4.	Linear and nonlinear methods for equilibrium isotherm analyses and kinetic studies	143
7.5.	Adsorption isotherm studies	144
7.6.	Kinetics studies	146
7.7.	Thermodynamic studies	148
7.8.	Proposed mechanism	149
7.9.	Reusability of the adsorbent	150
7.10.	Achieving the WHO and USEPA permissible limits	152
7.11.	Adsorption studies in simulated seawater condition	154
7.12.	Summary	154
	References	154
	CHAPTER VIII:	157-162
8.1.	Summary and conclusions	157
8.2.	New achievements	159
8.3.	Challenges	160
8.4.	Directions for the future research work	160
	References	161

LIST OF ABBREVIATIONS

ACs	Activated carbons
ASCD	Asymmetric supercapacitor device
BET	Brunauer–Emmett–Teller
BSE	Back scattered electron
CNC	Cyanuric chloride
COFs	Covalent organic frameworks
CPMAS	Cross polarization magic angle spinning
CV	Cyclic voltammetry
DCM	Dichloromethane
DFT	Density functional theory
DMSO	Dimethyl sulfoxide
DOE	Department of energy
DTG	Differential thermogravimetry
DI	De-ionized
EDX	Energy dispersive X-ray analysis
EDL	Electrical double layer
EIS	Electrochemical impedance spectroscopy
FESEM	Field emission scanning electron microscopy
FTIR	Fourier transform infrared spectroscopy
GCD	Galvanostatic charge-discharge
GCE	Glassy carbon electrode
GC-MS	Gas chromatography-mass spectrometry
IAST	Ideal adsorbed solution theory
IUPAC	International union of pure and applied chemistry
ICP-OES	Inductively coupled plasma-optical emission spectrometry
LED	Light emitting diode
LSV	Linear sweep voltammetry
MOFs	Metal organic frameworks
MWP	Microwave power
NENP	Nitrogen-enriched nanoporous polytriazine
NMR	Nuclear magnetic resonance
PSD	Pore size distribution

PTFE	Polytetrafluoroethylene
Q_{st}	Isosteric heat of adsorption
RMSE	Residual root mean square error
RT	Room temperature
SA_{BET}	Specific surface area estimated by BET equation
SA_{LANG}	Specific surface area estimated by Langmuir equation
SAED	Selected area electron diffraction
SWV	Square-wave voltammetry
TEA	Triethylamine
TEM	Transmission electron microscopy
TGA	Thermogravimetric analysis
THF	Tetrahydrofuran
USEPA	United states environmental protection agency
WHO	World health organization
XPS	X-ray photoelectron spectroscopy
XRD	X-ray diffraction
ZIFs	Zeolite imidazolate frameworks

LIST OF PUBLICATIONS

Publications in Journals:

1. **Monika Chaudhary**, Arpan Kumar Nayak, Raeesh Muhammad, Debabrata Pradhan and Paritosh Mohanty*, “Nitrogen-enriched nanoporous polytriazine for high-performance supercapacitor application”, *ACS Sustainable Chem. Eng.*, 2018, **6**, 5895-5902. **Impact factor: 6.14**
2. **Monika Chaudhary** and Paritosh Mohanty*, “Nitrogen enriched polytriazine as metal-free heterogeneous catalyst for the Knoevenagel reaction in mild condition”, *New. J. Chem.*, 2018, **42**, 12924-12928. **Impact factor: 3.27**
3. **Monika Chaudhary**, Raeesh Muhammad, C. N. Ramachandran and Paritosh Mohanty*, “Nitrogen amelioration driven carbon dioxide capture by nanoporous polytriazine”, *Langmuir*, 2019, **35**, 4893-4901. **Impact factor: 3.78**
4. **Monika Chaudhary**, Lovjeet Singh, Pawan Rekha, Vimal Chandra Srivastava and Paritosh Mohanty* “Adsorption of uranium from aqueous solution as well as seawater conditions by nitrogen-enriched nanoporous polytriazine” *Chem. Eng. J.*, 2019, **378**, 122236, <https://doi.org/10.1016/j.cej.2019.122236>. **Impact factor: 8.35**
5. **Monika Chaudhary** and Paritosh Mohanty*, “Pre-carbonization: an efficient route to improve the textural and gas sorption properties of nitrogen-enriched nanoporous polytriazine” (Submitted)

Other Publication:

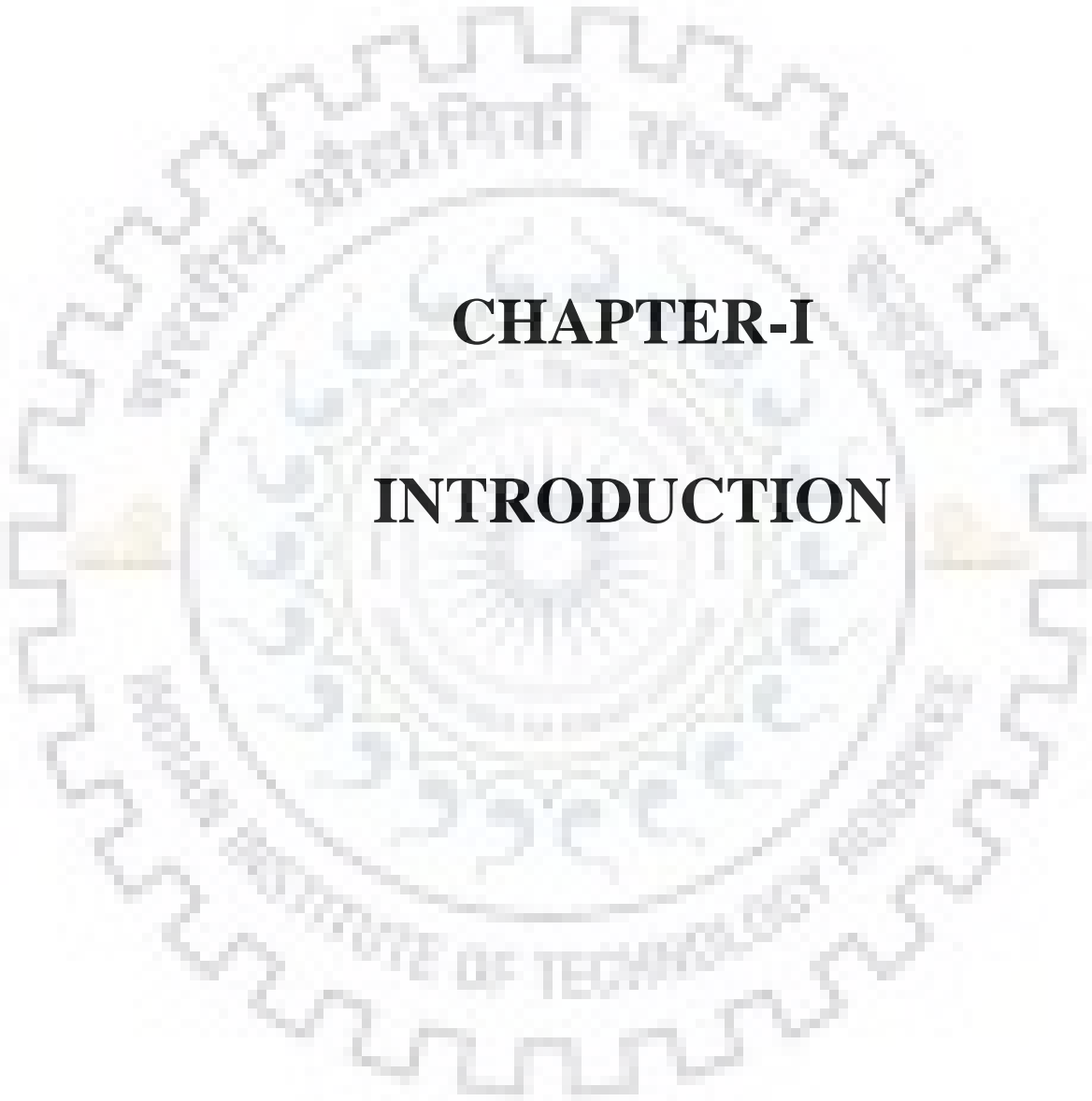
1. Raeesh Muhammad, **Monika Chaudhary** and Paritosh Mohanty*, “Harnessing electron-rich framework in cyclophosphazene derived hybrid nanoporous materials for organocatalytic C-C bond formation and gas sorption applications”, *J. CO₂ Util.*, 2018, **25**, 302-309. **Impact factor: 5.5**

Patent:

1. **Monika Chaudhary** and Paritosh Mohanty* “Process for synthesis of nitrogen enriched high surface area nanoporous polytriazines and their multi-functional applications” Indian Patent Application 2018, File No. **201811045502**.

Conference presentations:

1. **Monika Chaudhary**, Raeesh Muhammad and Paritosh Mohanty*, “Microwave assisted synthesis of nanoporous polytriazine as electrode material for supercapacitor” International meeting on energy storage devices, IIT Roorkee, Roorkee, Uttarakhand, India, December 10-12, 2018.
2. **Monika Chaudhary** and Paritosh Mohanty*, “Superior CO₂ capture by nitrogen-enriched nanoporous polytriazine”, ICEFN & SEM 2019, Kumaun University, Nainital, Uttarakhand, India, May 24-26, 2019.
3. **Monika Chaudhary** and Paritosh Mohanty*, “Nitrogen-enriched nanoporous polytriazine for gas sorption applications”, ICMAT 2019, Marina Bay Sands, Singapore, June 23-28, 2019. [**Best poster award**]



CHAPTER-I

INTRODUCTION

1. Introduction

1.1. Overview

This chapter deals with the extensive literature study on polytriazines and triazine based polymers that includes the preparation methods, textural properties and their applications in various fields. Special attention was given to the textural properties of these polymeric materials. The applications of these materials are correlated with their textural & microstructural properties, composition and stability under different environmental conditions. The applications in the energy and environmental fields have been emphasized. Based on the knowledge gained from these literatures, the aims and objectives of the present research have been outlined.

1.2. Statement of the problem

The energy need for humans before the industrial revolution was mostly restricted to the domestic use only for making food after humans learned to derive chemical energy from wood by using fire.[1,2] Use of camels, horses and donkeys etc. have supported for the transportation and other purposes. These have an ecosystem which was having a self-sustainability. Moreover, the less population has supported the sustainability due to less demand. Such a scenario continued until the industrial revolution began around 1750 AD.[1,2] With the industrialization, the requirement of much more fuel than that was required for cooking and other household use has forced to look for alternatives and use of coal was quite successful as it was economical to mine from earth and also satisfied the energy requirement. Coal, along with its liquid and gaseous cousins, petroleum and natural gas, were believed to come from the ancient vegetative and animal matter and are commonly known as “fossil fuels”.[3,4] These fossil fuels not only provided concentrated and convenient energy for dramatic economic growth but also supported the drastic expansion of the earth’s population far beyond the sustainable levels via natural processes. In fact, the fossil fuels allowed sustained population growth with a better living standards across almost all nations with an increased affluence leads to longer and more productive lives.[1-5]

Burning of fossil fuels produces huge amounts of gaseous products while providing the required energy that have large scale impact on the environment. Moreover, the detrimental environmental effect associated with the extraction, purification/production, and use of fossil fuels goes beyond tailpipe emissions.[4,5] In fact, the geologically sequestered fossil fuels added to the biosphere contaminants is highly inimical to human life. Not only that, other downstream processes

to produce various chemicals and finished products created pollutants that were never existing before on earth. All these environmental concerns, such as water and air pollution, global warming, and sustainability, have led to the creation of several organization-based societal responses. Some of the notable laws governing on these issues are Geneva and Rio Conventions, the U.S. Clean Air Act, the European Waste Electrical and Electronic Equipment Directive, and the Japanese Home Electronics Recycling Law along with consumer action on different levels. The success of all these are restricted to a greater extent due to the significant regional differences to accept these owing to the economical and societal implications.[1-10]

There is a consensus globally on how to produce energy economically priced, environmental friendly, reliable and safe. The major focus in this direction at this moment are expansion of nuclear power sources to different geographical locations, harvesting of renewable energy from sources where vastly available, while using the fossil fuels in an environmental friendly processes. However, even with a lot of efforts across the globe, the use of renewable energy could not exceeds 20% of the total energy need.[11,12] The major challenges remain the distribution potential of the renewable energy as it is very much uneven; some countries have huge sources and others only have a limited potential. Theoretically, it can be safe to say that renewable energy could power most of the countries but the uneven resources have limited their large scale use to a greater extent. The inability to store big amounts of electric energy still remain the main problem. Some technical solutions which are not economically feasible do exist, but won't be useful as long as the fossil base energy sources do not become far more expensive.[6-12]

Thus, it can easily be understood that we are not yet matured enough to avoid using the fossil based energy sources but could try to use these keeping in mind the environmental concerns, while exploring the possibility of lowering the cost of the harvesting and storage of the renewable energy. For all these, the advanced materials could play significant role.[13-16] For having a sustainability, a solution could be finding the right materials which could help to produce energy without having a large scale negative implications to the environment. According to the Buddhist philosophy "Materials are not nothing but mere illusions". The elements of the periodic table are the only materials forever, everything else is a collection of these elements linked by specific chemical bonds, a transient incarnation of chemical and mechanical assembly processes.[13] The job of a chemist is to work with this illusion and dream to create materials by joining the elements through various chemical bonds with specific properties that could solve particular purposes.[13-16] The defining

moment of the pre-historic and historic era are based on the materials that the civilization used during that period for their living and survival. Be it stone age, iron age, bronze age to the most recent information technology, nanotechnology and biotechnology age, always materials play significant roles for the mankind.[12-16]

Inspired by the nature and history of the development of human civilization, the current trend in solving the energy and environmental issue lies mostly on finding suitable materials and technological use of these for a sustainable growth. For example, to address the global warming effect, which is mainly due to the excess CO₂ content in the atmosphere that reaches as high as 414 ppm in the recent time, tremendous efforts are being made to find suitable liquid organic amines and various high surface area solid adsorbents that can separate CO₂ from the flue gas stream.[16-34] However, due to one or other drawbacks, none of the method is commercially sustainable at present. Still continued efforts in this direction are made in research and development of superior adsorbents which can capture large quantity of CO₂. [31-43] Different approaches were adopted to increase the CO₂ capture capacity that include the increase in the specific surface area, pore volume and use of various surface functionalities.[20-48] Moreover, inclusion of electron rich heteroatoms such as N, P, O, etc. in the high surface area nanoporous organic polymeric materials, which could interact strongly with Lewis acidic gas such as CO₂, SO₂ etc. leading the research due to the encouraging outcome both from the theoretical investigation and experimental studies.[40-52]

Moreover, the disastrous environmental effects associated with the global warming has put a pressure on extensive use of non-conventional and renewable energy sources that require sustainable harvesting and storage devices.[53-57] The widespread adoption of electric vehicles and the rise of portable electronic devices have created a huge demand on energy storage devices capable of delivering high energy and power densities. Commercial batteries with high energy density and supercapacitors with high power density are at two extreme ends.[53-55] Development of supercapacitor devices that could maintain its energy density at par with the batteries is the need of the time.[55-60] Metal based electrode materials have extensively explored for the supercapacitor device fabrication but recently metal free electrode materials has been preferred owing to their cost-effectiveness and environmental friendly nature. Three major research areas that have taken the forefront of the supercapacitor research are (i) designing suitable electrode materials, (ii) finding of appropriate electrolytes, and (iii) fabricating the devices.[56-60] As most of the modern day supercapacitors are based on the electric double layer capacitor (EDLC) concept, synthesizing

materials with superior textural properties such as high specific surface area (S_{BET}) and controlled pore size distribution (PSD) is desirable.[55-60] The presence of heteroatoms in the high surface area materials is an additional advantage.[55-60] Many of the above expected properties could be realized by synthesizing nitrogen enriched nanoporous polymeric materials with controlled PSD and high S_{BET} .

Moreover, the major developments in the chemical industries for carrying out organic or inorganic transformations lies on the development of efficient catalysts.[61-70] This is one of the prominent research problems that draw attention from diverse research fields. Traditionally, metal based molecules and materials have dominated the research area, however, very recently there is a growing demand for the development of efficient metal-free organocatalysts owing to their environmental and cost benefits.[71-85] Initially, the metal-free organocatalysis was mostly focussed on the use of small organic molecules under homogeneous conditions.[71-74] Catalyst recovery and recyclability are two major concerns in homogenous catalysis that further encouraged to develop their solid catalyst counterparts to carry out the catalysis in the heterogeneous conditions.[69,70] Some of the recently explored metal-free heterogeneous catalysts are functionalized porous aromatic frameworks, triazine based polymers, porous organic frameworks (POFs), conjugated microporous polymers (CMPs).[61-68,77] Among these, the electron rich triazine functionalized polymers have been shown to perform efficient catalytic activity for organic transformations.[77,81]

Use of nuclear energy for energy need is growing exponentially throughout the world. Uranium is extensively used for this purpose, which produces a large amount of radioactive wastes in the nuclear power industries. This is considered as one of the major pollutants and hazardous to both environment and humans due to its radioactive and toxic nature.[86-92] Thus, efficient removal of uranium from these nuclear wastes as well as the other water bodies could make the uranium based nuclear energy technology economically and environmentally sustainable. Moreover, uranium as crucial raw material of the nuclear industry, its extraction from seawater is very important for a sustainable growth. From an estimated 4.5 billion ton of uranium present in oceans around the world which is considered as the major uranium source, only about 10^3 tonnes is recovered annually.[86-88] This amount is not high enough in the perspective of required quantity for sustainable development of nuclear power plants to solve the energy crisis while taking care the environmental concerns. Thus, for a viable growth of nuclear energy, methodologies for the efficient and selective

extraction of uranium from seawater is required without disturbing the seawater eco-culture. The adsorptive removal of uranium from the nuclear power effluents and enrichment of uranium from seawater could provide a pathway for generating the greener energy.[86-94]

1.3. Nanoporous polymers

Porous materials have cavities, voids or channels which are more deep and less wide. According to the IUPAC (International Union of Pure and Applied Chemistry), these materials can be categorized into three main types (i) microporous, (ii) mesoporous, and (iii) macroporous based on their pore diameters.[95] Microporous materials have pore diameter less than 2 nm while mesoporous materials lies between 2 to 50 nm and above this pore size regime, the materials are called macroporous materials.[95] Porous materials can also be classified on the basis of their pores arrangement in the frameworks, such as, (i) ordered pore system (in which pores are well-ordered with very well-defined pore sizes) and (ii) disordered pore system (having wide variety of pores of different shapes and sizes).[96] There are several important structural characteristics of porous materials that includes pore geometry, pore size, pore surface functionality, and framework structure including composition and microstructures define their properties and applications. This class of materials are known to the mankind since a long time. Many natural occurring materials are porous in nature such as zeolites and carbons.[15] These have been used for many industrial applications since a long time. Some of their drawbacks related to the textural parameters, thermal, hydrothermal and chemical stability have forced the scientific community to look for other alternatives. Be it the improvement of the pore size distribution of the zeolites, or the breakthrough work of Mobil researchers to create large pore mesoporous silicas, MCMs, or the evolution of the incorporation of organic moieties to the inorganic silicas by post-synthesis functionalization or development of the methodology for making periodic mesoporous organosilicas (PMOs), every time a new invention in this line created a buzz in the materials chemistry community.[97-99] With recent advancement in the field by the Yaghi and workers on synthesizing various framework materials such as metal organic frameworks (MOFs), covalent organic frameworks (COFs) and zeolitic imidazolate frameworks (ZIFs) created a huge impact in the porous materials horizon.[14-17] Furthermore, the development of inorganic-organic hybrid nanoporous materials by many research groups throughout the world exploring several applications in the field of energy, environment, nanotechnology and biotechnology have made a significant impact. In this direction, organic polymeric materials have marked its presence by contributing substantially towards the applications in diverse fields owing to ease of tuning the

framework functionalities (Figure 1.1).[51,55,61] Conventionally, polymeric materials known for their chemical stability and as structural materials, have contributed towards the applications in many other areas. This paradigm shift has made nanoporous polymeric materials as one of the most sought advanced functional materials of recent times.[15,94]

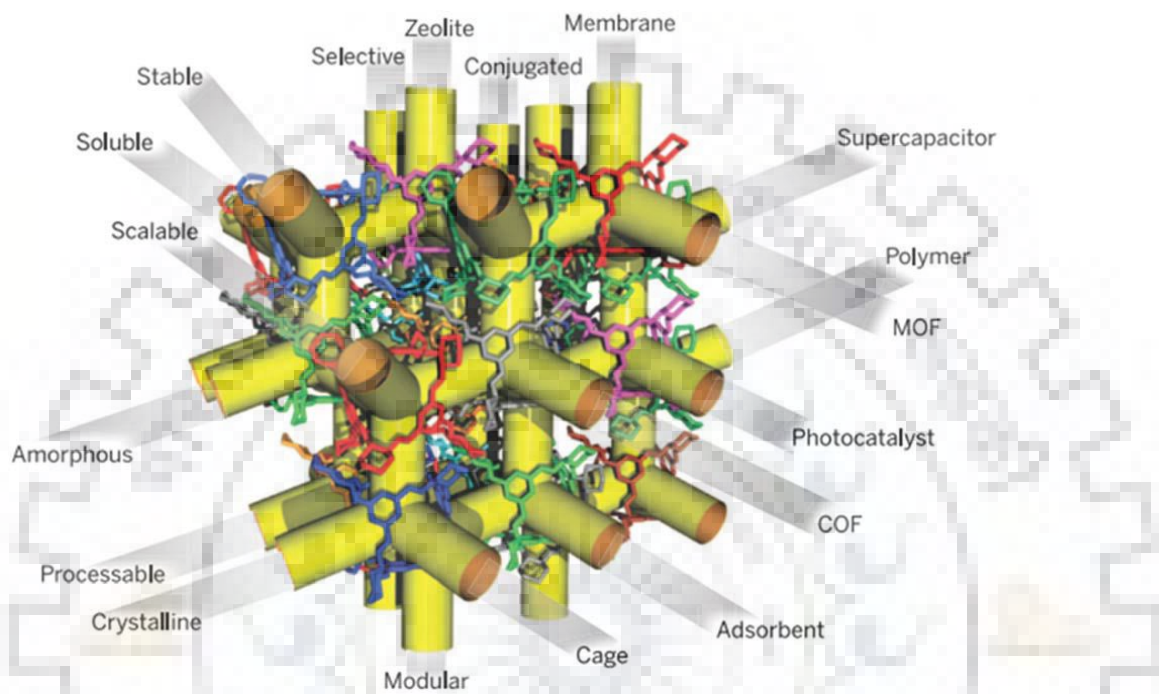


Figure 1.1. Porous materials can be defined by type or by function, but it is the function that will determine the scope for practical applications. [Reprinted with permission from ref. 15 © 2015 AAAS]

Porous organic polymers have proficient growth due to the continuous development of the advanced polymerization techniques and nanotechnology.[100-103] Porous polymeric materials having high surface area, good chemical stability and amendable chemical components are generally fabricated by various approaches such as condensation, hyper-crosslinking, template synthesis and phase separation etc.[101-105] Moreover, suitable synthetic methods for the designing of porous polymers with tailor-made pore structures and incorporation of various functionalities while retaining necessary framework stability remains a great challenge.[98-107]

1.4. Nitrogen enrichment in nanoporous polymers: polytriazines and triazine based polymers

Nanoporous polymers with controlled textural properties that includes high specific surface area, narrow pore size distribution and large pore volume, have already attracted the research community

owing to their applications in various fields (Figure 1.2).[100-105] However, incorporation of heteroatoms such as, nitrogen, oxygen, sulphur, and phosphorus in the frameworks have shown a great hope towards superior applications in these areas along with envisioning new application avenues.[108-114] Theoretical studies in this direction have further provided hope. For example, it was theoretically predicted that incorporation of nitrogen into the organic frameworks and carbonaceous materials could substantially improve the electrochemical applications.[111,114]

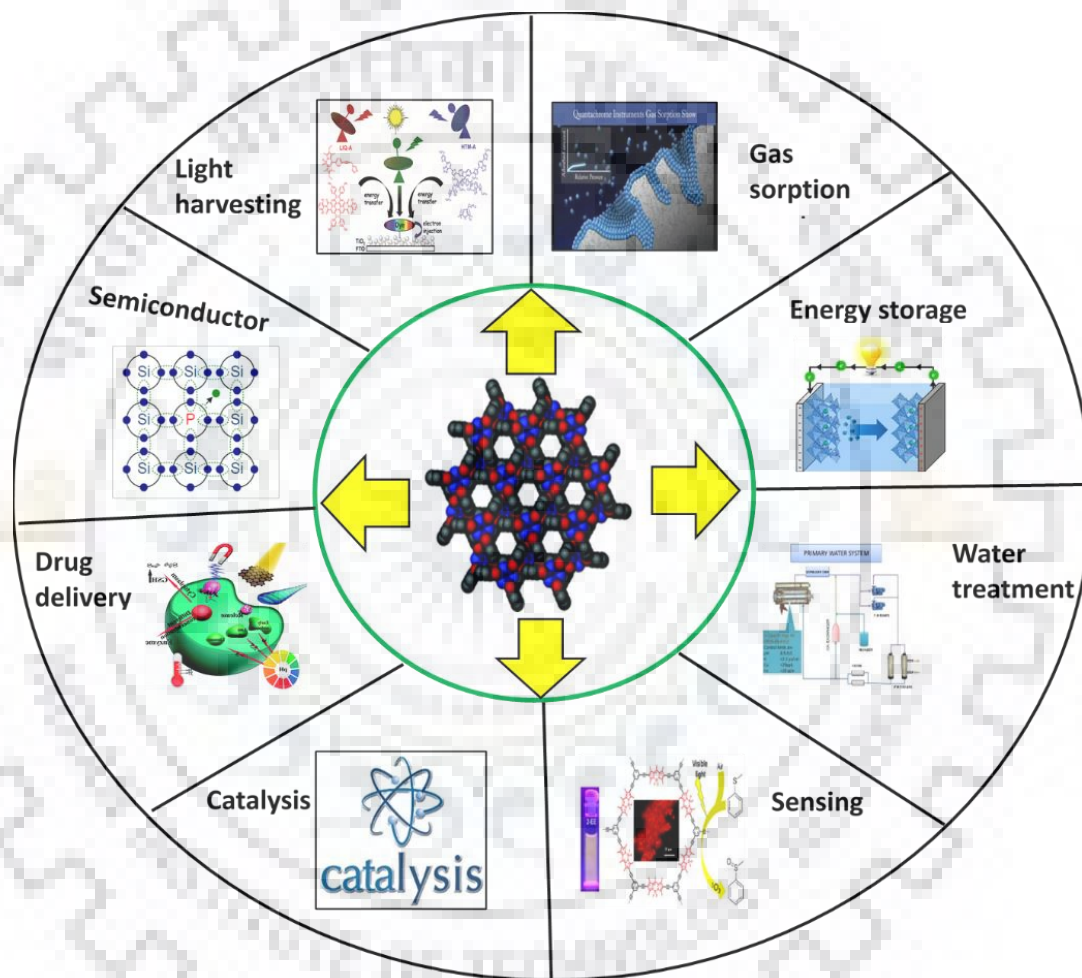


Figure 1.2. Applications of nanoporous organic polymers in different fields.

The nitrogen containing nanoporous polymers represent an important class of polymeric materials and have gained wide attention. The availability of the lone pair of electrons in the framework could potentially be utilized to share within the framework to pertain a better activity. Among various explored nitrogen enriched polymeric materials, triazine based polymers, covalent triazine frameworks (CTFs), conjugated microporous polymers (CMPs), polymers of intrinsic

microporosity (PIMs) and hypercrosslinked polymers (HCPs) etc. have already shown their potential as adsorbents, catalysts, catalyst supports, drug delivery systems, CO₂ capture, H₂ and CH₄ storage, supercapacitors and optoelectronics etc.[75-78,106-112]

Particularly, the triazine based polymers are quite interesting because of the lone pair of electrons present in the nitrogen, the alternating single and double bonds (conjugation) and the frameworks with large nitrogen content which could reach as high as 60 wt%.[109,110] All of these make this class of polymeric materials commonly known as “polytriazines” stand tall among its peers. The large nitrogen contents and conjugated double bonds could provide a sea of electrons that could be exploited for several advanced applications such as adsorption of Lewis acidic gases (CO₂), electrocatalysis, advanced electrodes for electrochemical devices, clean-energy production and storage, and other applications related to the abatement of air and water pollutions.[47-50,110-115]

However, their synthesis remains a challenge as these thermodynamically metastable materials often lose the porosity during the harsh experimental conditions.[115-117] Moreover, keeping nitrogen content high remains a great challenge.[118-140] Finding inexpensive precursors that could potentially produce polytriazine with large nitrogen content is also a big bottleneck.[140-170] The recent progress made in the synthesis and applications of triazine based polymeric materials and polytriazines has been summarized below.

1.5. Synthesis of polytriazines and triazine based polymers

Several nitrogen-enriched triazine based polymers have been reported recently by choosing suitable precursors and adopting different experimental approaches. Some of the commonly used precursors are molecules with triazine ring or nitrile group such as, cyanuric chloride, melamine, aliphatic and aromatic nitriles *etc.*[48-51] Mostly, mild experimental conditions and pre-designable modification approaches have been preferred to construct these nanoporous nitrogen enriched triazine based polymers (*Figure 1.3*).

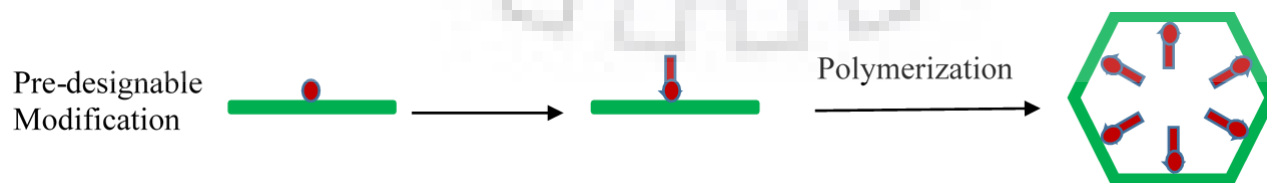


Figure 1.3. Schematic representation of pre-designable strategies.

1.5.1. Triazine based polymers made from the cyclotrimerization of nitriles

One of the most explored approach for the synthesis of triazine based nanoporous polymeric frameworks is the use of various nitriles and cyclotrimerize them under appropriate experimental conditions. For example, Thomas *et al.* in 2008 reported covalent triazine frameworks (CTFs) by using the cyclotrimerization of carbonitrile groups at reaction temperature up to 600 °C in molten ZnCl₂. [116] Textural properties of these CTFs have been tuned by selecting the appropriate nitrile monomers. *Figure 1.4* summarizes use of various aromatic nitrile group containing precursors for the synthesis of the CTFs. [116] Further, the effect of variation in experimental conditions on the textural properties has been studied for the synthesis of triazine based polymers.

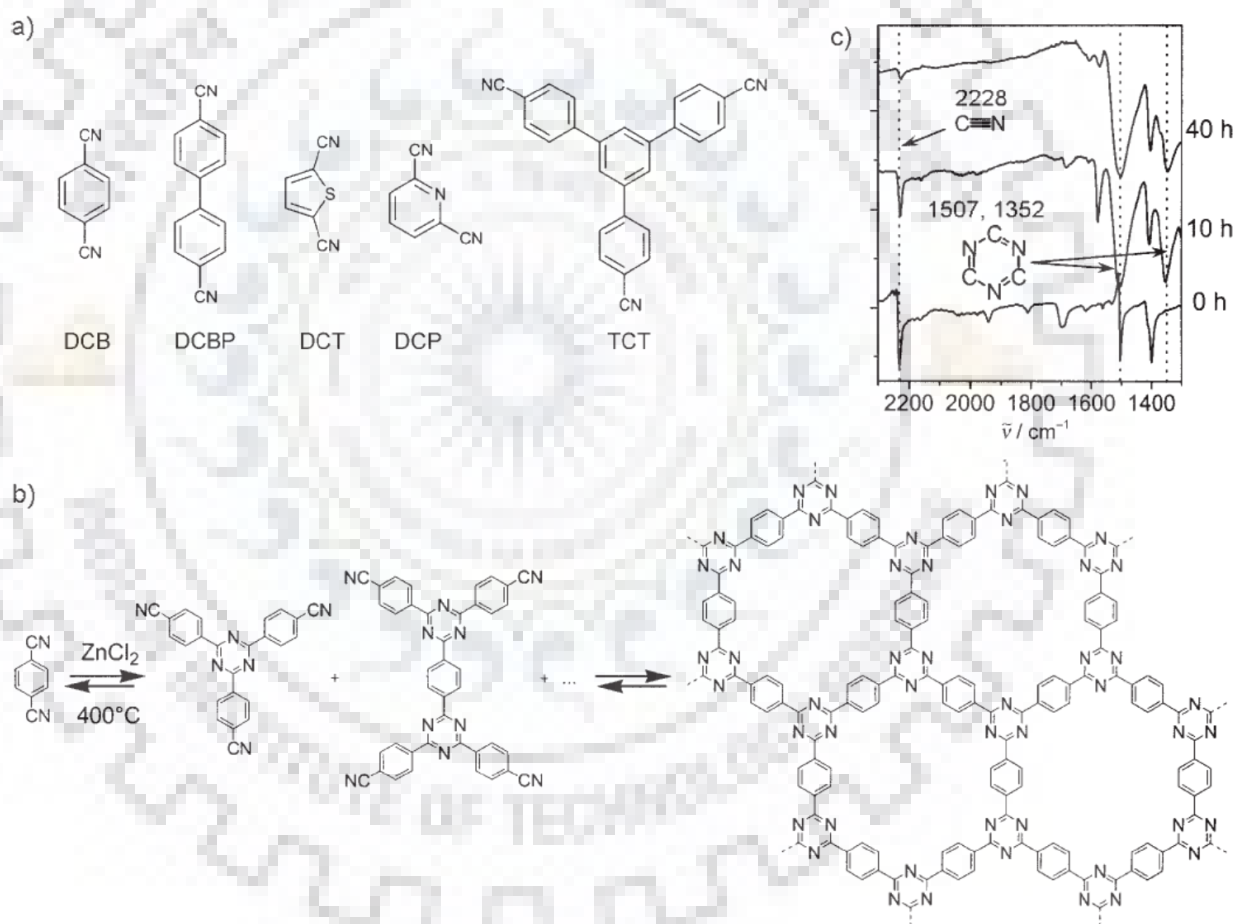


Figure 1.4. (a) Nitrile Precursors (b) trimerization of dicyanobenzene in molten ZnCl₂ to form covalent triazine-based framework (CTF-1) (c) FTIR spectra following the progress of the condensation. [Reprinted with permission from ref. 116 © 2008 Wiley-VCH]

Cooper *et al.* have reported the trifluoromethanesulfonic acid ($\text{CF}_3\text{SO}_3\text{H}$) catalyzed synthesis of covalent triazine frameworks through trimerization of nitriles at room temperature as well as under microwave assisted conditions.[117] Different specimens have been made by selecting different precursors as shown in *Figure 1.5*. The specimen P6 has shown highest specific surface area (S_{BET}) of $1152 \text{ m}^2 \text{ g}^{-1}$, among all the synthesized specimens, which was synthesized by cyclotrimerization of 4,4',4'',4'''-methanetetrayltetrabenzonitrile at room temperature in the presence of catalyst.

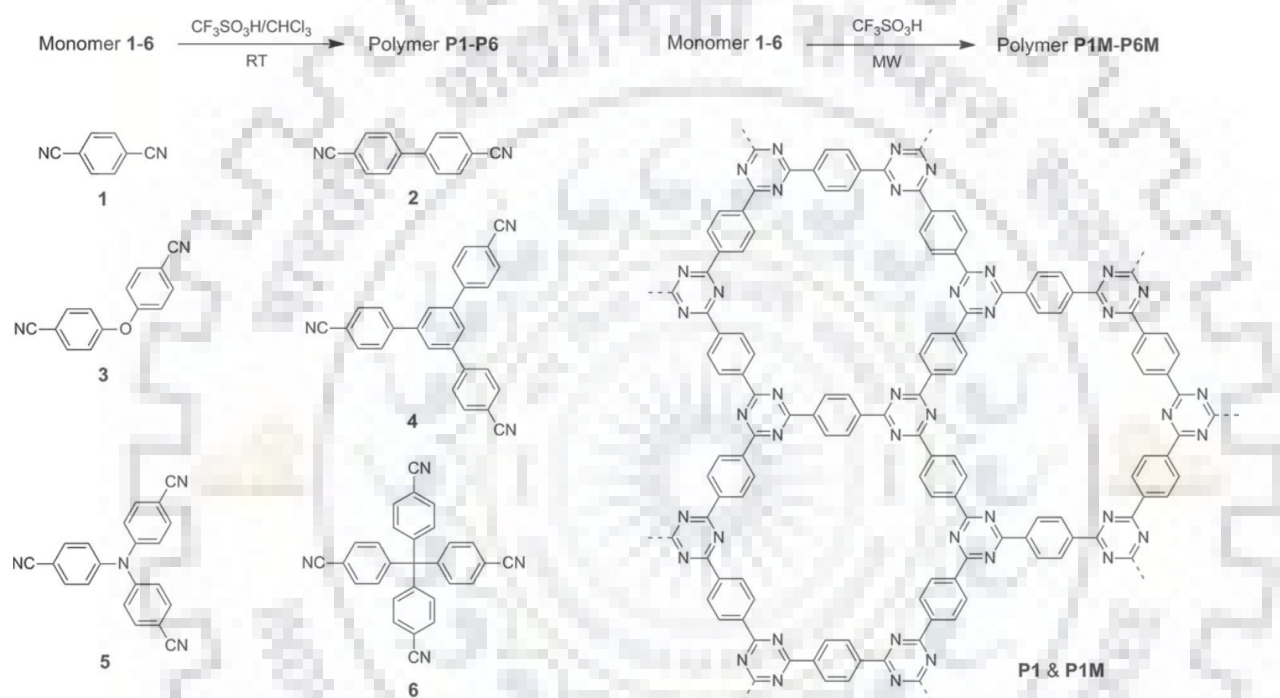


Figure 1.5. Synthesis of the CTF-type polymers P1-P6 and P1M-P6M and representative structure of P1 and P1M. [Reprinted with permission from ref. 117 © 2012 Wiley-VCH]

Zhao and coworkers have further demonstrated a superior performance for the adsorption and separation of CO_2 using the fluorinated CTFs when the fluorine atoms were introduced into the CTFs by using tetra-fluoroterephthalonitrile as a precursor.[118] The specimen FCTF-1 was observed to have maximum S_{BET} of $752 \text{ m}^2 \text{ g}^{-1}$ with pore size distribution centered in the microporous range (0.46 and 0.54 nm). Moreover, a hydrazone functionalized triazine based polymer COF (TFPT-COF) have been fabricated by Stegbauer *et al.* using 1,3,5-tris-(4-formylphenyl)triazine (TFPT) and 2,5-diethoxy-terephthalohydrazide (DETH) as building blocks.[119] The

S_{ABET} was estimated to be $1603 \text{ m}^2 \text{ g}^{-1}$ which was found to be the highest among all hydrazone based porous polymers.

Further, it has been observed by Liu *et al.* that surface functionalization of triazine framework with carbazole moieties can tune the surface polarity as well as binding affinity for adsorbent molecules.[120] Moreover, triazine and imide groups with high N content could also be considered as ideal precursors to develop high performance polymeric materials. For example, Wu *et al.* have fabricated imide functionalized 1,3,5-triazine frameworks using trimerization approach, possessed S_{ABET} upto $1053 \text{ m}^2 \text{ g}^{-1}$ with narrow pore size distribution in the microporous region (1.48 and 0.54 nm, respectively).[121] Buyukcakir *et al.* have reported charged covalent triazine framework (cCTF) using cyanophenyl substituted viologen dication as a monomer through ionothermal trimerization reaction.[122] The textural properties of cCTFs showed strong dependence on the reaction temperature. The products formed at $400 \text{ }^\circ\text{C}$ are mostly microporous whereas, a gradual increase in the reaction temperature up to $500 \text{ }^\circ\text{C}$ resulted in the formation of well-developed mesoporous structure along with micropores, forming a hierarchical network structure. cCTFs have possessed S_{ABET} of 744, 861 and $1247 \text{ m}^2 \text{ g}^{-1}$ at 400, 450 and $500 \text{ }^\circ\text{C}$, respectively.[122] Dai and coworkers have reported hexaazatriphenylene-based conjugated triazine frameworks (HAT-CTFs) synthesized by trimerization of trimethoxy-tricyano-hexaazatriphenylene at temperatures varying from 400 to $600 \text{ }^\circ\text{C}$. Specimen HAT-CTF-450/600 which was prepared by trimerization of precursor at $450 \text{ }^\circ\text{C}$ for initial 20 h and another 20 h at $600 \text{ }^\circ\text{C}$. A maximum S_{ABET} of $1090 \text{ m}^2 \text{ g}^{-1}$ and pore size less than 1 nm were estimated for HAT-CTF-450/600.[124]

1.5.2. Triazine based polymers made by Schiff's base condensation

Recently, Schiff's base condensation is extensively used for the polymerization of framework materials with various functionalities. In general, an aldehyde (both aliphatic and aromatic) reacts with an organic amine forming aminal-linked polymeric materials.[125-133] This popular approach was also extensively employed by several research groups throughout the world to prepare triazine based polymeric materials. For this, appropriate precursors with triazine ring and an amine functionality condenses with an aldehyde under appropriate reaction conditions. Moreover, the nanoporous materials synthesized through Schiff base condensation with aromatic rings have extended conjugation and hence, display robust stability towards moisture in comparison to the aliphatic polymers.[127-138] Although, initially Schiff based nanoporous materials have extensively

been used for gas storage, but later on the incorporation of various functionalities led to their applications in catalysis, energy storage, sensor, drug delivery, solar and optoelectronic devices.[127-140] The most important selling point of this method is that it does not need any metal-based catalyst and possess self-correction feature under thermodynamic condition owing to reversibility of imine bond. Although, most of the framework synthesis needed acid as catalyst but precursor with high basicity such as melamine undergoes Schiff base condensation without catalyst.

Schwab *et al.* reported condensation of melamine with terephthalaldehyde in a catalyst-free reaction using DMSO as solvent at 180 °C (Figure 1.6).[131] The obtained nanoporous triazine based polymer has S_{BET} of $1377 \text{ m}^2 \text{ g}^{-1}$ with narrow PSD. Similarly, Song *et al.* synthesized nitrogen-enriched aminal-linked nanoporous polymeric materials (APOPs) using melamine and its derivatives with various benzaldehydes.[129] The S_{BET} of APOP materials was estimated to be 724 to $1402 \text{ m}^2 \text{ g}^{-1}$ depending up on the synthesis conditions and precursors selected for the condensation. Long and co-workers reported the facile hydrothermal synthesis of nitrogen-rich melamine-resorcinol-formaldehyde (MRF) polymeric materials with microporous structures using melamine, resorcinol and formaldehyde as the starting materials.[132] Puthiaraj *et al.* has developed imine-based CTPs via the Schiff base reaction of 1,3,5-tris-(4-formyl-phenyl) triazine (TFPT) and phenylenediamine or terephthalohydrazide.[77] Senker *et al.* have used 2,4,6-tris-(4-aminophenyl)-1,3,5-triazine (TAPT) with various dianhydride precursors to develop nitrogen rich polymers using Schiff base approach.[135]

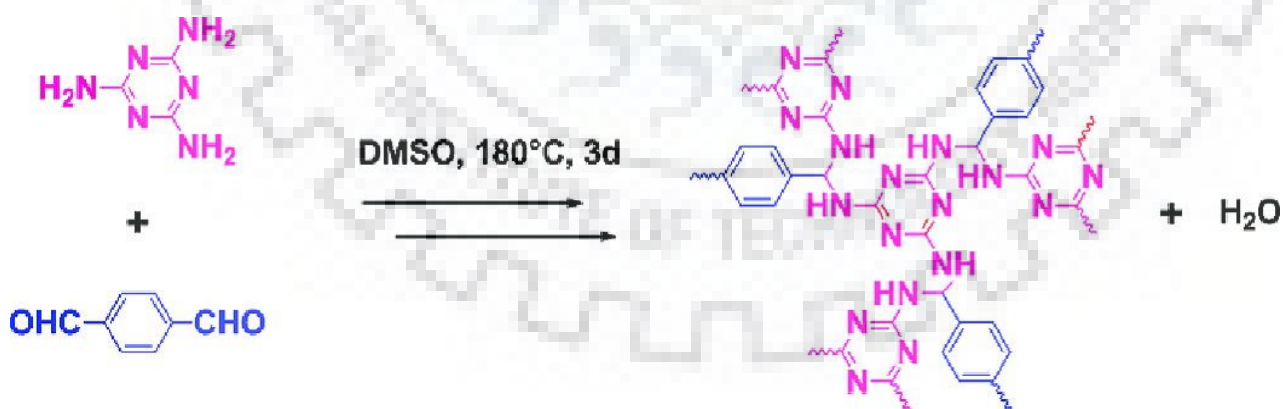


Figure 1.6. Synthesis of amorphous POP (SNW-1) by Schiff base condensation of terephthalaldehyde and melamine under catalyst free condition.[Reprinted with permission from ref. 131 © 2009 American Chemical Society]

Recently, Abdelmoaty and coworkers reported the synthesis of two nitrogen-enriched porous polymers (NRPPs) by reacting 1,4-bis-(2,4-diamino-1,3,5-triazine)-benzene with terephthalaldehyde and 1,3,5-tris(4-formylphenyl)benzene in DMSO. The resulting polymers have high S_{ABET} of $1579 \text{ m}^2 \text{ g}^{-1}$ and exhibit high CO_2 uptake as well as high capacity for iodine adsorption from both vapor and liquid phases (Figure 1.7).[136]

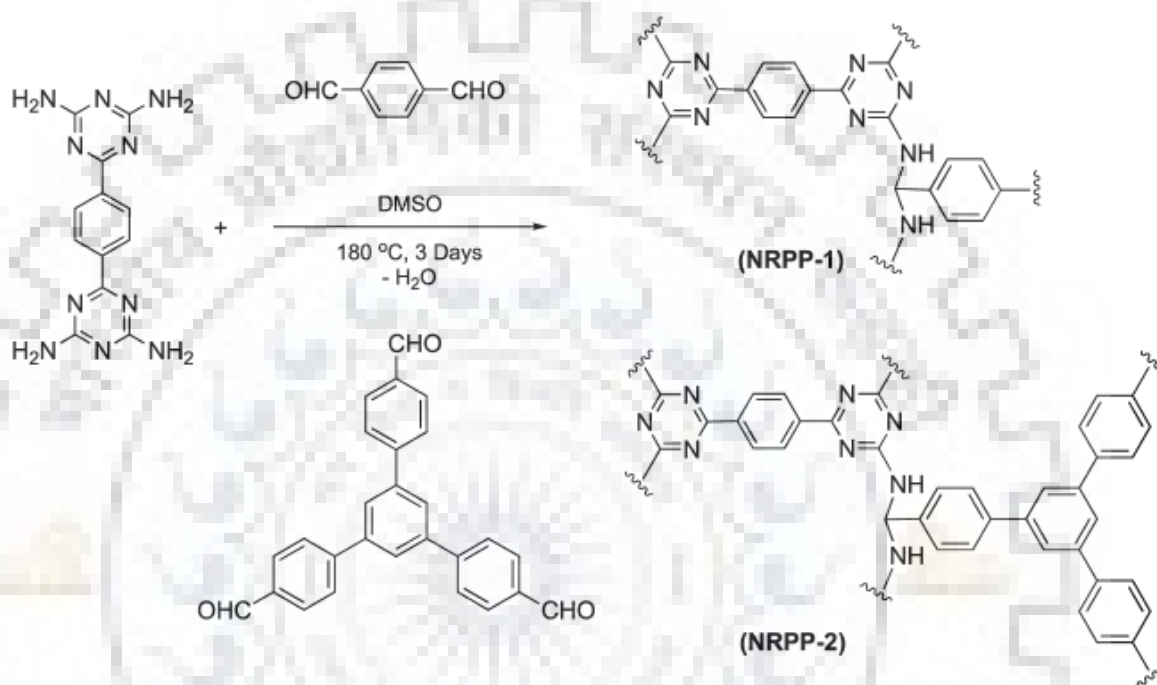


Figure 1.7. Synthesis of nitrogen rich porous polymers (NRPP-2). [Reprinted with permission from ref. 136 © 2018 American Chemical Society]

1.5.3. Triazine based polymers made by Friedal-Craft reaction

Friedal-Craft reaction is also getting wide attention for the synthesis of nitrogen enriched nanoporous polymeric materials. A series of nitrogen enriched triazine based polymers were synthesized through Friedel-Craft reaction using cyanuric chloride and aromatic precursors and methane-sulfonic acid as a catalyst. The S_{ABET} of these polymers varied between 749 to $894 \text{ m}^2 \text{ g}^{-1}$ depending upon the precursors.[137] In general, it has been observed that, the textural properties varies to a greater extent by changing the precursors, which was also supported by report of Xiong *et al.*[118] Similarly, Puthiaraj and coworkers have synthesized nitrogen enriched triazine based polymers by Friedal-Crafts reaction of cyanuric chloride and other aromatic monomers using AlCl_3 as a catalyst.[138] Dai *et al.* fabricated nitrogen enriched nanoporous polymers via a Friedel-Crafts reaction between

triazine-functionalized carbazole monomers and formaldehyde dimethyl acetal (Figure 1.8). Further, type IV isotherm was shown by the N_2 sorption isotherm of specimen TSP-2 and maximum S_{ABET} was observed to be $913 \text{ m}^2 \text{ g}^{-1}$. [139]

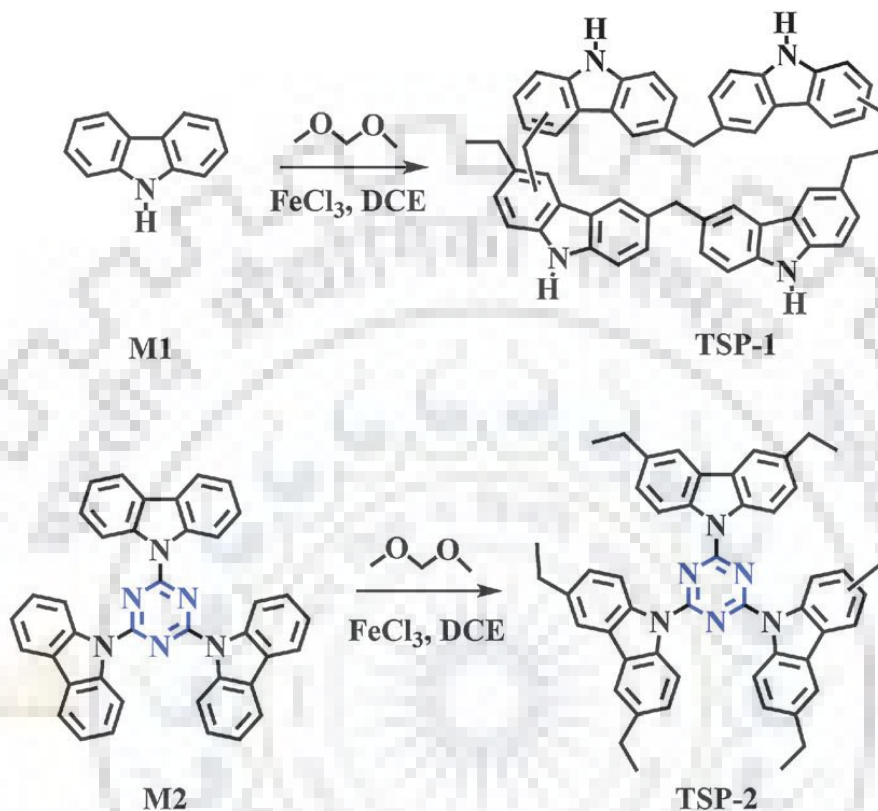


Figure 1.8. The synthesis of TSPs via Friedel-Craft reaction. [Reprinted with permission from ref. 140 © 2014 Royal Society of Chemistry]

1.5.4. Triazine based polymers made by nucleophilic substitution reaction

Nucleophilic substitution reaction is considered as an efficient method for the synthesis of triazine based polymers and polytriazines as both the amine and the leaving group such as chloride attached to the triazine ring act as good nucleophile and leaving group, respectively. A wide range of precursors have been used for the synthesis of nanoporous polytriazine and triazine based polymers using this approach. Wang *et al.* have reported the synthesis of a porous aromatic framework (PAF-54) by the reaction of melamine and cyanuric chloride in a solvent mixture of dimethylacetamide/*N,N*-diisopropylethylamine at 0°C for 30 min, followed by heating at 50°C for 12 h and 95°C for 24 h. [140] Although, the authors claim it as a porous framework, but the specific surface area of $93 \text{ m}^2 \text{ g}^{-1}$ remains in the lower end of such materials considering the presence

of only light weight elements in the framework that can have low density. Zhang *et al.* have fabricated nitrogen enriched CNH nanocages by conventional heating method using nitrogen rich precursors i.e. melamine and cyanuric chloride. The S_{BET} was estimated to be $655 \text{ m}^2 \text{ g}^{-1}$ with hierarchical pore structure and pore size distribution centered at 1.4 nm.[109] Very recently, Xue *et al.* have reported a covalent organic framework (NWNNU-COF-1) by the condensation reaction of melamine and cyanuric chloride in DMF at $150 \text{ }^\circ\text{C}$ for four days, followed by aging for 12 hours. The S_{BET} of NWNNU-COF-1 is estimated to be $301 \text{ m}^2 \text{ g}^{-1}$, with pore size centered at 1.41 nm.[141] Moreover, several other precursors have also been used for the development of various nitrogen enriched triazine based polymers.[142,143] For example, Yavuz *et al.* have synthesized covalent organic polymers (COP-1 and COP-2) by the nucleophilic condensation of cyanuric chloride with piperazine and 4,4-bipiperidine in a solvent mixture of dioxane/N,N-diisopropylethylamine (DIPEA). Synthesized COP-1 and COP-2 exhibited specific surface area of 168 and $158 \text{ m}^2 \text{ g}^{-1}$, respectively.[142] Further, Yavuz and coworkers synthesized triazine based polymers (PA-1 and PA-2) by the nucleophilic substitution of 1,3,5-benzenetricarbonyl trichloride with melamine using two different solvents (DMAc/NMP and 1,4-dioxane) at room temperature.[123] The N_2 isotherms of PA-1 and PA-2 were close to those of type II and III, S_{BET} of 84.5 and $22 \text{ m}^2 \text{ g}^{-1}$ with average pore sizes of 13.6 and 17.9 nm , respectively. The textural properties of PA-1 (using DMAc/NMP) was superior to those of PA-2 (using 1,4-dioxane), indicating that the DMAc/NMP mixture is a better reaction medium to synthesize amide-based polymeric materials.[143]

Moreover, several other approaches such as Yamamoto couplings, Sonogashira cross-couplings, oxidative couplings, and radical polymerizations have also been employed to synthesize triazine based nitrogen enriched nanoporous polymers.[64,78,103,168] Inclusion of triazine ring in the framework of the high surface area nanoporous materials have been shown to improve substantially many of the energy and environmental related applications such as gas storage, catalysis, energy storage and water treatment etc.

1.6. Applications of nitrogen enriched nanoporous polytriazines and triazine based polymers

The nitrogen enriched nanoporous polytriazines and triazine based polymers have few features that make these class of materials distinct among various high surface area polymeric materials. The frameworks rich in electrons, use of aromatic moieties that provide sufficient pi-electrons to the framework along with the alternative double and single bonds making a conjugated system have

often exploited. Moreover, the advancement of synthesis methodology that provides sufficient control over the textural properties have made research in this class of materials more rewarding. Some of the recently explored applications of these materials are summarized in *Figure 1.9*.

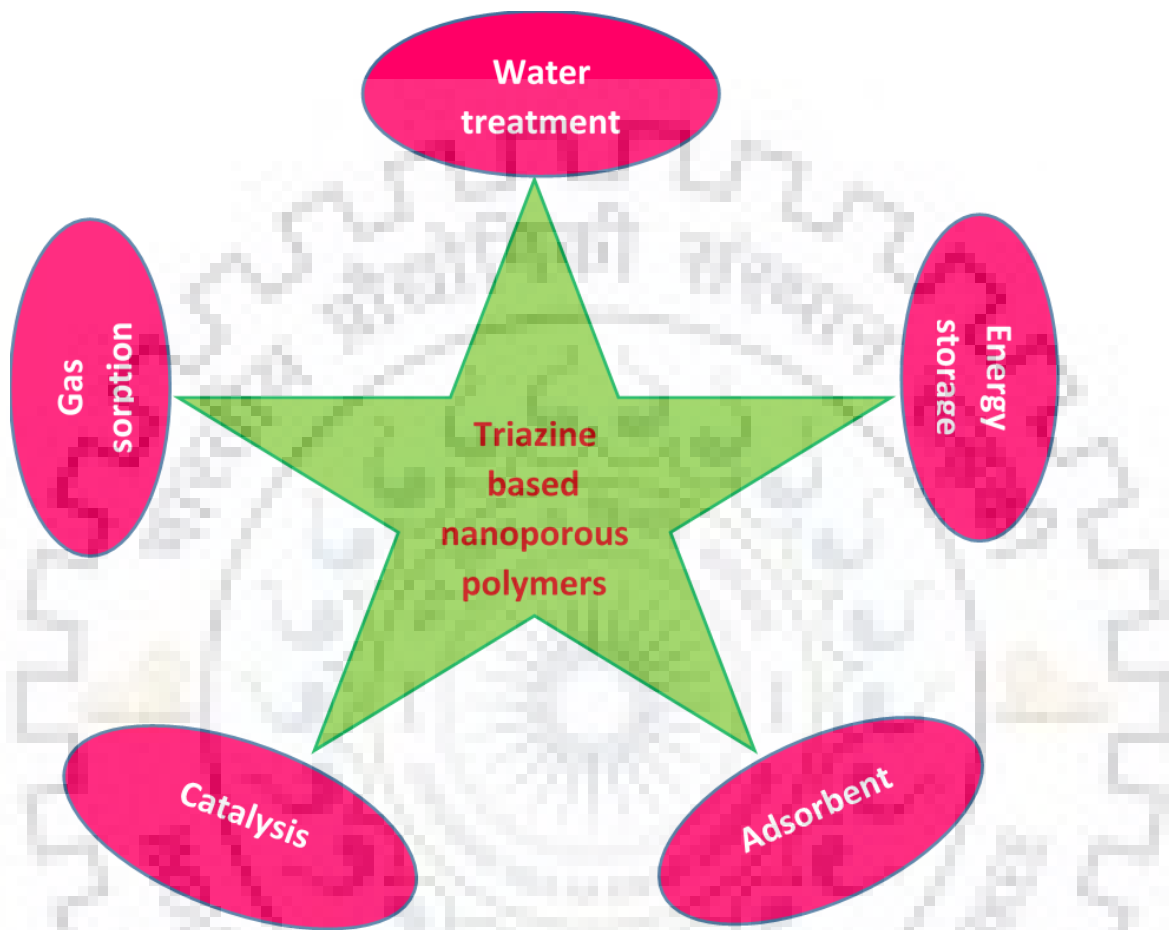


Figure 1.9. Various applications of nitrogen enriched triazine based polymeric materials.

1.6.1. Gas sorption and storage

Over past several decades, significant research effort has been devoted to carbon capture and sequestration (CCS) projects due to widespread concerns of the rapid increase in the CO₂ level in the atmosphere owing to the large scale use of fossil fuels for energy production, which creates adverse effects such as global climate change and ocean acidification.[19-25] An alternative way to tackle this problem is to use H₂ for energy production. The large energy density of 33.3 kWh kg⁻¹ (three times higher as compared to gasoline) and free from pollutants are the major advantages although, lower volumetric energy density sometimes limit its use.[49,50] Thus, efforts are made to store more hydrogen in smaller volumes through various chemical and physical interactions with

adsorbents have provided some hope for the future use. The U.S. Department of Energy (DOE), has set a target of 5.5 wt% gravimetric storage capacity and 40 g l⁻¹ volumetric capacity of H₂ using adsorbent technology near ambient working conditions. However, this goal is way higher than the best-reported hydrogen storage capacity by any solid adsorbent.[49,50] A similar scenario is also persistent for CH₄ storage. Efforts are being made to make suitable adsorbents that can have a sustainable adsorption of H₂ and CH₄.[52,140]

Gu *et al.* have designed triazine and spirobifluorene-based microporous polymers (Sbf-TMPs) by tuning the ratios of precursors and created a competitive environment between Friedel-Crafts reaction and Scholl coupling reaction (*Figure 1.10*). These materials exhibit CO₂ capture capacities of 9.2-13.3 wt% at 0 °C and 1 bar and Q_{st} values in the range of 27.9-30.7 kJ mol⁻¹ at zero coverage, which fall in the desirable range for the regenerability of CO₂ sorbents.[102]

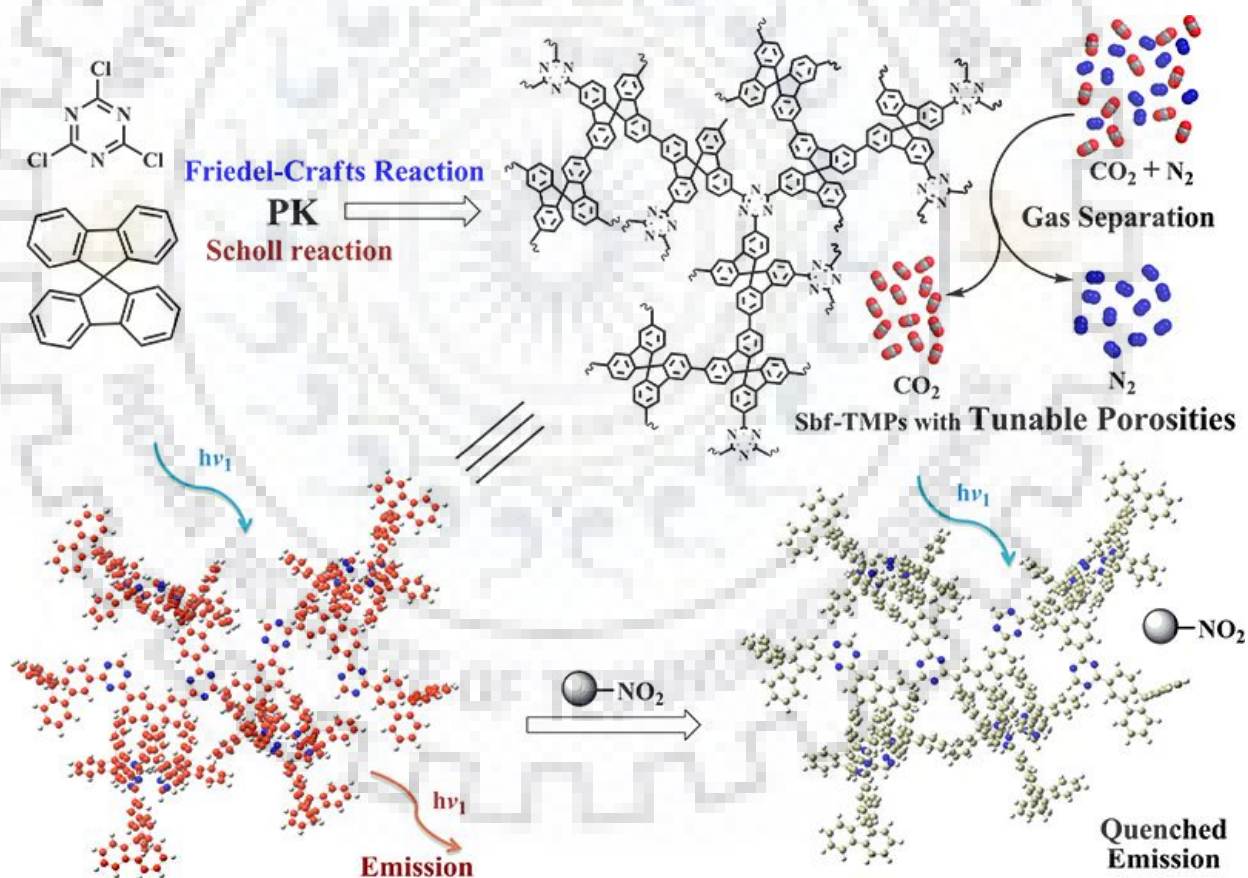


Figure 1.10. Diagram of the preparation of Sbf-TMPs from the concurrent chemical reactions and its applications in CO₂ capture and fluorescent sensing. [Reprinted with permission from ref. 102 © 2017 American Chemical Society]

Further, copolymerization of 1,4-bis-(2,4-diamino-1,3,5-triazine)-benzene with terephthalaldehyde and 1,3,5-tris(4-formylphenyl)benzene in DMSO at 180 °C afforded highly porous NRPP-1 and NRPP-2 with S_{ABET} of 1579 and 1028 $\text{m}^2 \text{g}^{-1}$, respectively. The combination of high nitrogen content, π -electron conjugated structure, and microporosity make NRPPs very effective in CO_2 uptake and I_2 capture. NRPPs exhibit high CO_2 uptakes (NRPP-1, 26.8 wt% and NRPP-2, 31.1 wt%) at 0 °C and 1.0 bar (Figure 1.11). The CO_2 uptake of 31.1 wt% by NRPP-2 is the second highest value reported to date for porous organic polymers. According to vapor iodine uptake studies, the polymers display high capacity and rapid reversible uptake for I_2 (NRPP-1, 192 wt% and NRPP-2, 222 wt%).[136]

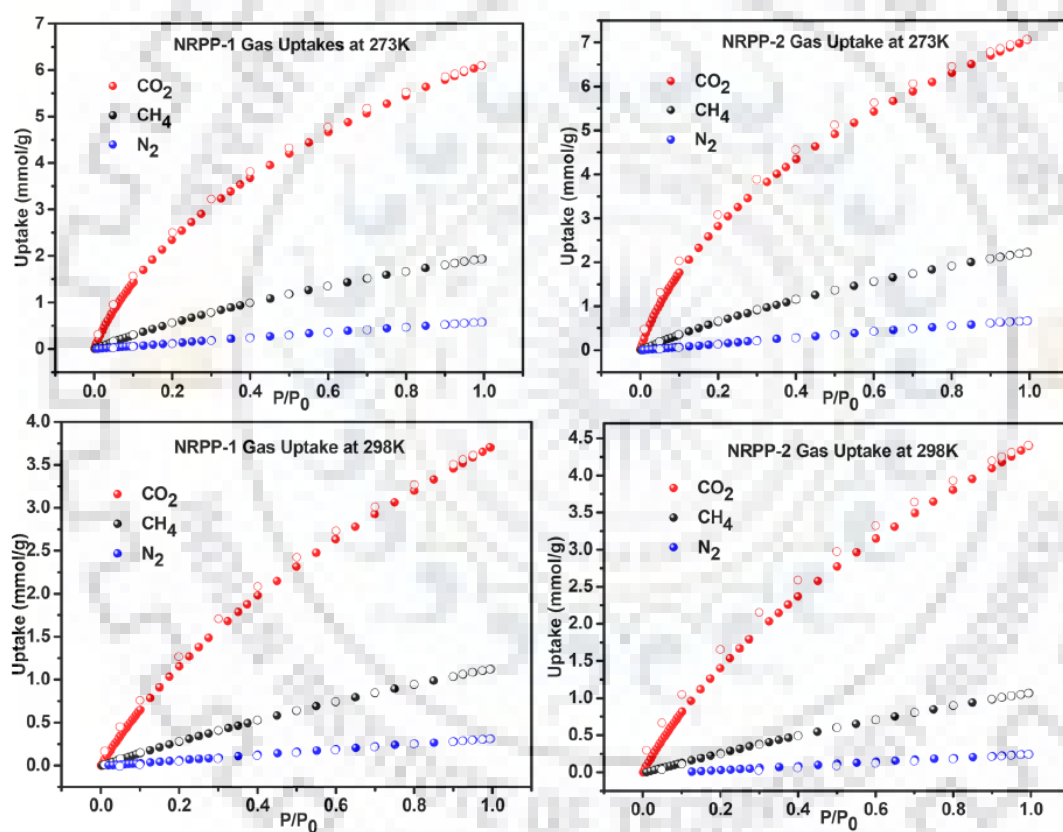


Figure 1.11. CO_2 , CH_4 , and N_2 uptake isotherms of NRPP-1 and NRPP-2 at 0 and 25 °C. [Reprinted with permission from ref. 136 © 2018 American Chemical Society]

Recently, Dai et.al have synthesized triazine and carbazole bifunctionalized task-specific polymer which exhibits CO_2 uptake of 18 wt% at 1 bar and 0 °C .[139] Kundu *et al.* have observed that copolymers composed of triazine and thiophene moieties within the (HMCs) network increases the electron donating properties of the frameworks. Thus, these porous polymers displayed efficient

adsorption of Lewis acidic CO₂ molecules and showed good CO₂/N₂ adsorption selectivity. The maximum CO₂ uptake of 62.4 wt% at 0 °C under 3 bar pressure has been observed. Maximum CO₂/N₂ selectivity was observed to be 72:1 at 0 °C.[144]

Buyukcakir have reported charged covalent triazine framework (cCTF) using cyanophenyl substituted viologen dication as a monomer through ionothermal trimerization reaction using ZnCl₂ as both catalyst and reaction medium. The resulting cCTFs showed high specific surface areas up to 1247 m² g⁻¹, and high physicochemical stability. The incorporation ionic moieties to porous organic polymers improved substantially their CO₂ affinity up to 13 wt%, at 1 bar and 0 °C along with high Q_{st} values of 40 kJ mol⁻¹ and efficiency as an organocatalysts for CO₂ conversion.[122] Further, triazine-based polyimides (TPIs) synthesized by Liebl shows specific surface areas up to 809 m² g⁻¹ (TPI-1) with pore size distribution ranging from 0.4 to 3 nm. The maximum uptake values for CO₂ (10.7 wt%) were observed for TPI-1 at 0 °C and 1 bar. The selectivity of 56 for CO₂ over N₂ at 25 °C was observed for TPI-7.[135] Jena *et al.* have synthesized covalent triazine frameworks functionalized with acetylacetonate group (acac-CTFs). These are obtained from the polymerization of 4,4-malonyldibenzonitrile under ionothermal conditions and exhibit S_{ABET} of 1626 m² g⁻¹. The materials show CO₂ uptake of 13.3 wt% at 0 °C and 1 bar and H₂ storage capacity of 1.53 wt% at 0 °C and 1 bar, with CO₂/N₂ selectivity of 46 at 25 °C. The enhanced CO₂ uptake value and good selectivity are due to the presence of dual polar sites (N and O) throughout the material.[145]

Dai and coworkers investigated the CO₂ and H₂ capture and storage capacities of CTFs modified by lutidine, pyrimidine and bipyridine units. The maximum CO₂ uptake of 24.5 wt% was observed for bipyridine-CTF synthesized at 600 °C at 0 °C and 1 bar. Moreover, selectivity of CO₂ vs N₂ of a nitrogen-rich pyrimidine-based CTF synthesized at 500 °C (Henry: 189, IAST: 502) is the highest reported among all porous organic polymers. Maximum H₂ uptake of 2.12 wt% at -196 °C was observed for CTF1 synthesized at 600 °C at 1 bar.[50] Functionalized perfluorinated covalent triazine-based frameworks FCTF-1, and FCTF-1-600 with specific surface area 623 and 752 m² g⁻¹, respectively, have shown a better CO₂ capture capacities upto 20.5 and 24.3 wt%, respectively, as compared to the pristine CTF-1 and CTF-1-600.[103] Further, breakthrough experiments for CO₂ capture using pristine and functionalized CTFs by passing CO₂-N₂ (10:90 v/v) mixture under kinetic flow conditions at 25 °C have shown a capacity of 3.2 wt% in FCTF- 1 > FCTF-1-600 (2.8 wt%) > CTF-1-600 (1.2 wt%) > CTF-1 (0.5 wt%).[146]

There are many other reports where nanoporous polytriazines and triazine based polymers have shown CO₂ capture capacities ranging from 4 to 26 wt% with varying values of SA_{BET}. All these materials have their own merits for the synthesis as well as the explored applications. In general, a common concept that arises in these research lies in the pathway to synthesize these materials by choosing appropriate precursors. The presence of the electron rich moieties and the aromatic system have shown better interaction between the CO₂ molecules and the frameworks through a Lewis basic-Lewis acidic interactions.[140-150] Moreover, the micropores in some examples have shown to improve the hydrogen storage behavior.[52,140,145]

1.6.2. Supercapacitors

The demand for energy storage systems that could drive the ever-increasing requirement of storing the energy harvested from the non-conventional sources beyond batteries put a pressure on exploring the development of supercapacitors with high energy density.[151-154] Although, various advanced batteries such as lithium ion, sodium ion batteries etc. have been extensively used at this moment but their power densities and huge volume remain bottle necks.[155-160] Generally, supercapacitors have shown high power density and long life cycles as compared to batteries. The high power density required for the electric vehicles, portable electronic devices, and power sources for memory backup could be possible when the batteries are integrated with the supercapacitors. The commonly accepted mechanism that works for the storage of energy by supercapacitors based on the electric double layer capacitor (EDLC) and pseudocapacitive concepts (*Figure 1.12*).

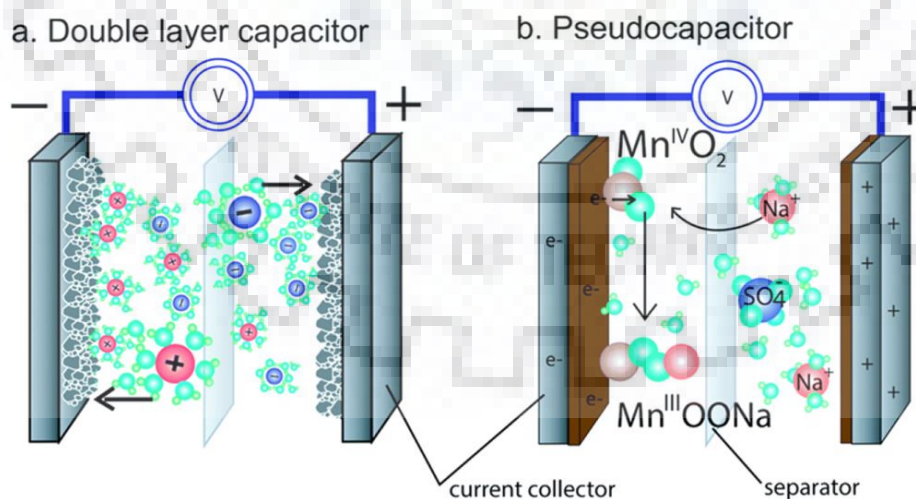


Figure 1.12. Supercapacitors based on the electric double layer capacitor (EDLC) and pseudocapacitive concepts. [Reprinted with permission from ref. 152 © 2014 Royal Society of Chemistry]

The EDLC contributes greatly to the capacitive performance of the supercapacitors and hence, an increased surface area always remains beneficial. Therefore, the use of high surface area nanoporous materials as active electrode materials for the supercapacitor application is always sought. Moreover, presence of heteroatom such as nitrogen in the framework further improves the performance of the supercapacitors. Based on this, many of the nanoporous polytriazines and triazine based polymers have been explored for the supercapacitor applications as discussed below.

Triazine based framework, TDFP-1, synthesized by Schiff base condensation of 1,3,5-tris-(4-aminophenyl)-triazine and 2,6-diformyl-4-methylphenol using solvothermal approach has S_{BET} of $651 \text{ m}^2 \text{ g}^{-1}$. This specimen when used as active electrode material for supercapacitor application has shown specific capacitance of 354 F g^{-1} at scan rate of 2 mV s^{-1} with 95% retention of its initial specific capacitance after 1000 cycles at current density of 10 A g^{-1} . The performance of the material was attributed to the extended conjugation as well as ionic conductivity of polymeric framework, which makes TDFP-1 a promising candidate for supercapacitor applications (Figure 1.13).[161]

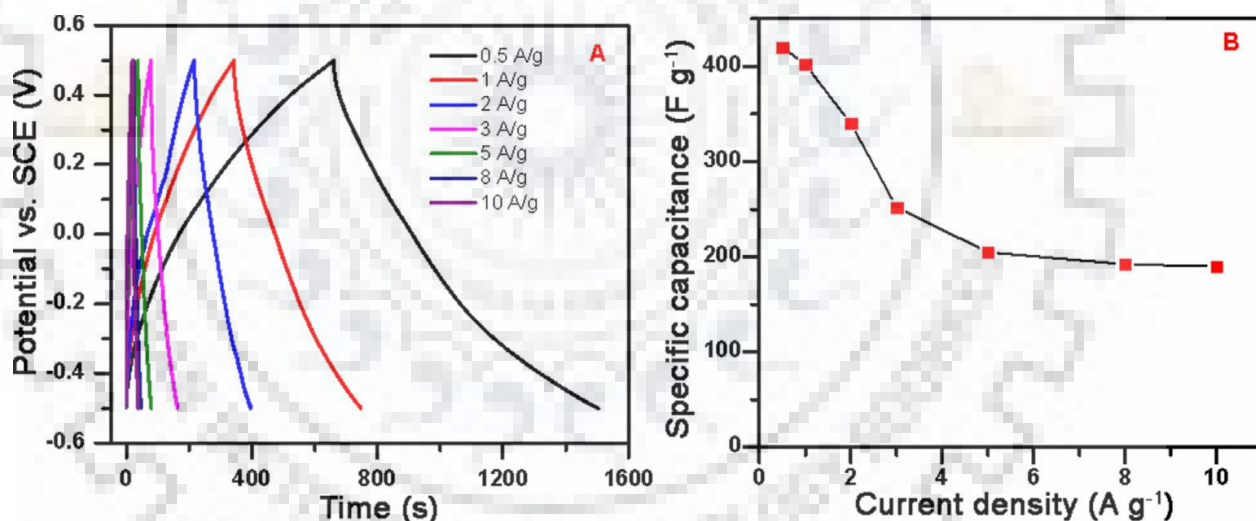


Figure 1.13. Electrochemical performance of TDFP-1 polymer: (a) GCD cycles (b) C_{sp} vs. current density. [Reprinted with permission from ref. 161 © 2017 Wiley VCH]

Bhanza *et al.* have also reported porous triazine based polymer TPDA-1 via Schiff base condensation between, 2,4,6-trihydroxyisophthalaldehyde and 1,3,5-tris(4-aminophenyl)triazine. The TPDA-1 has S_{BET} of $545 \text{ m}^2 \text{ g}^{-1}$ and high specific capacitance of 469 F g^{-1} , at scan rate of 2 mV s^{-1} . The cyclic stability with 95% retention of its initial specific capacitance was observed after

1000 cycles at 5 A g^{-1} . This performance was also attributed to the high SA_{BET} and extended π -conjugation (Figure 1.14).[162]

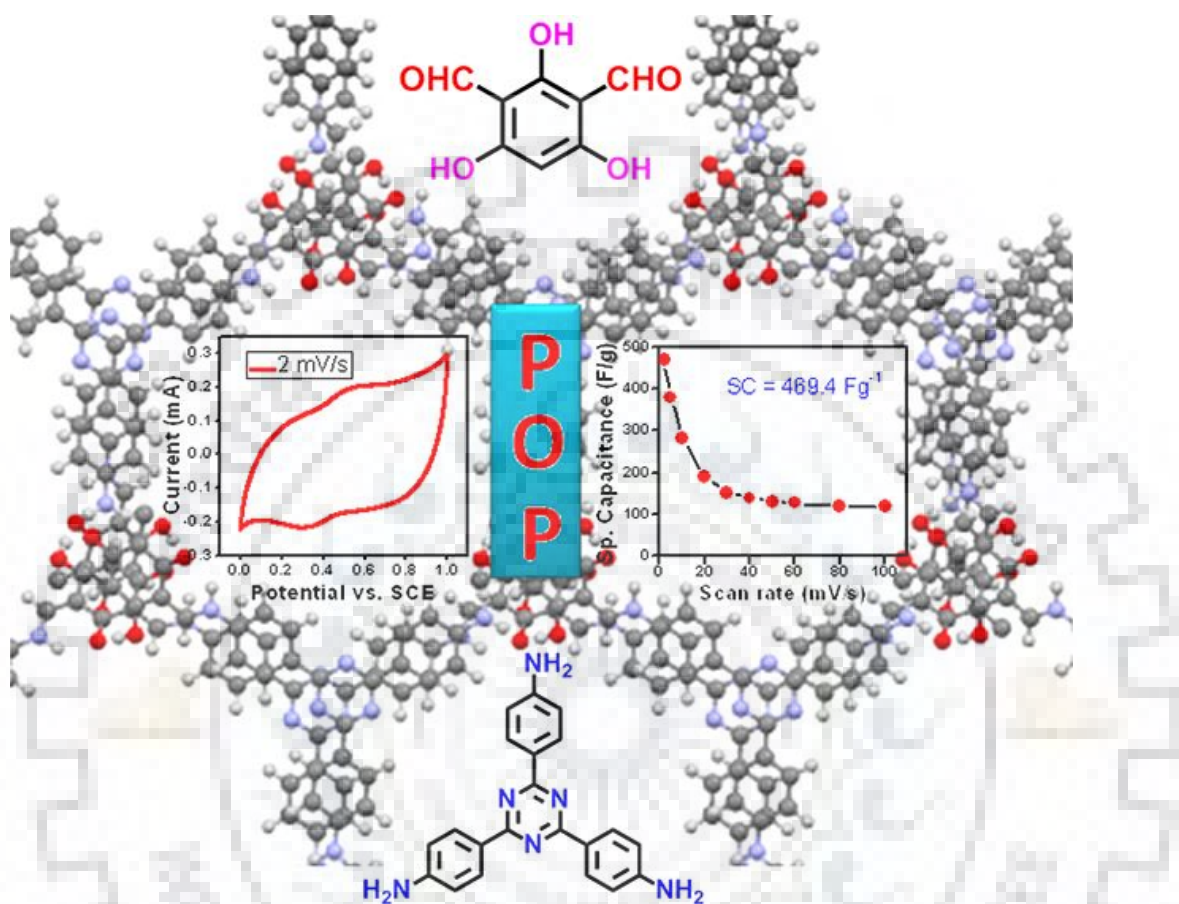


Figure 1.14. Schematic representation for the synthesis of TPDA-1 and its electrochemical performance. [Reprinted with permission from ref. 162 © 2018 American Chemical Society]

A series of nitrogen-enriched, microporous triazine-based frameworks (PTFs) was synthesized by the cyclotrimerization reaction of the 1,3,5 tri-cyanobenzene using ZnCl_2 as a catalyst (Figure 1.15). The nitrogen content has enhanced the supercapacitor performance. The energy density of 62.7 Wh kg^{-1} was estimated at 8750 W kg^{-1} . Interestingly, when the reaction temperature raised from 550 to $700 \text{ }^\circ\text{C}$, the specific surface area increases from 1212 to $2482 \text{ m}^2 \text{ g}^{-1}$, however, no appreciable change in the supercapacitor performance was observed. The C_{sp} changes from 147.1 to 151.3 F g^{-1} at a current density of 0.1 A g^{-1} . [163] Li and coworkers have designed nitrogen-rich triazine based frameworks TCNQ-CTFs by the cyclotrimerization reaction of tetracyanoquinodimethane with nitrile groups. Very high SA_{BET} of $3600 \text{ m}^2 \text{ g}^{-1}$ was reported in the

specimen synthesized at 800 °C designated as TCNQ-CTF-800, which has shown C_{sp} of 380 F g⁻¹ with the energy density of 42.8 Wh kg⁻¹ and no loss in capacitance even after 10,000 cycles (Figure 1.16).[164]

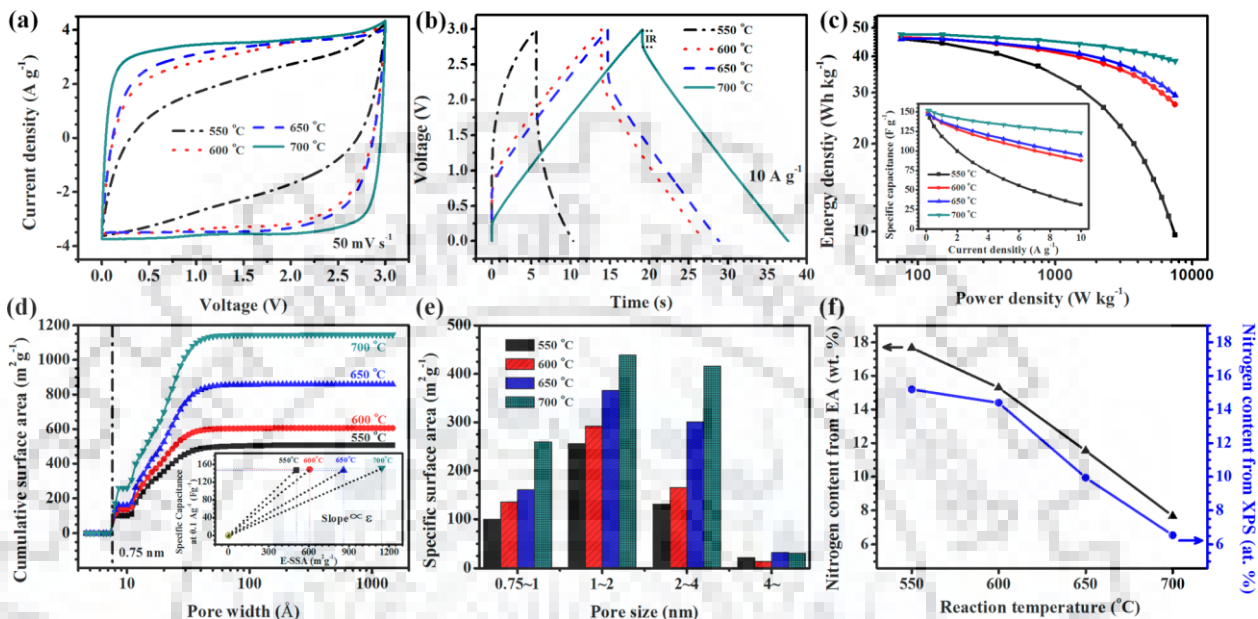


Figure 1.15. (a-c) Electrochemical properties of the PTFs: (a) CV curves, (b) GCD curves, and (c) Ragone plots (d-f) performances of PTFs. [Reprinted with permission from ref. 163 ©2014 American Chemical Society]

Xu *et al.* have synthesized conjugated microporous covalent triazine-based organic polymer POPM-TFP by condensation of melamine and triformylphloroglucinol using solvothermal approach. The role of nitrogen in this example was not only to improve the specific capacitance by introducing pseudocapacitance to the electrode due to the presence of nitrogen in the framework, but also improved the wettability of the electro-active surface area of the electrode material. The maximum specific capacitance of POPM-TFP is calculated to be 178.0 F g⁻¹ at 0.5 A g⁻¹ and slight decrease in specific capacitance was observed with increasing current density, due to the hierarchical pore structure, which facilitates the smooth transfer of ions at higher current densities. The energy density of 25.8 Wh kg⁻¹ was calculated at power density of 727 Wkg⁻¹. [165] Very recently, Xue *et al.* have reported a covalent organic framework (NWNCOF-1) by the condensation reaction of melamine and 2,4,6-trichloro-1,3,5-triazine at 150 °C for four days, followed by aging for 12 hours. The S_{ABET} of NWNCOF-1 is 301 m² g⁻¹, with pore size centered at 1.41 nm. This material exhibits C_{sp} of

155 F g⁻¹ at 0.25 A g⁻¹ current density using 6 M KOH in a three electrode configuration. This COF material has shown 100% capacitance retention after 20,000 GCD cycles.[141]

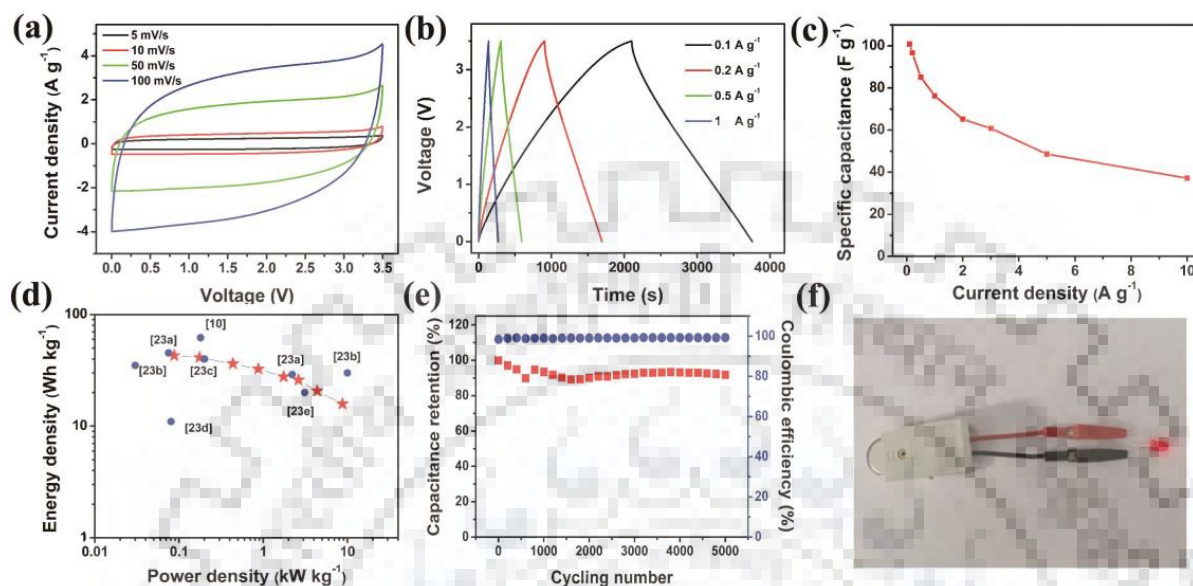


Figure 1.16. Electrochemical characterizations of TCNQ-CTF-800 (a) CV curves. (b) GCD curves. (c) C_{sp} at different current densities (d) Ragone plot (e) cyclic stability (f) snapshot of LED. [Reprinted with permission from ref. 165 ©2018 Wiley VCH]

All of the above literatures have suggested that the presence of nitrogen in the polymeric framework could improve the performance of the supercapacitors. In general, the specific surface area and pore size distribution played significant role in the performance too, but these are not the only factors that could tune the C_{sp} values.[152-165] For example, in very high surface area materials also the C_{sp} is inferior than many of the materials with low SA_{BET} . Hence, materials must be designed keeping in mind that neither the control of textural properties nor the presence of nitrogen could provide the best performance rather a suitable combination of both could be highly beneficial for the supercapacitor applications. This put a lot of pressure on the experimentalist to find the exact parameters for making the ideal materials, however, once found the research is highly rewarding.

1.6.3. Organocatalysis using nanoporous polytriazines and triazine based polymers

For decades, metals and metal based materials have dominated the catalysis field. Some of the major advantages being the ease of losing electrons, availability of vacant orbitals and some of the catalysts are inexpensive in nature.[166-168] Conversion of industrial chemicals are still carried out by the metal based catalyst. On many occasions, these catalysts are immobilized/incorporated in various matrices that include polymers too. The leaching of metals, poisoning of catalysts, problems

associated with the recyclability and cost have forced the scientific community to look for other alternatives. This, in turn, have made the way for exploring metal-free small organic molecules as catalysts for various organic conversions. The availability of pathways to functionalize these molecules further strengthen the research area. These homogeneous catalysts are used in several organic conversions in the recent times. However, on many occasions, separation of these small molecules are quite difficult. The recent trend was to create functionality similar to the small molecules in the frameworks and polymeric materials so that these could be useful for the organic conversion in the heterogeneous manner. High surface area nanoporous polymeric materials have been explored as heterogeneous catalysts for different organic transformations owing to the major advantages such as (i) metal free catalysts hence, no chance of leaching out of metals, and (ii) ease of separation from the product compared to the homogenous catalysts (both metal based catalysts and organocatalysts). These made these heterogeneous catalysts as safe, green, environmental friendly and cost effective alternatives to produce high quality molecules of significant importance.[166-168]

Recently, nitrogen-enriched polymeric materials have emerged as promising metal-free candidates for heterogeneous catalytic applications. Significantly, triazine functionality incorporated framework exhibit high basicity due to the lone pair of electrons to catalyze organic transformations. Further, high surface area and hierarchical pore structure also contribute to access of exposed active sites. There are several reactions catalyzed by triazine based nanoporous polymers, among these Knoevenagel reaction could be considered as an important base-catalysed reaction for the development of C-C bond formation.[167-169] The Knoevenagel reaction could be considered to be a key step for the synthesis of natural products, cosmetics, herbicides, insecticides, perfumes, therapeutic and pharmacological important drugs.[167-169] Initially, Knoevenagel condensation reaction was carried out using homogeneous organocatalysts. Catalyst recovery and recyclability are the two major concerns that further encouraged researchers to develop their solid catalyst counterparts to carry out the catalysis in heterogeneous conditions.

Park *et al.* reported a triazine-based microporous polymeric network for the microwave assisted catalysis of Knoevenagel reaction between ethylcyanoacetate with various aromatic aldehydes.[67] The material could catalyze the reaction efficiently within 10 min in aqueous condition and recovered easily and can be reused for three times without significant loss in its catalytic activity.[67] Mu *et al.* examined the catalytic activity of a triazine based polymeric material, MFCMP-1, for the Knoevenagel reaction of malononitrile with aromatic aldehydes, cyclic

ketones and heterocyclic aldehydes. High yield and complete conversion of precursors into products was observed for all aldehydes with electron-donating and withdrawing groups and catalyst has shown recyclability upto ten cycles without any major loss in the activity.[168]

Triazine-based porous organic polymer, TPOP-2, was used as a organocatalyst for the synthesis of 2-amino-chromenes in a one-pot three component reaction using aromatic aldehyde, malononitrile and phenols (resorcinol or 2-naphthol) under both solvent-free conditions (for resorcinol) and in aqueous medium (for 2-naphthol). Importantly, good yields (~85%) of corresponding 2-amino-4H-chromenes were obtained with several other aldehydes containing strong electron-donating or withdrawing groups, owing to the high basicity of amine and triazine groups in the TPOP-2 polymeric material (*Figure 1.17*).[169]

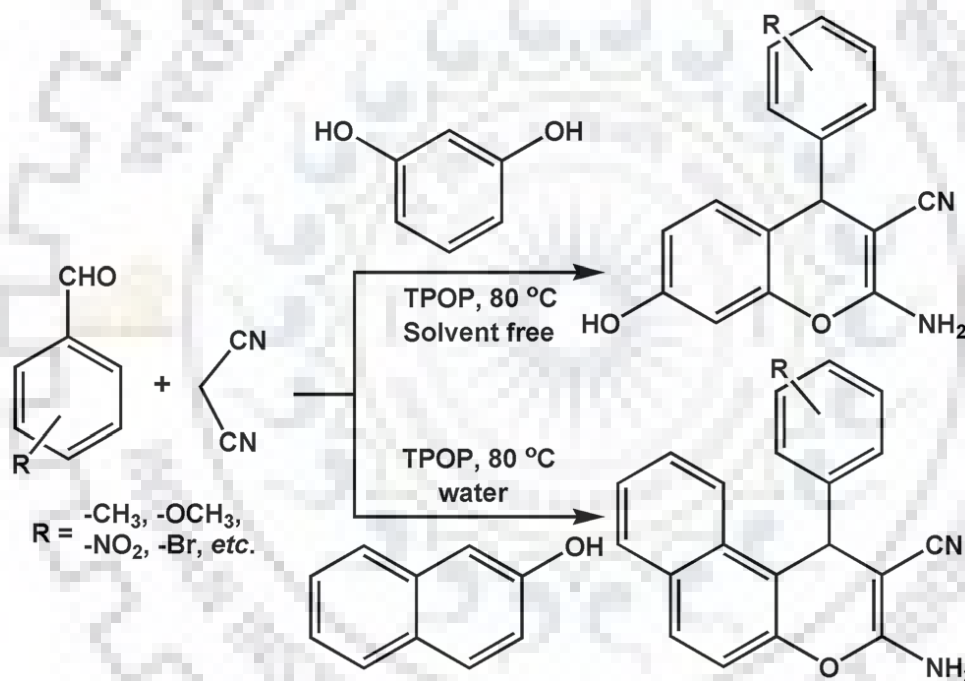


Figure 1.17. Synthesis of 2-aminochromene derivatives using organocatalyst TPOP. [Reprinted with permission from ref. 169 © 2015 Royal Society of Chemistry]

The triazine-based microporous polymer (TMP) was employed as a metal-free catalyst for the epoxidation of styrene in a mixture of solutions of H₂O₂ and NaHCO₃ under ambient conditions and 98% yield was obtained within 6 h.[170] The higher activity under aqueous conditions was observed due to the stabilization of peroxymonocarbonate ion (HCO₄⁻) (catalytically active species) with TMP framework. Catalyst was recovered and could be reused four consecutive cycles without any loss in its selectivity and activity.

Utilization of CO₂ gas is another way for controlling the growing CO₂ productions from fossil fuel based power plants, responsible for various hazardous environmental impacts.[171,172] Recently, conversion of CO₂ into valuable products has drawn considerable attention of scientific community and one of the most followed route is the conversion of CO₂ into epoxides to produce cyclic carbonates.[172-173] Currently, triazine-based organic polymers were used for the synthesis of cyclic carbonates from carbon dioxide and epoxides, as a catalyst due of their high basicity.[173,174] The frameworks CTF-1, CTF-1-HAS and CTF-P-HSA were employed for the catalytic conversion of CO₂ into cyclic carbonates. The CTF-1, CTF-1-HSA and CTF-P-HSA have shown 81.2, 100, and 100% conversion with a selectivity of 94.4, 95.8 and 94.6%, respectively, whereas, without the catalyst only 2.3% conversion was realized. Lower product selectivity was observed due to decrease in surface area and pore volume when catalysts were recovered by filtration and reused without any activation. After the activation of recovered catalyst at 150 °C for 1 h, no significant loss of activity was observed up to six cycles.[77] Other catalytic reactions, like oxidation of benzyl alcohol and conversion of methane to methanol were also explored using triazine based polymers.[175-177]

Zhang *et al.* have employed mesoporous poly-melamine-formaldehyde (mPMF) as a catalyst for the chemoselective acetylation of aldehydes with high turnover frequency using MeOH and/or 1,3-propanediol as solvents.[176] One of the major advantage using mPMF as a catalyst is the selective formation of dimethyl acetal from trans-cinnamaldehyde without going cis-trans isomerization. A variety aliphatic and aromatic aldehydes were also examined and good yields (95 %) of the corresponding acetals were produced. Further, the mPMF catalyst have shown excellent recyclability without any loss of its catalytic activity upto five consecutive runs. They observed a synergistic hydrogen bonding activation mechanism for the acetalization reaction, and proposed that basic nature of aminal (–NH–CH₂–NH–) groups and triazine rings in the mPMF network were responsible for the selectivity of this mPMF catalyst. The ease and low-cost synthesis, stability, and reusability of mPMF makes it a promising catalyst for large scale acetylation processes for practical applications.

Additionally, triazine based materials have been shown to be excellent support for immobilizing metal ions and metal nanoparticles, which facilitated strong interaction between the reactants and the active sites, and improving the catalytic performance for various organic transformations such as oxidation of alcohols, oxygen reduction reaction (ORR), water splitting reaction, Suzuki-Miyaura cross-coupling, hydration of nitriles, oxidation of methane and carbon

monoxide, Sonogashira cross-coupling reaction, Mizoroki-Heck cross-coupling reaction, Ullmann O-arylation reaction and Chan-Lam cross-coupling reaction.[177-183] Further, aggregation and metal leaching could be avoided using triazine-based polymeric materials owing to strong interaction of framework with nanoparticles. However, the discussion of catalytic activity of metal immobilized/incorporated triazine based polymers are not in the scope of this work.

1.6.4. Abatement of water pollution by nanoporous polytriazines and triazine based polymers

A common statement that is said regarding the water crisis is “The third world war will be fought for water only”. This shows the importance of water and also the crisis related to it at present time as well as that is expected in the near future. Scarcity of clean and drinkable water is not a problem of any particular region or nation but a problem of whole mankind.[184-190] The industrialization that satisfy the need of large increase in the population contributed greatly to this problem. The sustainability of most of the industries depends a lot on the availability of water which in turn produces enormous amount of polluted water released with and without treatment. Moreover, widespread anthropogenic activities such as industrial processes, mining, agricultural developments and disposal of industrial waste are responsible for raising the concentration of toxic materials to dangerous levels.[185-194] In some cases, the waste water treatment was not given enough importance due to the lack of pressure from the law enforcement agencies as well no concrete policies for the same. However, very recently in the developed and in most of the developing countries the water pollution is taken very seriously. The “Namami Gange-national mission for clean ganga” project is a perfect example for the same.

The water pollution can be addressed only if it is abated from the sources. Treating the industrial waste water before it is released to any water bodies could be the best way to take care the problem. The industrial waste water carries wide range of pollutants such as heavy metals, radioactive elements, small organic molecules and solvents, organic dyes, biomolecules etc. depending upon the industry from where it is released.[184-195] The negative impact of these pollutants vary depending upon the concentration and other physicochemical properties. Among the heavy metals nickel, chromium, lead, zinc, arsenic, cadmium, selenium and uranium are the major components in the industrial waste.[184-199] The speciation of these metals also play significant role in their impact on the quality of water.

To date, various efficient methods have been applied for the removal of heavy metals such as chemical precipitation, ion exchange, reverse osmosis, electrodialysis, ultrafiltration,

nanofiltration, coagulation, flocculation, floatation, etc. However, these methods have several disadvantages such as high cost, unpredictable recovery, generation of toxic sludge. Among these methods, adsorption process is the most preferred method for removal of toxic pollutants from wastewater due to its various advantages such as high efficiency, cost effectiveness, low energy consumption and easy operation.[195-200] Recently, various adsorbents such as metal oxides, activated carbon, activated carbon-silica aerogel composite materials, conjugated polymers, ion-imprinted polymers, polyphenolic compounds, mesoporous silica, porous organic polymers (POPs), metal organic frameworks (MOFs), zeolites, and graphene oxide have been employed for water treatment.[80-90] Moreover, functionalization of the high surface area adsorbents with various moieties has substantially improved the performance as compared to the pristine specimen. In some of the recent reports, MOFs, chitosan, zeolites, and POPs, functionalized with amine and amidoxime groups have been explored.[85-94] Now a days, nitrogen enriched triazine based polymeric materials are very popular for the removal of toxic ions because of their high surface area, hierarchical pore structure and strong binding affinity towards metal ions and dye molecules.[200-209]

Recently, microporous triazine based framework (CTF-1) with specific surface area of $490 \text{ m}^2 \text{ g}^{-1}$ and pore size distribution centered at 1.3 nm has been employed for Cd^{2+} ions removal from aqueous solution, with adsorption capacity of 29.26 wt% at pH of 7. The kinetic studies indicated that the adsorption was pseudo-second order, and was highly dependent on *pH* and temperature of the system. Ghazi *et al.* have suggested the electrostatic interaction between cadmium (II) ions and triazine based framework.[200] Very recently, Dinari *et al.* have synthesized a triazine based covalent organic framework (COF) with high S_{BET} of $1935 \text{ m}^2 \text{ g}^{-1}$ and pore size in the range of 2.2 nm and high N content. The synthesized specimen has been employed for Cd^{2+} removal from aqueous solution, with adsorption capacity of 396 mg g^{-1} .[201] Wang *et. al* have also investigated the adsorption of organic dyes using CTF-1 as an adsorbent (*Figure 1.18*). Specimen, CTF-1 exhibited adsorption capacity of 1.01 mmol g^{-1} for organic dye RhB, with high efficiency and good recyclability.[202] Moreover, CTF was also has been proved efficient adsorbent for the removal of aromatic compounds from aqueous solution. It has been observed that adsorption of the hydroxyl-, amino-, nitro-, and sulfonate-substituted monocyclic and bicyclic aromatic compounds was generally stronger than their non-substituted, nonpolar counterparts (benzene and naphthalene). The adsorption efficiency of CTF was explained by several specific interactions between CTF and aromatic compounds such as hydrogen bonding (hydroxyl- and amino-substituted compounds), and

p-p electron-donor–acceptor (EDA) interaction (nitroaromatic compounds) with the triazine structure of CTF.[203]

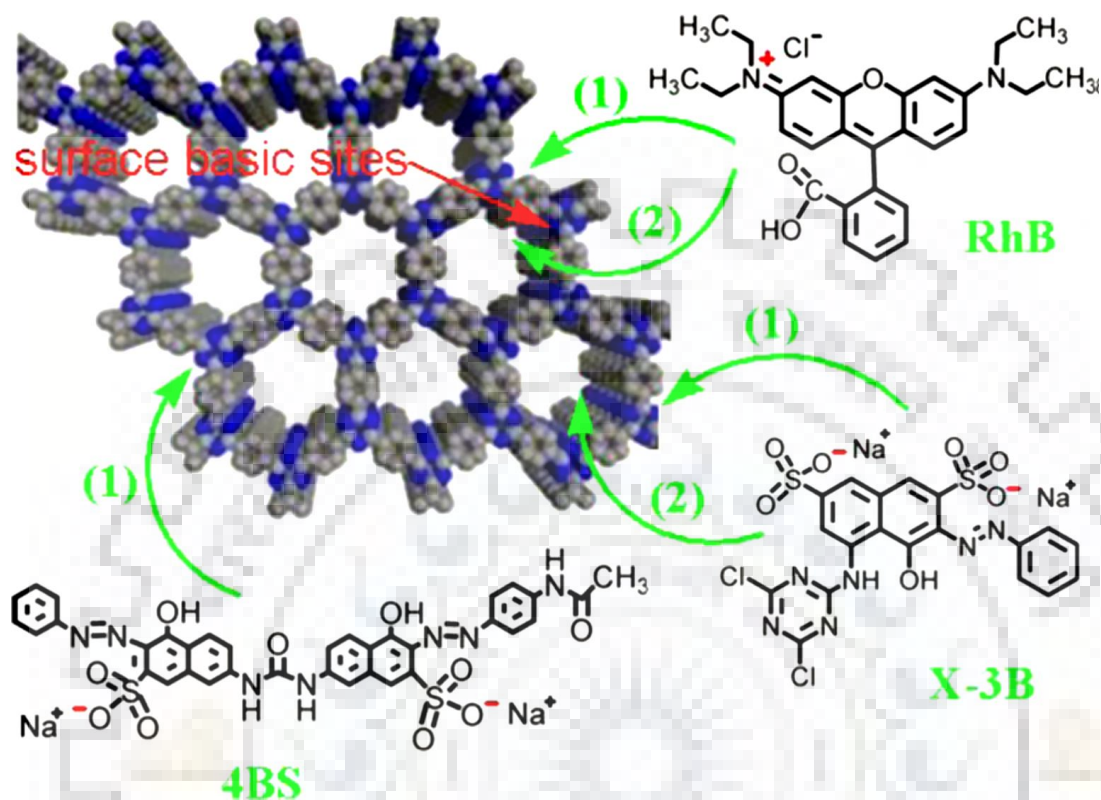


Figure 1.18. Proposed mechanism for the adsorption of organic dyes onto CTF. [Reprinted with permission from ref. 202 © 2014 Elsevier]

Task specific triazine-polyimide functionalized COF (TS-COF-1) with S_{ABET} of $1484 \text{ m}^2 \text{ g}^{-1}$ and pore volume of $0.90 \text{ cm}^3 \text{ g}^{-1}$, was synthesized by Zhu *et al.* which has shown superior adsorption capacity of 1691 mg g^{-1} for the adsorption of methylene blue (MB) from aqueous solution. The superior efficiency of the specimen was attributed to high surface area, intrinsic pore-size of the TS-COF-1.[204] Recently, SNW-1, a triazine based cross-linked polymer has been synthesized by Yang *et al.* using Schiff base chemistry. It has been employed for the selective removal of Hg^{2+} ions in presence of various ions such as Cd^{2+} , Ni^{2+} , Zn^{2+} , Cu^{2+} , Co^{2+} , Ca^{2+} , Mn^{2+} and Mg^{2+} from aqueous solution with a high adsorption capacity of 1172 mg g^{-1} . The superior performance was attributed to the chelate formation ability of the framework with Hg^{2+} ions due the high N content (50 wt%) and S_{ABET} of $301 \text{ m}^2 \text{ g}^{-1}$. [205] Further, SNW-1 specimen was also utilized for sensing of nitro-aromatic explosives such as 2,4,6-trinitrotoluene (TNT), 2,4,6-trinitrophenylmethylnitramine and picric acid (PA) without any interference in presence of common organic solvents.[206] Furthermore, triazine

based covalent organic framework (CTF-CTTD) having S_{ABET} of $1684 \text{ m}^2 \text{ g}^{-1}$ with hierarchical pore structure synthesized by Jiang *et al.* shows high adsorption capacity of 387 wt% for iodine. The high efficiency of the material was attributed to the hierarchical pore structure, N content of triazine ring (1.48%), as well as conjugation within the framework. Furthermore, CTF-CTTD also shows an excellent adsorptive performance for removing Rhodamine B (RhB) with adsorption capacity of 684.9 mg g^{-1} . [207]

Further, three triazine-based conjugated microporous polymers viz. TMDATA, TTPA, TTDATA and TTMDATA were synthesized using Friedel-Crafts reaction in methanesulfonic acid. The synthesized polymers possessed specific surface area of 308, 491 and $456 \text{ m}^2 \text{ g}^{-1}$ and shown iodine uptake of 4.92, 4.72 and 44.9 wt% in vapor phase, respectively. Adsorbed iodine was released slowly into ethanol or quickly upon heating (with a high degree of control). Further, investigations proposed that the strong affinity for I_2 is primarily due to porous nature, conjugated π -electron aromatic system and polarizable sites of triazine ring. Furthermore, luminescent analysis shows TTPA have high sensitivity to iodine molecules through fluorescence quenching. [208]

1.7. Motivation and objectives

“Energy and environment” are the two major research avenues that fascinated the author to contribute towards these during this doctoral research. The profound interest in these led to find many literatures through various search engines and finalizing the one that will have the best impact, was not an easy job. After many thoughtful and constructive discussions, it was decided to carry out research related to the development of high surface area polymeric materials which could potentially solve problems related to energy and environment. During this period, literatures related to the doping and incorporation of nitrogen into various carbonaceous and polymeric materials have shown some potential towards their use for both energy harvesting and storage as well as cleaning the environment. Not only the experimental evidence but also the theoretical predictions in this regard have provided the much needed boost to finalize the topic on synthesizing nanoporous high surface area polymeric materials that are rich in nitrogen. Unlike doping, where mostly the nitrogen content restricted to few wt%, the current research aims to produce materials with very high nitrogen content that could reach as high as 50 wt%. Based on all these facts and thorough investigation of the literatures, the objectives of the present research work are drawn;

- To synthesize metal-free high surface area Nitrogen-Enriched Nanoporous Polytriazines (NENPs) with controlled textural properties using inexpensive nitrogen-rich precursors such as melamine and cyanuric chloride
- To explore various conventional and non-conventional synthesis approaches tuned by varying the experimental parameters that could yield materials with desired properties
- To characterize the synthesized materials using the state of the art facilities that includes but not limited to FTIR, NMR, XPS, XRD, TGA/DTG, FESEM, TEM, CHNSO, ICP-OES etc.
- To investigate the textural properties of the NENPs by N₂ sorption analysis
- To investigate the applications related to
 - ✓ gas sorption and storage,
 - ✓ electrode materials for supercapacitors,
 - ✓ organocatalysis, and
 - ✓ uranium removal from effluent and enrichment from seawater conditions

1.8. Thesis outline

The present thesis consists of eight chapters;

Chapter I

- The detailed literature studies of polytriazines and triazine based polymers were carried out in this chapter.
- Various synthetic approaches used to make polytriazines and triazine based polymers are described in detail.
- Applications of polytriazines and triazine based polymers in the various fields such as gas sorption, supercapacitor, organocatalysis and water treatment have been emphasized.
- Based on the above, the objectives of the research are defined and included in this chapter.

Chapter II

- The detailed experimental procedures adopted for the synthesis of various specimens investigated in this research is given.
- The synthesis of nitrogen enriched nanoporous polytriazine by adopting various methods such as conventional heating, solvothermal, sonochemical and microwave assisted approaches.
- Basic principles of various analytical methods used for the characterization of the synthesized specimens have been discussed.

- Experimental methods related to the applications have been discussed in detail.

Chapter III

- The detailed structural and microstructural characterizations of NENPs synthesized by various conventional and non-conventional methods, have been carried out in this chapter. Based on the results the conclusions have been derived on the method that could produce the best materials.

Chapter IV

- The textural and gas sorption properties of the NENPs synthesized by different methods have been studied and discussed in this chapter. Selected materials are studied in detail to further recommend their applications.

Chapter V

- The electrochemical supercapacitor applications of the selected specimens were investigated using both three electrode configurations and investigated thoroughly in this chapter.
- Asymmetric supercapacitor device has been fabricated using representative specimen and tested to lit LEDs of different colours.

Chapter VI

- The organocatalytic activity of NENP-1 for the Knoevenagel reaction for the C-C bond formation have been carried out and the obtained results were discussed in detail.

Chapter VII

- The adsorption applications of NENP-1 for the removal of uranium from both aqueous and simulated seawater have been discussed. The achievement of uranium removal that could satisfy the WHO and USEPA limits is the focus point of this chapter. Furthermore, the uranium enrichment from the simulated seawater condition is discussed in details.

Chapter VIII

- The summary of the works that have been carried out in this research is given in this chapter along with the conclusions.
- The challenges faced during the research and the future prospects of the research area are also outlined and recommended.

References

1. R. Lee, The outlook for population growth, *Science*, 2011, **333**, 569-573.
2. S. Chu and A. Majumdar, Opportunities and challenges for a sustainable energy future, *Nature*, 2012, **488**, 294-303.
3. P. Mckendry, Energy production from biomass (part 1): Overview of biomass, *Biores. Technol.*, 2002, **83**, 37-46.
4. M. Hook and X. Tang, Depletion of fossil fuels and anthropogenic climate change-A review, *Energy Policy*, 2013, **52**, 797-809.
5. P. A. Owusu and S. Asumadu-Sarkodie, A review of renewable energy sources, sustainability issues and climate change mitigation, *Cogent Engg.*, 2016, **3**, 1167990. DOI:Org/10.1080/23311916.2016.1167990.
6. I. Dincer, Renewable energy and sustainable development: A crucial review, *Renew. Sust. Energ. Rev.*, 2000, **4**, 157-175.
7. R. H. Wiser, The role of public policy in emerging green power markets: An analysis of marketer preferences, *Renew. Sust. Energ. Rev.*, 2000, **4**, 177-212.
8. H. Lund, Renewable energy strategies for sustainable development, *Energy*, 2007, **32**, 912-919.
9. F. Hvelplund, Renewable energy and the need for local energy markets, *Energy*, 2006, **31**, 2293-2302.
10. N. L. Panwar, S. C. Kaushik and S. Kothari, Role of renewable energy sources in environmental protection: A review, *Renew. Sust. Energ. Rev.*, 2011, **15**, 1513-1524.
11. M. Dittmar, Nuclear Energy: Status and Future Limitations, *Energy*, 2012, **37**, 35-40.
12. A. Froggatt, M. Schneider, Nuclear power versus renewable energy-A trend analysis, *Proc. IEEE*, 2015, **103**, 487-490.
13. A. R. V. Hippel, Molecular Designing of Materials, *Science*, 1962, **138**, 91-108.
14. M. O'Keeffe, M. Eddaoudi, H. Li, T. Reineke and O. M. Yaghi, Frameworks for extended solids: Geometrical design principles, *J. Solid State Chem.*, 2000, **152**, 3-20.
15. A. G. Slater and A. I. Cooper, Function-led design of new porous materials, *Science*, 2015, **348**, aaa8075-10.
16. D. M. D'Alessandro, B. Smit and J. R. Long, Carbon dioxide capture: Prospects for new materials, *Angew. Chem. Int. Ed.*, 2010, **49**, 6058-6082.
17. J. Yu, L. H. Xie, J. R. Li, Y. Ma, J. M. Seminario and P. B. Balbuena, CO₂ capture and separations using MOFs: Computational and experimental studies, *Chem. Rev.*, 2017, **117**, 9674-9754.
18. S. Zeng, X. Zhang, L. Bai, X. Zhang, H. Wang, J. Wang, D. Bao, M. Li, X. Liu and S. Zhang, Ionic-liquid-based CO₂ capture systems: Structure, interaction and process, *Chem. Rev.*, 2017, **117**, 9625-9673.
19. S. D. Kenarsari, D. Yang, G. Jiang, S. Zhang, J. Wang, A. G. Russell, Q. Wei and M. Fan, Review of recent advances in carbon dioxide separation and capture, *RSC Adv.*, 2013, **3**, 22739-22773.
20. J. Wang, L. Huang, R. Yang, Z. Zhang, J. Wu, Y. Gao, Q. Wang, D. O'Hare and Z. Zhong, Recent advances in solid sorbents for CO₂ capture and new development trends, *Energy Environ. Sci.*, 2014, **7**, 3478-3518.
21. Q. Wang, J. Luo, Z. Zhong and A. Borgna, CO₂ capture by solid adsorbents and their applications: Current status and new trends, *Energy Environ. Sci.*, 2011, **4**, 42-55.
22. <http://www.esrl.noaa.gov/gmd/ccgg/trends/>.
23. B. Metz, O. Davidson, H. D. Coninck, M. Loos and L. Meyer, *IPCC (International Panel on Climate Change)*, Cambridge University Press, UK, 2005.
24. J. Davison, Performance and costs of power plants with capture and storage of CO₂, *Energy*, 2007, **32**, 1163-1176.
25. D. Schrag, Preparing to capture carbon, *Science*, 2007, **315**, 812-813.
26. EPRI (Electric Power Research Institute), *Advanced Coal Power Systems with CO₂ Capture: EPRI's Coal Fleet for Tomorrow Vision-2011 update*, 1023468, 2011.

27. N. Hildebrand and H. J. Herzog, Optimization of carbon capture percentage for technical and economic impact of near-term CCS implementation at coal-fired power plants, *Energy Procedia*, 2009, **1**, 4135-4142.
28. NETL (National Energy Technology Laboratory) “Coal-fired power plants in the United States; Examination of the costs of retrofitting with CO₂ capture technology”, Revision 3, DOE/NETL-402/102309, 2011.
29. N. Stern, *Stern review on the economics of climate change*, Cambridge University Press, Cambridge, UK, 2006.
30. Image source: <http://timetobebold.wordpress.com/tag/ipcc>.
31. R. S. Haszeldine, Carbon capture and storage: How green can black be?, *Science*, 2009, **325**, 1647-1652.
32. G. Sartori and D. W. Savage, Sterically hindered amines for CO₂ removal from gases, *Ind. Eng. Chem. Fundam.*, 1983, **22**, 239-249.
33. P. D. Vaidya and E. Y. Kenig, CO₂-alkanolamine reaction kinetics: A review of recent studies, *Chem. Eng. Technol.*, 2007, **30**, 1467-1474.
34. E. D. Bates, R. D. Mayton, I. Ntai and J. H. D. Jr, CO₂ capture by a task-specific ionic liquid, *J. Am. Chem. Soc.*, 2002, **124**, 926-927.
35. P. Lamagni, B. L. Pedersen, A. Godiksen, S. Mossin, X. M. Hu, S. U. Pedersen, K. Daasbjerg and N. Lock, Graphene inclusion controlling conductivity and gas sorption of metal-organic framework, *RSC Adv.*, 2018, **8**, 13921-13932.
36. H. Yang, Z. Xu, M. Fan, R. Gupta, R. B. Slimane, A. E. Bland and I. Wright, Progress in carbon dioxide separation and capture: A review, *J. Environ. Sci.*, 2008, **20**, 14-27.
37. A. Samanta, A. Zhao, G. K. H. Shimizu, P. Sarkar and R. Gupta, Post-combustion CO₂ capture using solid sorbents: A review, *Ind. Eng. Chem. Res.*, 2012, **51**, 1438-1463.
38. F. Geyer, C. Schönecker, H. J. Butt and D. Vollmer, Enhancing CO₂ capture using robust super omniphobic membranes, *Adv. Mater.*, 2017, **29**, 1603524-1603529.
39. L. Zou, Y. Sun, S. Che, X. Yang, X. Wang, M. Bosch, Q. Wang, H. Li, M. Smith, S. Yuan, Z. Perry and H. C. Zhou, Porous organic polymers for post-combustion carbon capture, *Adv. Mater.*, 2017, **29**, 1700229-1700263.
40. A. Darabi, P. G. Jessop and M. F. Cunningham, CO₂-responsive polymeric materials: Synthesis, self-assembly, and functional applications, *Chem. Soc. Rev.*, 2016, **45**, 4391-4436.
41. Z. Xie, M. Zhu, A. Nambo, J. B. Jasinski and M. A. Carreon, Microwave-assisted synthesized SAPO-56 as a catalyst in the conversion of CO₂ to cyclic carbonates, *Dalton Trans.*, 2013, **42**, 6732-6735.
42. D. P. Hanak, E. J. Anthony and V. Manovic, A review of developments in pilot-plant testing and modelling of calcium looping process for CO₂ capture from power generation systems, *Energy Environ. Sci.*, 2015, **8**, 2199-2249.
43. Y. Tang and K. Landskron, CO₂-sorption properties of organosilicas with bridging amine functionalities inside the framework, *J. Phys. Chem. C*, 2010, **114**, 2494-2498.
44. A. Goepfert, M. Czaun, J. P. Jones, G. K. S. Prakash and G. A. Olah, Recycling of carbon dioxide to methanol and derived products—closing the loop, *Chem. Soc. Rev.*, 2014, **43**, 7995-8048.
45. S. R. Venna and M. A. Carreon, Metal organic framework membranes for carbon dioxide separation, *Chem. Eng. Sci.*, 2015, **124**, 3-19.
46. P. Carraro, V. Elías, A. García Blanco, K. Sapag, S. Moreno, M. Oliva and G. Eimer, Synthesis and multi-technique characterization of nickel loaded MCM-41 as potential hydrogen-storage materials, *Micropor. Mesopor. Mater.*, 2014, **191**, 103-111.
47. R. T. Woodward, L. A. Stevens, R. Dawson, M. Vijayaraghavan, T. Hasell, I. P. Silverwood, A. V. Ewing, T. Ratvijitvech, J. D. Exley, S. Y. Chong, F. Blanc, D. J. Adams, S. G. Kazarian, C. E. Snape, T. C. Drage and A. I. Cooper, Swellable, water- and acid-tolerant polymer sponges for chemoselective carbon dioxide capture, *J. Am. Chem. Soc.*, 2014, **136**, 9028-9035.
48. B. Kokoszka, N. K. Jarrah, C. Liu, D. T. Moore and K. Landskron, Supercapacitive swing adsorption of carbon dioxide, *Angew. Chem. Int. Ed.*, 2014, **53**, 3698-3701.

49. S. Hug, L. Stegbauer, H. Oh, M. Hirscher and B. V. Lotsch, Nitrogen-rich covalent triazine frameworks as high-performance platforms for selective carbon capture and storage. *Chem. Mater.*, 2015, **27**, 8001-8010.
50. R. Muhammad, P. Rekha, and P. Mohanty, Amino linked inorganic-organic hybrid nanoporous materials (HNMs) for CO₂ capture and H₂ storage applications, *RSC Adv.*, 2016, **6**, 17100-17105.
51. G. Wang, K. Leus, S. Zhao and P. V. D. Voort, Newly designed covalent triazine framework based on novel N-heteroaromatic building blocks for efficient CO₂ and H₂ capture and storage, *ACS Appl. Mater. Interfaces*, 2018, **10**, 1244-1249.
52. Q. Q. Dang, C. -Y. Liu, X. -M. Wang and X. -M. Zhang, Novel covalent triazine framework for high-performance CO₂ Capture and alkyne carboxylation reaction. *ACS Appl. Mater. Interfaces*, 2018, **10**, 27972-27978.
53. P. Mohanty, L. D. Kull and K. Landskron, Porous covalent electron-rich organonitridic frameworks as highly selective sorbents for methane and carbon dioxide, *Nat. Commun.*, 2011, **2**, 401-406.
54. W. Shannon, N. C. Strandwitz, M. Schierhorn, N. Lock, M. C. Lonergan and G. D. Stucky, Tunable electronic interfaces between bulk semiconductors and ligand-stabilized nanoparticle assemblies, *Nat. Mater.*, **6**, 2007, 592-596.
55. B. Kartick, S. K. Srivastava and S. Mahanty, TiS₂-MWCNT hybrid as high performance anode in lithium-ion battery, *J. Nanopart. Res.*, 2013, **15**, 1950-1955.
56. A. Sumboja, C. Y. Foo, J. Yan, C. Yan, R. K. Gupta and P. S. Lee, Significant electrochemical stability of manganese dioxide/polyaniline coaxial nanowires by self-terminated double surfactant polymerization for pseudocapacitor electrode, *J. Mater. Chem.*, 2012, **22**, 23921-23928.
57. M. Zhi, C. Xiang, J. Li, M. Li and N. Wu, Nanostructured carbon-metal oxide composite electrodes for supercapacitors: A review, *Nanoscale*, 2013, **5**, 72-88.
58. P. Roy and S. K. Srivastava, Nanostructured anode materials for lithium ion batteries, *J. Mater. Chem. A*, 2015, **3**, 2454-2484
59. C. Y. Zhong, W. Deng, W. Hu, J. Qiao and L. Zhang, A review of electrolyte materials and compositions for electrochemical supercapacitors, *J. Chem. Soc. Rev.*, 2015, **44**, 7484-7539.
60. Z. Zhao, Y. Wang, M. Li and R. Yang, High performance N-doped porous activated carbon based on chicken feather for supercapacitors and CO₂ capture, *RSC Adv.*, 2015, **5**, 34803-34811.
61. T. B. Schon, B. T. McAllister, P. F. Li and D. S. Seferos, The rise of organic electrode materials for energy storage, *Chem. Soc. Rev.*, 2016, **45**, 6345-6404.
62. A. P. Wight and M. E. Davis, Design and preparation of organic-inorganic hybrid catalysts, *Chem. Rev.*, 2002, **102**, 3589-3614.
63. L. L. Chng, N. Erathodiyil and J. Y. Ying, Nanostructured catalysts for organic transformations, *Acc. Chem. Res.*, 2013, **46**, 1825-1837.
64. P. Munnik, P. E. D. Jongh and K. P. D. Jong, Recent developments in the synthesis of supported catalysts, *Chem. Rev.*, 2015, **115**, 6687-6718.
65. A. Modak, J. Mondal, M. Sasidharan and A. Bhaumik, Triazine functionalized ordered mesoporous polymer: A novel solid support for Pd-mediated C-C cross-coupling reactions in water, *Green Chem.*, 2011, **13**, 1317-1331.
66. X. Zhou, H. P. Zhang, G. Y. Wang, Z. G. Yao, Y. R. Tang and S. S. Zheng, Zeolitic imidazolate framework as efficient heterogeneous catalyst for the synthesis of ethyl methyl carbonate *J. Mol. Catal. A: Chem.*, 2013, **366**, 43-47.
67. H. Sardon, A. Pascual, D. Mecerreyes, D. Taton, H. Cramail and J. L. Hedrick, Synthesis of polyurethanes using organocatalysis: A perspective *Macromol.*, 2015, **48**, 3153-3165.
68. S. Y. Park, I. Hwang, H. J. Lee and C. E. Song, Biomimetic catalytic transformation of toxic α-oxoaldehydes to high-value chiral α-hydroxythioesters using artificial glyoxalase I, *Nat. Comm.*, 2017, **8**, 14877 (1-8).

69. L. Zhu, X. Liu, H. Jiang and L. Sun, Metal-organic frameworks for heterogeneous basic catalysis, *Chem. Rev.*, 2017, **117**, 8129-8176.
70. C. V. Doorslaer, J. Wahlen, P. Mertens, K. Binnemans and D. D. Vos, Immobilization of molecular catalysts in supported ionic liquid phases, *Dalton Trans.*, 2010, **39**, 8377-8390.
71. R. Srivastava, D. Srinivas and P. Ratnasamy, CO₂ activation and synthesis of cyclic carbonates and alkyl/aryl carbamates over adenine-modified Ti-SBA-15 solid catalysts, *J. Catal.*, 2005, **233**, 1-15.
72. N. Mase and T. Horibe, Organocatalytic Knoevenagel condensations by means of carbamic acid ammonium salts *Org. Lett.*, 2013, **15**, 1854-1857.
73. D. M. Flanigan, F. R. M., N. A. White and T. Rovis, Organocatalytic reactions enabled by N-heterocyclic carbenes, *Chem. Rev.*, 2015, **115**, 9307-9387.
74. X. Gu, Y. Tang, X. Zhang, Z. Luo and H. Lu, Organocatalytic Knoevenagel condensation by chiral C₂-symmetric tertiary diamines *New J. Chem.*, 2016, **40**, 6580-6583.
75. A. M. F. Phillips and A. J. L. Pombeiro, Recent advances in organocatalytic enantioselective transfer hydrogenation, *Org. Biomol. Chem.*, 2017, **15**, 2307-2340.
76. M. G. Goesten, A. Szecsenyi, M. F. D. Lange, A. V. Bavykina, K. B. S. S. Gupta, F. Kapteijn and J. Gascon, Sulfonated porous aromatic frameworks as solid acid catalysts, *ChemCatChem*, 2016, **8**, 961-967.
77. Y. Yang, X. Zou, P. Cui, Y. Zhou, S. Zhao, L. Wang, Y. Yuan, and G. Zhu, Porous aromatic frameworks for size-selective halogenation of aryl compounds *ACS Appl. Mater. Interfaces*, 2017, **9**, 30958-30963.
78. P. Puthiaraj, Y. Lee, S. Zhang and W. Ahn, Triazine-based covalent organic polymers: Design, synthesis and applications in heterogeneous catalysis, *J. Mater. Chem. A*, 2016, **4**, 16288-16311.
79. S. Ren, R. Dawson, A. Laybourn, J.-X. Jiang, Y. Khimyak, D. J. Adams and A. I. Cooper, Functional conjugated microporous polymers: From 1,3,5-benzene to 1,3,5-triazine, *Polym. Chem.*, 2012, **3**, 928-934.
80. S. K. Dey, N. D. S. Amadeu and C. Janiak, Microporous polyurethane material for size selective heterogeneous catalysis of the Knoevenagel reaction, *Chem. Commun.*, 2016, **52**, 7834-7837.
81. Y. B. Zhou, Y. Q. Wang, L. C. Ning, Z. C. Ding, W. L. Wang, C. K. Ding, R. H. Li, J. J. Chen, X. Lu, Y. J. Ding and Z. P. Zhan, Conjugated microporous polymer as heterogeneous ligand for highly selective oxidative Heck reaction *J. Am. Chem. Soc.*, 2017, **139**, 3966-3969.
82. A. Tyagi, K. M. Tripathi, N. Singh, S. Choudhary and R. K. Gupta, Green synthesis of carbon quantum dots from lemon peel waste: Applications in sensing and photocatalysis, *RSC Adv.*, 2016, **6**, 72423-72432.
83. M. U. A. Prathap, V. Anuraj, B. Satpati and R. Srivastava, Facile preparation of Ni(OH)₂-MnO₂ hybrid material and its application in the electrocatalytic oxidation of hydrazine, *J. Hazard. Mater.*, 2013, **262**, 766-774.
84. L. Zhang, H. Wang, W. Shen, Z. Qin, J. Wang and W. Fan, Controlled synthesis of graphitic carbon nitride and its catalytic properties in Knoevenagel condensations, *J. Catal.*, 2016, **344**, 293-302.
85. A. Dittmar, Nuclear Energy: Status and Future Limitations, *Energy*, 2012, **37**, 35-40.
86. M. Schneider, A. Froggatt, The World Nuclear Industry Status Report 2017, <https://www.worldnuclearreport.org/IMG/pdf/20170912wnisr2017-executivesummary-en.pdf>.
87. Q. Sun, B. Aguila, L. D. Earl, C. W. Abney, L. Wojtas, P. K. Thallapally and S. Ma, Covalent organic frameworks as a decorating platform for utilization and affinity enhancement of chelating sites for radionuclide sequestration, *Adv. Mater.*, 2018, **30**, 1-9.

88. D. S. Sholl and R. P. Lively, Seven chemical separations to change the world, *Nature*, 2016, **532** 435-437.
89. Y. Lu, Uranium extraction: Coordination Chemistry in the Ocean, *Nat. Chem.*, 2014, **6**, 175-177.
90. R. V. Davies, J. Kennedy, R. W. McIlroy, R. Spence and K. M. Hill, Extraction of uranium from sea water, *Nature*, 1964, **203**, 1110-1115.
91. K. Morris and R. Raiswell, Chapter 4: Biogeochemical cycles and remobilisation of the actinide elements, *Radioactiv. Environ.*, 2002, **2**, 101-141.
92. T. Zhang, G. Asakura and G. Uchiyama, The adsorption mechanism of uranium(VI) from seawater on a macroporous fibrous polymeric adsorbent containing amidoxime chelating functional group, *React. Funct. Polym.* 2003, **57**, 67-76.
93. U. Bardi, Extracting minerals from seawater: An energy analysis, *Sustainability*, 2010, **2**, 980-992.
94. W. Zhang, B. Aguila and S. Ma, Potential applications of functional porous organic polymer materials, *Polym. Chem.*, 2016, **7**, 6413-6421.
95. Haber, IUPAC "Manual on catalyst characterization", *Pure and Appl. Chem.*, 1991, **63**, 1227-1246.
96. F. Rouquerol, J. Rouquerol and K. Sing, *Adsorption by powders and porous solids: Principle, methodology and applications*, Academic press, London, UK, 1999.
97. K. Landskron and G. A. Ozin, Periodic mesoporous organosilicas: Self-assembly from bridged cyclic silsesquioxane precursors, *Angew. Chem. Int. Ed.*, 2005, **44**, 2107-2109.
98. T. Asefa, M. J. MacLachlan, N. Coombs and G. A. Ozin, Periodic mesoporous organosilicas with organic groups inside the channel walls, *Nature*, 1999, **402**, 867-871.
99. S. Inagaki, S. Guan, Y. Fukushima, T. Ohsuna and O. Terasaki, Novel mesoporous materials with a uniform distribution of organic groups and inorganic oxide in their frameworks, *J. Am. Chem. Soc.*, 1999, **121**, 9611-9614.
100. S. Das, P. Heasman, T. Ben and S. Qiu, Porous organic materials: Strategic design and structure-function correlation, *Chem. Rev.*, 2017, **117**, 1515-156.
101. Thomas, Functional materials: From hard to soft porous frameworks, *Angew. Chem. Int. Ed.*, 2010, **49**, 8328-8344.
102. S. Gu, J. Guo, Q. Huang, J. He, Y. Fu, G. Kuang, C. Pan and G. Yu, 1,3,5-Triazine-based microporous polymers with tunable porosities for CO₂ capture and fluorescent sensing, *Macromolecules*, 2017, **50**, 8512-8520.
103. Z. Xiang and D. Cao, Synthesis of luminescent covalent-organic polymers for detecting nitroaromatic explosives and small organic molecules. *Macromol. Rapid Commun.*, 2012, **33**, 1184-1190.
104. T. Islamoglu, S. Behera, Z. Kahveci, T. D. Tessema and P. Jena and H. M. El-Kaderi, Enhanced carbon dioxide capture from landfill gas using bifunctionalized benzimidazole-linked polymers, *ACS Appl. Mater. Interfaces*, 2016, **8**, 14648-14655.
105. C. Gu, N. Huang, J. Gao, F. Xu, Y. Xu, and D. Jiang, Controlled synthesis of conjugated microporous polymer films: versatile platforms for highly sensitive and label-free chemo- and biosensing, *Angew. Chem. Int. Ed.*, 2014, **53**, 4850-4855.
106. P. Kaur, J. T. Hupp, and S. T. Nguyen, Porous organic polymers in catalysis: opportunities and challenges, *ACS Catal.*, 2011, **1**, 819-835.
107. Q. Fang, J. Wang, S. Gu, R. B. Kaspar, Z. Zhuang, J. Zheng, H. Guo, S. Qiu and Y. Yan, 3D porous crystalline polyimide covalent organic frameworks for drug delivery, *J. Am. Chem. Soc.*, 2015, **137**, 8352-8355.
108. H. Bohra, S. Y. Tan, J. S. Cangjie Y. A. Efrem, Y. Zhao and M. Wang, Narrow bandgap thienothiadiazole-based conjugated porous polymers: From facile direct arylation

- polymerization to tunable porosities and optoelectronic properties, *Polym. Chem.*, 2016, **7**, 6413-6421.
109. J. Zhang, Z. Wang, L. Li, J. Zhao, J. Zheng, H. Cui and Z. Zhu, Self-assembly of CNH nanocages with remarkable catalytic performance, *J. Mater. Chem. A*, 2014, **2**, 8179-8183.
 110. K. Wang, H. Huang, D. Liu, C. Wang, J. Li and C. Zhong, Covalent triazine-based frameworks with ultramicropores and high nitrogen contents for highly selective CO₂ capture, *Environ. Sci. Technol.*, 2016, **50**, 4869-4876.
 111. L. Wang, Z. Gao, J. Chang, X. Liu, D. Wu, F. Xu, Y. Guo and K. Jiang, Nitrogen doped porous carbons as electrode materials for high-performance supercapacitor and dye sensitized solar cell, *ACS Appl. Mater. Interfaces*, 2015, **7**, 20234-20244.
 112. H. Jurcakova, A. M. Puziy, O. I. Poddubnaya, F. S. Garcia, J. M. D. Tascon and G. Q. Lu, Highly stable performance of supercapacitors from phosphorus-enriched carbons, *J. Am. Chem. Soc.*, 2009, **131**, 5026-5027.
 113. L. Hao, B. Luo, X. Li, M. Jin, Y. Fang, Z. Tang, Y. Jia, M. Liang, A. Thomas, J. Yang and L. Zhi, Terephthalonitrile-derived nitrogen-rich networks for high performance supercapacitors, *Energy Environ. Sci.*, 2012, **5**, 9747-9751.
 114. A. M. Khattak, Z. A. Ghazi, B. Liang, N. A. Khan, A. Iqbal, L. Li and Z. Tang, A redox-active 2D covalent organic framework with pyridine moieties capable of faradaic energy storage, *J. Mater. Chem. A*, 2016, **4**, 16312-16317.
 115. Y. Fu, Z. Wang, X. Fu, J. Yan, C. Liu, C. Pana and G. Yu, Acid/hydrazide-appended covalent triazine frameworks for low-pressure CO₂ capture: pre-designable or post-synthesis modification, *J. Mater. Chem. A*, 2017, **5**, 21266-21274.
 116. M. Kuhn, M. Antonietti, and A. Thomas, Porous, Covalent triazine-based frameworks prepared by ionothermal synthesis, *Angew. Chem. Int. Ed.*, 2008, **47**, 3450-3453.
 117. S. Ren, M. J. Bojdys, R. Dawson, A. Laybourn, Y. Z. Khimiyak, D. J. Adams, and A. I. Cooper, Porous, fluorescent, covalent triazine-based frameworks via room-temperature and microwave-assisted synthesis, *Adv. Mater.*, 2012, **24**, 2357-2361.
 118. Z. Z. Yang, Y. Zhao, H. Zhang, B. Yu, Z. Ma, G. Ji and Z. Liu, Fluorinated microporous organic polymers: Design and applications in CO₂ adsorption and conversion, *Chem. Commun.*, 2014, **50**, 13910-13913.
 119. L. Stegbauer, K. Schwinghammer and B. V. Lotsch, A hydrazone-based covalent organic framework for photocatalytic hydrogen production, *Chem. Sci.*, 2014, **5**, 2789-2793.
 120. Y. Liu, S. Wu, G. Wang, G. Yu, J. Guan, C. Pan and Z. Wang, Control of porosity of novel carbazole-modified polytriazine frameworks for highly selective separation of CO₂-N₂, *J. Mater. Chem. A*, 2014, **2**, 7795-7801.
 121. S. Wu, S. Gu, A. Zhang, G. Yu, Z. Wang, J. Jian and C. Pan, A rational construction of microporous imidebridged covalent-organic polytriazines for high enthalpy small gas absorption, *J. Mater. Chem. A*, 2015, **3**, 878-885.
 122. O. Buyukcakir, S. H. Je, S. N. Talapaneni, D. Kim, and A. Coskun, Charged covalent triazine frameworks for CO₂ capture and conversion, *ACS Appl. Mater. Interfaces*, 2017, **9**, 7209-7216.
 123. X. Zhu, C. Tian, G. M. Veith, C. W. Abney, J. Dehaut, and S. Dai, In situ doping strategy for the preparation of conjugated triazine frameworks displaying efficient CO₂ capture performance, *J. Am. Chem. Soc.* 2016, **138**, 11497-11500.
 124. M. X. Tan, Y. Zhang and J. Y. Ying, Mesoporous poly(melamine-formaldehyde) solid sorbent for carbon dioxide capture, *ChemSusChem*, 2013, **6**, 1186-1190.
 125. M. Kohlmayr, G. Zuckerstatter and A. Kandelbauer, Modification of melamine-formaldehyde resins by substances from renewable resources, *J. Appl. Polym. Sci.*, 2012, **124**, 4416-4423.
 126. M. G. Schwab, D. Crespy, X. Feng, K. Landfester and K. Mullen, Preparation of microporous melamine-based polymer networks in an anhydrous high-temperature miniemulsion, *Macromol. Rapid Commun.*, 2011, **32**, 1798-1803.

127. S. W. Won, P. Kotte, W. Wei, A. Lim and Y. S. Yun, Biosorbents for recovery of precious metals, *Bioresour. Technol.*, 2014, **160**, 203-212.
128. M. X. Tan, Y. N. Sum, J. Y. Ying and Y. Zhang, A mesoporous poly-melamine-formaldehyde polymer as a solid sorbent for toxic metal removal, *Energy Environ. Sci.*, 2013, **6**, 3254–3259.
129. W. -C. Song, X. -K. Xu, Q. Chen, Z. -Z. Zhuang and X. -H. Bu, Nitrogen-rich diaminotriazine-based porous organic polymers for small gas storage and selective uptake *Polym. Chem.*, 2013, **4**, 4690–4696.
130. M. K. Bhunia, S. K. Das, P. Pachfule, R. Banerjee and A. Bhaumik, Nitrogen-rich porous covalent imine network (CIN) material as an efficient catalytic support for C–C coupling reactions, *Dalton Trans.*, 2012, **41**, 1304-1311.
131. M. G. Schwab, B. H. Fassbender, W. Spiess, A. Thomas, X. Feng and K. Mullen, Catalyst-free preparation of melamine-based microporous polymer networks through Schiff base chemistry, *J. Am. Chem. Soc.*, 2009, **131**, 7216-7217.
132. H. Zhou, S. Xu, H. Su, M. Wang, W. Qiao, L. Ling and D. Long, Facile preparation and ultra-microporous structure of melamine–resorcinol–formaldehyde polymeric microspheres, *Chem. Commun.*, 2013, **49**, 3763-3765.
133. P. Puthiaraj and K. Pitchumani, Triazine-based mesoporous covalent imine polymers as solid supports for copper-mediated Chan–Lam cross-coupling N-Arylation Reactions, *Chem. Eur. J.*, 2014, **20**, 8761-8770.
134. H. Zhao, Z. Jin, H. Su, X. Jing, F. Sun and G. Zhu, Targeted synthesis of a 2D ordered porous organic framework for drug release, *Chem. Commun.*, 2011, **47**, 6389-6391.
135. M. R. Liebl and J. Senker, Microporous Functionalized Triazine-Based Polyimides with High CO₂ Capture Capacity, *Chem. Mater.*, 2013, **25**, 970-980.
136. Y. H. Abdelmoaty, T. D. Tessema, F. A. Choudhury, O. M. El-Kadri and H. M. El-Kaderi, Nitrogen-rich porous polymers for carbon dioxide and iodine sequestration for environmental remediation, *ACS Appl. Mater. Interfaces*, 2018, **10**, 16049-16058.
137. S. Xiong, X. Fu, L. Xiang, G. Yu, J. Guan, Z. Wang, Y. Du, X. Xiong and C. Pan, Liquid acid-catalysed fabrication of nanoporous 1,3,5-triazine frameworks with efficient and selective CO₂ uptake, *Polym. Chem.*, 2014, **5**, 3424-3431.
138. P. Puthiaraj, S. S. Kim and W. S. Ahn, Covalent triazine polymers using a cyanuric chloride precursor *via* Friedel–Crafts reaction for CO₂ adsorption/separation, *Chem. Eng. J.*, 2016, **283**, 184-192.
139. X. Zhu, S. M. Mahurin, S. An, C. Do-Thanh, C. Tian, Y. Li, L. W. Gill, E. W. Hagaman, Z. Bian, J. Zhou, J. Hu, H. Liu and S. Dai, Efficient CO₂ capture by a task-specific porous organic polymer bifunctionalized with carbazole and triazine groups, *Chem. Commun.*, 2014, **50**, 7933-7936.
140. W. Wang, Y. Yuan, F. Sun and G. Zhu, Targeted synthesis of novel porous aromatic frameworks with selective separation of CO₂/CH₄ and CO₂/N₂, *Chin. Chem. Lett.*, 2014, **25**, 1407-1410.
141. R. Xue, H. Guo, L. Yue, T. Wang, M. Wang, Q. Li, H. Liu and W. Yang, Preparation and energy storage application of a long-life and high rate performance pseudocapacitive COF material linked with –NH– bonds, *New J. Chem.*, 2018, **42**, 13726-13731.
142. H. A. Patel, F. Karadas, A. Canlier, J. Park, E. Deniz, Y. Jung, M. Atilhan and C. T. Yavuz, High capacity carbon dioxide adsorption by inexpensive covalent organic polymers. *J. Mater. Chem.*, 2012, **22**, 8431-8437.
143. S. Zulfiqar, M. I. Sarwar and C. T. Yavuz, Melamine based porous organic amide polymers for CO₂ capture, *RSC Adv.*, 2014, **4**, 52263-52269.
144. S. K. Kundu and A. Bhaumik, Novel nitrogen and sulfur rich hyper-cross-linked microporous poly-triazine-thiophene copolymer for superior CO₂ capture, *ACS Sustainable Chem. Eng.*, 2016, **4**, 3697-3703.
145. H. S. Jena, C. Krishnaraj, G. Wang, K. Leus, J. Schmidt, N. Chaoui and P. V. D. Voort, Acetylacetonate covalent triazine framework: an efficient carbon capture and storage material and a highly stable heterogeneous catalyst, *Chem. Mater.*, 2018, **30**, 4102-4111.

146. Y. Zhao, K. X. Yao, B. Teng, T. Zhang and Y. Han, A perfluorinated covalent triazine-based framework for highly selective and water-tolerant CO₂ capture, *Energy Environ. Sci.*, 2013, **6**, 3684-3692.
147. L. Shao, S. Wang, M. Liu, J. Huang and Y. Liu, Triazine-based hyper-cross-linked polymers derived porous carbons for CO₂ capture, *Chem. Eng. J.*, 2018, **339**, 509-518.
148. A. Liu, J. Zhang and X. Lv, Novel hydrazine-bridged covalent triazine polymer for CO₂ capture and catalytic conversion, *Chin. J. Catal.*, 2018, **39**, 1320-1328.
149. W. Wang, H. Ren, F. Sun, K. Cai, H. Ma, J. Du, H. Zhao and G. Zhu, Synthesis of porous aromatic framework with tuning porosity via ionothermal reaction, *Dalton Trans.*, 2012, **41**, 3933-3936.
150. S. K. Das, X. Wang and Z. Lai, Facile synthesis of triazine-triphenylamine-based microporous covalent polymer adsorbent for flue gas CO₂ capture, *Microporous Mesoporous Mater.*, 2018, **255**, 76-83.
151. M. Saleh, S. B. Baek, H. M. Lee, and K. S. Kim, Triazine-based microporous polymers for selective adsorption of CO₂, *J. Phys. Chem. C*, 2015, **119**, 5395-5402.
152. K. Jost, G. Dion and Y. Gogotsi, Textile energy storage in perspective, *J. Mater. Chem. A*, 2014, **2** 10776-10787.
153. A. Tyagi, K. M. Tripathi and R. K. Gupta, Recent progress in micro-scale energy storage devices and future aspects, *J. Mater. Chem. A*, 2015, **3**, 22507-22541.
154. A. Tyagi and R. K. Gupta, *Carbon nanostructures from biomass waste for supercapacitor applications, nanomaterials: a guide to fabrication and applications*, CRC Press, India. 2016.
155. M. Beidaghi and Y. Gogotsi, Capacitive energy storage in micro-scale devices: recent advances in design and fabrication of micro-supercapacitors, *Energy Environ. Sci.*, 2014, **7**, 867-884.
156. G. Wang, L. Zhang and J. Zhang, A review of electrode materials for electrochemical supercapacitors, *Chem. Soc. Rev.*, 2012, **41**, 797-828.
157. S. Ratha, S. R. Marri, J. N. Behera and C. S. Rout, High-energy-density supercapacitors based on patronite/single-walled carbon nanotubes/reduced graphene oxide hybrids, *Eur. J. Inorg. Chem.*, 2016, **2016**, 259-265.
158. S. R. Marri, S. Ratha, C. S. Rout and J. N. Behera, 3D cuboidal vanadium diselenide embedded reduced graphene oxide hybrid structures with enhanced supercapacitor properties, *Chem. Commun.*, 2017, **53**, 228-231.
159. R. Lukatskaya, B. Dunn and Y. Gogotsi, Multidimensional materials and device architectures for future hybrid energy storage, *Nat. Commun.*, 2016, **7**, DOI:10.1038/ncomms12647.
160. A. Eftekhari, L. Li and Y. Yang, Polyaniline supercapacitors, *J. Power Sources*, 2017, **347**, 86-107.
161. P. Bhanja, K. Bhunia, S. K. Das, D. Pradhan, R. Kimura, Y. Hijikata, S. Irlle and A. Bhaumik, A new triazine-based covalent organic framework for high-performance capacitive energy storage, *ChemSusChem*, 2017, **10**, 921-929.
162. P. Bhanja, S. K. Das, K. Bhunia, D. Pradhan, T. Hayashi, Y. Hijikata, S. Irlle and A. Bhaumik, A new porous polymer for highly efficient capacitive energy storage, *ACS Sustainable Chem. Eng.*, 2018, **6**, 202-209.
163. L. Hao, J. Ning, B. Luo, B. Wang, Y. Zhang, Z. Tang, J. Yang, A. Thomas and L. Zhi, Structural evolution of 2D microporous covalent triazine-based framework toward the study of high-performance supercapacitors, *J. Am. Chem. Soc.*, 2015, **137**, 1219-225.
164. Y. Li, S. Zheng, X. Liu, P. Li, L. Sun, R. Yang, S. Wang, Z. -S. Wu, X. Bao and W. -Q. Deng, Conductive microporous covalent triazine-based framework for high-performance electrochemical capacitive energy storage, *Angew. Chem. Int. Ed.*, 2018, **57**, 7992-7996.
165. L. Xu, R. Liua, F. Wanga, S. Yana, X. Shia and J. Yang, Preparation of triazine containing porous organic polymer for high performance supercapacitor applications, *RSC Adv.*, 2019, **9**, 1586-1590.
166. M. Choi, H. Cho, R. Srivastava, C. Venkatesan, D. Choi and R. Ryo, Amphiphilic organosilane-directed synthesis of crystalline zeolite with tunable mesoporosity, *Nat. Mater.*, 2006, **5**, 718-723.
167. P. Rani and R. Srivastava, Cu(I) metal organic framework catalyzed C-C and C-N coupling reactions, *Tetrahedron. Lett.*, 2014, **55**, 5256-5260.

168. Y. Zhang, S. A. Y. Zou, X. Luo, Z. Li, H. Xia, X. Liu and Y. Mu, Gas uptake, molecular sensing and organocatalytic performances of a multifunctional carbazole-based conjugated microporous polymer, *J. Mater. Chem. A*, 2014, **2**, 13422-13430.
169. S. K. Kundu and A. Bhaumik, A triazine-based porous organic polymer: a novel heterogeneous basic organocatalyst for facile one-pot synthesis of 2-amino-4H-chromenes, *RSC Adv.*, 2015, **5**, 32730-32739.
170. M. B. Ansari, E. -Y. Jeong and S. -E. Park, Styrene epoxidation in aqueous over triazine-based microporous polymeric network as a metal-free catalyst, *Green Sustainable Chem.*, 2012, **2**, 1-7.
171. T. Sakakura, J. -C. Choi and H. Yasuda, Transformation of carbon dioxide, *Chem. Rev.*, 2007, **107**, 2365-2387.
172. F. Jutz, J. -D. Grunwaldt and A. Bäiker, Mn (III) (salen)-catalyzed synthesis of cyclic organic carbonates from propylene and styrene oxide in "supercritical" CO₂, *J. Mol. Catal. A Chem.*, 2008, **279**, 94-103.
173. J. Roeser, K. Kailasam and A. Thomas, Covalent triazine frameworks as heterogeneous catalysts for the synthesis of cyclic and linear carbonates from carbon dioxide and epoxides, *ChemSusChem*, 2012, **5**, 1793-1799.
174. C. E. Chan-Thaw, A. Villa, P. Katekomol, D. Su, A. Thomas, L. Prati, Covalent triazine framework as catalytic support for liquid phase reaction, *Nano Lett.* 2010, **10**, 537-541.
175. R. Palkovits, M. Antonietti, P. Kuhn, A. Thomas, F. Schuth, Solid catalysts for the selective low-temperature oxidation of methane to methanol, *Angew. Chem. Int. Ed.*, 2009, **48**, 6909-6912.
176. M. X. Tan, L. Gu, N. Li, J. Y. Ying and Y. Zhang, Mesoporous poly-melamine-formaldehyde (mPMF)-a highly efficient catalyst for chemoselective acetalization of aldehydes, *Green Chem.*, 2013, **15**, 1127-1132.
177. C. E. Chan-Thaw, A. Villa, L. Prati and A. Thomas, Triazine-based polymers as nanostructured supports for the liquid-phase oxidation of alcohols, *Chem. Eur. J.*, 2011, **17**, 1052-1057.
178. G. A. Edwards, M. A. Trafford, A. E. Hamilton, A. M. Buxton, M. C. Bardeaux and J. M. Chalker, Melamine and melamine-formaldehyde polymers as ligands for palladium and application to Suzuki-Miyaura cross-coupling reactions in sustainable solvents, *J. Org. Chem.*, 2014, **79**, 2094-2104.
179. K. Kamiya, R. Kamai, K. Hashimoto and S. Nakanishi, Platinum-modified covalent triazine frameworks hybridized with carbon nanoparticles as methanol-tolerant oxygen reduction electrocatalysts, *Nat. Commun.*, 2014, **5**, 5040.
180. P. Puthiaraj and W.-S. Ahn, Synthesis of copper nanoparticles supported on a microporous covalent triazine polymer: an efficient and reusable catalyst for *O*-arylation reaction, *Catal. Sci. Technol.*, 2016, **6**, 1701-1709.
181. A. Modak, M. Pramanik, S. Inagaki and A. Bhaumik, A triazine functionalized porous organic polymer: Excellent CO₂ storage material and support for designing Pd nanocatalyst for C-C cross-coupling reactions, *J. Mater. Chem. A*, 2014, **2**, 11642-11650.
182. M. B. Ansari, H. Jin, M. N. Parvin and S. Park, Mesoporous carbon nitride as a metal-free base catalyst in the microwave assisted Knoevenagel condensation of ethylcyanoacetate with aromatic aldehydes, *Catal. Today*, 2012, **185**, 211-216.
183. M. Shunmughanathan, P. Puthiaraj and K. Pitchumani, Melamine-based microporous network polymer supported palladium nanoparticles: A stable and efficient catalyst for the Sonogashira coupling reaction in water, *ChemCatChem*, 2015, **7**, 666-673.
184. Y. Liu, C. Luo, J. Sun, H. Li, Z. Suna and S. Yan, Enhanced adsorption removal of methyl orange from aqueous solution by nanostructured proton containing δ -MnO₂, *J. Mater. Chem. A*, 2015, **3**, 5674-5682.
185. J. Ma, F. Yu, L. Zhou, L. Jin, M. Yang, J. Luan, Y. Tang, H. Fan, Z. Yuan and J. Chen, Enhanced adsorptive removal of methyl orange and methylene blue from aqueous solution by alkali-activated multiwalled carbon nanotubes, *ACS Appl. Mater. Interfaces*, 2012, **4**, 5749-5760.

186. Q. Peng, J. Guo, Q. Zhang, J. Xiang, B. Liu, A. Zhou, R. Liu and Y. Tian, Unique lead adsorption behavior of activated hydroxyl group in two-dimensional titanium carbide, *J. Am. Chem. Soc.*, 2014, **136**, 4113-4116.
187. V. Kumari, M. Sasidharan and A. Bhaumik, Mesoporous BaTiO₃@SBA-15 derived via solid state reaction and its excellent adsorption efficiency for the removal of hexavalent chromium from water, *Dalton Trans.*, 2015, **44**, 1924-1932.
188. I. Ali, New generation adsorbents for water treatment, *Chem. Rev.*, 2012, **112**, 5073-5091.
189. M. K. Dinker and P. S. Kulkarni, Recent advances in silica-based materials for the removal of hexavalent chromium: A review, *J. Chem. Eng. Data*, 2015, **60**, 2521-2540.
190. J. K. Bediako, W. Wei, S. Kim and Y. S. Yun, Removal of heavy metals from aqueous phases using chemically modified waste Lyocell fiber, *J. Hazard. Mater.*, 2015, **299**, 550-561.
191. Y. S. Karnjkar, R. M. Dinde, N. M. Dinde, K. N. Bawankar, S. P. Hinge, A. V. Mohod and P. R. Gogate, Degradation of magenta dye using different approaches based on ultrasonic and ultraviolet irradiations: Comparison of effectiveness and effect of additives for intensification, *Ultrason. Sonochem.*, 2015, **27**, 117-124.
192. J. Guo, D. Jiang, Y. Wu, P. Zhou and Y. Lan, Degradation of methyl orange by Zn(0) assisted with silica gel, *J. Hazard. Mater.*, 2011, **94**, 290-296.
193. S. Shylesh, S. P. Mirajkar and A. P. Singh, Influence of silica source in the catalytic activity and heterogeneity of mesoporous vanadosilicates, *J. Mol. Catal. A*, 2005, **239**, 57-63.
194. L. Zhou, C. Gao and W. Xu, Magnetic dendritic materials for highly efficient adsorption of dyes and drugs, *ACS Appl. Mater. Interfaces*, 2010, **2**, 1483-1491.
195. A. Stafiej and K. Pyrzynska, Adsorption of heavy metal ions with carbon nanotubes, *Sep. Purif. Technol.*, 2007, **58**, 49-52.
196. V. H. Montoya, M. A. P. Cruz, D. I. M. Castillo, M. R. M. Virgen and A. B. Petriciolet, Competitive adsorption of dyes and heavy metals on zeolitic structures, *J. Environ. Manage.*, 2013, **116**, 213-221
197. E. Haque, J. E. Lee, I. T. Jang, Y. K. Hwang, J. S. Chang, J. Jegal and S. H. Jung, Adsorptive removal of methyl orange from aqueous solution with metal-organic frameworks, porous chromium-benzenedicarboxylates, *J. Hazard. Mater.*, 2010, **181**, 535-542.
198. N. C. Burch, H. Jasuja and K. S. Walton, Water stability and adsorption in metal-organic frameworks, *Chem. Rev.*, 2014, **114**, 10575-10612.
199. J. Wang and C. Chen, Biosorbents for heavy metals removal and their future, *Biotechnol. Adv.*, 2009, **27**, 195-226.
200. Z. A. Ghazi, A. M. Khattak, R. Iqbal, R. Ahmad, A. A. Khan, M. Usman, F. Nawaz, W. Ali, Z. Felegari, S. U. Jan, A. Iqbal and A. Ahmad, Adsorptive removal of Cd²⁺ from aqueous solutions by a highly stable covalent triazine-based framework, *New J. Chem.*, 2018, **42**, 10234-10242.
201. M. Dinari and M. Hatami, Novel N-riched crystalline covalent organic framework as a highly porous adsorbent for effective cadmium removal, *J. Environ. Chem. Eng.*, 2019, **7**, 102907-102917.
202. T. Wang, K. Kailasam, P. Xiao, G. Chen, L. Chen, L. Wang, J. Li, and J. Zhu, Adsorption removal of organic dyes on covalent triazine framework (CTF), *Microporous Mesoporous Mater.*, 2014, **187**, 63-70.
203. J. Liu, E. Zong, H. Fu, S. Zheng, Z. Xu and D. Zhu, Adsorption of aromatic compounds on porous covalent triazine-based framework, *J. Colloid Interface Sci.*, 2012, **372**, 99-107.
204. X. Zhu, S. An, Y. Liu, J. Hu, H. Liu, C. Tian, S. Dai, X. Yang, H. Wang, C. W. Abney and S. Dai, Efficient removal of organic dye pollutants using covalent organic frameworks, *AIChE J.*, 2017, **63**, 3470-3478.
205. G. Yang, H. Han, C. Du, Z. Luo and Y. Wang, Facile synthesis of melamine-based porous polymer networks and their application for removal of aqueous mercury ions, *Polymer*, 2010, **51**, 6193-6202.
206. W. Zhang, L. -G. Qiu, Y. -P. Yuan, A. -J. Xie, Y. -H. Shen and J. -F. Zhu, Microwave-assisted synthesis of highly fluorescent nanoparticles of a melamine-based porous covalent organic framework for trace-level detection of nitroaromatic explosives, *J. Hazard. Mater.*, 2012, **147**, 221-222.

207. Q. Jiang, Qin Jiang, H. Huang, Y. Tang, Y. Zhang and C. Zhong, Highly porous covalent triazine frameworks for reversible iodine capture and efficient removal of dye, *Ind. Eng. Chem. Res.*, 2018, **57**, 15114-15121.
208. T. Geng, W. Zhang, Z. Zhu and X. Ka, Triazine-based conjugated microporous polymers constructing triphenylamine and its derivatives with nitrogen as core for iodine adsorption and fluorescence sensing I₂, *Microporous Mesoporous Mater.*, 2019, **273**, 163-170.
209. T. L. Silva, A. L. Cazetta, P. S. C. Souza, T. Zhang, T. Asefa and V. C. Almeida, Mesoporous activated carbon fibers synthesized from denim fabric waste: Efficient adsorbents for removal of textile dye from aqueous solutions, *J. Clean. Prod.*, 2018, **171**, 482-490.





CHAPTER-II

MATERIALS AND METHODS

2.1. Introduction

In this chapter, comprehensive experimental procedures used for the synthesis and characterization of nitrogen-enriched nanoporous polytriazines (NENPs) is given. In the present research, the NENPs have been synthesized by various methods such as conventional heating, solvothermal, microwave assisted (both domestic microwave oven and microwave reactor), and ultrasonic method. The synthesized NENPs have been characterized extensively using the available state of the art analytical facilities and employed for various applications such as gas sorption, supercapacitor, uranium adsorption and organocatalysis. The working principle and detailed experimental procedure of all the analytical techniques that have been used for the structural characterizations and application of all the synthesized material in this research work have been discussed.

2.2. Experimental details

2.2.1. Materials

The following chemicals and solvents have been bought from various sources as given below and are used as-received without further purification. Melamine (99%, Sigma Aldrich, USA), Cyanuric chloride (CNC) (99%, Sigma Aldrich, Switzerland), Triethylamine (TEA) (Fisher Scientific, India), Uranyl nitrate hexahydrate (Associated Chemical Industries, India), Benzaldehyde (Himedia, India), 4-Methoxybenzaldehyde (Avra Synthesis, India), 3-Methoxybenzaldehyde (Avra Synthesis, India), 2-Bromobenzaldehyde (Avra Synthesis, India), 4-Bromobenzaldehyde (Avra Synthesis, India), 2-Nitrobenzaldehyde (Avra Synthesis, India), 4-Nitrobenzaldehyde (Avra Synthesis), α -Naphthaldehyde (Avra Synthesis), 1,4-Dioxane (Rankem, India), Dimethylsulfoxide (DMSO) (Fisher Scientific, India), Sodium sulphate (Fisher Scientific, India), Tetrahydrofuran (THF) (Fisher Scientific, India), Dichloromethane (DCM) (Fisher Scientific, India), Methanol (Rankem, India), Ethanol (Rankem, India), Hydrochloric acid and Sulphuric acid (98%, Rankem, India) were of analytical grade.

2.3. Synthesis of NENPs

High surface area nanoporous polymeric materials are widely used for various applications such as adsorption, environmental remediation, and energy storage etc.[1-4] Introduction of heteroatoms such as N, S and P into these frameworks could further improve their properties and applications significantly.[5-8] Among various heteroatom enriched high surface area polymeric materials, polytriazine is in the forefront owing to its high nitrogen content and availability of wide variety of

inexpensive precursors.[8-10] However, controlling microstructure and textural properties are always remain great challenge. For this various synthetic approaches have been adopted that include the post-synthesis functionalization.[11,12] Pore wall collapse and deterioration of their textural characteristics are often encountered.[11,12] In this research, both conventional and non-conventional synthetic approaches have been adopted to synthesize polytriazine that is rich in nitrogen and have controlled textural properties. Two inexpensive precursors, melamine and cyanuric chloride, have been used keeping in mind the presence of the triazine ring in both the molecules that can provide polymeric frameworks with maximum nitrogen contents.

2.3.1. Conventional heating method

Among various methods adopted by the researchers to synthesize materials, conventional heating method is considered as the oldest and widest used method because of its simplicity and ease of operation.[13,14] In this method, the reactants are dissolved in appropriate solvents and employed to elevated temperatures. The heat treatment provides adequate energy to the reactants to cross the activation barrier for the formation of the product(s).

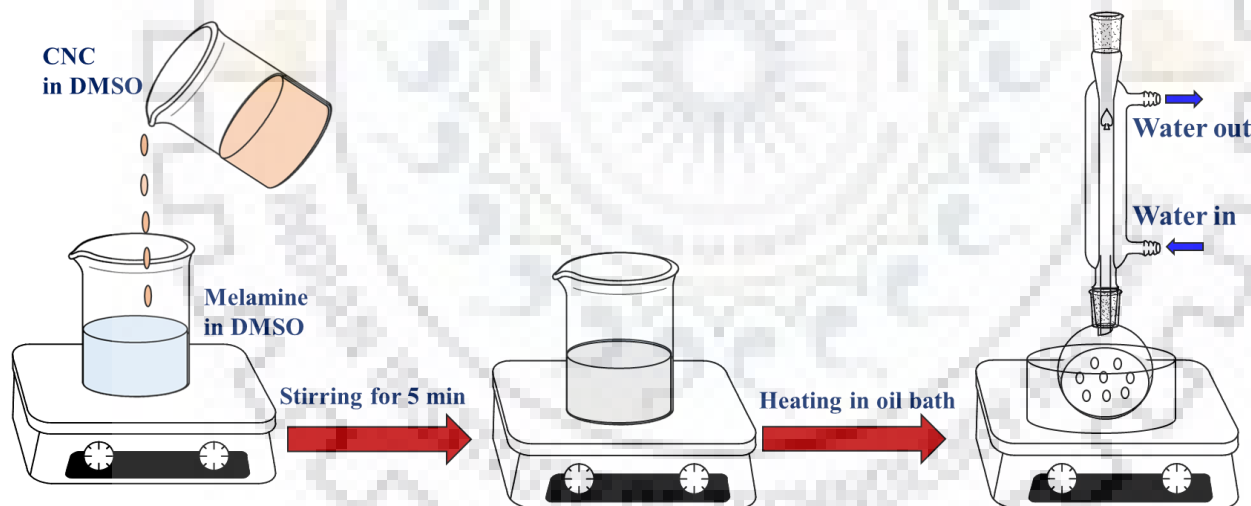


Figure 2.1. Procedure for the synthesis of NENP-C-x using conventional heating method.

For the synthesis of NENPs, typically, 1 mmol each of melamine (0.126 g) and cyanuric chloride (0.184 g) were dissolved in 20 ml of DMSO in two separate beakers (*Figure 2.1*). Melamine solution was added dropwise into cyanuric chloride solution under constant stirring. The resulting solution was stirred for 5 min followed by the dropwise addition of TEA as a proton absorber. The reaction mixture was subjected to heating at 120 °C in an oil-bath. A white precipitate appeared within 12 h and the experiment was continued for 24 h. The product as white powder was filtered

and washed several times with water, THF and dried under vacuum at 100 °C and the yield was estimated to be ~20%. In order to further understand the effect of the temperature on the product formation, experiments have been carried out at the temperatures of 140 and 160 °C, keeping all other experimental conditions identical. In both the cases, as expected white precipitates were obtained. The yield of 30 and 45% were estimated when synthesized at 140 and 160 °C, respectively. The synthesized specimens were designated as NENP-C-x (x = 120, 140 and 160 °C).

2.3.2. Solvothermal method

Solvothermal method is one of the most common and widely used synthetic route for the synthesis of advanced functional materials such as zeolites, MOFs, COFs, ZIFs, metal oxides, polymers and inorganic-organic hybrid materials.[15-19] In this method, reactions are carried out in a closed reactor using organic solvent at a temperature preferably above the boiling point of the solvent that could increase the pressure depending upon the reactor design and other experimental parameters.[15,16] Specially designed sealed reactors commonly called high-pressure autoclave that can withstand high temperature and pressure conditions and also resistant to most of the chemical reactions are used.[15] The high temperature and pressure conditions inside the reactor in the presence of a solvent could create critical and supercritical conditions that can facilitate the formation of the products with controlled microstructure and textural properties.[15] On some occasions, reactions that are not easy or even not possible in conventional heating methods could be executed in solvothermal method with high yield and completely condensed products.[8,15-17]

The synthesis of NENPs was also carried out solvothermally using Teflon lined stainless steel autoclave. The reaction mixture and precursors ratios used for the synthesis is similar to that of the conventional heating method. Typically, dropwise addition of melamine solution (1 mmol in 10 ml of DMSO) to the cyanuric chloride solution (1 mmol in 10 ml of DMSO) under constant stirring for 5 min and addition of TEA to it followed by transferring the reaction mixture into a teflon-lined autoclave (*Figure 2.2*). The autoclave was placed in a hot-air oven for 24 h with fixed temperatures of 120, 140 and 160 °C. No precipitate was formed when the experiment was carried out at 120 °C and white precipitates were obtained at 140 and 160 °C. The products were filtered and washed several times with water, THF and dried under vacuum at 100 °C. The yield of 30 and 40% were estimated when synthesized at 140 and 160 °C, respectively. The synthesized specimens were designated as NENP-S-x (x =140, 160 °C).

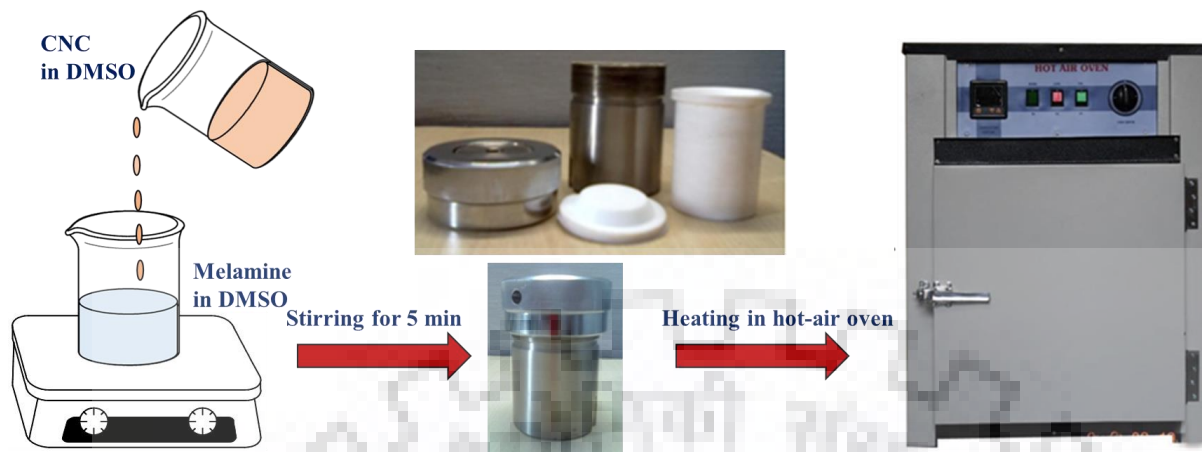


Figure 2.2. Procedure for the synthesis of NENP-S-x using solvothermal method.

2.3.3. Sonochemical method

Sonochemical is a non-conventional method often used to speed up the reactions and the products are formed in very short time with a high yield. Use of sonochemistry for the synthesis of materials was first reported by Suslick and coworkers in 1990.[20-22] The same group has pioneered in the use of sonochemistry for synthesis of various materials and their detailed synthesis mechanism.[20-22] The well accepted mechanism for the ultrafast synthesis was due to a chemical effect called “*acoustic cavitation*” on the exposure of the high energy ultrasonic waves.[20-22] The formation, growth and implosive collapse of bubbles in a solution under the influence of an ultrasonic field generates shock waves of localized hot spots with lifetimes of a few microseconds and a very high transient temperature of 19,727 °C, pressures of several atmospheres, and heating/cooling rates of $>466\text{ }^{\circ}\text{C s}^{-1}$. [20-22] In last few decades, a wide range of materials have been synthesized using this novel method.[22-24]

In this research, sonochemistry was also used for the synthesis of NENPs. The reaction mixtures with the same composition as was used for the conventional heating and solvothermal methods was exposed to an ultrasonic wave in a probe sonicator (*Q700 Sonica* with 1/2" diameter probe size) at an ultrasonic power of 600 W for 1 h (*Figure 2.3*). A white precipitate was obtained and filtered under reduced pressure and washed several times with water, THF and dried under vacuum at 100 °C with estimated yield of 25%. The obtained specimen was designated as NENP-U.

2.3.4. Synthesis using microwave radiation

The microwave (MW) has been emerged as a useful non-conventional approach for the synthesis of organic compounds, polymers, inorganic materials, and nanomaterials.[25-29] The major

advantages of microwave assisted method is the control over the experimental parameters such as temperature, pressure, and microwave power and choice of solvent that could lead to design the synthesis of advanced functional materials.[25-30] Microwave radiation of frequency in the range of 0.3 to 300 GHz and wavelengths in millimeters is used in this technique. Absorption of this radiation by polar molecules induces the heating effect either by dipolar-polarization (a process by which heat is generated in polar molecules) or conduction mechanism (generates heat through resistance to an electric field), or both.[30] In a microwave synthesis, an oscillating electromagnetic field of appropriate frequency is applied which tends to align the polar molecules of reaction mixture in the direction of field.[30] However, inter-molecular attraction between polar molecules tend to keep the molecules unchanged and heat generated through random motion of particles. Furthermore, microwave-assisted chemical reactions depend on the ability of the reaction mixture to efficiently absorb microwave energy, which often depends on choice of solvents for the reaction. The ability of a specific solvent or material to convert microwave energy into heat is determined by the so-called loss tangent (δ); the higher the $\tan \delta$ value, the better the solvent is for MW absorption and efficient heating.[25-30] Among, all solvents ethylene glycol, ethanol and DMSO have highest ability to adsorb and convert microwave radiation into heat *i.e.* highest value of δ .[30] Microwave radiation being absorbed specifically by the reaction components can accelerates the reaction quickly which results in higher product yield. In the present research both domestic microwave oven and microwave reactor have been used.

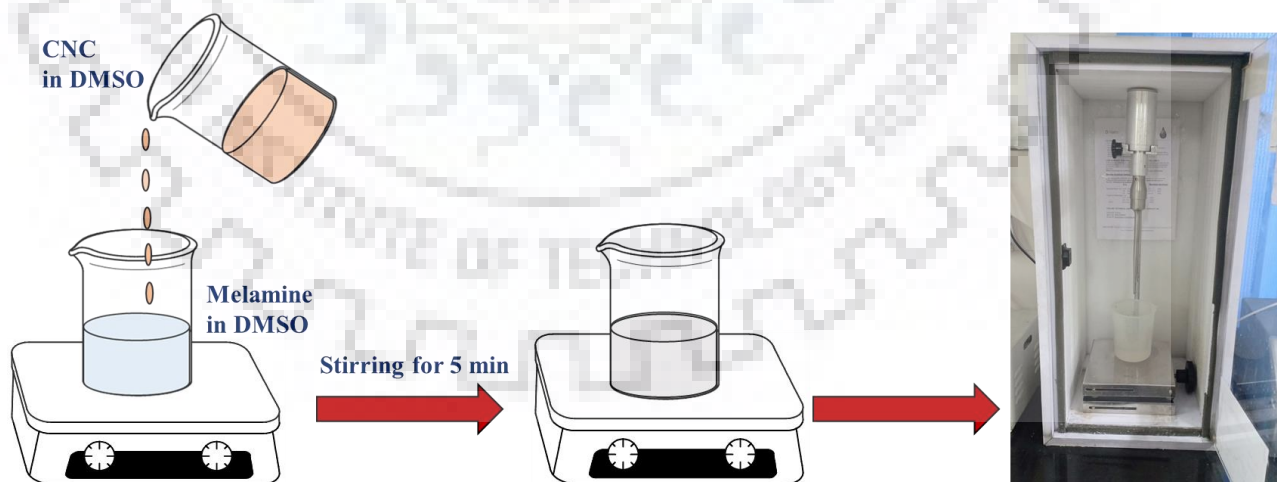


Figure 2.3. Procedure for the synthesis of NENP-U using ultrasonic method.

2.3.4.1. Domestic microwave oven

The reactants and solvent recipe used for this was same as above. Typically, the reaction mixture was placed in a domestic microwave oven (model no. IFB 20SC2, IFB India) at a microwave power of 200 W for 60 min (*Figure 2.4*). However, reaction could not be performed successfully due to bumping of solvent in an open vessel system within a short time period of 10 min. Moreover, both temperature and microwave power could not be controlled simultaneously in domestic microwave oven. In 10 min, no appreciable amount of product could be obtained. Hence, a more sophisticated commercial microwave reactor was used for the synthesis.



Figure 2.4. Procedure for the synthesis of NENP using domestic microwave oven.

2.3.4.2. Microwave reactor

In the present work, a commercial microwave reactor (MARS6, CEM, USA) is employed for the synthesis of NENPs (*Figure 2.5*). One of the primary reason for using the microwave reactor was to overcome the difficulties associated with the experiments carried out using domestic microwave oven. The not so uniform heating as well as knowing the exact temperature in the reaction beaker was some of the additional draw backs of using the domestic microwave.

Herein, the systematic synthesis of NENPs by condensing melamine and cyanuric chloride was carried out by varying the experimental parameters such as microwave power, solvent amount, reaction temperature and time. Typically, 1 mmol each of melamine (0.126 g) and cyanuric chloride (0.184 g) were condensed in V ml of DMSO (V = 10, 20 and 30) in a microwave reactor at T °C (T = 120, 140 and 160) with a microwave power (MWP) of M W (M = 200, 300 and 400) for t min (t = 10, 30, 60) in presence of 3 mmol (0.303 g) of TEA. White precipitates were formed in all cases

as expected and filtered under reduced pressure and washed several times with water, THF, and dried under vacuum at 100 °C (Scheme 2.1). The synthesized specimens were designated as NENP-x (x = 1 to 9) with estimated yield of 81-90%.



Figure 2.5. Procedure for the synthesis of NENPs using microwave-reactor assisted method.

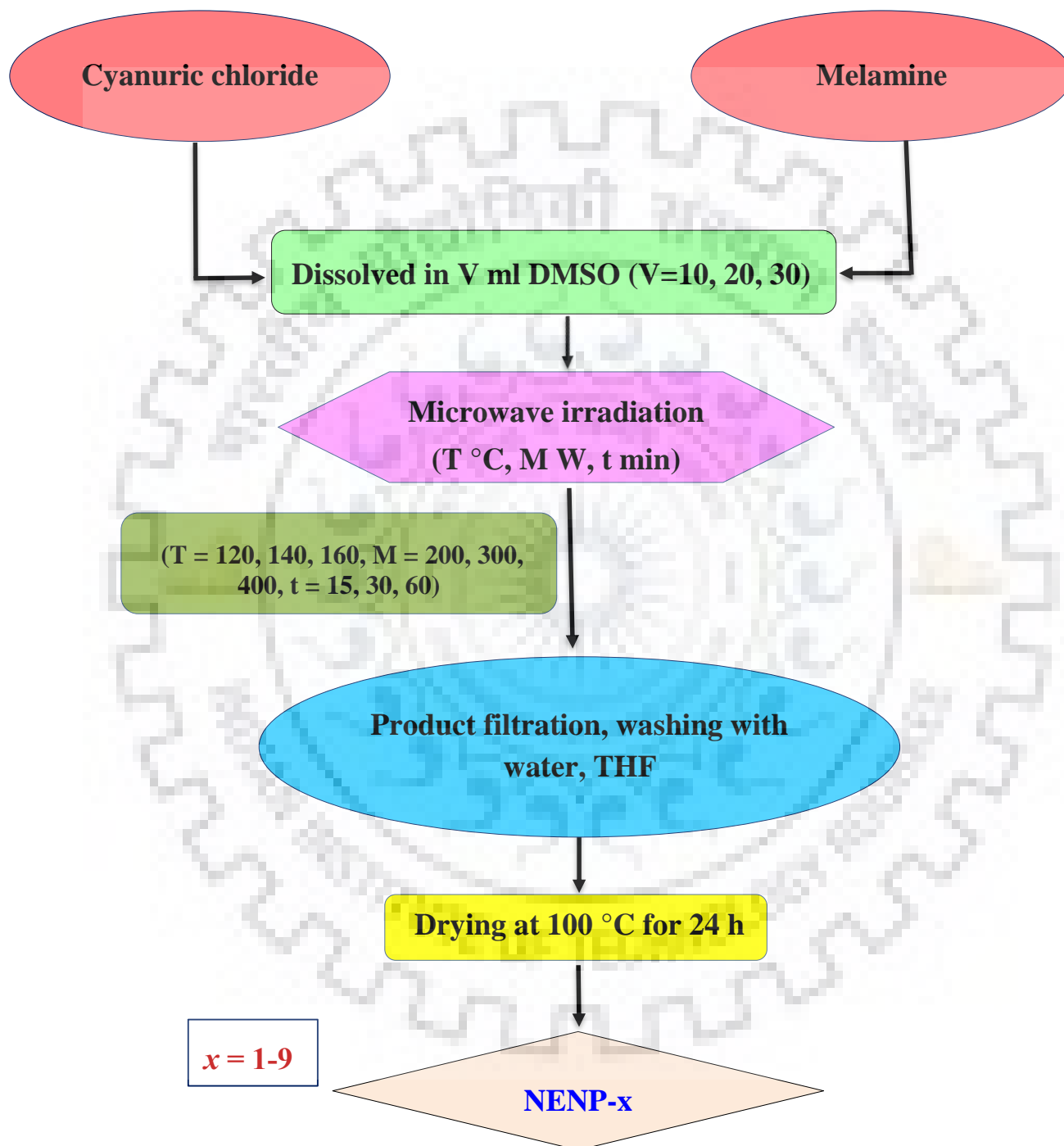
2.4. NENPs as electrode materials for electrochemical supercapacitor

As per our objectives of having large contents of nitrogen in the framework and high surface area, NENPs are expected to show good electrochemical supercapacitor performance. Thus, in the present work NENPs were used as active materials for fabricating electrodes and these were utilized for supercapacitor applications. The electrochemical analysis has been carried out by using a *CH Instruments 660D* electrochemical work station (*CH Instruments USA*). Different techniques such as cyclic voltammetry (CV), galvanostatic charge/discharge (GCD) and electrochemical impedance spectroscopy (EIS) have been utilized. The CV and GCD investigations were performed at scan rate of 1 to 100 mV s⁻¹ and current density of 1 to 9 A g⁻¹, respectively, at potential window from -0.6 to 1.0 V. Moreover, electrochemical study of synthesized specimens was carried out in both three and two electrode systems using 0.1 M H₂SO₄ an electrolyte.

2.4.1. Electrode fabrication for three-electrodes system

Prior to preparation of the working electrode, the glassy carbon electrode (GCE) surface was cleaned using a slurry of alumina powder and performing ultrasonication for 30 min. For the electrode fabrication the active material slurry was prepared by dispersing 5 µl of PTFE (5 wt% of ethanol) and 5 mg of active material in requisite amount of ethanol through ultrasonication for 30 min. The geometric surface area of GCE used for the electrochemical studies was 0.07 cm². 50 µl of the slurry was taken and drop casted on the GCE surface carefully and allowed to dry for overnight at 60 °C

for the electrochemical investigations. A three-electrode configuration system was made-up with active material modified GCE, Pt wire, and saturated calomel electrode as working, counter and reference electrodes, respectively.



Scheme 2.1: Reaction scheme for the synthesis of NENPs via microwave assisted condensation of melamine and cyanuric chloride.

2.4.2. Electrode fabrication for two-electrodes system

Asymmetric supercapacitor device (ASCD) of specimen NENP-1 was fabricated using commercially available Whatman 54 filter paper, active material, and activated carbon, as separator, negative and positive electrode materials, respectively. First, the active material slurry was prepared by mixing either active material or activated carbon and 5 μl of PTFE (5 wt% of ethanol) in 9:1 mass ratio using ethanol (5 mg ml^{-1}) with the help of ultrasonication for 30 min. The as-prepared slurries were then drop casted individually on the graphite sheet of $0.5 \times 0.5 \text{ cm}^2$ area and dried at $60 \text{ }^\circ\text{C}$ for overnight. The graphite sheet coated with active material and activated carbon was used as negative and positive electrodes, respectively.

2.5. Catalysis

In the present work, NENP-1 has been used as a heterogeneous metal free organocatalyst for the Knoevenagel reaction of malononitrile with various aromatic aldehydes. In a model reaction, benzaldehyde (1 mmol) and malononitrile (1 mmol) were reacted in 1:1 volume ratio of dioxane- H_2O (total volume of the reaction mixture is 1 ml) at $25 \text{ }^\circ\text{C}$ in the presence of 5 mg of NENP-1 and the product was isolated after recrystallization with ethanol. Various experimental parameters such as catalyst loading, reaction time and solvent ratio were varied to optimize the product yield. Total of eight aromatic aldehydes have been reacted with malononitrile to conclude the versatility of the metal free organocatalyst NENP-1.

2.6. Uranium sorption experiments

A large number of radioactive wastes are being produced with the development of nuclear power industries.[31-33] Uranium is considered as one of the main contaminants and a hazard to the environment and humans due to its radioactive and toxic nature. Thus, efficient removal of uranium from these nuclear waste as well as the other water bodies could make the uranium based nuclear energy technology economically and environmentally sustainable.[34,35] Moreover, World Health Organization (WHO) and United States Environmental Protection Agency (USEPA) have defined the maximum permissible limit of uranium in drinking water to be 0.015 and 0.030 mg l^{-1} , respectively.[36,37] This in-turn has forced the scientific community to develop suitable technology for removing uranium from the nuclear industry effluents prior to disposal for minimizing the adverse impact on environment and human health.

Moreover, from an estimated 4.5 billion ton of uranium present in oceans around the world which is considered as the major uranium source only about 10^3 tonnes is recovered annually.[38-41] This amount is not high enough in the perspective of required quantity for sustainable development of nuclear power plants to solve the energy crisis while taking care the environmental concerns.[38-41] Thus, for a viable growth of nuclear energy, methodologies for the efficient and selective extraction of uranium from seawater is required without disturbing the seawater eco-culture.

2.6.1. Sorption experiments in aqueous solution

In this research, uranium adsorption experiments were carried out using a stock solution of 1000 mg l^{-1} of uranium in de-ionized (DI) water [2.11 g of $\text{UO}_2(\text{NO}_3)_2 \cdot 6\text{H}_2\text{O}$ in 1000 ml of DI water]. For the adsorption experiments, desired concentrations of uranium were prepared by diluting the stock solution. In the adsorption studies, 10 mg of the adsorbent, NENP-1, was introduced into 10 ml of uranium solution of desired concentration. The adsorption at optimum *pH* was investigated by carrying out the adsorption experiments at *pH* of 3, 4, 5, 6, 7 and 8 by adjusting the *pH* of uranium solution using 0.1 M HNO_3 and 0.1 M NaOH . In order to study the adsorption isotherms and effect of concentration on adsorption capacity, the concentration of uranium was varied from 5 to 1000 mg l^{-1} . The adsorption kinetics was investigated by varying the contact time of 5, 30, 60 and 120 min. Similarly, thermodynamics of adsorption process was studied at temperatures of 5, 25, 35, 55 and 75°C .

2.6.2. Sorption experiments in simulated seawater condition

The use of the adsorbent NENP-1 for the uranium adsorption in simulated seawater condition was performed following the previous report.[42] Simulated seawater was prepared by dissolving 0.017 g of uranyl nitrate hexahydrate, 25.6 g of sodium chloride and 0.193 g of sodium bicarbonate in 1000 ml of DI water. Then, 50 mg of adsorbent was continuously stirred in 200 ml of the simulated seawater for 24 h contact time and after centrifugation and filtration, the filtrate was subjected to ICP-OES analysis for determining the uranium concentration. The regeneration of the specimen was done by washing with 0.1 M HCl solution, three times and finally drying it at 80°C for 12 h.

2.7. Characterization

2.7.1. Fourier transform infrared (FTIR) spectroscopy

Fourier transform infrared (FTIR) spectroscopy is one of the primary techniques used by chemists and materials scientist for investigating the product formation both in academic research and industrial R&D laboratories.[43-45] Analysis of molecules and materials based on the functional groups present in it, is the principal working principle of FTIR. Absorption of IR radiation by polar molecules can induce transition between the vibronic energy levels.[43-45] The frequency at which the molecule absorb the IR radiation is characteristic for each functional group and provides vital information. The FTIR technique can analyze the materials in solid, liquid and gaseous states. Moreover, this technique can also be used to analyze stereochemistry, hydrogen bonding, polymers identification, resins, impurities and reaction intermediates.[44-50] In this research, all synthesized specimens have been characterized by FTIR technique using *Perkin Elmer Spectrum 2 FTIR* spectrophotometer for structural confirmation. In this technique, ~1 mg of sample and ~200 mg of KBr were taken and grinded well in a mortar-pestle to form a uniform mixture of fine particles. After making the fine mixture, a transparent pellet is formed using a hydraulic press at a pressure range of 150 psi. These pallets were employed for scanning in the IR range of 4000 to 400 cm^{-1} with a resolution of 4 cm^{-1} for 16 scans.

2.7.2. Nuclear magnetic resonance (NMR) spectroscopy

Nuclear magnetic resonance (NMR) spectroscopy, is a foremost spectroscopic technique widely used by chemist, biologist and physicist for the identification of materials, purity of samples, structural confirmation, chemical composition, intermolecular interactions, stereochemistry, analysis of biopolymers and magnetic resonance imaging scanning.[43,51-56] The basic principle of this technique is based on the fact that magnetically active nuclei such as ^1H , ^5B , ^9F , ^{13}C , ^{15}N , ^{31}P , and ^{29}Si etc. absorb radiowaves of characteristic frequency under the influence of external magnetic field. Both solid and liquid samples could be analyzed using this non-destructive technique. The solution NMR spectra consist of a series of very sharp signals, due to suppressing of anisotropic interactions by rapid motion of molecules in liquid state. In contrast, broad signals are observed in solid state NMR spectra due to the large number of anisotropic dipolar interactions. In order to overcome these interactions and to get resolved signals, the sample is rotated at the magic angle (54.74°) with respect to the external magnetic field.[52] This technique is known as magic angle spinning (MAS).[52] In cross polarization (CP) technique, transfer of polarization from more abundant nuclei (^1H , ^{19}F and ^{31}P) to the low abundant nuclei (^{13}C , ^{15}N and ^{29}Si) resulted in the improvement of the signal to noise ratio in the NMR spectrum and combination of both is termed as

CPMAS NMR.[53,54] In the present research, *JEOL resonance JNM-ECX-400II* spectrometer with frequency of 400 MHz, has been utilized. The liquid state NMR spectra were recorded by dissolving the specimens in CDCl_3 and deuterated DMSO. The ^{13}C CPMAS NMR spectra were recorded at 400 MHz by rotating the samples at 54.74° (magic angle) with sample spinning frequency of 10 kHz. The chemical shifts for ^{13}C nucleus was referenced at 39.47 ppm using adamantane.[52]

2.7.3. X-ray photoelectron spectroscopy (XPS)

X-ray photoelectron spectroscopy (XPS) has been proved a very informative spectroscopic technique, developed in 1951 by the research group of Swedish Professor Kai Siegbahn for analysis of surface composition.[43,57,58] This technique detects the chemical environment and electronic state of elements present in the specimens. Monochromatic low energy X-ray of 1486.6 eV (with Al-K_α radiation source) or 1253.3 eV (with Mg-K_α radiation source) are being used for excitation of photoelectron from the surface of materials. Hemispherical analyzer has been used to measure the kinetic energy of the emitted photoelectrons to find the chemical composition and information about the speciation of various elements present up to 10 nm thickness of the surface of solid samples. In the present research, *PHI-5000 VersaProbe III*, spectrophotometer equipped with multichannel detector and hemispherical analyzer has been used. The analysis was performed by mounting the sample over carbon tape and keeping it in the sample introduction chamber under vacuum for 6 h and then analyzed using monochromatic Al-K_α radiation source ($h\nu = 1486.6$ eV) under ultra-high vacuum condition. The binding energy scale was referenced with respect to C1s at 284.8 eV.[18]

2.7.4. X-ray diffraction (XRD)

The X-ray diffraction (XRD) has been extensively employed as non-destructive analytical technique for the structural and phase analysis of materials.[43,59-62] It has been widely used for quality control in industries.[59-62] This technique has also been used for the investigation of thermal expansion, phase diagrams and stability under varying temperature. It can provide in depth information for the crystalline materials only. However, it fails to provide structural information for amorphous materials. Moreover, phase identification and quantitative analysis may be hindered by peak overlapping. XRD patterns are observed based on interaction of monochromatic X-ray with crystalline material and constructive interference produced by satisfying Bragg's Law (equation 2.1);[58-61]

$$n\lambda = 2d \sin\theta \quad (2.1)$$

In the present work, XRD analysis was performed on *Ultima IV (Rigaku, Japan)* X-ray diffractometer with Cu-K α radiation source ($\lambda = 0.15405$ nm) to analyze the diffraction patterns of samples.[59-63] The XRD patterns were recorded with scanning speed of 6° min^{-1} in the 2θ range of 10 to 90° .

2.7.5. Field emission scanning electron microscopy (FESEM)

Field emission scanning electron microscopy (FESEM) is an indispensable technique that has been used worldwide.[43,64-67] This technique is mainly employed for the microstructural analysis of the specimens. In FESEM analysis, high energy electrons produced from electron gun used to strike the surface of the specimen which generates secondary electrons from the surface.[65-67] Ejection speed and angle of these electrons depends upon the nature of the elements present in the specimens. The secondary electron detector converts these signals to the images. Similarly, back scattered electrons detected by BSE detector are also used for image the structure which give very important information about the nature of the elements present on the surface of specimens. Moreover, X-rays are formed due to the bombardment of these high energy electrons, which are characteristics of the elements present in the sample and EDAX detectors are used to provide information about the elemental composition.[67] In the present research, microstructural analysis of the samples was performed using *TESCAN MIRA3 FESEM* at an operating voltage of 10-20 kV. Before the FESEM analysis, standard sputtering technique was used for the gold coating of the specimens.

2.7.6. Transmission electron microscopy (TEM)

Transmission electron microscopy (TEM) is a microscopic technique that uses high energy electron beams that transmit through ultrathin specimen (in general thickness < 200 nm). These transmitted electrons are used to create image of the specimen at very high magnification with a greater resolution. It provides images with high resolution and magnification as compared to FESEM due to the use of high energetic electron beams.[68,69] The powder samples in general are dispersed over carbon-coated copper grid.[68,69] This beam interacts with sample to provide the information about the microstructure, chemical composition, crystal structure and defects in the sample.[70,71] In the present research, *TECNAI G² TEM* microscope at an operating voltage of 200 kV, was used to analyze the pore structure of specimens. Before the analysis, samples were prepared by dispersing it in ethanol using a sonicator for 5 to 15 min followed by placing a drop of this suspension over carbon coated holy copper grid of 200 mesh size and dried in air.

2.7.7. Thermal analysis

Thermogravimetric analysis (TGA) is a very popular technique that measures change of mass of a specimen as a function of temperature.[72-77] TGA have been also used to study the important properties of materials such as thermal stability, degradation, oxidation, reduction, etc.[72-77] TGA measures weight loss of a material when it heated over a wide temperature range at predetermined heating rate using different atmospheric conditions such as air, Ar, N₂, and CO₂ etc.[77] Both solid and liquid specimens could be characterized using this technique.[78] In this study, "EXSTAR TG/DTA 6300" TGA instrument was employed to measure the thermal stability of the synthesized specimens. The TGA experiments were performed by measuring the weight loss in the temperature range of 25 to 850 °C with a heating rate of 5 °C min⁻¹ by taken about 4-6 mg of specimen in an alumina sample holder under air atmosphere.

2.7.8. Elemental analysis

2.7.8.1. CHNS(O)

CHNS(O) elemental analysis is a technique used for quantification of carbon, nitrogen, hydrogen, sulphur and oxygen contents present in the specimens.[79-81] All type of materials (solid, liquid, volatile and gaseous compounds) can be characterized using this technique which is based on the principle of "Dumas method" *i.e.* the complete and instant oxidation of the specimen by burning it in the presence of excess oxygen.[79-81] The combustion products of C (CO₂), N (NO₂ and NO), H (H₂O) and S (SO₂) are carried by carrier gas (helium gas), separated by a chromatographic column and quantified by thermal conductivity detector.[79] In the present research, C, N, H and S composition analysis of NENPs was done using *Thermo scientific, Flash 2000* elemental analyzer. In a typical experiment, 1-2 mg of sample was packed in tin capsules followed by loading it in the instrument. Prior to analysis, the instrument was calibrated using analytical reagent grade sulphanilic acid and aspartic acid as reference materials.

2.7.8.2. Inductively coupled plasma-optical emission spectrometry (ICP-OES)

ICP-OES is an important analytical technique widely used for the determination of elemental composition of elements with atomic number 3 (Lithium) and higher.[43,82,83] It is an emission spectroscopy that produces excited atoms and ions from samples using inductively coupled plasma. Excited atoms and ions emits electromagnetic radiation of a particular wavelength when they return to their low energy levels.[43,82,83] These characteristic wavelengths can be used for the

determination of elements. In the present research, the ICP-OES (*prodigy SPEC, Teledyne Leemans lab, USA*) was employed to determine the concentration of uranium present in the specimens. Before analysis, a calibration curve was plotted using different concentrations of standard solutions.

2.7.9. Gas sorption

Gas sorption technique is used for analyzing the textural properties such as specific surface area, pore size and pore volume in porous materials.[84-92] For surface area analysis, inert gases such as N₂ and Ar are mainly employed as probe molecules at -196 and -186 °C, respectively.[85] The amount of gas adsorbed over the surface of solid has been used to estimate the specific surface area using Brunauer-Emmett-Teller (BET) method. The linear form of BET equation, as shown in *equation 2.2* can be written as:[85,86]

$$\frac{1}{v\left[\left(\frac{p_0}{p}\right)-1\right]} = c - \frac{1}{v_m c} \left(\frac{p}{p_0}\right) + \frac{1}{v_m c} \quad (2.2)$$

where, v is amount of gas adsorbed, v_m is monolayer adsorbed gas amount, p and p_0 are the equilibrium and saturation pressure of adsorbate at its boiling temperature of adsorption and c is the BET constant. This BET equation can be employed to measure the total surface area (S_{total}) and specific surface area (SA_{BET}) by given *equations 2.3 and 2.4*:[85,86]

$$S_{total} = \frac{(v_m N s)}{V} \quad (2.3)$$

$$SA_{BET} = \frac{S_{total}}{a} \quad (2.4)$$

where, N is Avogadro's number, V is the adsorbate (probe as) molar volume, s is adsorbate cross section and a is adsorbent mass.

Langmuir surface area of the adsorbent could be calculated using the *equation 2.5*:[93]

$$SA_{Lang} = \frac{(X_m \times N \times S)}{M} \quad (2.5)$$

where, X_m is the maximum amount of adsorbate adsorbed per gram of adsorbent for monolayer formation, M is the molecular weight of the adsorbate (mg/molecule), N = Avogadro's number and S is the contact surface area per each molecule (m²).

In the present research, *Autosorb-iQ2, Quantachrome Instruments, USA* was used to measure the N₂ sorption isotherm at -196 °C using liquid N₂. Prior to gas adsorption measurements, the samples were degassed at 120 °C for 6 h to remove the adsorbed gas and moisture. The relative

pressure range for calculation of S_{ABET} using BET model was obtained using Rouquerol plots.[84-88] Density functional theory (DFT) was applied to adsorption or desorption branch of N_2 isotherm to estimate the pore size distribution (PSD) The total pore volume was estimated from adsorption branch at a relative pressure (P/P_0) of 0.95.[90]

Gas sorption applications such as CO_2 , CH_4 and H_2 sorption analysis were also performed using the instrument. The sorption isotherms for CO_2 and CH_4 were measured at 0 and 25 °C up to 1 bar. The chiller circulator containing ethylene glycol and water (1:1 volumetric ratio) was used to maintain the bath temperature. H_2 uptake was estimated at -196 °C and 1 bar. The isosteric heat of adsorption (Q_{st}) for CO_2 and CH_4 was calculated by fitting the CO_2 and CH_4 adsorption data into Clausius Clapeyron equation (equation 2.6);[91,92]

$$\ln \frac{p_1}{p_2} = \frac{\Delta H}{R} \left(\frac{1}{T_2} - \frac{1}{T_1} \right) \quad (2.6)$$

where, p_1 and p_2 are pressures (bar) at absolute temperature T_1 (K) and T_2 (K). R and ΔH are gas constant ($8.3145 \text{ J mol}^{-1} \text{ K}^{-1}$) and isosteric heat of adsorption (kJ mol^{-1}), respectively.

Ideal Adsorbed Solution Theory (IAST): Gas sorption selectivity study

The pure component experimental isotherm of CO_2 and N_2 were fitted to dual site Langmuir model (equation 2.7) and single site Langmuir model (equation 2.8), respectively;

$$q = \frac{b_1 p q_1}{1 + b_1 p} + \frac{b_2 p q_2}{1 + b_2 p} \quad (2.7)$$

$$q = \frac{b_3 p q_3}{1 + b_3 p} \quad (2.8)$$

where,

q = amount of gas adsorbed per unit mass of the adsorbent experimentally

p = bulk gas phase pressure (bar)

q_1 and q_2 = saturation capacities of site 1 and 2 for CO_2 adsorption

b_1 and b_2 = affinity coefficient of sites 1 and 2 for CO_2 adsorption

q_3 = saturation capacity of the material for N_2 adsorption

b_3 = affinity coefficient of sites for N_2 adsorption

The fitting parameters were used to estimate the IAST binary gas sorption selectivity, S defined as;

$$S = \frac{q_1/q_2}{p_1/p_2} \quad (2.9)$$

where q_1 and q_2 are the molar loadings and p_1 and p_2 are the partial pressures of species 1 and 2, respectively.

2.7.10. Electrochemical workstation

Electrochemical workstation is used to study the electrochemical properties of the specimens including cyclic voltammetry (CV), linear sweep voltammetry (LSV), square-wave voltammetry (SWV), amperometry, galvanostatic charge discharge (GCD) and electrochemical impedance spectroscopy (EIS) *etc.*[94] In the present research work, the supercapacitor studies of selected NENPs using various techniques such as CV, GCD, and EIS were carried out at *CH Instruments 660D* electrochemical work station.

2.7.11. Gas chromatography-mass spectrometry (GC-MS)

GC-MS is a very powerful and universal analytical technique widely used in chemistry, toxicology, forensics, food science and environmental research.[43,95,96] GC-MS is a combination of two different analytical techniques viz. gas chromatography and mass spectrometry, extensively used to analyze complex chemical mixtures. GC can separate volatile compounds with high resolution and MS can record mass spectrum of the various components. This hybrid instrument provides detailed structural information of compounds in an organic or biological mixture. GC is a type of chromatography in which the mobile phase is an inert gas such as helium or nitrogen, and the stationary phase is a microscopic layer of liquid sample on an inert solid support, inside a column.[43] The sample is passed over the column by a stream of carrier gas. Components in a sample are separated from each other and fragmented by ionization and arranged by mass to form a fragmentation spectrum. The fragmentation spectrum for a particular component of a sample is characteristic of that component. It is so specific that it is often referred to as the molecular fingerprint. In this research work, GC-MS was used to determine the purity of the products obtained by Knoevenagel condensation of different aldehydes with malononitrile. GC-MS analysis was performed on GC (Perkin Elmer GC Clarus 680) and MS (Perkin Elmer MS Clarus SQ8T).

References

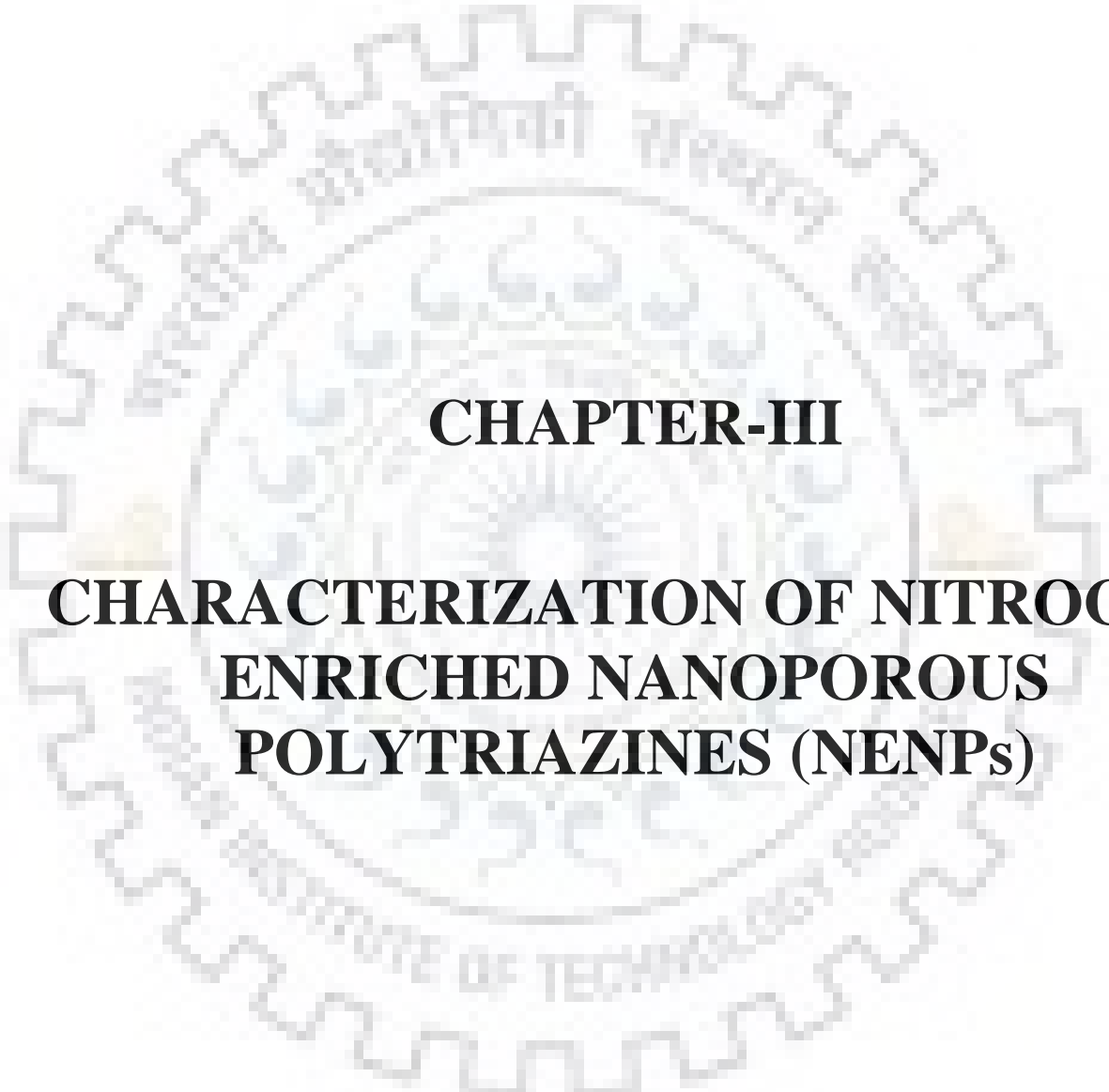
1. J. Wang, L. Huang, R. Yang, Z. Zhang, J. Wu and Y. Gao, Recent advances in solid sorbents for CO₂ capture and new development trends, *Energy Environ. Sci.*, 2014, **7**, 3478-3518.
2. T. Ben, C. Pei, D. Zhang, J. Xu, F. Deng, X. Jinga and S. Qiu, Gas storage in porous aromatic frameworks (PAFs), *Energy Environ. Sci.*, 2011, **4**, 3991-3999.
3. V. Sharma, S. Khilari, D. Pradhan and P. Mohanty, Solvothermally synthesized nanoporous hypercrosslinked polyaniline: Studies of the gas sorption and charge storage behavior, *RSC Adv.*, 2015, **6**, 56421-56428.
4. B. Li, Q. Sun, Y. Zhang, C.W. Abney, B. Aguila, W. Lin and S. Ma, Functionalized porous aromatic framework for efficient uranium adsorption from aqueous solutions, *ACS Appl. Mater. Interfaces*, 2017, **9**, 12511-12517.
5. D. H. Jurcakova, A. M. Puziy, O. I. Poddubnaya, F. S. Garcia, J. M. D. Tascon and G. Q. Lu, Highly stable performance of supercapacitors from phosphorus-enriched carbons, *J. Am. Chem. Soc.*, 2009, **131**, 5026-5027.
6. L. Hao, B. Luo, X. Li, M. Jin, Y. Fang, Z. Tang, Y. Jia, M. Liang, A. Thomas, J. Yang and L. Zhi, Terephthalonitrile-derived nitrogen-rich networks for high performance supercapacitors, *Energy Environ. Sci.*, 2012, **5**, 9747-9751.
7. A. M. Khattak, Z. A. Ghazi, B. Liang, N. A. Khan, A. Iqbal, L. Li and Z. Tang, A redox-active 2D covalent organic framework with pyridine moieties capable of faradaic energy storage, *J. Mater. Chem. A*, 2016, **4**, 16312-16317.
8. J. Zhang, Z. Wang, L. Li, J. Zhao, J. Zheng, H. Cui and Z. Zhu, Self-assembly of CNH nanocages with remarkable catalytic performance, *J. Mater. Chem. A*, 2014, **2**, 8179-8183.
9. S. Hug, L. Stegbauer, H. Oh, M. Hirscher and B. V. Lotsch, Nitrogen-rich covalent triazine frameworks as high-performance platforms for selective carbon capture and storage, *Chem. Mater.*, 2015, **27**, 8001-8010.
10. K. Wang, H. Huang, D. Liu, C. Wang, J. Li and C. Zhong, Covalent triazine-based frameworks with ultramicropores and high nitrogen contents for highly selective CO₂ capture, *Environ. Sci. Technol.*, 2016, **50**, 4869-4876.
11. L. Wang, Z. Gao, J. Chang, X. Liu, D. Wu, F. Xu, Y. Guo and K. Jiang, Nitrogen doped porous carbons as electrode materials for high-performance supercapacitor and dye sensitized solar cell, *ACS Appl. Mater. Interfaces*, 2015, **7**, 20234-20244.
12. P. Puthiaraj, Y. Lee, S. Zhang and W. Ahn, Triazine-based covalent organic polymers: Design, synthesis and applications in heterogeneous catalysis, *J. Mater. Chem. A*, 2016, **4**, 16288-16311.
13. R. Muhammad, P. Rekha and P. Mohanty, Facile synthesis of a thermally stable imine and benzimidazole functionalized nanoporous polymer (IBFNP) for CO₂ capture application, *Greenhouse Gases: Sci. Technol.*, 2016, **6**, 150-157.
14. R. Muhammad, Jyoti and P. Mohanty, Nitrogen enriched triazine bridged mesoporous organosilicas for CO₂ capture and dye adsorption applications, *J. Mol. Liq.*, 2017, **248**, 127-134.
15. S. Feng and G. Li, *Hydrothermal and solvothermal syntheses*, in: *Modern inorganic synthetic chemistry*, Elsevier B.V, Amsterdam, The Netherlands, 2011, 63-93.
16. E. Zhang, Y. Tang, K. Peng, C. Guo and Y. M. Zhang, Synthesis and magnetic properties of core-shell nanoparticles under hydrothermal conditions, *Solid State Commun.*, 2008, **148**, 496-500.
17. R. Muhammad, P. Rekha and P. Mohanty, Amino linked inorganic-organic hybrid nanoporous materials (HNMs) for CO₂ capture and H₂ storage applications, *RSC Adv.*, 2016, **6**, 17100-17105.

18. R. Muhammad, M. Chaudhary and P. Mohanty, Harnessing electron-rich framework in cyclophosphazene derived hybrid nanoporous materials for organocatalytic C-C bond formation and gas sorption applications, *J. CO₂ Util.*, 2018, **25**, 302-309.
19. K. Huang, F. Liu and S. Dai, Solvothermal synthesis of hierarchically nanoporous organic polymers with tunable nitrogen functionality for highly selective capture of CO₂, *J. Mater. Chem. A*, 2016, **4**, 13063-13070.
20. K. S. Suslick, Sonochemistry, *Science*, 1990, **247**, 1439-1445
21. K. S. Suslick and G. J. Price, Applications of ultrasound to materials chemistry, *Annu. Rev. Mater. Sci.*, 1999, **29**, 295-326.
22. K. S. Suslick and D. J. Flannigan, Inside a collapsing bubble: Sonoluminescence and the conditions during cavitation, *Annu. Rev. Phys. Chem.*, 2008, **59**, 659-683.
23. P. Mohanty, N. M. K. Linn and K. Landskron, Ultrafast sonochemical synthesis of methane and ethane bridged periodic mesoporous organosilicas, *Langmuir*, 2010, **26**, 1147-1151.
24. P. Rekha, R. Muhammad and P. Mohanty, Sonochemical synthesis of cyclophosphazene bridged mesoporous organosilicas and their application in methyl orange, congo red and Cr(VI) removal, *RSC Adv.*, 2015, **5**, 67690-67699.
25. J. A. Gerbec, D. Magana, A. Washington and G. F. Strouse, Microwave-enhanced reaction rates for nanoparticle synthesis, *J. Am. Chem. Soc.*, 2005, **127**, 15791-15800.
26. S. Faraji and F. N. Ani, Microwave-assisted synthesis of metal oxide/hydroxide composite electrodes for high power supercapacitors-A review, *J. Power Sources*, 2014, **263**, 338-360.
27. Y. Wang, J. Tian, C. Fei, L. Lv, X. Liu, Z. Zhao and G. Cao, Microwave-assisted synthesis of SnO₂ nanosheets photoanodes for dye-sensitized solar cells, *J. Phys. Chem. C*, 2014, **118**, 25931-25938.
28. M. G. Schwab, B. Fassbender, H. W. Spiess, A. Thomas, X. Feng and K. Mullen, Catalyst-free preparation of melamine-based microporous polymer network through Schiff base chemistry, *J. Am. Chem. Soc.*, 2009, **131**, 7216-7217.
29. P. Puthiaraj, S. S. Kim and W. S. Ahn, Covalent triazine polymers using a cyanuric chloride precursor via Friedel-Crafts reaction for CO₂ adsorption/separation, *Chem. Eng. J.*, 2016, **283**, 184-192.
30. K. K. Rana and S. Rana, Microwave reactors: A brief review on its fundamental aspects and applications, *OALib*, 2014, **1**, 1-16 DOI: 10.4236/oalib.1100748.
31. Q. Sun, B. Aguila, L. D. Earl, C. W. Abney, L. Wojtas, P. K. Thallapally and S. Ma, Covalent organic frameworks as a decorating platform for utilization and affinity enhancement of chelating sites for radionuclide sequestration, *Adv. Mater.*, 2018, **30**, 1-9.
32. D. S. Sholl and R. P. Lively, Seven chemical separations to change the world, *Nature*, 2016, **532**, 435-437.
33. Y. Lu, Uranium extraction: Coordination chemistry in the ocean, *Nat. Chem.*, 2014, **6**, 175-177.
34. L. Ling and W. X. Zhang, Enrichment and encapsulation of uranium with iron nanoparticle, *J. Am. Chem. Soc.*, 2015, **137**, 2788-2791.
35. S. Ma, L. Huang, L. Ma, Y. Shim, S. M. Islam, P. Wang, L. D. Zhao, S. Wang, G. Sun, X. Yang and M. G. Kanatzidis, Efficient uranium capture by polysulfide/layered double hydroxide composites, *J. Am. Chem. Soc.*, 2015, **137**, 3670-3677.
36. World Health Organization, Uranium in drinking-water-background document for development of WHO guidelines for drinking-water quality, WHO Press; Geneva, Switzerland: 2012, <https://apps.who.int/iris/handle/10665/75365>.
37. United States Environmental Protection Agency, drinking water contaminants radionuclides, <https://www.epa.gov/ground-water-and-drinking-water/national-primary-drinking-water-regulations#main-content>.

38. R.V. Davies, J. Kennedy, R.W. McIlroy, R. Spence and K.M. Hill, Extraction of uranium from sea water, *Nature*, 1964, **203**, 1110-1115.
39. K. Morris and R. Raiswell, Chapter 4: Biogeochemical cycles and remobilisation of the actinide elements, *Radioactiv. Environ.*, 2002, **2**,101-141.
40. T. Zhang, G. Asakura and Uchiyama, The adsorption mechanism of uranium(VI) from seawater on a macroporous fibrous polymeric adsorbent containing amidoxime chelating functional group, *React. Funct. Polym.*, 2003, **57**, 67-76.
41. U. Bardi, Extracting minerals from seawater: An energy analysis, *Sustainability*, 2010, **2**, 980-992.
42. C. Gunathilake, J. Gorka, S. S. Dai and M. Jaroniec, Amidoxime-modified mesoporous silica for uranium adsorption under seawater conditions, *J. Mater. Chem. A*, 2015, **3**, 11650-11659.
43. F. A. Settle, *Handbook of instrumental techniques for analytic chemistry*, Prentice Hall, New Jersey, USA, 1997.
44. B. Stuart, *Infrared spectroscopy: Fundamentals and applications*, John Wiley and Sons, Chichester, UK, 2004.
45. B. C. Smith, *Fundamentals of Fourier transform infrared spectroscopy*, CRC Press, Taylor and Francis Group, London, UK, 2011.
46. M. Tasumi and A. Sakamoto, *Introduction to experimental infrared spectroscopy*, John Wiley and Sons, Chichester, UK, 2015.
47. R. A. Shaw and H. H. Mantsch, *Infrared spectroscopy in clinical and diagnostic analysis*, John Wiley & Sons Ltd, Chichester, UK, 2000.
48. V. P. Tolostoy, I. V. Chernyshova and V. A. Skryshevsky, *Handbook of infrared spectroscopy of ultrathin films*, John Wiley & Sons Ltd, Hoboken, New Jersey, USA, 2003.
49. M. L. McKelvy, T. R. Britt, B. L. Davis, J. K. Gillie, F. B. Graves and L. A. Lentz, Infrared spectroscopy, *Anal. Chem.*, 1998, **70**, 119-177.
50. E. A. Carter, C. P. Marshall, M. H. M. Ali, R. Ganendren, T. C. Sorrell, L. Wright, Y.-C. Lee, C.-I. Chen and P. A. Lay, *New approaches in biomedical spectroscopy, Infrared spectroscopy of microorganisms: characterization, identification, and differentiation*, ACS Symposium Series, 963, American Chemical Society, 2007.
51. J. Keeler, *Understanding NMR spectroscopy*, John Wiley & Sons Ltd, Chichester, UK, 2002.
52. F. A. Bovey, L. Jelinski and P. A. Mirau, *Nuclear magnetic resonance spectroscopy*, Academic Press, Inc., San Diego, USA, 1988.
53. N. E. Jacobsen, *NMR spectroscopy explained*, John Wiley & Sons, Inc., Hoboken, New Jersey, USA, 2007.
54. M. J. Duer, *Solid-state NMR spectroscopy principles and applications*, Blackwell Science Ltd, London, UK, 2002.
55. H. N. Cheng and A. D. English, *NMR spectroscopy of polymers in solution and in the solid state*, ACS Symposium Series, American Chemical Society, Washington, DC, USA, 2002.
56. G. S. Rule and T. K. Hitchens, *Fundamentals of protein NMR spectroscopy*, Springer, Dordrecht, Netherlands, 2006.
57. S. Suga and A. Sekiyama, *Photoelectron spectroscopy: Bulk and surface electronic structures*, Springer, Berlin, Germany, 2014
58. C. D. Wagner, W. M. Riggs, L. E. Davis, J. E. Moulder and G. E. Mulenberg, *Handbook of x-ray photoelectron spectroscopy*, Perkin Elmer Corp., Minnesota, USA, 1979.
59. E. Korin, N. Froumin and S. Cohen, Surface analysis of nanocomplexes by X-ray photoelectron spectroscopy (XPS), *ACS Biomater. Sci. Eng.*, 2017, **3**, 882-889.

60. K. Tsuji, J. Injuk and R. V. Grieken, *X-ray Spectrometry: Recent technological advances*, John Wiley and Sons, Chichester, UK, 2004.
61. E. P. Bertin, *Introduction to x-ray spectrometric analysis*, Springer, Berlin, Germany, 1978.
62. J. D. Hanawalt, H. W. Rinn and L. K. Frevel, Chemical analysis by X-ray diffraction, *Ind. Eng. Chem. Anal. Ed.*, 1938, **10**, 457-512.
63. G. A. Jeffrey and M. Sax, X-Ray diffraction, crystal structure analysis, and the high-speed computer, *Anal. Chem.*, 1962, **34**, 339-343.
64. O. C. Wells, *Scanning electron microscopy*, McGraw-Hill, New York, USA, 1974.
65. S. Wischnitzer, *Introduction to electron microscopy*, Pergamon Press, New York, USA, 1962.
66. M. E. Haine and V. E. Cosslett, *The electron microscope*, Spon, London, UK, 1961.
67. A. Laskin and J. P. Cowin, Automated single-particle SEM/EDX analysis of submicrometer particles down to 0.1 μm , *Anal. Chem.*, 2001, **73**, 1023-1029.
68. M. D. Graef, *Introduction to conventional transmission electron microscope*, Cambridge University Press, Cambridge, UK, 2003.
69. D. B. Williams and C. B. Carter, *Transmission electron microscopy: A textbook for materials science*, Springer, 2009.
70. J. C. Yang, M. W. Small, R. V. Grieshaber and R. G. Nuzzo, Recent developments and applications of electron microscopy to heterogeneous catalysis, *Chem. Soc. Rev.*, 2012, **41**, 8179-8194.
71. P. Goodhew, J. Humphreys and R. Beanland, *Electron Microscopy and Analysis*, Taylor & Francis, London, 2001.
72. M. E. Brown, *Introduction to thermal analysis techniques and applications*, Kluwer Academic Publishers, New York, USA, 2001.
73. C. B. Murphy, Differential thermal analysis, *Anal. Chem.*, 1958, **30**, 867-872.
74. P. Gabbott, *Principles and applications of thermal analysis*, Blackwell Publishing Ltd, Oxford, UK, 2008.
75. B. E. Erickson, Product review: The many faces of thermal analysis, *Anal. Chem.*, 1999, **71**, 689-692.
76. I. G. Anisimov, M. G. Mitrofanov, O. I. Soletskii, Z. V. Fedorova and A. V. Melikhova, Study of solid hydrocarbons by differential thermal analysis, *Chem Technol Fuels Oils*, 1969, **5**, 451-457.
77. B. V. L'vov, *Thermal decomposition of solids and melts: New thermochemical approach to the mechanism, kinetics and methodology*, St. Petersburg, USA, 2007.
78. M. E. Brown and P. K. Gallagher, *Handbook of thermal analysis and calorimetry: Recent advances, techniques and applications*, Elsevier, Amsterdam, Netherlands, 2011.
79. T. S. Ma and M. Gutterson, Organic elemental analysis, *Anal. Chem.*, 1970, **42**, 105-114.
80. W. J. Kirsten, *Organic elemental analysis: Ultramicro, micro, and trace methods*, Academic Press, New York, USA, 1983.
81. M. Thompson, *CHNS elemental analysers*, Royal Society of Chemistry, London, UK, 2008.
82. C. B. Boss and K. J. Fredeen, Concepts, instrumentations, techniques in inductively coupled plasma optical emission spectrometry, The Perkin-Elmer Corporation, USA, 1997.
83. H. Hou and B. T. Jones, Inductively coupled plasma/optical emission spectrometry, John Wiley and Sons, Chichester, UK, 2000.
84. F. Rouquerol, J. Rouquerol and K. Sing, *Adsorption by powders and porous solids: Principle, methodology and applications*, Academic press, London, UK, 1999.
85. S. J. Gregg and K. S. W. Sing, *Adsorption, Surface Area and Porosity*, Academic press, London, UK, 1982.

86. M. Thommes, K. Kaneko, A. V. Neimark, J. P. Olivier, F. R. Reinoso, J. Rouquerol and K. S.W. Sing, Physisorption of gases, with special reference to the evaluation of surface area and pore size distribution (IUPAC technical report), *Pure Appl. Chem.*, 2015, DOI:10.1515/pac-2014-1117.
87. K. A. Cychoz, R. Guillet-Nicolas, J. Gracia-Martinez and M. Thommes, Recent advances in the textural characterization of hierarchically structure nanoporous materials, *Chem. Soc. Rev.*, 2017, **46**, 189-414.
88. J. U. Keller and R. Staudt, *Gas adsorption equilibria: Experimental methods and adsorptive isotherms*, Springer Science & Business Media, Inc., Boston, USA, 2005.
89. W. Rudziński, W. A. Steele and G. Zgrablich, *Equilibria and dynamics of gas adsorption on heterogeneous solid surfaces*, Academic Press, Amsterdam, Netherlands, 1997.
90. P. I. Ravikovitcha, G. L. Hallera and A. V. Neimarkab, Density functional theory model for calculating pore size distributions: pore structure of nanoporous catalysts, *Adv. Colloid Interface Sci.*, 1998, **76-77**, 203-226.
91. H. Pan, J. A. Ritter and P. B. Balbuena, Examination of the approximations used in determining the isosteric heat of adsorption from the Clausius-Clapeyron equation, *Langmuir*, 1998, **14**, 6323-6327.
92. D. Ramirez, S. Qi and M. J. Rood, Equilibrium and heat of adsorption for organic vapors and activated carbons, *Environ. Sci. Technol.*, 2005, **39**, 5864-5871.
93. I. Langmuir, The adsorption of gases on plane surfaces of glass, mica and platinum, *J. Am. Chem. Soc.*, 1918, **40**, 1361-1403
94. A. Bard and L. Faulkner, *Electrochemical methods-fundamental and applications*, John Wiley and Sons, New Jersey, USA, 2001.
95. A. M. Curran, S. I. Rabin, P. A. Prada and K. G. Furton, Comparison of the volatile organic compounds present in human odor using SPME-GC/MS, *J. Chem. Ecol.*, 2005, **31**, 1607-1619.
96. K. G. Asano, C. K. Bayne, K. M. Horsman, and M. V. Buchanan, Chemical composition of fingerprints for gender determination, *J. Forensic Sci.*, 2002, **47**, 805-807.



CHAPTER-III

**CHARACTERIZATION OF NITROGEN
ENRICHED NANOPOROUS
POLYTRIAZINES (NENPs)**

3.1. Introduction

This chapter deals with the detailed characterization of NENPs synthesized by various methods as discussed in *Chapter-II*, understanding the extent of condensation and product formation by using the state of the art instrumentation facilities. Among various explored methods, NENPs synthesized by microwave-assisted method have shown better polymerization, high N content and possessed good thermal stability. Analytical techniques such as FTIR, ^{13}C CPMAS NMR, XPS, XRD, TGA/DTG, FESEM and TEM have been used for studying the structural and microstructural characteristics.

3.2. Characterization of NENPs

3.2.1. NENP-C-x synthesized by conventional heating method

As discussed in *section 2.3.1.* in *Chapter-II*, conventional heating at different temperatures such as 120, 140 and 160 °C was used for the synthesis of NENPs designated as NENP-C-120, NENP-C-140 and NENP-C-160, respectively. For the synthesis of all these materials DMSO was used as solvent and the reactions were carried out for 24 h. After thorough washing, the specimens have been dried in hot air oven at 100 °C and the final dried powders were used for various characterization. The first and foremost analytical techniques used for the analysis was the FTIR, as it provides useful structural information at a very quick time.

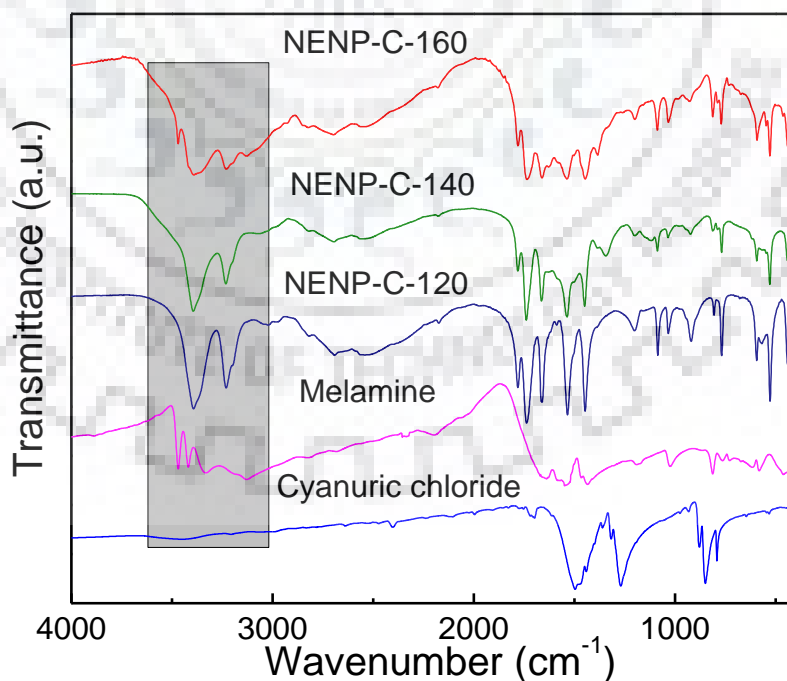


Figure 3.1. FTIR spectra of specimens NENP-C-120, NENP-C-140 and NENP-C-160. The FTIR spectra of the specimens were further compared with precursors melamine and cyanuric chloride.

The FTIR spectra of the specimens as shown in *Figure 3.1* are compared with the FTIR spectra of the precursors to get an overview of the extent of condensation.[1-15] The observation of a broad doublet above 3150 cm^{-1} assigned to the N-H stretching vibration of the primary amine indicates the partial condensation of the framework. Had the condensation been completed, a broad band could have been observed due to the 2° N-H stretching. The partial condensation resulting in the formation of oligomers can also be expected due to the absence of the C-Cl stretching vibrations $\sim 840\text{ cm}^{-1}$. [15] A partial condensation of the framework (formation of oligomers) that may not be suitable in the application perspective. Although, a little broadness of the N-H stretching vibrations can be seen in the specimens with an increase in the synthesis temperature indicates an increased condensation but a complete condensation is not realized even in the NENP-C-160 specimen made at 160°C . [12-21] Detailed assignment of the IR bands is given in *Table 3.1*.

Table 3.1. Assignment of FTIR bands of specimens NENP-C-x.

Bands (cm^{-1})	NENP-C-120	NENP-C-140	NENP-C-160	Ref.
3465	-	-	N-H stretching	[12-17]
3390	NH ₂ stretching	NH ₂ stretching	NH ₂ stretching	[12-17]
3234	N-H stretching	N-H stretching	N-H stretching	[12-17]
3132	-	-	N-H stretching	[12-17]
3041	N-H...N stretching	N-H...N stretching	N-H...N stretching	[14-17]
2940	-	-	C-H stretching	[12-17]
1780	NH ₂ scissoring	NH ₂ scissoring	NH ₂ scissoring	[15-17]
1735	C-N stretching	C-N stretching	C-N stretching	[15-19]
1665	δNH_2	δNH_2	δNH_2	[15,16]
1540	(-C=N-)	(-C=N-)	(-C=N-)	[15,16]
1445	$\nu(\text{CN}) + \delta\text{NH}_2$	$\nu(\text{CN}) + \delta\text{NH}_2$	$\nu(\text{CN}) + \delta\text{NH}_2$	[15,16]
1350	(-C=N-) bending vib.	(-C=N-) bending vib.	(-C=N-) bending vib.	[12-18]
1206	(-C=N-) stretching	(-C=N-) stretching	(-C=N-) stretching	[12-15]
1083	N-H Torsional vib.	N-H Torsional vib.	N-H Torsional vib.	[12-18]
920	$\delta(\text{CNC}) + \delta(\text{NCN})$	$\delta(\text{CNC}) + \delta(\text{NCN})$	$\delta(\text{CNC}) + \delta(\text{NCN})$	[14-18]
880	(-C=N-) vib.	(-C=N-) vibration	(-C=N-) vibration	[16-18]
808	Ring bending and stacked rings stretching	Ring bending and stacked rings stretching	Ring bending and stacked rings stretching	[16-21]
528	ωCCl	-	-	[15]

In order to further understand the chemical environment and product formation, and support the observation of the FTIR, the representative specimens NENP-C-140 and NENP-C-160 were subjected to the XPS analysis which provide detailed insight on the chemical environment and binding states of the elements present in these specimens (*Figure 3.2a*). As can be seen in the survey scan shown in *Figure 3.2a*, both these specimens have peaks originated from C1s, O1s and N1s. The origin of the O1s can be attributed to the carbon tape used for mounting the sample for the XPS analysis. It is also given in the *Figure 3.2a* for comparison. The detailed chemical environment of C1s and N1s could be understood on studying the high resolution spectra. As shown in the *Figure 3.2b*, four different types of carbon can be seen in NENP-C-140 and NENP-C-160 at 284.7, 286.0, 287.9 and 289.4 eV. The peaks at 284.7 and 286.0 eV are originated from the carbon tape. The peaks at 287.9, and 289.4 eV are attributed to the carbon of the triazine ring that is fully condensed and the carbon in the partially condensed ring as well as the carbon at the end group functionality, respectively.[22-28] Decrease in the ratio of the peak area of 289.4 eV peak in the sample NENP-C-160 further support the claim. A similar observation can be seen in the N1s spectrum. Three types of nitrogen can be envisioned in these specimens owing to the partially condensation forming the oligomeric units. The peaks at 401.1, 400.2, and 398.9 eV are attributed to the -NH_2 , -NH- and =N- , respectively.[22-28] There is only minor decrease in the peak area of the 401.1 peak in the specimen made at higher temperature. However, the peak area at 400.2 eV is reduced to a greater extent while the peak area at 398.9 eV is increased by $\sim 140\%$. This further supports the observation of FTIR and confirms a partial condensation of the product forming oligomers. The elemental analysis of these specimens as shown in *Table 3.2* further provides similar conclusion.

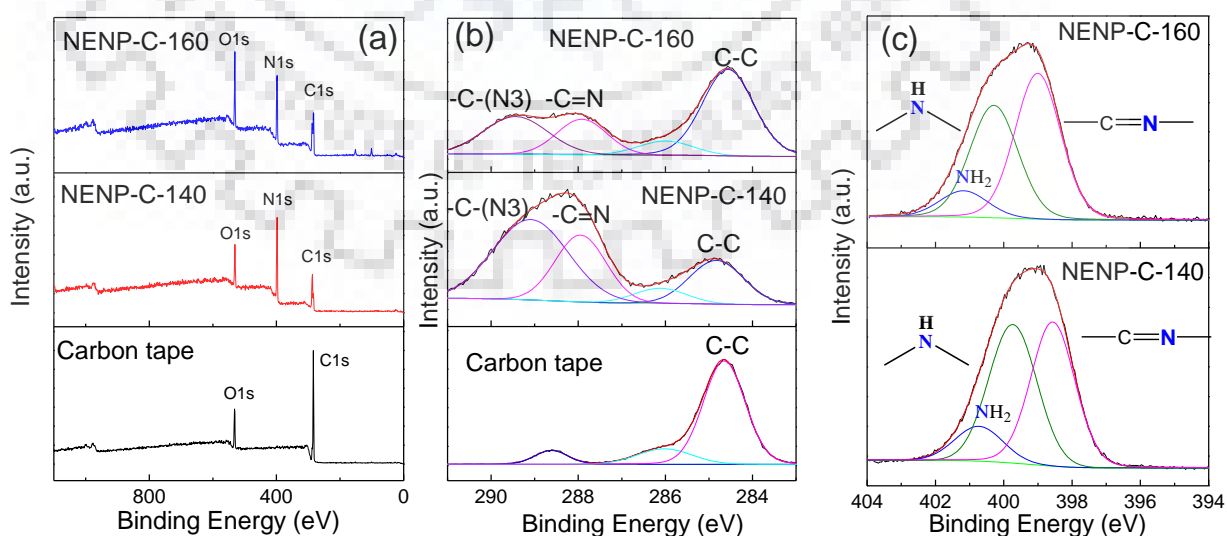


Figure 3.2. XPS spectra (a) survey scan (Su 1s) (b) high resolution (C 1s) (c) high resolution (N 1s), of carbon tape, NENP-C-140 and NENP-C-160.

Microstructural investigation of the specimens has been carried out by FESEM and TEM (*Figure 3.3*). Sheet like microstructure can be seen in the FESEM and TEM images of NENP-C-120 in *Figure 3.3a* and *3.3b*. The thickness of these sheets are in nanometer range and the other two dimensions extends up to several micrometers.

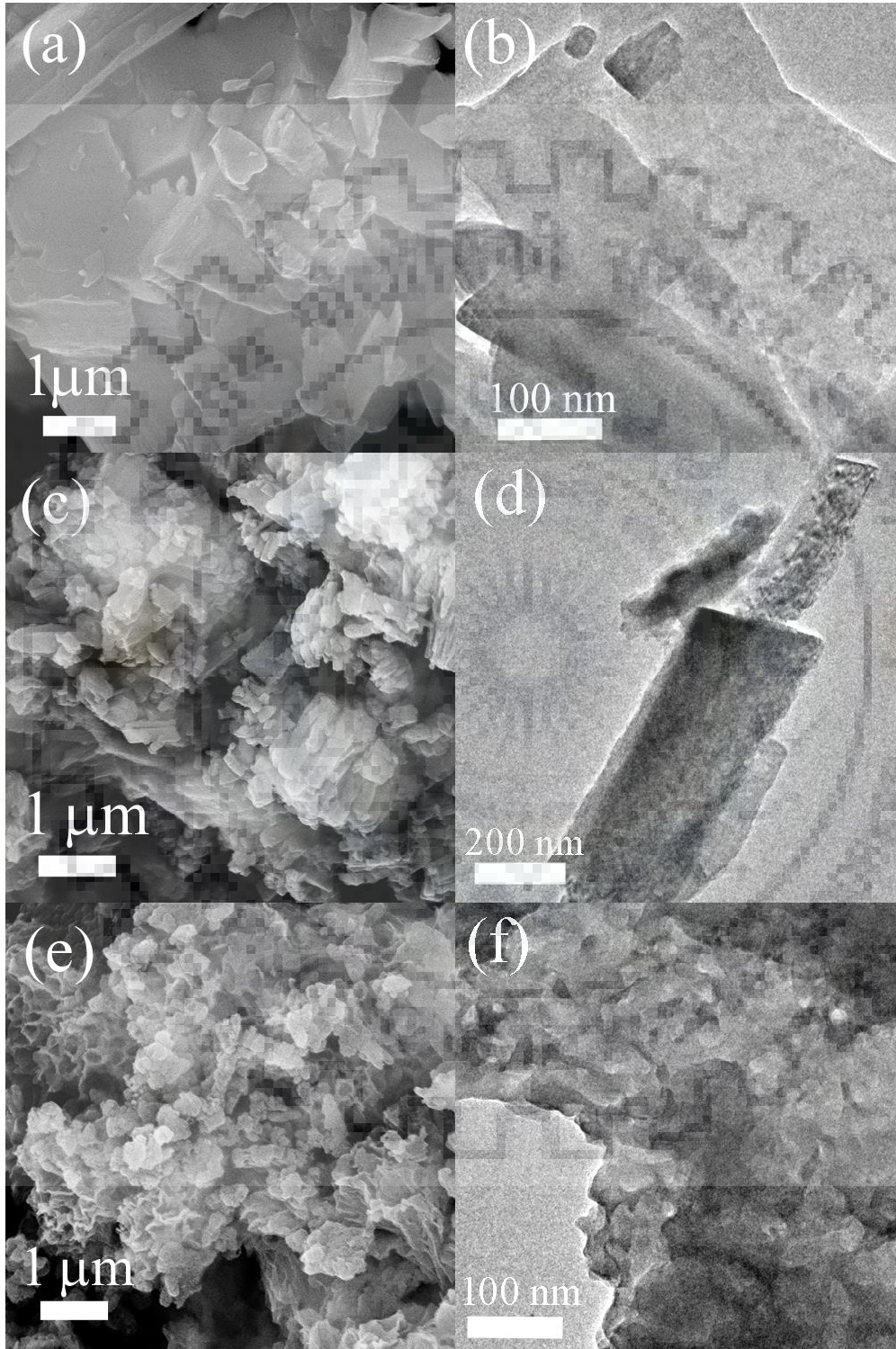


Figure 3.3. (a) & (b) FE-SEM, TEM images of NENP-C-120, respectively (c) & (d) FE-SEM, TEM images of NENP-C-140, respectively, and (e) & (f) FE-SEM, TEM images of NENP-C-160, respectively.

In NENP-C-140, rod shaped particles can be observed both in the FESEM and TEM images. These rods are irregular in shape and size and in most of the cases form bundles (*Figure 3.3c and 3.3d*). The diameter of these rod shape particles are 50 to 500 nm and their length varies between 500 nm to 2 μm . Unlike both these specimens, the NENP-C-160 has porous structure with many of the particles have open pore frameworks. These particles are irregular in shape and mostly are agglomerated forming larger structures (*Figure 3.3e and 3.3f*).

Table 3.2. Elemental analysis for NENPC-*x*.

Specimens	Elemental compositions (wt%)		
	N	C	H
Theoretical	62.0	35.8	1.5
NENP-C-120	37.5	40.0	2.1
NENP-C-140	40.0	40.5	2.4
NENP-C-160	43.1	39.2	3.2

These specimens were further investigated by XRD to get insightful information regarding the crystallinity. All the three specimens have exhibited crystalline structure as shown in *Figure 3.4*. Sharp peaks are observed in the 2θ range from 10 to 70 confirms the crystalline nature of the specimens. Observation of such sharp peaks further indicates the formation of the oligomers which often form layered structure.[29-35] Decrease in the peak intensity, increase in the peak width, disappearance of some of the peaks and observation of broad haloes in the XRD pattern of the NENP-C-160 specimen confirm the increase in the extent of the condensation of the polymerization process. The increase in the polymerization temperature could improve the extent of polymerization. Moreover, polymeric frameworks made by condensation polymerization are often obtained in amorphous structure.[36-38]

Formation of the oligomeric products at low synthesis temperature and increase in the extent of condensation on increasing the polymerization temperature was further supported by the thermal analysis as evident from the TGA and DTG thermograms. The typical TGA/DTG thermograms investigated in argon atmosphere in the temperature range of 25 to 900 $^{\circ}\text{C}$ with a heating rate of 10 $^{\circ}\text{C}/\text{min}$ has been shown in *Figure 3.5*. In specimen NENP-C-120, a complete weight loss occurs in a sharp single step between 325 to 425 $^{\circ}\text{C}$ which can be clearly seen in the DTG thermogram. This could be attributed to the decomposition/defragmentation of the oligomeric frameworks on heating. This was further evident from the TGA/DTG thermograms of NENP-C-140 and NENP-C-160 specimens.

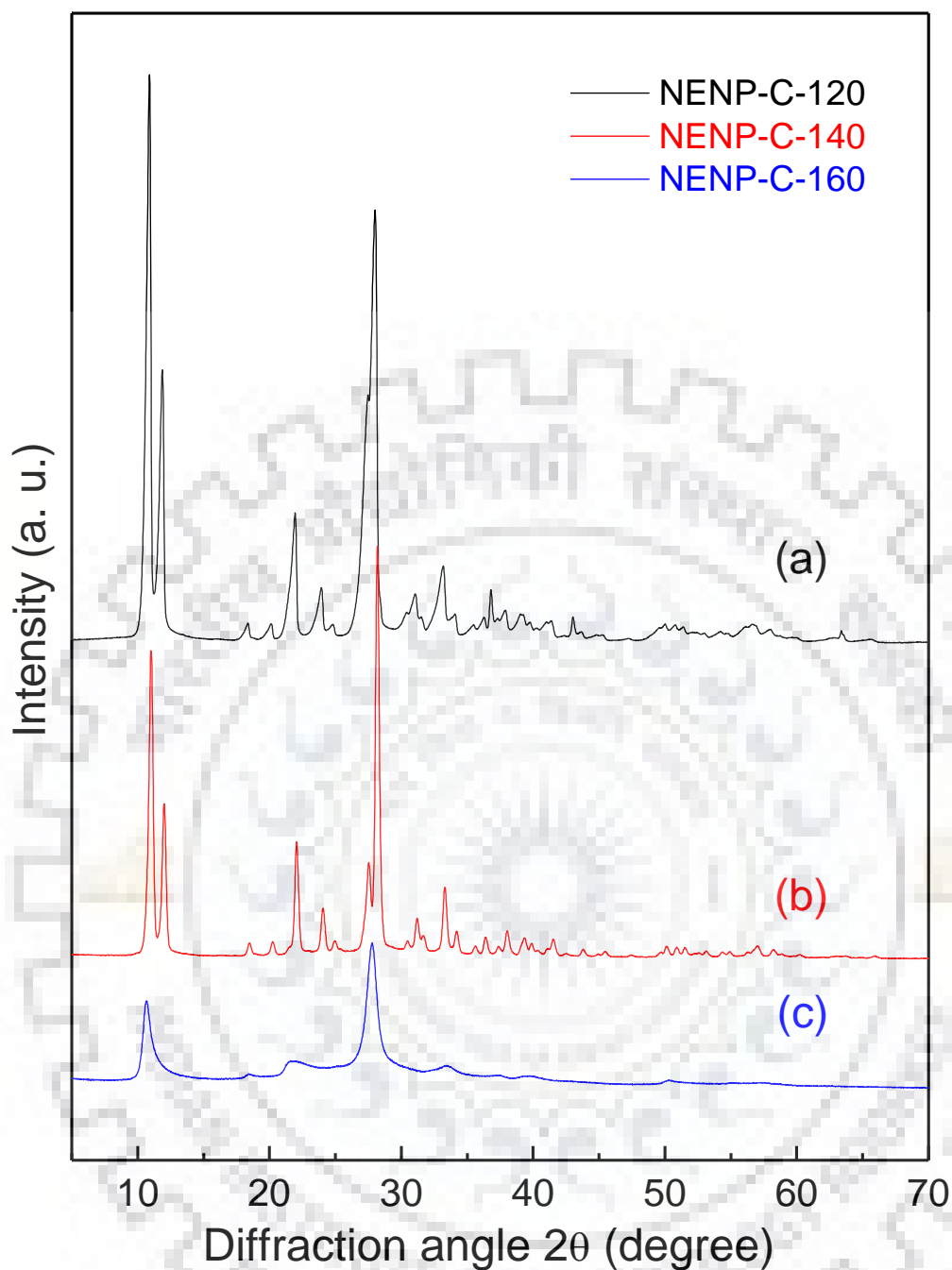


Figure 3.4. XRD patterns of (a) NENP-C-120 (b) NENP-C-140 and (c) NENP-C-160.

Although in all these specimens the sharp weight loss at this temperature zone is observed but unlike the NENP-C-120 there was not a complete weight loss observed at this temperature. In the NENP-C-140 this step contributed 89% weight loss, where as in NENP-C-160 this step is restricted to only 55% weight loss. The NENP-C-140 has a second weight loss step at 660 °C which contribute around 11%. In the NENP-C-160, multiple weight loss steps can be observed in addition to the major weight loss between 325 to 425 °C. The first step weight loss around 100 °C can be attributed to the adsorbed gas and moistures which is commonly observed in porous materials and the second step above 200 °C could be attributed to the trapped DMSO.

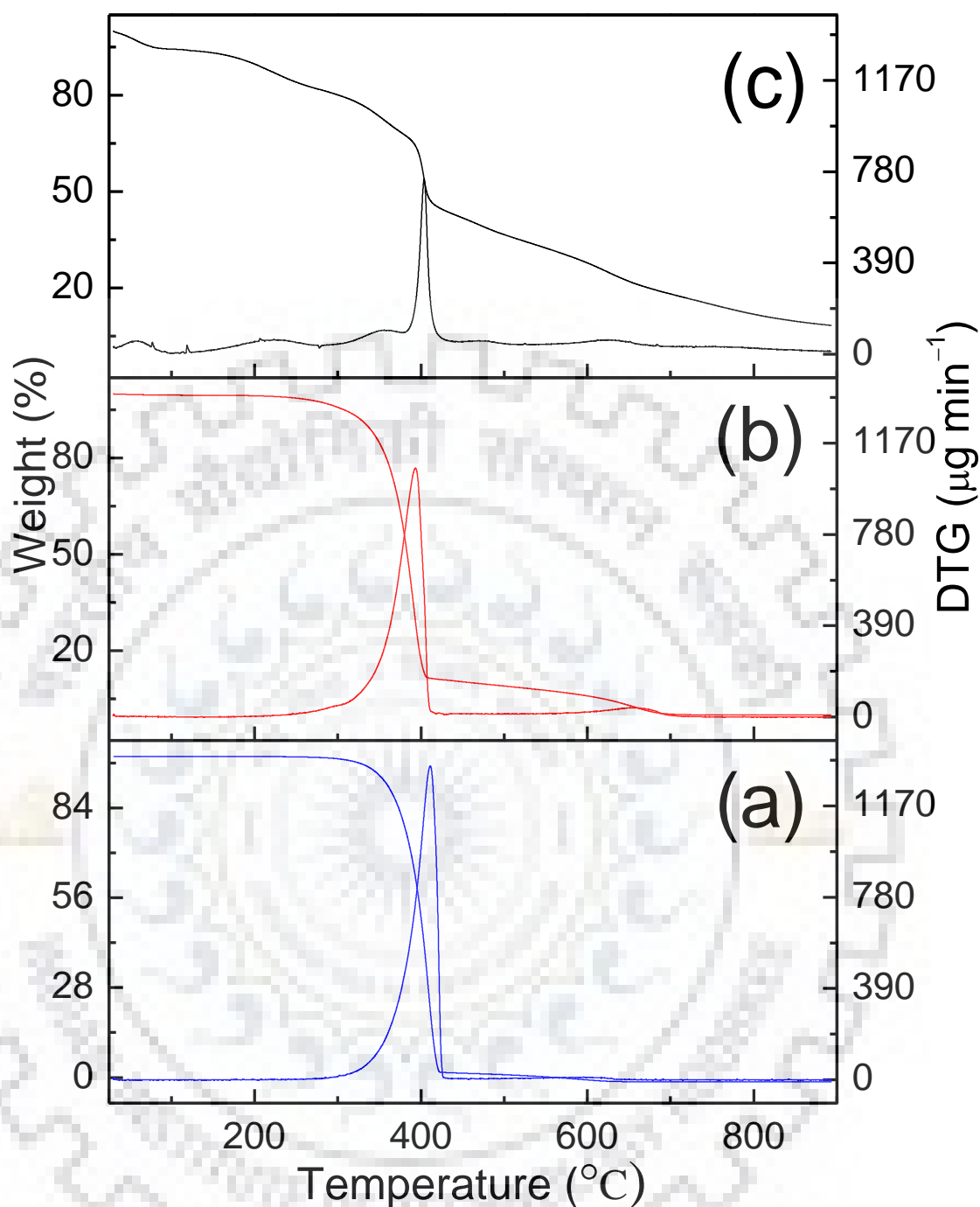


Figure 3.5. TGA of (a) NENP-C-120, (b) NENP-C-140 and (c) NENP-C-160 in argon atmosphere.

There was gradual weight loss in the high temperature zone owing to the condensation/carbonization/decomposition of the polymeric frameworks. Even at the high temperature of 900 °C, around 8 wt% of the mass is left which can be the carbon skeleton of the polymeric framework. All these observations corroborate the conclusions derived from FTIR, XPS, and XRD analysis that the increase in the polymerization temperature could improve the condensation, however, there exists a lot of oligomeric moieties in the frameworks even at a high synthesis temperature of 160 °C.

3.2.2. NENP-S-x synthesized by solvothermal method

In order to find out the experimental conditions that can polymerize the melamine and cyanuric chloride in an effective way, solvothermal treatment was also adopted. For the solvothermal synthesis, two different reaction temperatures 140 and 160 °C are selected and the reaction was carried out using DMSO as solvent. After heating the reaction mixture in a Teflon lined stainless steel high pressure reactor for 24 h, the precipitate was washed repeatedly and dried in hot air oven at 100 °C to get the final dried products designated as NENP-S-140 and NENP-S-160 made at 140 and 160 °C, respectively.

The condensation was investigated by FTIR spectra as shown in *Figure 3.6a*, which indicates a similar oligomeric formation as in the case of conventional heating method. There is no substantial difference in the structure of the specimens made at same reaction temperatures both in the conventional heating and solvothermal synthesis as evident from the FTIR investigation. Although, a better condensation was expected from the solvothermal synthesis as it is considered as a method to enhance the kinetics of the reaction, but in the present case, it did not provide any improvement in the polymerization. A similar conclusion was also derived from the XPS, XRD, TGA/DTG investigations as shown in *Figure 3.6*. As expected, the XPS survey scan shows the presence of C, N and O (*Figure 3.6b*) and a small peak from S. The peaks at 287.9 and 289.4 eV in C1s spectrum are attributed to $-C=N-$ and $C-(N_3)$ of the triazine ring, respectively, and almost equal peak area could be seen for both peaks because of the partial condensation (*Figure 3.6c*).[22-28] The N1s XPS spectrum in *Figure 3.6d*. shows various chemical states of N present in the specimen similar to conventionally synthesized specimens, as evidenced by the presence of three peaks at 398.7, 400.1 and 401.1 eV.[22-28] The XRD (*Figure 3.6e*) pattern showing the crystalline nature of specimen further confirms the formation of oligomeric framework.[29-35]

The typical TGA/DTG thermograms (*Figure 3.6f*) have shown complete decomposition of the NENP-S-140 in a single step whereas multiple weight loss steps could be observed in NENP-S-160. Although, in both specimens major weight loss occurred at ~420 °C but a complete degradation of NENP-S-160 was observed at a high temperature of 700 °C. The elemental compositions of these specimens is given in *Table 3.3*.

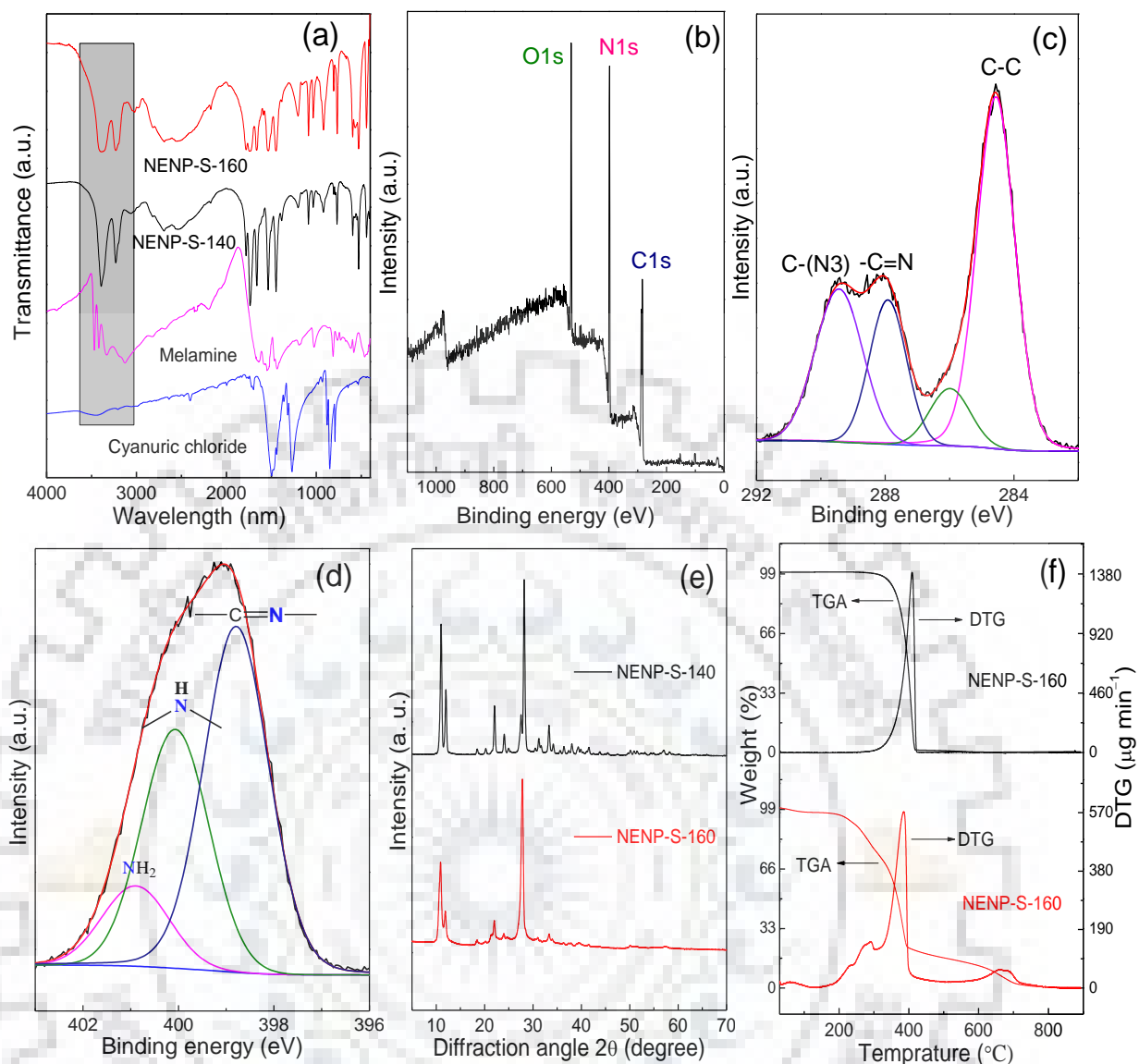


Figure 3.6. (a) FTIR spectra, (b) XPS survey scan (Su1s) (c) high resolution (C1s) (d) high resolution (N1s), (e) XRD patterns and (f) TGA/DTG thermograms measured in argon atmosphere for NENP-S-140 and NENP-S-160.

Table 3.3. Elemental analysis for NENPS-*x*.

Specimens	Elemental compositions (wt%)		
	N	C	H
Theoretical	62.6	35.8	1.4
NENP-S-140	38.5	44.1	2.6
NENP-S-160	41.0	40.2	3.0

However, the microstructures of the specimens synthesized by solvothermal methods are somehow different than the samples synthesized by conventional method as investigated by

FESEM and TEM. The FESEM and TEM images of both the specimens have shown agglomerated particles of diameter varying from 200 to 400 nm (*Figure 3.7*).

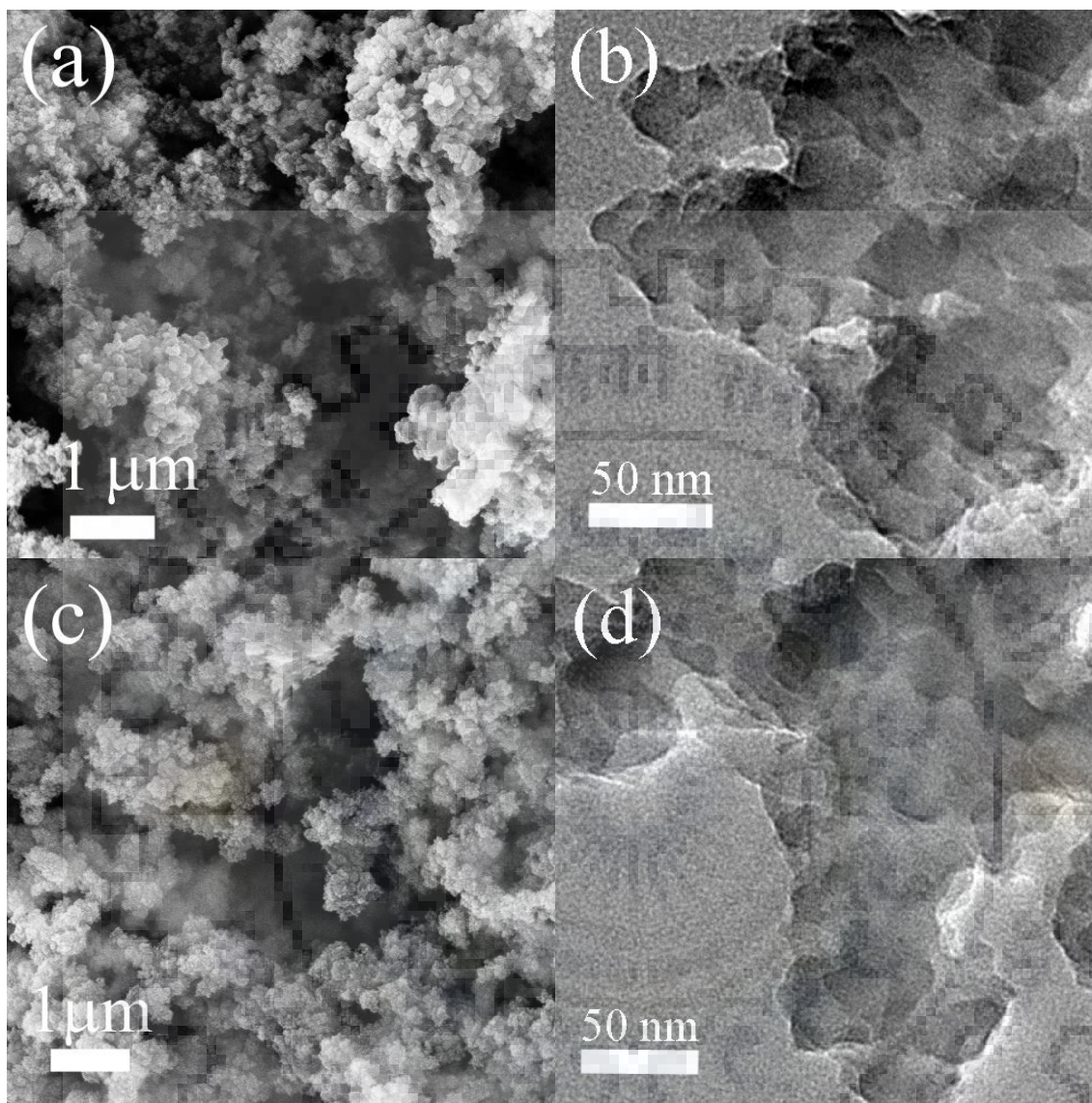


Figure 3.7. (a), (b) FE-SEM and TEM images of NENP-S-140, and (c), (d) FE-SEM and TEM images of images of NENP-S-160, respectively.

3.2.3. NENP-U synthesized by sonochemical method

Sonochemical method is another approach, generally adopted to carry out polymerization reactions in a fast and efficient way.[36-39] In the present research, melamine and cyanuric chloride have been reacted in DMSO for 60 min using ultrasonic power of 600 W. Synthesized precipitate was washed repeatedly in water and THF and dried in hot air oven at 100 °C to get the final dried product designated as NENP-U.

The structural investigation of NENP-U was carried out using various techniques such as FTIR, XPS, XRD, CHNSO and TGA/DTG as shown in *Figure 3.8* and *Table 3.4.*, which confirms that sonochemical method also didn't provide completed condensed products, rather,

oligomeric framework was formed similar to the previously discussed methods.[28-35] Agglomerated nanoparticles of diameter 50-90 nm could be seen from FESEM and TEM images (Figure 3.9).

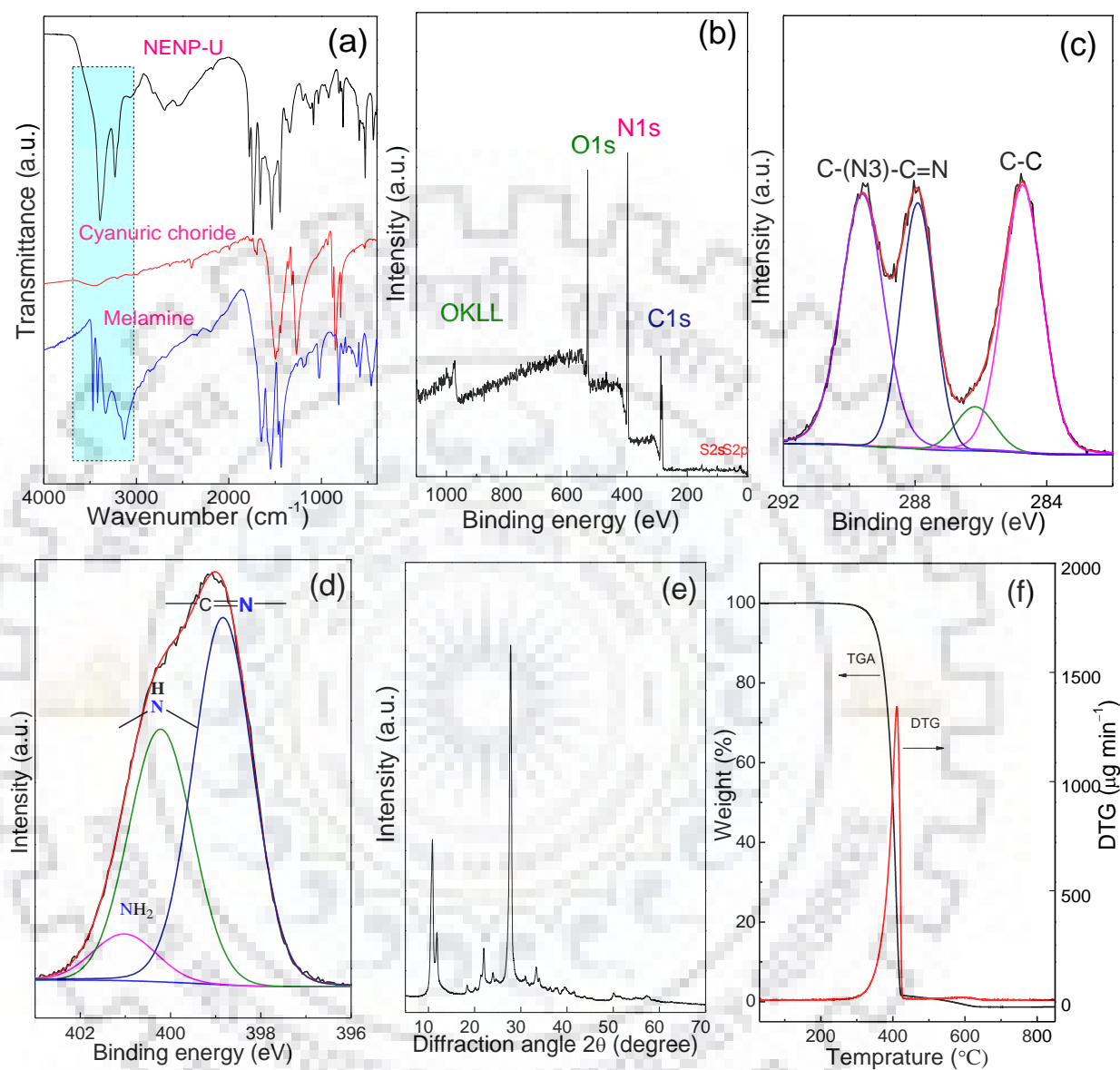


Figure 3.8. (a) FTIR spectra, (b) XPS survey scan (Su1s) (c) high resolution (C1s) (d) high resolution (N1s), (e) XRD patterns and (f) TGA/DTG thermograms measured in argon atmosphere for NENP-S-140 and NENP-S-160.

Table 3.4. Elemental analysis for NENP-U.

Specimens	Elemental compositions (wt%)		
	N	C	H
Theoretical	62.0	35.8	1.5
NENP-U	38.0	37.9	2.2

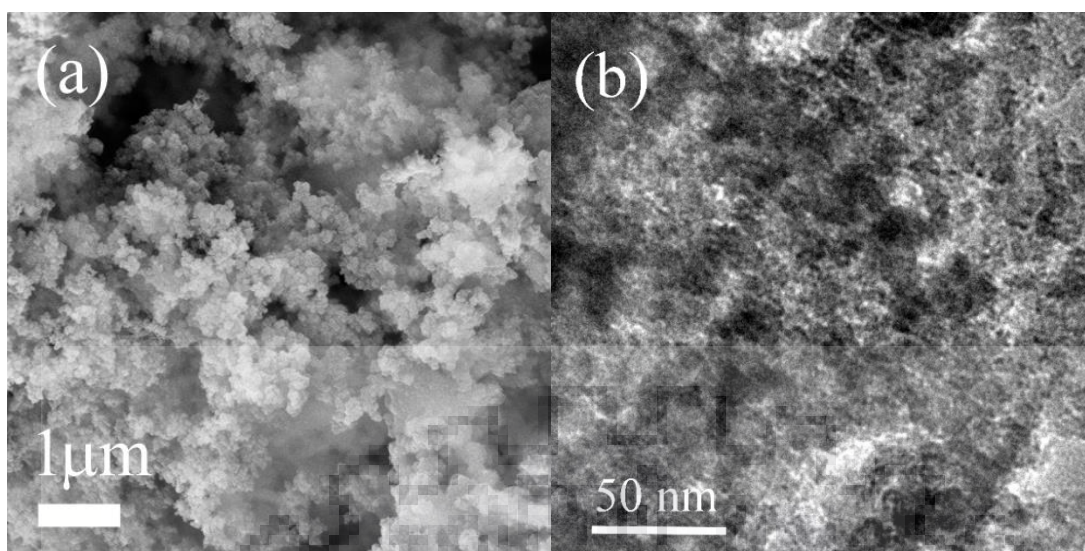


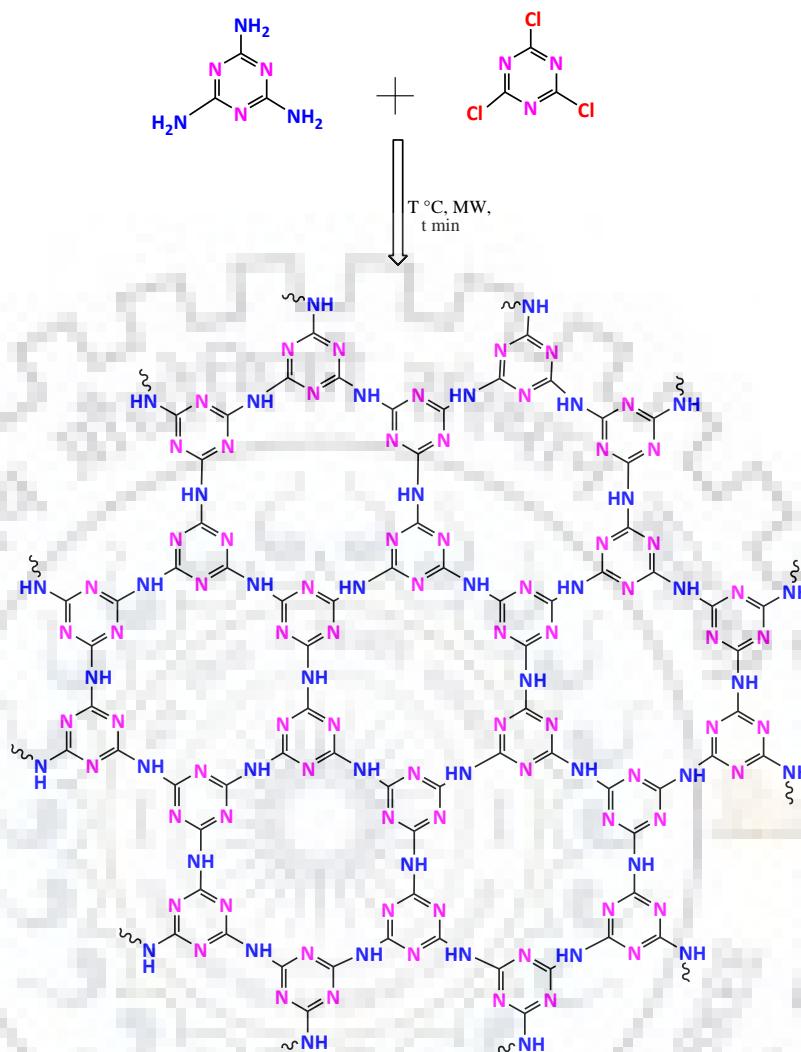
Figure 3.9. FE-SEM and TEM images of the specimen NENP-U.

3.2.4. NENP-x synthesized by microwave assisted method

After exploring several methods unsuccessfully, microwave assisted condensation of melamine and cyanuric chloride to form polymeric framework materials was turned out to be a very good method. It successfully condenses melamine and cyanuric chloride to form the proposed polymeric framework shown in Scheme 3.1, as evident from various characterization techniques. The spectroscopic investigations such as ^{13}C CP-MAS NMR, FTIR and XPS. A strong signal at 166.7 ppm in the ^{13}C CP-MAS NMR spectrum as shown in *Figure 3.10a* assigned to the triazine ring carbon of a representative specimen NENP-1 strongly supports the structure as shown in Scheme 3.1, as it neither matches with the carbon of melamine nor the cyanuric chloride [inset of *Figure 3.10a*]. [8-11] Observation of a small signal at 153 ppm may be attributed to the side group functionalities originated from cyanuric chloride. [8-11]

Further, observation of only broad band (instead of multiple bands observed for primary amine) above 3350 cm^{-1} in the FTIR spectrum (*Figure 3.10b*) along with the absence of the band due to the C-Cl stretching vibration further corroborate the NMR results and confirm a successful condensation to form a polymeric framework. [1-11] All other NENPs synthesized by varying the experimental conditions as mentioned in *section 2.3.4.2* have very similar FTIR spectra (*Figure 3.11*). Detailed FTIR assignments are given in *Table 3.5*. This indicates the microwave assisted method is quite effective in polymerization of a system like the present one. When all other experimental pathways used to synthesize the polymeric framework failed to achieve the objective of a complete condensation of melamine and cyanuric chloride, the use of microwaves was found to be beneficial and could be extended to synthesize other such polymeric framework materials. It is quite interesting to note that neither varying the temperature, microwave power,

reaction time nor solvent amount could yield any oligomeric product rather polymeric framework formed invariably under all experimental conditions used in this work.



Scheme 3.1. Reaction scheme for the synthesis of NENP-1.

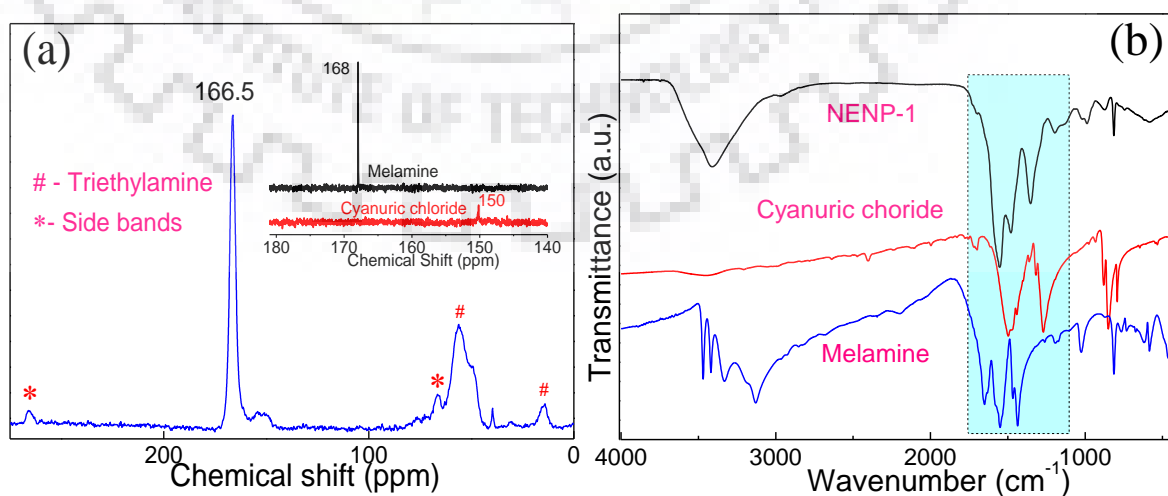


Figure 3.10. (a) ^{13}C CPMAS NMR spectrum, (b) FTIR spectra. The ^{13}C NMR spectra of melamine and cyanuric chloride are shown in the inset of (a).

Further, the NENP-1 was subjected to XPS analysis for the investigation of chemical environment of the elements present in the specimen (*Figure 3.12*). The high-resolution C1s spectrum (*Figure 3.12b*) has shown the peaks at 284.7, 286.4 and 288.1 eV which attributed to the three different types of carbon.[22-25] The peak allocated at 286.4 eV is assigned due to sp²-C of the triazine ring and other peaks at 284.7 and 288.1 eV are ascribed to the sp³-C of graphitic impurity from the carbon tape used to mount the specimen for XPS analysis.[26-29]

Table 3.5. Assignment of FTIR Bands.

Bands (cm ⁻¹)	Cyanuric chloride	Melamine	NENP-1	Ref.
3469	-	N-H stretching	-	[12-17]
3420	-	N-H stretching	N-H stretching	[12-17]
3332	-	N-H stretching	-	[12-17]
3130	-	N-H stretching	-	[12-17]
2940	-	-	C-H stretching	[12-18]
1705	C-N stretching	-	C-N stretching	[15-18]
1650	-	δNH ₂	-	[15-18]
1549	-	Quadrant stretching triazine ring (-C=N-)	Quadrant stretching triazine ring (-C=N-)	[15-19]
1498	-	v(CN)+ δNH ₂	-	[15,16]
1435	-	v(CN)+ δNH ₂	-	[15,16]
1357	(-C=N-) bending vib.	(-C=N-) bending vib.	-	[12-15]
1270	(-C=N-) stretching	-	-	[15-18]
1026	-	N-H Torisional vib.	-N-H Torisional vib.	[12-18]
988	-	-	δ (CNC) + δ (NCN)	[12-18]
880	(-C=N-) vib.	(-C=N-) vib.	(-C=N-) vib.	[12-18]
814	-	Out-of-plane ring bending of a triazine	Out-of-plane ring bending of a triazine	[17]
808	Ring bending	Ring bending	Ring bending	[16-21]
581	-	δ (NCN)+ τ(NH ₂)	δ (NCN)	[12-17]

The high-resolution N1s XPS spectrum shown in *Figure 3.12c* shows peaks at 398.4 and 399.7 eV due to pyridine (N6) and pyrrolic (N5) types of nitrogen, respectively.[22-28] The C, N, and H elemental analysis further provides useful information about the specimens. As can be seen from the *Table 3.6* high nitrogen content up to 52.6 wt% can be realized in the synthesized NENPs. It is in the higher side as compared to the reported literatures (*Table 3.7*). Moreover, the experimental C, N, and H composition of the NENPs were fairly matching with the theoretical values of 35.8, 62 and 1.49 wt %, respectively, (*Table 3.6*) with marginal mismatch considering the polymeric framework nature of the specimens. In organic polymeric frameworks, such marginal mismatch is commonly reported.[9,10]

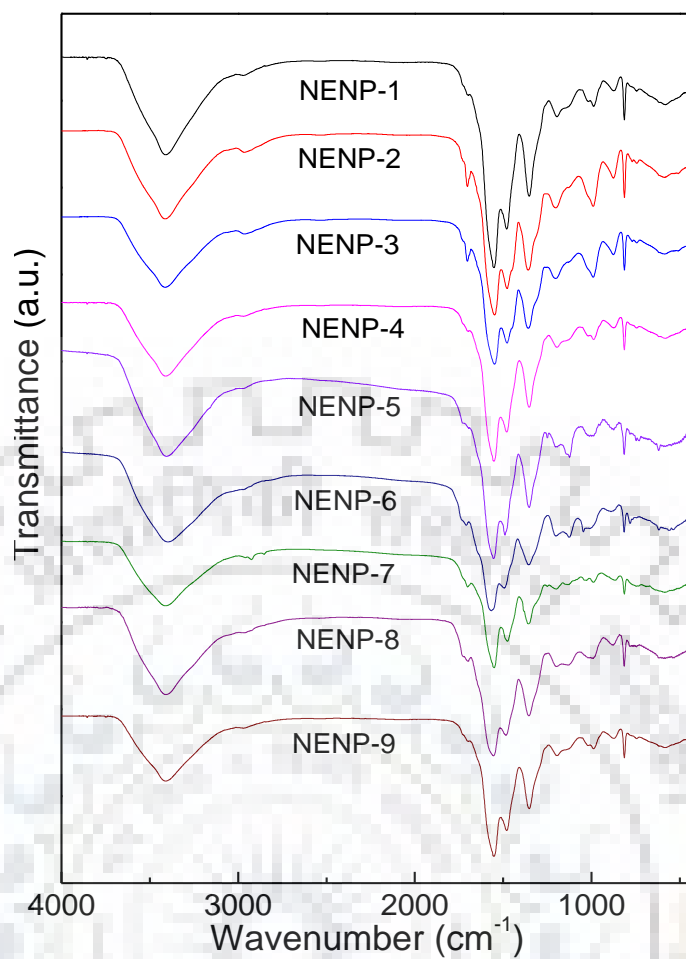


Figure 3.11. FT-IR spectra of NENP-x.

Table 3.6. Elemental composition of NENP-x.

Sample ID	Elemental compositions (wt%)		
	N	C	H
Theoretical	62.0	35.8	1.4
NENP-1	50.5	37.9	2.4
NENP-2	52.5	36.8	2.1
NENP-3	52.1	36.3	2.2
NENP-4	49.8	36.1	1.9
NENP-5	51.6	37.0	2.0
NENP-6	49.8	37.1	2.4
NENP-7	50.2	38.0	2.3
NENP-8	48.7	39.5	2.6
NENP-9	52.6	35.6	2.1

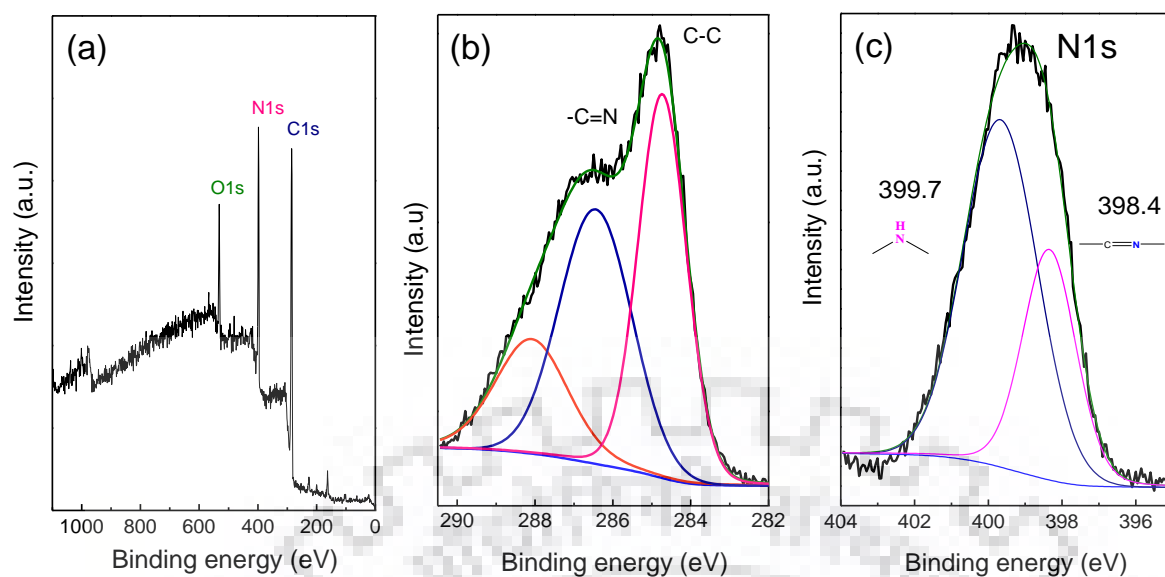


Figure 3.12. (a) Survey scan, high resolution XPS spectra of (b) C1s and (c) N1s of NENP-1.

Table 3.7. Some recently reported nitrogen-enriched high surface area nanoporous materials.

S. No	Material ID	N (wt%)	Ref.
1.	Pym-CTF	34.82	[2]
2.	CTF-FUM	27.64	[4]
3.	SNW-1	46.58	[8]
4.	CNH Nanocages	53.27	[11]
5.	SNW-4	41.73	[12]
6.	SNW-G	52.37	[13]
7.	NWNU-COF-1	51.48	[28]
8.	CMOP-1	18.17	[36]
9.	NUT-11	14.95	[37]

The change in the experimental conditions has reflected profoundly in the microstructures of the synthesized NENPs. As depicted in *Figure 3.13a*, the longer reaction time has resulted in the increase in particle size as well as smoother surface of the nearly spherical particles. For shorter reaction time of 15 min, smaller nanoparticles of size of 60 ± 25 nm in NENP-2 could be observed. On increasing the reaction time to 30 or 60 min, there was a substantial growth of these nanoparticles to a size of 250 ± 60 or 320 ± 60 nm in NENP-1 or NENP-3, respectively (*Figure 3.13a and 3.14*). It is interesting to note that the product yield (~ 90) is almost same in all these three specimens synthesized at different reaction time (*Table 3.8*).

This indicates that the reaction was completed even at a shorter reaction time of 15 min which was also evident from the FTIR analysis. Thus, the increase in the particle size from ~60 nm to >250 nm could be attributed to the Ostwald ripening.[40-43] A similar phenomenon was also observed when the reactions were carried out at higher MWP and temperature (*Figure 3.13b, 3.13c and 3.14*). Particles of nearly spherical shape with an increased particle sizes are obtained.

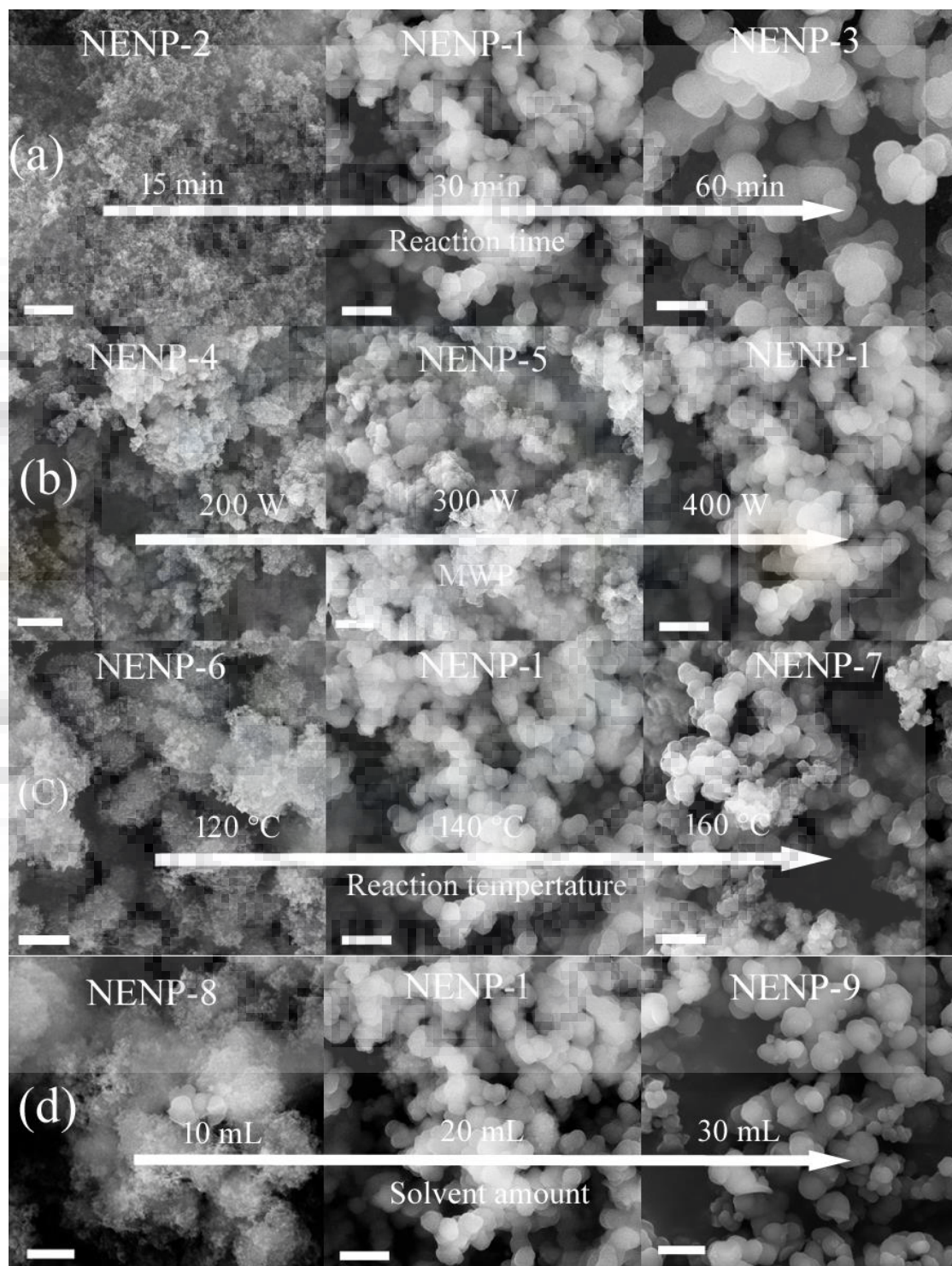


Figure 3.13. FE-SEM images of NENPs synthesized by varying (a) the reaction time, (b) MWP, (c) reaction temperature and (d) solvent amount (scale bar is 1 μm).

However, on increasing the solvent amount (dilution) keeping the reaction temperature, time and MWP identical, the increase in the particles size could be explained in terms of the supersaturation conditions (Figure 3.13).[41,42]

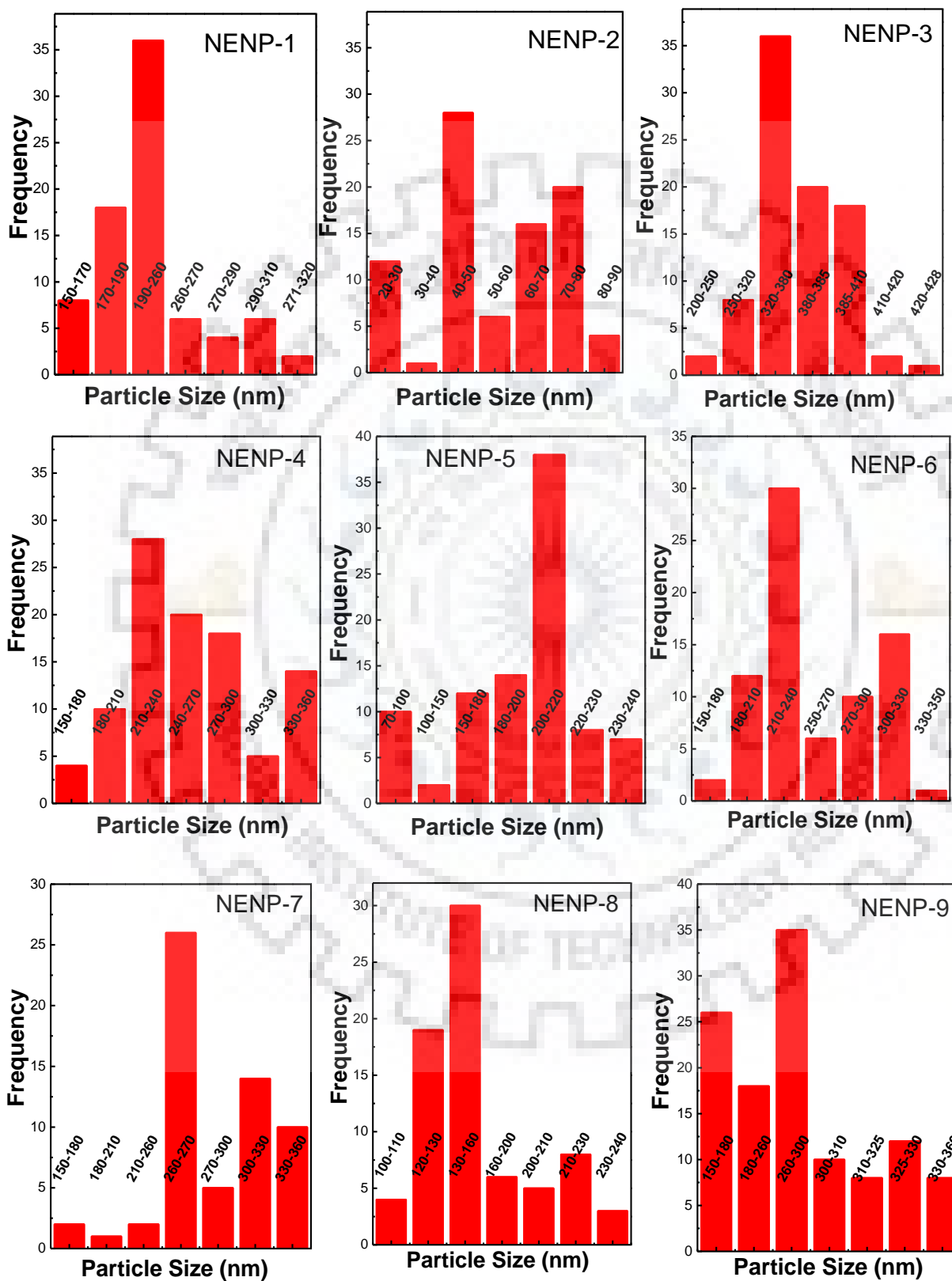


Figure 3.14. Particle size distribution of NENPs estimated from FESEM images.

The specimen synthesized at higher concentration (NENP-8) has smaller particle size and larger particles with smoother surface could be seen in the specimen synthesized at higher dilution (NENP-9) (*Figure 3.13d and 3.14*). This could be ascribed to different reaction kinetics under different experimental concentrations. At higher concentration due to a supersaturation condition, large numbers of nuclei could be formed at very early stage of the reaction and no reactant species is left for the further growth of the particles.[42,43]

Table 3.8. Reaction parameters for the microwave assisted synthesis of NENPs.

Sample	DMSO (ml)	Time (min)	Temperature (°C)	Microwave power (W)	Yield %
NENP-1	20	30	140	400	92
NENP-2	20	15	140	400	89
NENP-3	20	60	140	400	90
NENP-4	20	30	140	200	87
NENP-5	20	30	140	300	85
NENP-6	20	30	120	400	91
NENP-7	20	30	160	400	90
NENP-8	10	30	140	400	81
NENP-9	30	30	140	400	84

The TEM image of a representative specimen (NENP-1) as shown in *Figure 3.15* has nanoporous structure, although, no specific pore ordering could be seen. Such disordered pore structures are commonly observed in polymeric framework materials.[36,37]

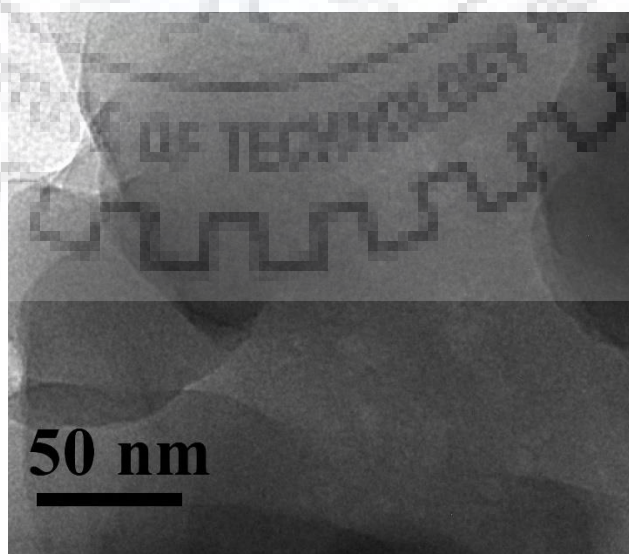


Figure 3.15. TEM image of NENP-1 showing nanoporous nature of the specimen.

The crystallinity of the specimen was investigated by XRD (Figure 3.16), where no sharp peak could be seen indicating the amorphous nature of the specimens. This indicates the formation of polymeric framework materials by the complete condensation of the precursors. The formation of oligomeric framework otherwise could have yielded a crystalline material as seen in the specimens synthesized by other methods.[28-35]

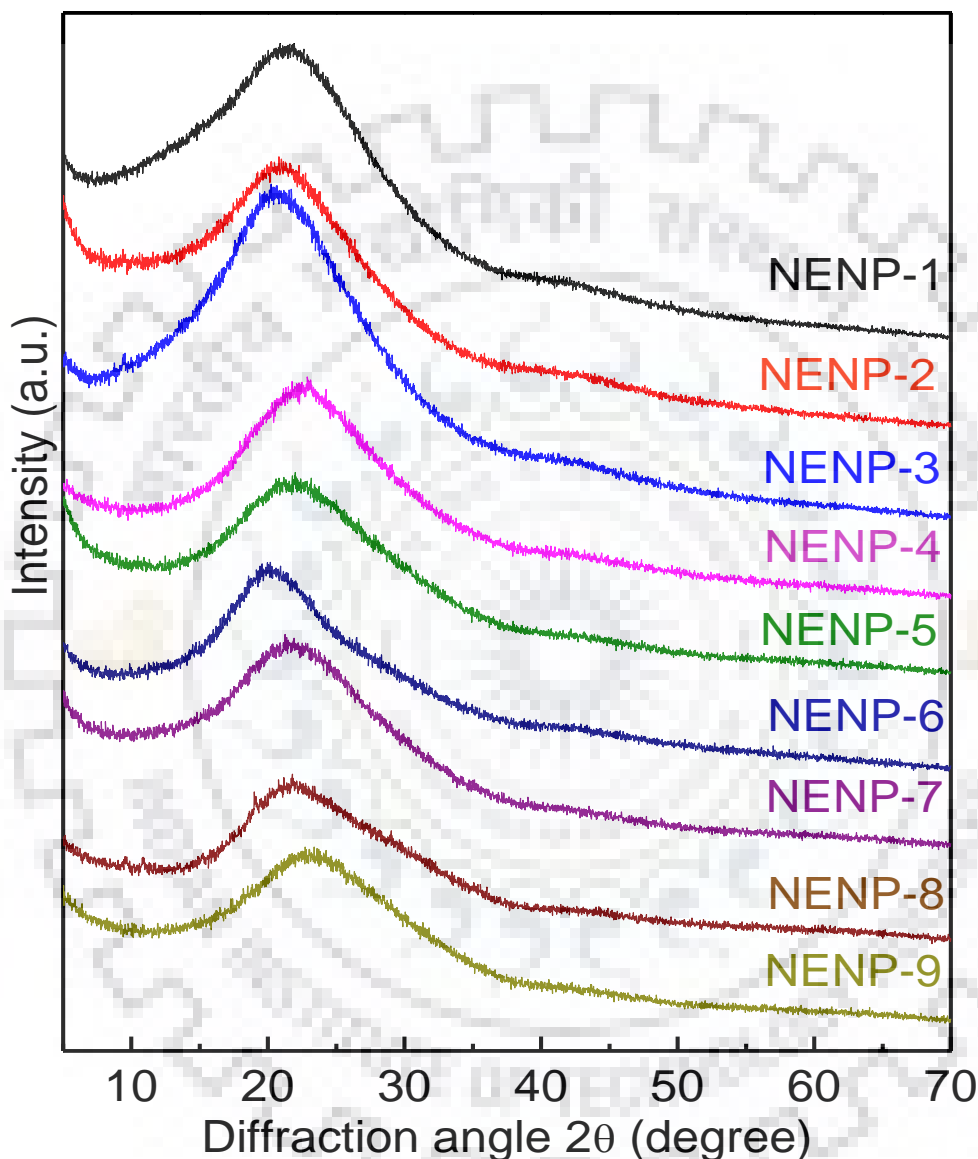


Figure 3.16. X-ray diffraction patterns of NENPs showing amorphous nature of the specimens.

The TGA/DTG analysis indicates that the framework of NENPs are stable up to 350 °C in argon atmosphere. The first weight loss below 100 °C could be due to removal of adsorbed moisture, trapped solvents and small gas molecules in the pores of material. The second weight loss around 350 °C could be attributed to the condensation of framework. Finally, the decomposition/oxidation of the material starts at a temperature of 400 °C and a complete weight loss was observed around 700 °C (Figure 3.17).

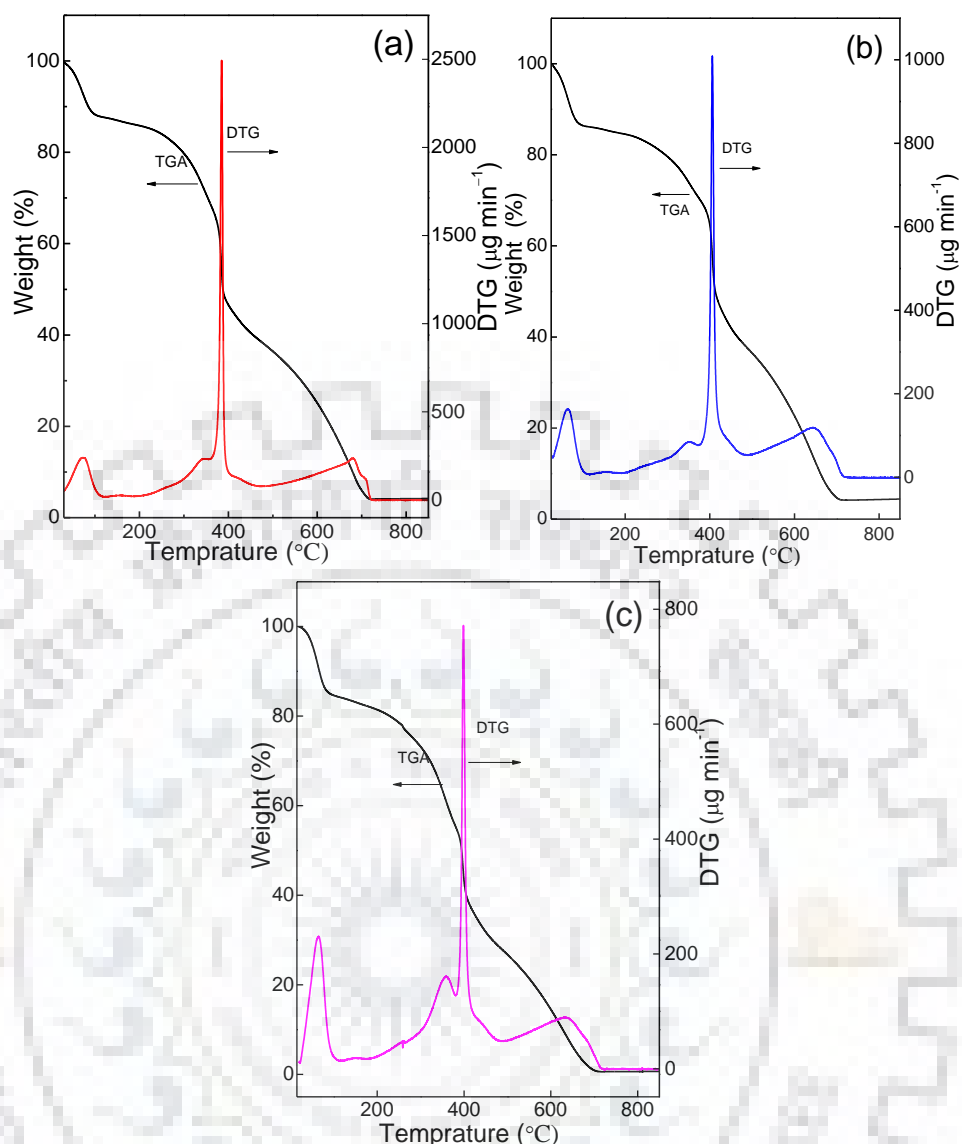


Figure 3.17. TGA and DTG thermograms of (a) NENP-1 (b) NENP-3 and (c) NENP-9 with a heating rate of $10\text{ }^{\circ}\text{C min}^{-1}$ measured in argon atmosphere.

3.3. Summary

In summary, various experimental procedures have been adopted for the synthesis of nitrogen enriched nanoporous polytriazine (NENP) frameworks. In synthesis methods such as conventional heating, solvothermal treatment using teflon lined stainless steel high pressure reactor or use ultrasonic wave, the materials synthesized did not show an indication of the formation of polymeric structure by complete condensation of the precursors, melamine and cyanuric chloride. However, the use of microwave for the synthesis have produced polymeric framework materials with a complete condensation of the reactants. Even by changing various reaction parameters have not produced any oligomeric frameworks. One of the major objectives of synthesizing the polymeric framework materials with high nitrogen content was achieved, as

the nitrogen content up to ~52 wt% was realized in the specimens synthesized by the microwave assisted method which could be beneficial for exploiting the Lewis basic character needed for several applications.

References

1. Y. Zeng, R. Zou and Y. Zhao, Covalent organic frameworks for CO₂ capture, *Adv. Mater.*, 2016, **28**, 2855-2873.
2. S. Hug, L. Stegbauer, H. Oh, M. Hirscher and B. V. Lotsch, Nitrogen-rich covalent triazine frameworks as high-performance platforms for selective carbon capture and storage, *Chem. Mater.*, 2015, **27**, 8001-8010.
3. S. Wu, Y. Liu, G. Yu, J. Guan, C. Pan, Y. Du, X. Xiong and Z. Wang, Facile preparation of dibenzoheterocycle-functional nanoporous polymeric networks with high gas uptake capacities, *Macromolecules*, 2014, **47**, 2875-2882.
4. K. Wang, H. Huang, D. Liu, C. Wang, J. Li and C. Zhong, Covalent triazine-based frameworks with ultramicropores and high nitrogen contents for highly selective CO₂ capture, *Environ. Sci. Technol.*, 2016, **50**, 4869-4876.
5. G. Wang, K. Leus, S. Zhao and P. Van Der Voort, Newly designed covalent triazine framework based on novel n-heteroaromatic building blocks for efficient CO₂ and H₂ capture and storage, *ACS Appl. Mater. Interfaces*, 2018, **10**, 1244-1249.
6. Q. Dang, C. -Y. Liu, X. -M. Wang and X. -M. Zhang, Novel covalent triazine framework for high-performance CO₂ capture and alkyne carboxylation reaction, *ACS Appl. Mater. Interfaces*, 2018, **10**, 27972-27978.
7. W. Wang, Y. Yuan, F. X. Sun and G. S. Zhu, Targeted synthesis of novel porous aromatic frameworks with selective separation of CO₂/CH₄ and CO₂/N₂, *Chin. Chem. Lett.*, 2014, **25**, 1407-1410.
8. M. G. Schwab, B. Fassbender, H. W. Spiess, A. Thomas, X. Feng and K. Mullen, Catalyst-free preparation of melamine-based microporous polymer network through Schiff base chemistry, *J. Am. Chem. Soc.*, 2009, **131**, 7216-7217.
9. P. Puthiaraj, S. S. Kim and W. S. Ahn, Covalent Triazine polymers using a cyanuric chloride precursor via Friedel-Crafts reaction for CO₂ adsorption/separation, *Chem. Eng. J.*, 2016, **283**, 184-192.
10. R. Muhammad, Jyoti and P. Mohanty, Nitrogen enriched triazine bridged mesoporous organosilicas for CO₂ capture and dye adsorption applications, *J. Mol. Liq.*, 2017, **248**, 127-134.
11. J. Zhang, Z. Wang, L. Li, J. Zhao, J. Zheng, H. Cui and Z. Zhu, Self-assembly of CNH nanocages with remarkable catalytic performance, *J. Mater. Chem. A*, 2014, **2**, 8179-8183.
12. G. Yang, H. Han, C. Du, Z. Luo and Y. Wang, Facile synthesis of melamine-based porous polymer networks and their application for removal of aqueous mercury ions, *Polymer*, 2010, **51**, 6193-6202.
13. R. Muhammad, P. Rekha and P. Mohanty, Amino linked inorganic-organic hybrid nanoporous materials (HNMs) for CO₂ capture and H₂ storage applications, *RSC Adv.*, 2016, **6**, 17100-17105.
14. V. Krishnakumar and R. Ramasamy, Density functional theory study on the structure and vibrational spectra for cyanuric chloride, *Spectrochim. Acta Part A*, 2005, **61**, 3112-3116.
15. N. E. Mircescu, M. Oltean, V. Chis and N. Leopold, FTIR, FT-Raman, SERS and DFT study on melamine, *Vib. Spectroscopy*, 2012, **62**, 165-171.
16. M. Prabhakaran, A. R. Prabhakaran, S. Srinivasan and S. Gunasekaran, Experimental and theoretical spectroscopic analysis, HOMO-LUMO, and NBO studies of cyanuric chloride, *Spectrochim. Acta Part A*, 2005, **61**, 454-462.
17. G. R. Seifer, Cyanuric acid and cyanurates, *Russ. J. Coord. Chem.*, 2002, **28**, 301-324.

18. H. A. Patel, F. Karadas, A. Canlier, J. Park, E. Deniz, Y. Jung, M. Atilhan and C. T. Yavuz, High capacity carbon dioxide adsorption by inexpensive covalent organic polymers, *J. Mater. Chem.*, 2012, **22**, 8431-8437.
19. H. Zou, X. Yan, J. Ren, X. Wu, Y. Dai, D. Sha, J. Pan and J. Liu, Photocatalytic activity enhancement of modified G-C₃N₄ by ionothermal copolymerization, *J. Mater. Chem.*, 2015, **1**, 340-347.
20. Y. Ham, K. Maeda, D. Cha, K. Takanabe and K. Domen, Synthesis and photocatalytic activity of poly(triazine imide), *Chem. Asian J.*, 2013, **8**, 218-224.
21. L. Wang, Z. Gao, J. Chang, X. Liu, D. Wu, F. Xu, Y. Guo and K. Jiang, Nitrogen doped porous carbons as electrode materials for high-performance supercapacitor and dye sensitized solar cell, *ACS Appl. Mater. Interfaces*, 2015, **7**, 20234-20244.
22. Y. F. Nie, Q. Wang, X. Y. Chen and Z. J. Zhang, Nitrogen and oxygen functionalized hollow carbon materials: The capacitive enhancement by simply incorporating novel redox additives into H₂SO₄ electrolyte, *J. Power Sources*, 2016, **320**, 140-152.
23. M. K. Bhunia, S. Melissen, M. R. Parida, P. Sarawade, J. M. Basset, D. H. Anjum, O. F. Mohammed, P. Sautet, T. L. Bahers and K. Takanabe, Dendritic tip-on polytriazine-based carbon nitride photocatalyst with high hydrogen evolution activity, *Chem. Mater.*, 2015, **27**, 8237-8247.
24. L. Lin, H. Ou, Y. Zhang and X. Wang, Tri-s-triazine based crystalline graphitic carbon nitrides for highly efficient hydrogen evolution photocatalysis, *ACS. Catal.*, 2016, **6**, 3921-3931.
25. F. Dong, L. Wu, Y. Sun, M. Fu, Z. Wu and S. C. Lee, Efficient synthesis of polymeric g-C₃N₄ layered materials as novel efficient visible light driven photocatalysts, *J. Mater. Chem.*, 2011, **21**, 15171-15174.
26. X. X. Zou, G. D. Li, Y. N. Wang, J. Zhao, C. Yan, M. Y. Guo, L. Li and J. S. Chen, Direct conversion of urea into graphitic carbon nitride over mesoporous TiO₂ spheres under mild condition, *Chem. Commun.*, 2011, **47**, 1066-1068.
27. R. Xue, H. Guo, L. Yue, T. Wang, M. Wang, Q. Li, H. Liu and W. Yang, Preparation and energy storage application of a long-life and high rate performance pseudocapacitive COF material linked with -NH- bonds, *New J. Chem.*, 2018, **42**, 13726-13731.
28. P. Wen, C. Zhang, Z. Yang, R. Dong, D. Wang, M. Fan and J. Wang, Triazine-based covalent-organic frameworks: A novel lubricant additive with excellent tribological performances, *Tribol. Int.*, 2017, **111**, 57-65.
29. B. Jürgens, E. Irran, J. Senker, P. Kroll, H. Müller and W. Schnick, Melem (2,5,8-triamino-tri-s-triazine), an important intermediate during condensation of melamine rings to graphitic carbon nitride: Synthesis, structure determination by x-ray powder diffractometry, solid-state NMR, and theoretical studies, *J. Am. Chem. Soc.*, 2003, **125**, 10288-10300.
30. B. V. Lotsch and W. Schnick, From triazines to heptazines: Novel nonmetal tricyanomelaminates as precursors for graphitic carbon nitride materials, *Chem. Mater.* 2006, **18**, 1891-900
31. S. J. Yang, J. H. Cho, G. H. Oh, K. S. Nahm and C. R. Park, Easy synthesis of highly nitrogen-enriched graphitic carbon with a high hydrogen storage capacity at room temperature, *Carbon*, 2009, **47**, 1585-1591.
32. T. Komatsu, The first synthesis and characterization of cyameluric high polymers, *Macromol. Chem. Phys.*, 2001, **202**, 19-25.
33. X. Yuan, K. Luo, N. Liu, X. Ji, C. Liu, J. He, G. Tian, Y. Zhao and D. Yu, Cluster-model DFT simulations of the infrared spectra of triazine-based molecular crystals, *Phys. Chem. Chem. Phys.*, 2018, **20**, 20779-20784.
34. J. R. Song, W. G. Duan and D. P. Li, Synthesis of nitrogen-rich polymers by Click polymerization reaction and gas sorption property, *Molecules*, 2018, **23**, 1732-1739.
35. S. Mane, Y. X. Li, D. M. Xue, X. Q. Liu and L. B. Sun, Rational design and fabrication of nitrogen-enriched and hierarchical porous polymers targeted for selective carbon capture, *Ind. Eng. Chem. Res.*, 2018, **57**, 12926-12934.

36. K. S. Suslick and G. J. Price, Applications of ultrasound to materials chemistry, *Annu. Rev. Mater. Sci.*, 1999, **29**, 295-326.
37. K. S. Suslick and D. J. Flannigan, Inside a collapsing bubble: Sonoluminescence and the conditions during cavitation, *Annu. Rev. Phys. Chem.*, 2008, **59**, 659-683.
38. P. Mohanty, N. M. K. Linn and K. Landskron, Ultrafast sonochemical synthesis of methane and ethane bridged periodic mesoporous organosilicas, *Langmuir*, 2010, **26**, 1147-1151.
39. P. Rekha, R. Muhammad and P. Mohanty, Sonochemical synthesis of cyclophosphazene bridged mesoporous organosilicas and their application in methyl orange, congo red and Cr(VI) removal, *RSC Adv.*, 2015, **5**, 67690-67699.
40. D. Brailsford and P. Wynblatt, The dependence of Ostwald ripening kinetics on particle volume fraction, *Acta Met.*, 1979, **27**, 489-497.
41. P. W. J. Voorhees, The theory of ostwald ripening, *Stat. Phys.*, 1985, **38**, 231-252.
42. N. G. Bastus, J. Comenge and V. Puntès, Kinetically controlled seeded growth synthesis of citrate-stabilized gold nanoparticles of up to 200 nm: Size focusing versus Ostwald ripening, *Langmuir*, 2011, **27**, 11098-11105.
43. J. Aubry, F. Ganachaud, J. P. C. Addad and B. Cabane, Nanoprecipitation of polymethylmethacrylate by solvent shifting: 1. boundaries, *Langmuir*, 2009, **25**, 1970-1979.





CHAPTER-IV

**TEXTURAL AND GAS SORPTION
STUDIES OF NENPs**

4.1. Introduction

This chapter comprises the thorough investigation of the textural properties of the NENPs synthesized by different methods and the selection of material based on the best textural parameters for further applications. As discussed in *chapter III* by using state of the art characterization techniques, the synthetic methodology has a strong control over the formation of oligomeric and polymeric frameworks based on the extent of condensation. In order to further support these observations, the investigation of textural properties such as specific surface area, pore size distribution and pore volume by N₂ sorption analysis is highly beneficial and provide useful information regarding the usability of these materials. Among, the various methods explored, microwave assisted synthesis of NENPs have shown the formation of the polymeric framework unlike other methods where, mostly oligomeric or partial polymeric frameworks are formed. Knowledge of the detailed textural properties was further utilized to investigate the gas sorption properties such as CO₂ capture, CH₄ and H₂ storage of the selected materials.

4.2. Textural analysis of specimens NENP-C-x (x = 120, 140 and 160)

The specimens NENP-C-120, NENP-C-140 and NENP-C-160 synthesized by conventional heating method were employed for the N₂ sorption measured at $-196\text{ }^{\circ}\text{C}$ (*Figure 4.1*). All synthesized specimens have shown type-I isotherms, with sharp uptake at relatively low pressure below P/P_0 of 0.1. This indicates the presence of micropores in the specimens.

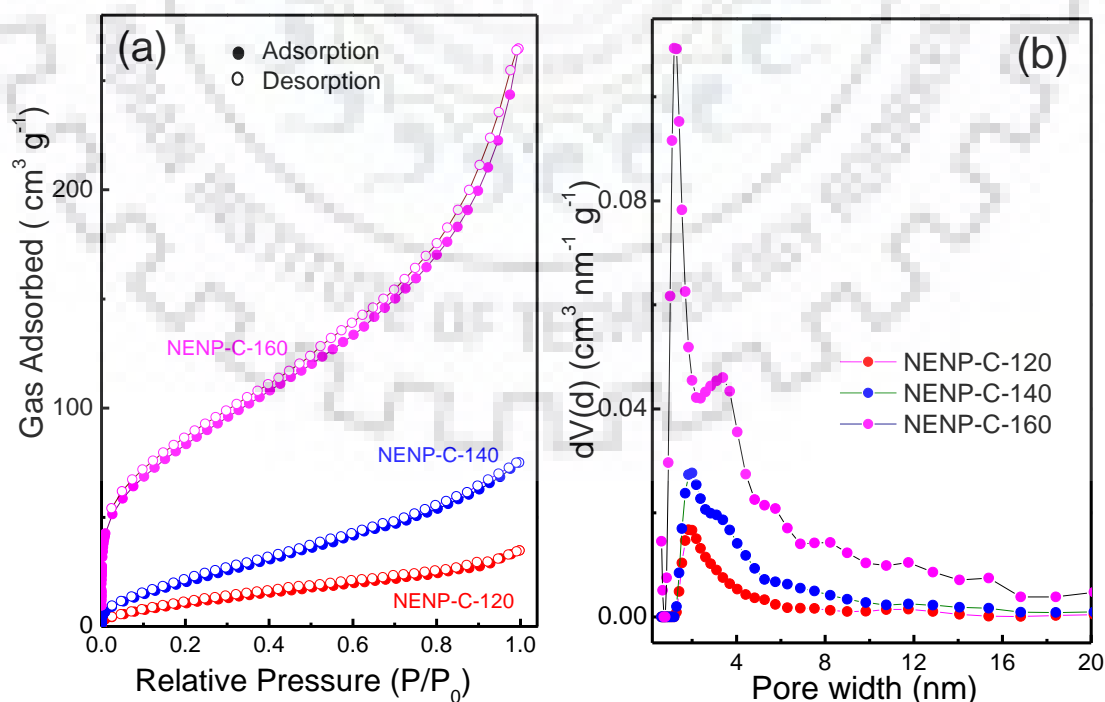


Figure 4.1. (a) N₂ sorption isotherm of NENP-C-120, NENP-C-140 and NENP-C-160 measured at $-196\text{ }^{\circ}\text{C}$, and (b) PSD estimated using DFT model.

Moreover, narrow hysteresis was also observed owing to the presence of mesopores in the frameworks forming a hierarchical pore structure. The S_{ABET} for NENP-C-120, NENP-C-140 and NENP-C-160 are 44, 85 and $302 \text{ m}^2 \text{ g}^{-1}$, respectively. As discussed in *chapter-III*, these specimens are mostly oligomers. The low S_{ABET} can be expected from the oligomeric frameworks. Moreover, the highest S_{ABET} of $302 \text{ m}^2 \text{ g}^{-1}$ in NENP-C-160 among these specimens further indicates a larger extent of polymerization. This supports the observations from XRD, TGA and other analytical techniques as discussed in previous chapter.

Thorough investigation of the pore size distribution (PSD) of all these specimens have further provided insightful information. The PSD was estimated using DFT model using N_2 kernel at $-196 \text{ }^\circ\text{C}$ on carbon (slit pore, QSDFT equilibrium model). As can be seen in *Figure 4.1b*, a PSD centred at $\sim 1.9 \text{ nm}$ was observed in NENP-C-120. However, in specimen NENP-C-140 multimodal PSD can be observed. The majority of the pores are in the micropore region (centred at $\sim 1.9 \text{ nm}$) and some of the pores with different sizes in the mesopore regions are also present. The majority of the pores in the NENP-C-160 are centred at $\sim 1.2 \text{ nm}$. This indicates a shift of the PSD towards the smaller pore regime on polymerization. Moreover, there is much narrower PSD as compared to the other specimens. The total pore volume (V_{m}) was estimated to be 0.05, 0.10 and $0.30 \text{ cm}^3 \text{ g}^{-1}$ for NENP-C-120, NENP-C-140 and NENP-C-160, respectively at relative pressure (P/P_0) of 0.95.

4.3. Textural analysis of NENP-S-x (x = 140 and 160)

Textural properties of NENP-S-140 and NENP-S-160 (synthesized in a Teflon lined high pressure reactor using solvothermal approach) have also been investigated by N_2 sorption. Both specimens show type-I isotherm with sharp uptake at low relative pressure region ($P/P_0 < 0.01$) owing to the presence of the micropores (*Figure 4.2a*). Moreover, a narrow hysteresis above P/P_0 of 0.3 indicates the presence of some mesopores in the specimens, thus forming a hierarchical pore structure. The S_{ABET} of 63 and $125 \text{ m}^2 \text{ g}^{-1}$ were estimated for the specimens NENP-S-140 and NENP-S-160, respectively. As expected, both specimens possessed inferior specific surface area and a multimodal PSD (*Figure 4.2b*) similar to conventionally synthesized specimens. This further supports the oligomeric framework formation. As expected, the increase in the temperature induces a better condensation and formation of a partial polymeric frameworks with a shift in the PSD towards small size region. As can be seen from the PSD, majority of pores centred at $\sim 2.2 \text{ nm}$ in NENP-S-140 is shifted to 1.8 nm in specimen NENP-S-160. The total V_{m} was estimated to be 0.07, $0.16 \text{ cm}^3 \text{ g}^{-1}$ for NENP-S-140, and NENP-S-160, respectively, at P/P_0 of 0.95.

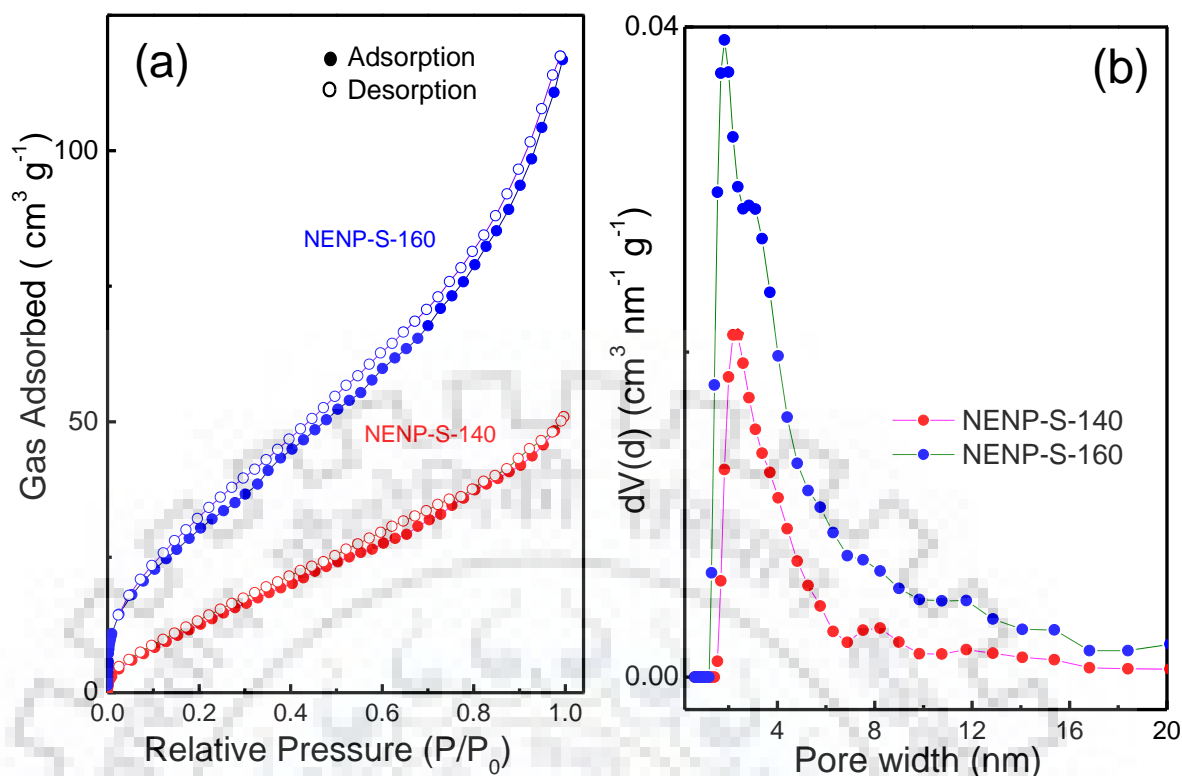


Figure 4.2. (a) N_2 sorption isotherm of NENP-S-140, and NENP-S-160 measured at $-196\text{ }^\circ\text{C}$, and (b) PSD estimated using DFT model.

Table 4.1. Textural properties of specimens NENP-C-x, NENP-S-x and NENP-U.

Sample ID	Textural Properties			
	$S_{\text{ABET}} (\text{m}^2 \text{g}^{-1})$	$S_{\text{Lang}} (\text{m}^2 \text{g}^{-1})$	PSD (nm)	$V_m (\text{cm}^3 \text{g}^{-1})$
NENP-C-120	44	101	1.9	0.05
NENP-C-140	85	145	1.9	0.10
NENP-C-160	302	500	1.2	0.30
NENP-S-140	63	147	2.2	0.09
NENP-S-160	125	244	1.8	0.07
NENP-U	75	140	2.0	0.16

4.4. Textural analysis of NENP-U

The N_2 sorption analysis of NENP-U synthesized by sonochemical method is shown in *Figure 4.3a*. The isotherm is a type-I isotherm and is very much similar to the isotherms of the specimens synthesized by conventional and solvothermal methods. The textural properties of all these specimens are compared in *Table 4.1*. The PSD further confirms the presence of both

microporosity and mesoporosity. The SA_{BET} for NENP-U was estimated to be $75 \text{ m}^2 \text{ g}^{-1}$ with a multimodal PSD. The majority of the pores centred at 2.0 nm (Figure 4.3b). The total V_m was estimated to be $0.09 \text{ cm}^3 \text{ g}^{-1}$ at P/P_0 of 0.95.

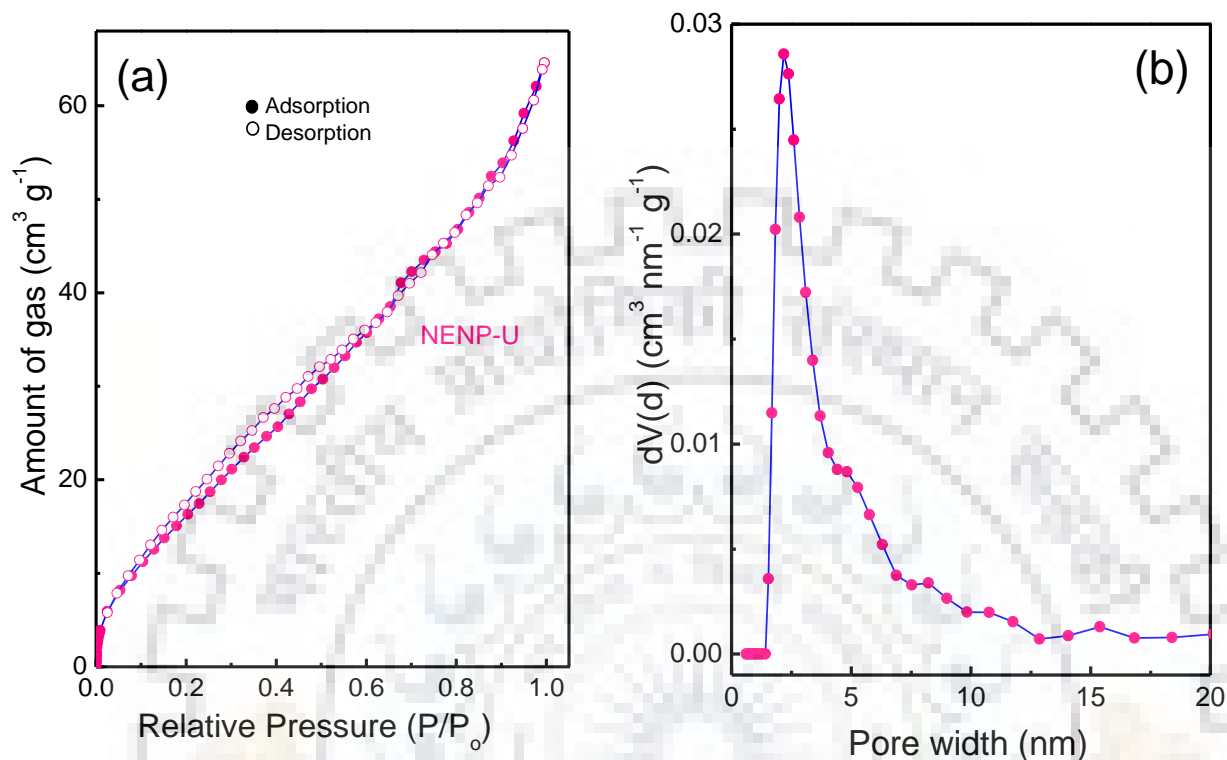


Figure 4.3. (a) N_2 sorption isotherm of NENP-U measured at $-196 \text{ }^\circ\text{C}$, (b) PSD, estimated using DFT model.

4.5. Textural analysis of NENP-x ($x = 1-9$)

As discussed in *chapter-III*, the specimens synthesized by microwave assisted method are X-ray amorphous in nature indicating the formation of polymeric frameworks which was further supported by the spectroscopic investigations (FTIR and CPMAS NMR) and thermal analysis. In order to get some insights on the specimens, the textural parameters have been investigated. The typical N_2 sorption isotherm of NENP-1 is shown in *Figure 4.4a* which reveals a type-I isotherm with sharp uptake at the low-pressure region. This indicates the presence of the micropores in the sample. The steady increase in the gas uptake with the increase in the relative pressure indicates an increased adsorbate-adsorbent interaction. Moreover, a narrow hysteresis that extends from the low to high pressure range indicates the presence of mesopores forming a hierarchical pore structure. A multimodal pore size distribution (PSD) (*Figure 4.4b*) with pores centered both in the micropore (1.3 nm) and mesopore (4.4 and 7.1 nm) regions confirms the observation. The SA_{BET} and SA_{Lang} models are 840 and $1061 \text{ m}^2 \text{ g}^{-1}$, respectively. This further

supports the formation of the polymeric framework in the specimens by the microwave assisted method. In order to further understand the effect of change of various experimental parameters on the synthesis and textural properties, several specimens have been made as discussed in *chapter-II and III*. The effect of change of these parameters on the microstructure was already seen and discussed in *chapter-III* and hence, a study of their textural properties would definitely provide useful information regarding the specimens.

4.5.1. Effect of reaction time on textural properties

The effect of experimental time has already been shown a substantial change on the microstructure as evident from the FESEM analysis in *Figure 3.13*. The bearing on the textural properties was also expected. It has been observed that neither by reducing the reaction time from 30 min (NENP-1) to 15 min (NENP-2) nor by increasing it to 60 min (NENP-3), keeping all other experimental parameters identical, have improved the textural properties as evident from *Figure 4.4*. The S_{ABET} estimated for NENP-2 and NENP-3 are 370 and 800 $\text{m}^2 \text{g}^{-1}$, respectively (*Table 4.2*). The S_{ABET} of NENP-3 is marginally less compared to NENP-1 could be attributed

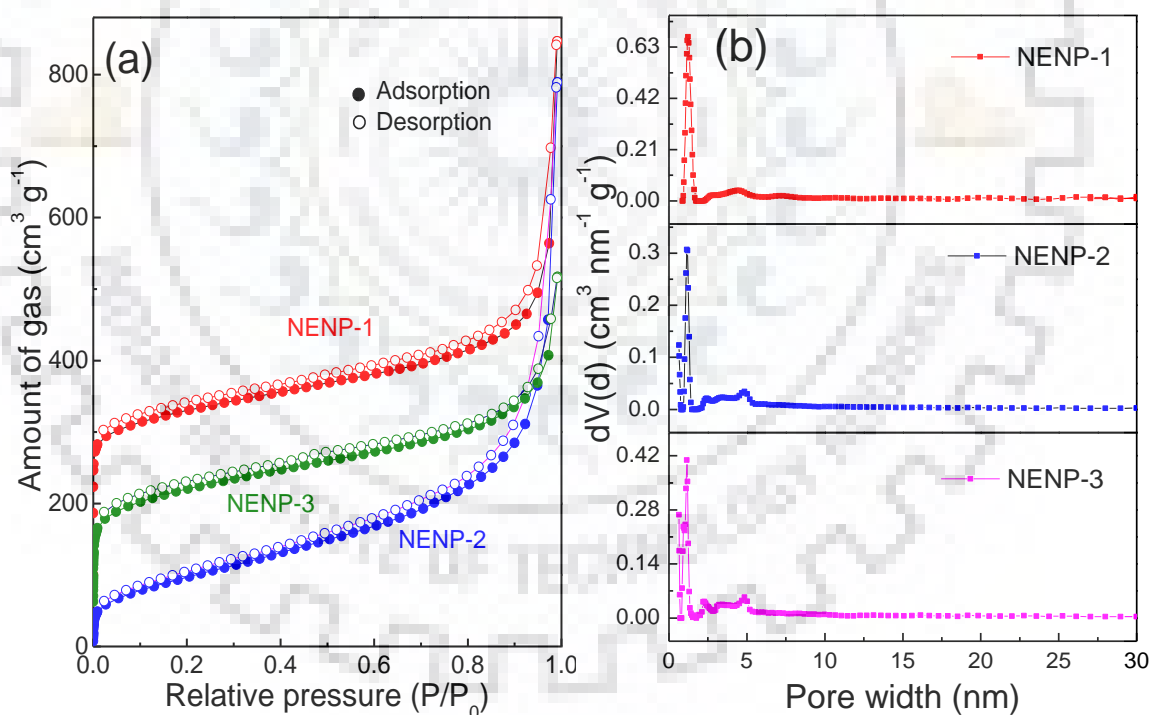


Figure 4.4. Gas sorption isotherms for NENP-1(+100), NENP-2, and NENP-3; (a) N_2 sorption isotherm collected at -196°C (b) PSD estimated using DFT model.

to the aging of the framework. This was further supported by the observation of smaller pores of average diameters of 1.0 nm in NENP-3 as compared to 1.3 nm in NENP-1 (*Table 4.2*). The total

V_m was estimated to be 0.71, 0.56, 0.57 $\text{cm}^3 \text{g}^{-1}$ at relative pressure (P/P_0) of 0.95 for NENP-1, NENP-2 and NENP-3, respectively.

4.5.2. Effect of microwave power (MWP) on textural properties

The MWP has a profound effect on the textural properties of the specimens. The S_{ABET} of the specimens synthesized at 200 (NENP-4), 300 (NENP-5) and 400 W (NENP-1) are 484, 627 and 840 $\text{m}^2 \text{g}^{-1}$, respectively (Figure 4.5). The PSD becomes narrower on increasing the MWP. On further increasing the MWP, there is a decrease in the S_{ABET} . Thus, the MWP of 400 W used for the synthesis of NENP-1 was optimum. The total V_m estimated at P/P_0 of 0.95, was found to be 0.41 and 0.62 $\text{cm}^3 \text{g}^{-1}$ for NENP-4 and NENP-5, respectively.

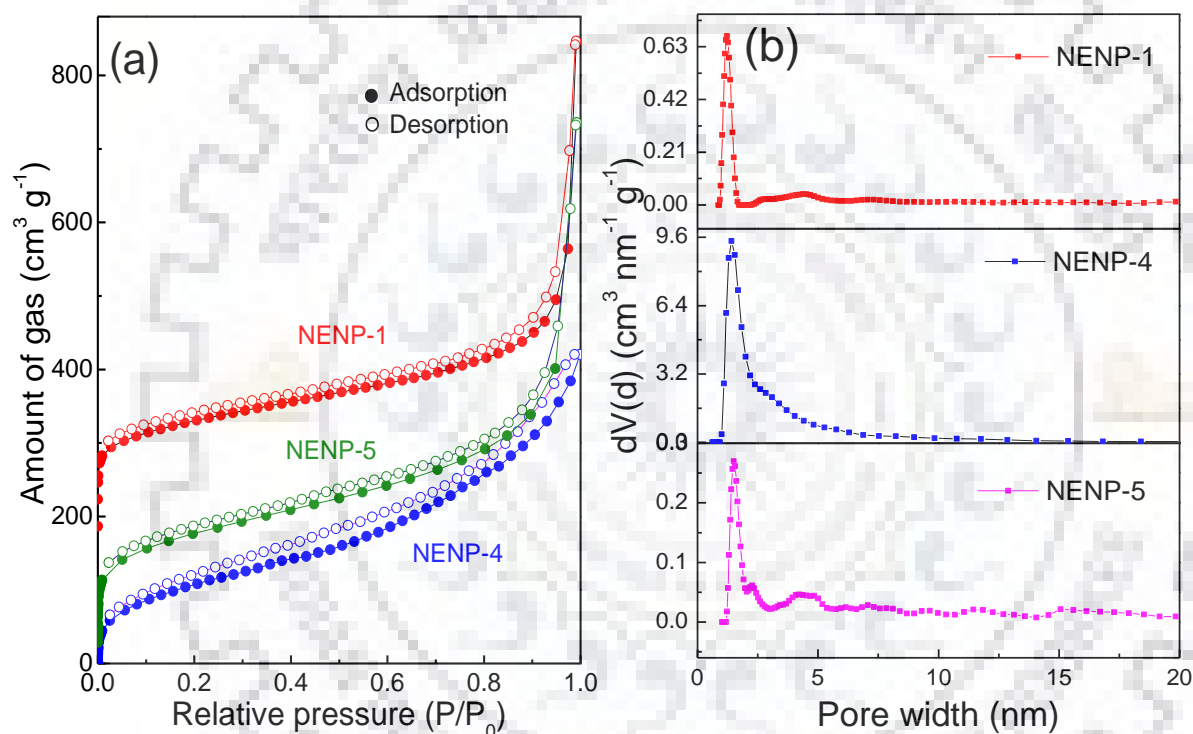


Figure 4.5. Gas sorption isotherms for NENP-1(+100), NENP-4, and NENP-5; (a) N_2 sorption isotherm collected at -196°C (b) PSD estimated using DFT model.

4.5.3. Effect of reaction temperature on textural properties

Neither a lower (120°C , NENP-6) nor higher (160°C , NENP-7) reaction temperature has improved the textural properties (Figure 4.6). The estimated S_{ABET} of NENP-6 ($402 \text{ m}^2 \text{g}^{-1}$) and NENP-7 ($676 \text{ m}^2 \text{g}^{-1}$) are lower than the S_{ABET} of NENP-1 ($840 \text{ m}^2 \text{g}^{-1}$). Thus, 140°C is considered as the optimal reaction temperature (Table 4.2). The PSD analysis performed by DFT method further confirms the presence of pores in micropore region and were centered at 1.7 and 1.6 nm in NENP-6 and NENP-7 respectively. NENP-1 has narrower PSD as compared to NENP-

6 and NENP-7, in which majority of the pores is centred at 1.3 nm. The total V_m for NENP-6 and NENP-7 were estimated to be 0.38 and 0.60 $\text{cm}^3 \text{g}^{-1}$ at P/P_0 of 0.95, respectively.

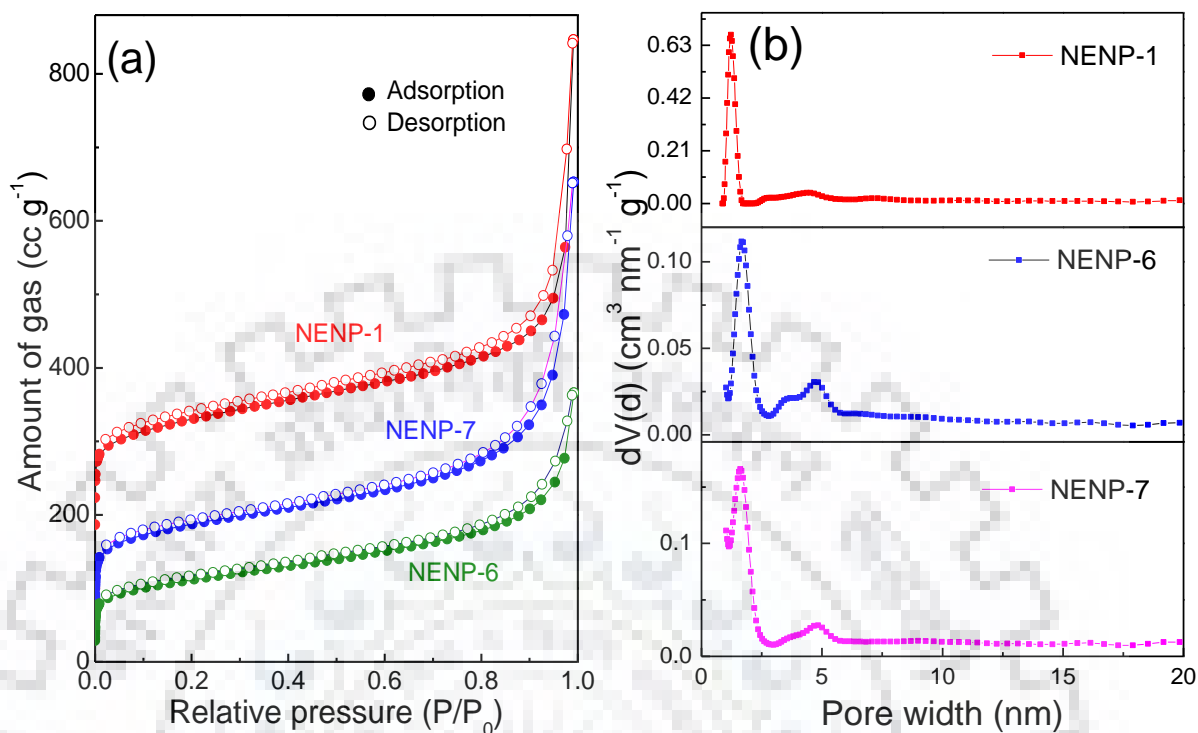


Figure 4.6. Gas sorption isotherms for NENP-1(+100), NENP-6, and NENP-7; (a) N_2 sorption isotherm estimated at -196°C (b) PSD estimated using DFT model.

4.5.4. Effect of solvent amount on textural properties

Further, the solvent amount has played a pivotal role in tuning the textural properties of the NENPs. As evident from the FESEM, the increase in the dilution has yielded particles with bigger size and smoother shapes, must have a bearing on the textural properties too. Reactions carried out with solvent amount of 10 ml in NENP-8 or 30 ml in NENP-9 have shown inferior S_{ABET} as compared to NENP-1, which was made with 20 ml of DMSO keeping other experimental conditions identical.

The S_{ABET} for NENP-8 and NENP-9 was estimated to be 40 and 320 $\text{m}^2 \text{g}^{-1}$, respectively (Figure 4.7) as against 840 $\text{m}^2 \text{g}^{-1}$ in NENP-1. The PSD was found to be centred at 3.0 and 4.0 nm (as against 1.3 nm in NENP-1). This indicates a shift of the PSD towards the wide regime. Total V_m was estimated to be 0.05, 0.35 $\text{cm}^3 \text{g}^{-1}$ at P/P_0 of 0.95 for NENP-8 and NENP-9, respectively. Based on the above experimental results, it is concluded that the best textural property obtained in the specimen synthesized by reacting melamine with cyanuric chloride in 20 ml of DMSO at 140°C using a MWP of 400 W with a reaction time of 30 min.

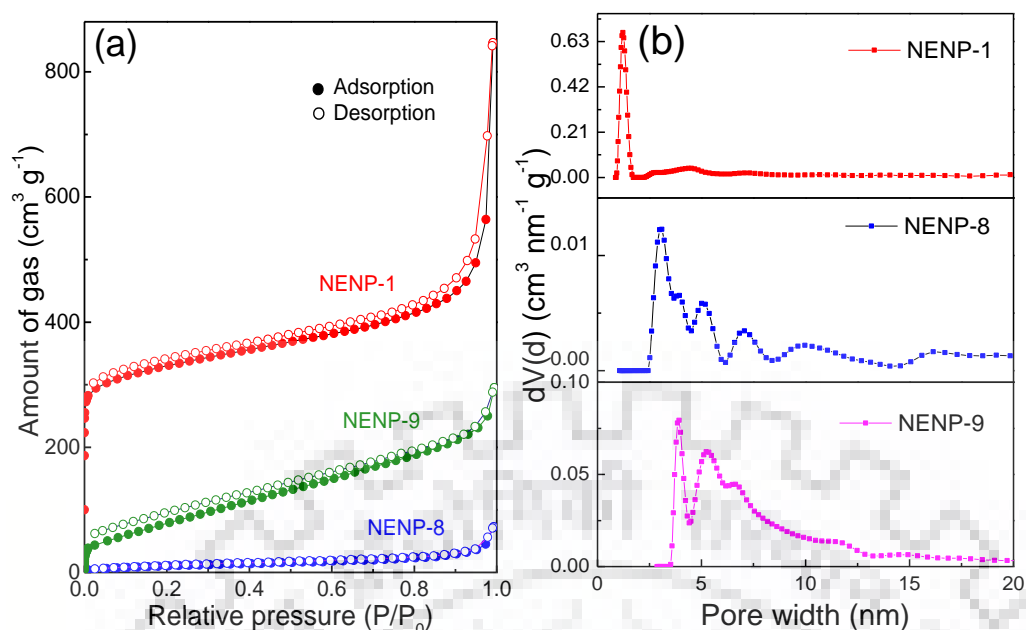


Figure 4.7. Gas sorption isotherms for NENP-1(+100), NENP-8, and NENP-9; (a) N₂ sorption isotherms at $-196\text{ }^{\circ}\text{C}$ (b) PSD estimated using DFT model.

4.6. CO₂ sorption studies of NENP-C-x, NENP-S-x and NENP-U.

Although, specimens synthesized by conventional heating, solvothermal and sonochemical methods didn't have very high S_{ABET} , which is considered as one of the critical parameters to investigate the CO₂ sorption capacity, still these specimens have been employed for CO₂ sorption analysis at 0 and 25 °C and 1 bar to investigate if any other textural or structural parameter could contribute positively towards the superior CO₂ sorption.

Table 4.2. Textural and CO₂ sorption properties of NENPs.

Sample ID	Textural Properties				CO ₂ Capture (wt%)	
	S_{ABET} (m ² g ⁻¹)	S_{Lang} (m ² g ⁻¹)	PSD (nm)	V_{m} (cm ³ g ⁻¹)	0 °C	25 °C
NENP-1	840	1061	1.3	0.71	22.9	13.1
NENP-2	370	637	2.2	0.56	11.8	5.6
NENP-3	800	1004	1.0	0.57	22.0	11.8
NENP-4	484	600	1.4	0.41	14.0	8.3
NENP-5	627	922	1.5	0.62	14.1	8.7
NENP-6	402	521	1.7	0.38	13.0	8.8
NENP-7	676	819	1.6	0.60	14.7	10.6
NENP-8	40	56	3.0	0.05	7.0	4.4
NENP-9	320	492	4.0	0.35	11.6	7.6

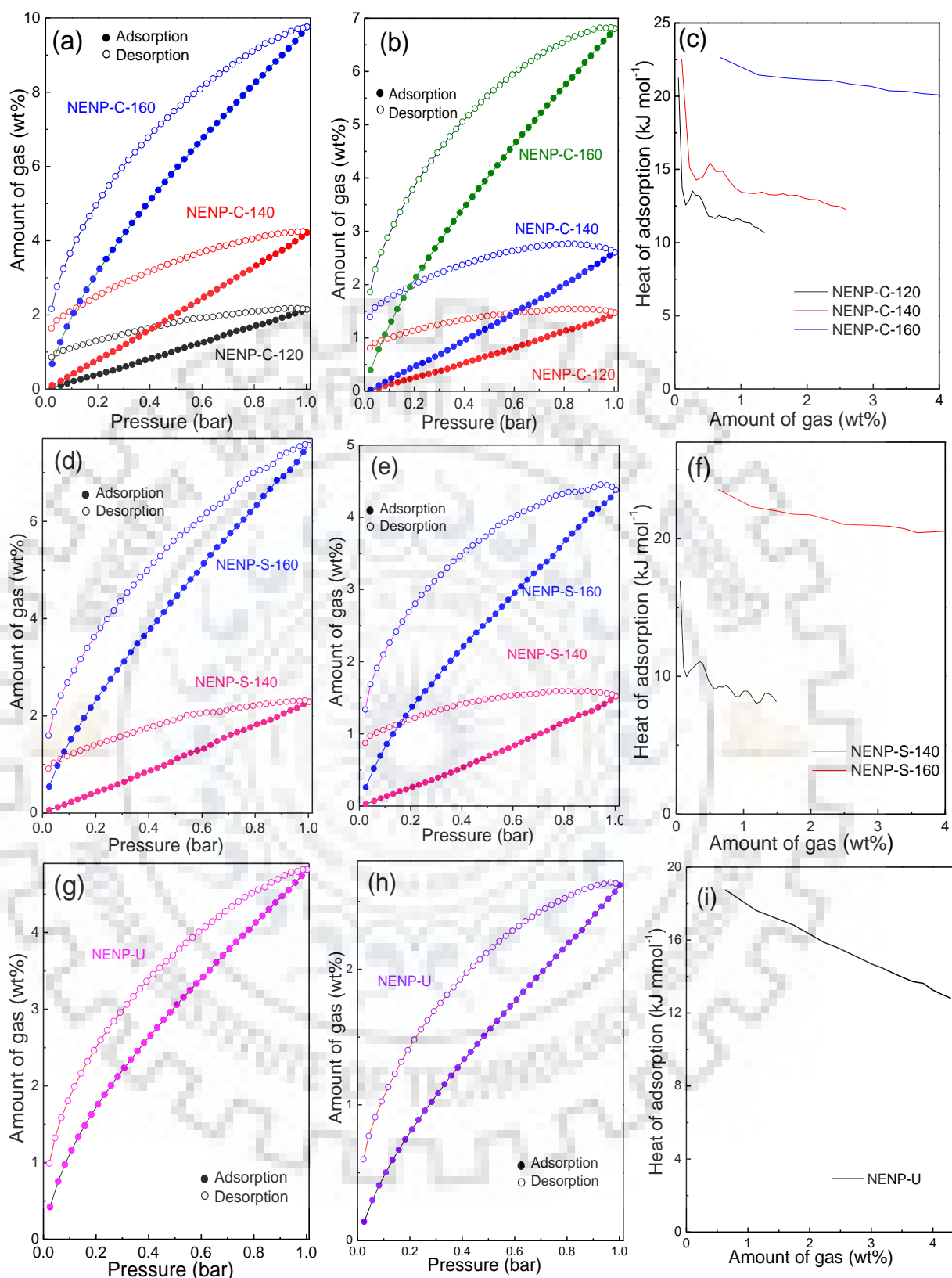


Figure 4.8. (a), (b) are CO₂ sorption isotherms, and (c) Q_{st} , for NENP-C-120, NENP-C-140 and NENP-C-160, (d), (e) are CO₂ sorption isotherms, and (f) Q_{st} , for NENP-S-140 and NENP-S-160, (g), (h) are CO₂ sorption isotherms and (i) Q_{st} , for NENP-U, respectively.

The maximum CO₂ sorption capacity of 2.1, 4.2 and 9.7 wt% was estimated in NENP-C-120, NENP-C-140 and NENP-C-160, respectively. As expected, the CO₂ uptake of these specimens decreases to 2.6, 1.5 and 6.6 wt%, respectively, when the measurement was carried out at 25 °C (*Figure 4.8a and 4.8b*). The isosteric heat of adsorption (Q_{st}) estimated using Clausius-Clayperon equation for CO₂ sorption was 21.2, 22.5 and 22.6 kJ mol⁻¹ at zero coverage in NENP-C-120, NENP-C-140 and NENP-C-160, respectively (*Figure 4.8c*). The specimens NENP-S-140 and NENP-S-160 have also shown low CO₂ uptake of 1.8 and 7.5 wt% at 0 °C and 1.4, and 4.3 wt% at 25 °C (*Figure 4.8d and 4.8e*). At zero coverage, the Q_{st} for CO₂ sorption was estimated to be 16.9 and 23.5 kJ mol⁻¹, for NENP-S-140 and NENP-S-160, respectively (*Figure 4.8f*). The CO₂ sorption isotherms at 0 and 25 °C, as given in *Figure 4.8f and 4.8g* show the CO₂ uptakes of 4.4 and 2.6 wt% for NENP-U with the Q_{st} of 18 kJ mol⁻¹ at zero coverage (*Figure 4.8i*). Detailed CO₂ sorption analysis is given in *Table 4.1*. As expected, these specimens have not shown appreciable CO₂ capture capacity. Therefore, these specimens were not employed for further gas sorption studies.

4.7. Gas sorption studies of NENP-x.

The large N content and superior textural properties observed in NENP-x (x = 1-9), synthesized by ultrafast microwave-assisted method, has encouraged to investigate these specimens for CO₂ sorption (*Figure 4.9*). The NENP-1, NENP-2 and NENP-3 exhibited good CO₂ uptake of 22.9, 11.8 and 22.0 wt%, respectively, at 0 °C. At a higher temperature of 25 °C the maximum adsorption capacity reduced to 13.1, 5.6 and 11.8 wt%, respectively (*Figure 4.9a and 4.9b*),

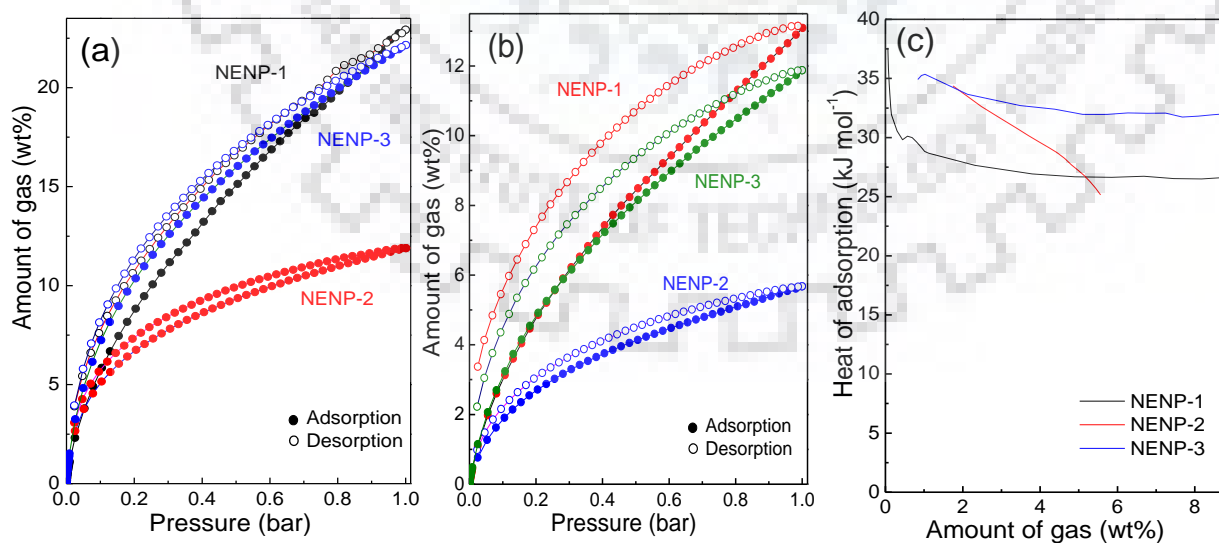


Figure 4.9. (a) and (b) are CO₂ sorption isotherms measured at 0 and 25 °C respectively, and (c) Q_{st} estimated using Clausius-Clayperon equation.

which are still high considering the adsorption temperature and maximum pressure of 1 bar only. The higher adsorption in NENP-1 could be ascribed to higher SA_{BET} in comparison to NENP-2 and NENP-3. The Q_{st} for NENP-1, NENP-2 and NENP-3 was estimated to be 37.5, 34.2 and 34.9 kJ mol^{-1} , respectively, at zero-coverage (*Figure 4.9c*).

Specimens NENP-4 and NENP-5 shows CO_2 uptake capacity of 14.0 and 14.1 wt% at 0 °C, and 8.3 and 8.7 wt% at 25 °C (*Figure 4.10a and 4.10b*). The Q_{st} for CO_2 was estimated to be 37.0 and 26.8 kJ mol^{-1} at zero-coverage for NENP-4 and NENP-5, respectively (*Figure 4.10c*). The NENP-6 and NENP-7 also exhibited good CO_2 uptake of 13.0 and 14.7 wt% at 0 °C, and 8.8 and 10.6 wt% at 25 °C as shown in *Figure 4.11a and 4.11b*, with Q_{st} of 34.9 and 31.8 kJ mol^{-1} (*Figure 4.11c*). The NENP-8 and NENP-9 have shown CO_2 uptake of 7.0, 11.6 wt % and 4.4, 7.6 wt% at 0 and 25 °C, respectively (*Figure 4.12a and 4.12b*). The Q_{st} for CO_2 was estimated to be 30.01 and 34.61 kJ mol^{-1} for NENP-8 and NENP-9, respectively (*Figure 4.12c*). Gas sorption studies shows that among all NENPs, highest CO_2 capture capacity was estimated for NENP-1. Moreover, the nitrogen content in high surface area nanoporous materials have profound role in CO_2 capture capacity.[1-4] There are many examples where the specific surface area is much higher with a low CO_2 capture capacity.[5-9] Hence, the role of heteroatoms such nitrogen in the framework for the CO_2 capture capacity cannot be neglected.

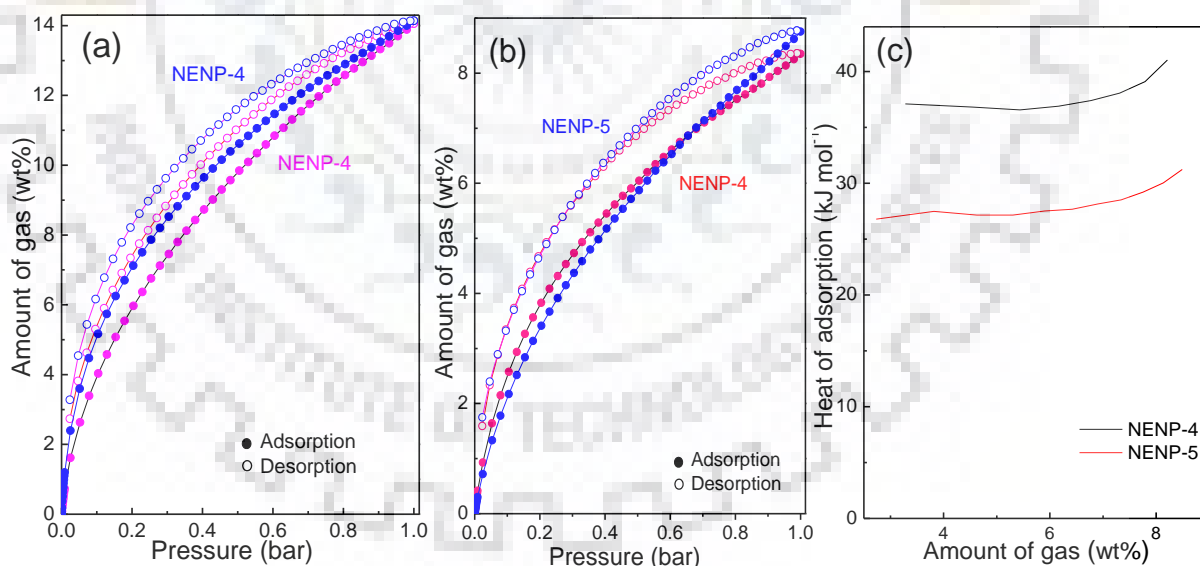


Figure 4.10. (a) and (b) are CO_2 sorption isotherms measured at 0 and 25 °C, respectively, and (c) Q_{st} estimated using Clausius-Clayperon equation.

The CO_2 capture efficiency of any material cannot be decided by only one factor, rather a complex combination of several parameters such as specific surface area, pore size distribution, pore volume, pore architecture and functionality of the framework. In the present case, although, most of the synthesized materials have similar nitrogen content, the CO_2 capture capacity

depends on several textural parameters and specific surface area is one of these, but not the only parameters that decide the CO₂ capture capacity. For example, NENP-4 and NENP-5 have almost equal CO₂ uptake but the S_{ABET} of these specimens differ by ~130 % (NENP-4; 484 m² g⁻¹ and NENP-5; 627 m² g⁻¹).

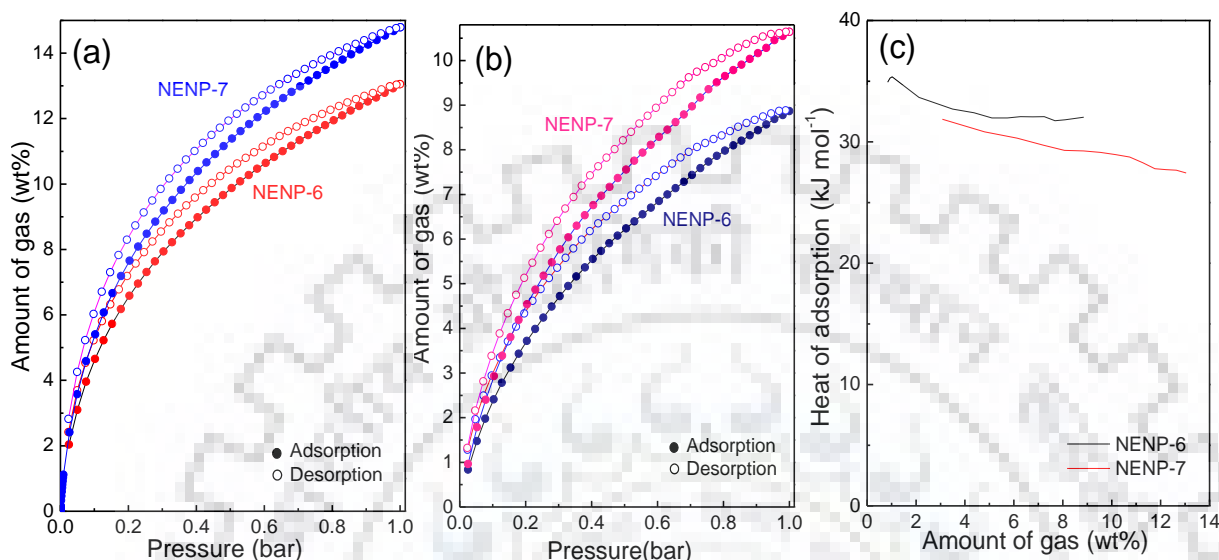


Figure 4.11. (a) and (b) are CO₂ sorption isotherms measured at 0 and 25 °C at 1 bar, respectively, and (c) Q_{st} estimated using Clausius-Clayperon equation.

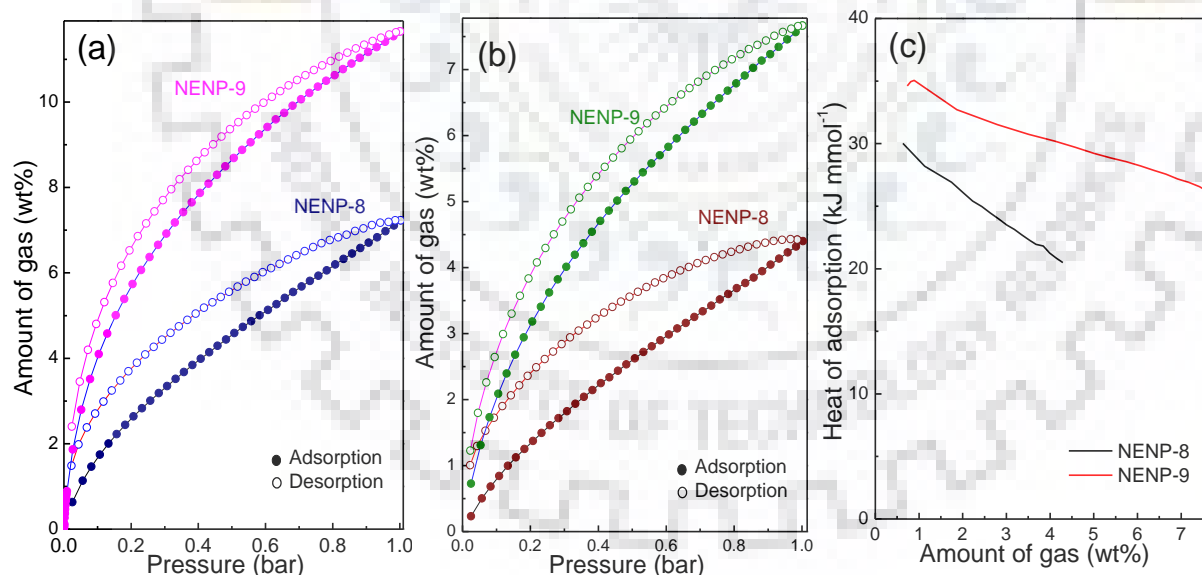


Figure 4.12. (a) and (b) are CO₂ sorption isotherms measured at 0 and 25 °C at 1 bar, respectively; (c) Q_{st} estimated using Clausius-Clayperon equation.

A comprehensive comparison of the CO₂ capture capacity of NENP-1 with some of the recently reported polymeric frameworks is given in *Table 4.3*. The Q_{st} of NENP-1 was 37.5 kJ mol⁻¹ at zero-coverage and decreases to 27.3 kJ mol⁻¹ at maximum CO₂ uptake. This moderately high Q_{st} indicates that the interaction of CO₂ with the NENP-1 is stronger than pure physisorption and weaker than pure

chemisorption.[9,10] This was possible mainly because of the high N content that facilitates the Lewis acid-Lewis base interaction between CO₂ and the framework which is considered as one of the major reasons for observing a high CO₂ capture capacity.[11] This increased interaction between the adsorbent and adsorbate delayed the desorption of the adsorbed CO₂ resulting in the formation of the hysteresis. However, this is not the only reason for the observation of the hysteresis. The ultra-small micropore in the specimen could also contribute towards a delayed desorption.

The selectivity of CO₂ over N₂ estimated to be 67 at 0 °C using the initial slope method (*Figure 4.13a*). Furthermore, the IAST method was also utilized to access the adsorption behavior of NENP-1 with binary gas composition of 15:85 (CO₂:N₂) similar to flue gas condition. The IAST CO₂ vs N₂ selectivity at 0 °C and 1 bar was estimated to be 111 [*Figure 4.13b*] which infer its potential application as an adsorbent in the post combustion CO₂ capture. As can be seen in *Figure 4.14*, the recyclability of the adsorbent for the CO₂ sorption has a little loss of the net adsorption capacity even without re-activating the adsorbent. Otherwise, the CO₂ adsorption capacity would decrease to a greater extent and the regeneration must be required, had only the thermodynamics control the adsorption. Furthermore, NENP-1 was also tested for the CH₄ and H₂ storage analysis. Interestingly, the NENP-1 store 2.3 wt% of H₂ at -196 °C and 1 bar (*Figure 4.15a*). It is worth mentioning that isotherm is completely reversible in nature and does not show saturation up to the measured pressure range of 1 bar. The H₂ sorption capacity comparison of some recently reported materials is given in *Table 4.4*.

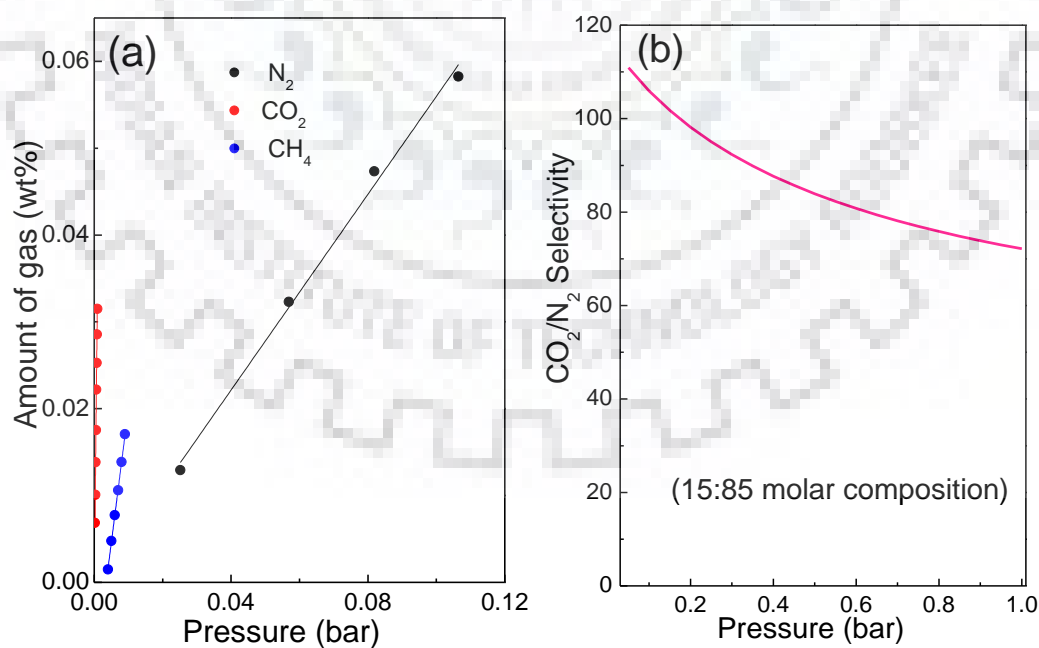


Figure 4.13. Selectivity of CO₂:N₂ estimated using (a) initial slope method (b) IAST method at 0 °C.

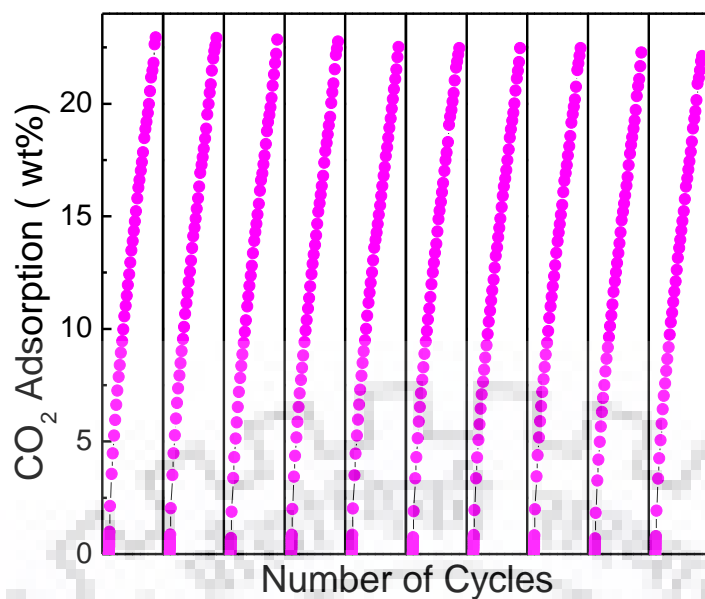


Figure 4.14. Recyclability experiment for CO₂ sorption of NENP-1 at 0 °C and at 1 bar.

Table 4.3. CO₂ sorption properties of some recently reported porous materials at low pressure.

Material ID	S _{ABET} (m ² g ⁻¹)	CO ₂ at 0 °C (wt%)	CO ₂ uptake (per m ² g ⁻¹)	Ref.
HNM-1	976	18.9	0.019	13
BILP-10(Cl)	924	11.9	0.012	14
NPAF	1790	15.2	0.008	15
HAT-CTF-450/600	1093	27.7	0.025	16
MCTP-1	1452	20.4	0.014	17
POP-1	983	8.45	0.008	18
PCTP-1	1200	21.6	0.018	19
BILP-4	1135	23.5	0.020	20
PECONF-3	851	15.3	0.017	21
PCTF-1	2235	14.3	0.006	22
PPF-1	1740	26.8	0.015	23
NOP-20	952	11.8	0.012	24
CPOP-1	2000	21.2	0.010	25
FCTF-1-600	1535	24.3	0.015	26
PAF-3	2932	15.0	0.005	07
bipy-CTF600	2479	24.5	0.009	02
NENP-1	840	22.9	0.027	This work

It is interesting to note that both the CO₂ capture and H₂ storage capacity of the NENP-1 per unit specific surface area (per m² g⁻¹) is among the best reported high surface area nanoporous organic frameworks. The CH₄ uptakes shown in *Figure 4.15b* for NENP-1 were estimated to be 1.8 and 0.8 wt% at 0 and 25 °C at 1 bar, respectively. The selectivity of CO₂ over CH₄ was as estimated to be 12 at 0 °C using Henry constant method (*Figure 4.13a*). It is important to note that NENP-1 could be kept in the ambient condition for years. We have conducted recyclability experiment of NENP-1 that was synthesized two years before and interestingly no change has been observed in the gas sorption properties. Furthermore, the recyclability studies of NENP-1 have also been performed without any specimen activation and the CO₂ adsorption capacity of 96.2% was retained even after ten cycles (*Figure 4.14*).

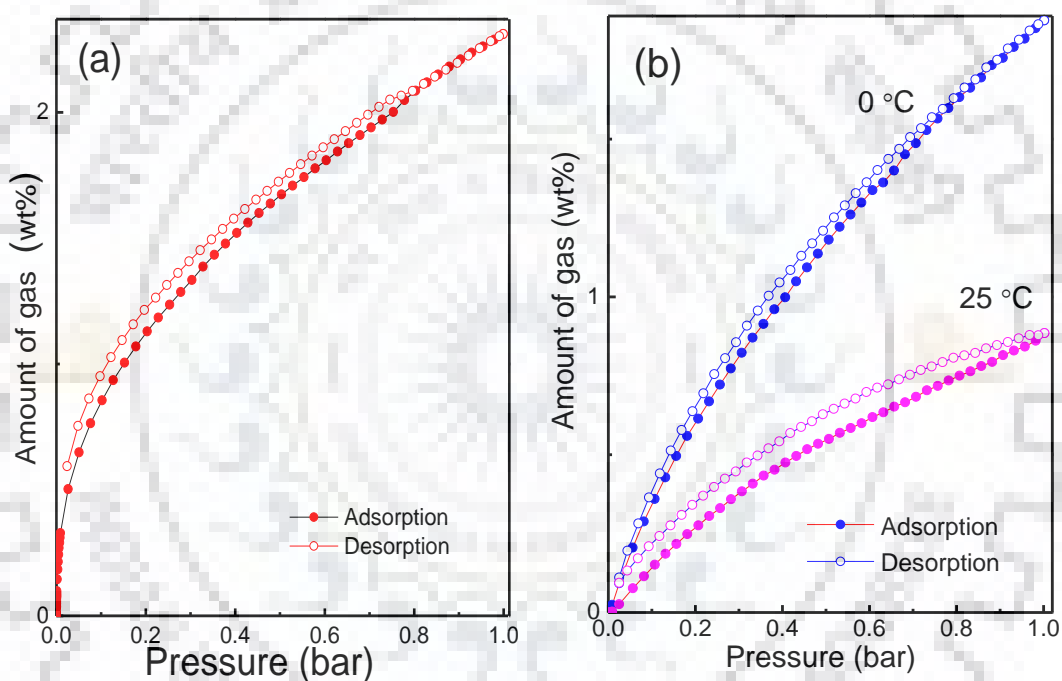


Fig 4.15. (a) H₂ sorption isotherm of NENP-1, estimated at -196 °C (b) CH₄ sorption isotherm of NENP-1, estimated at 0 and 25 °C.

Table 4.4. H₂ storage capacity of some recently reported porous adsorbents at low pressure.

Material ID	S _A BET (m ² g ⁻¹)	H ₂ @ -196 °C (wt%)	Ref.
PAF-3	2932	2.0	38
PPF-4	726	1.4	23
BILP-4	1135	2.3	20
ALP-1	1235	2.1	39
ALP-2	1065	1.7	39
PAF-47	956	1.1	40
NENP-1	840	2.3	This work

As discussed above, efforts were made to increase the CO₂ capture capacity by varying the experimental parameters. The best textural and gas sorption properties was observed in NENP-1. In order to further explore if any structural change in NENP-1 could improve the textural or gas sorption characteristics, the specimen was heat treated at 300, 350, 400 and 450 °C in argon atmosphere for 2 h and designated as NENP-1-300, NENP-1-350, NENP-1-400 and NENP-450, respectively. The FTIR investigation of these specimens indicates that there is no observable structural changes occurred when the specimen was heated up to 350 °C, but the structural changes are prominent in the specimen heated at 450 °C. FTIR investigation confirms the complete carbonization of the NENP-1 on heating at 400 °C and above (*Figure 4.16a*).[31-33] To further explore the structural changes that occurred on heating the specimens, selected

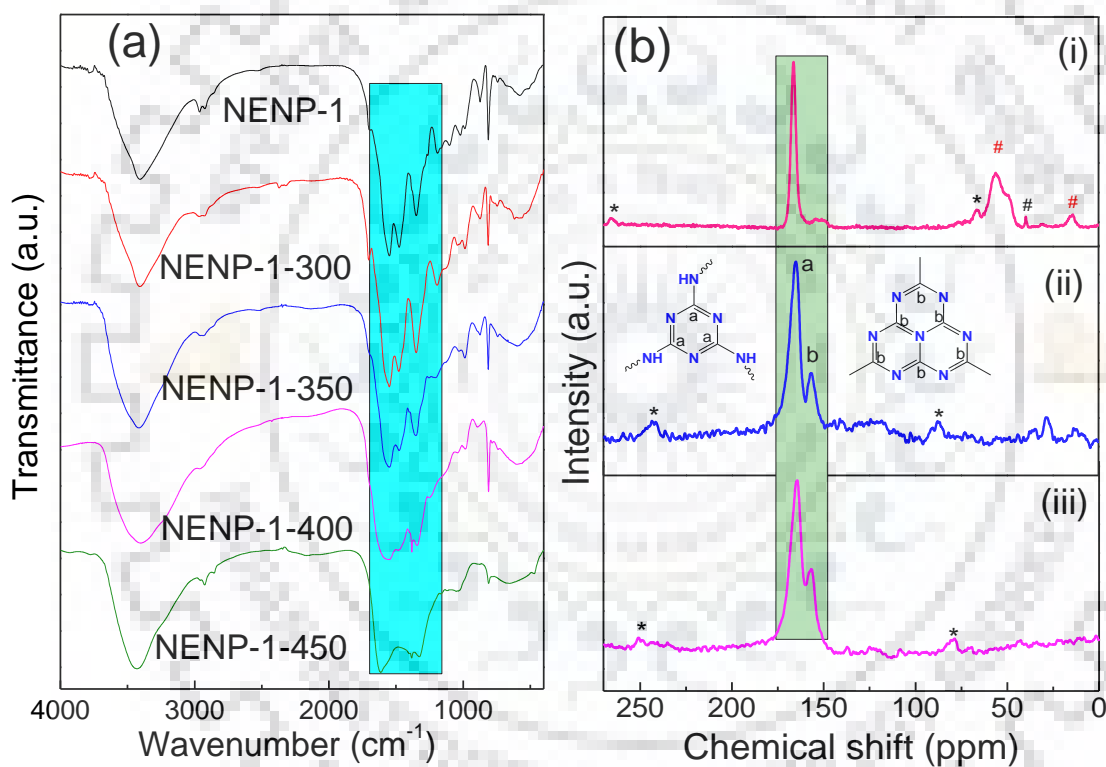


Figure 4.16. (a) FTIR spectra (b) ¹³C CPMAS NMR of (i) NENP-1 (ii) NENP-1-350 and (iii) NENP-1-450, respectively.

specimens have been investigated by ¹³C CPMAS NMR spectroscopy. The specimen heated at 350 °C indicates the change in the nitrogen environment investigated from the ¹³C CPMAS NMR data, although, the FTIR investigation didn't show any observable changes [*Figure 4.16b*].[31-37] Moreover, the sample colour changes from white in the NENP-1 to brown in NENP-1-350 to black in NENP-1-400 (*Figure 4.17*). Furthermore, C, N and H analysis provides important information about the specimens (*Table 4.5*). The experimental N content of the specimens has been increased from ~50 wt% in NENP-1 to ~52 wt% in NENP-1-350 due to removal of trapped

impurities and solvents. However, on further increasing the temperature up to 450 °C, N content was decreased due to deformation and degradation of the framework.

The effect of heat treatment on the textural properties was investigated by measuring the N₂ sorption at -196 °C. The S_ABET of 842, 880, 503 and 361 m² g⁻¹ was estimated for NENP-1-300, NENP-1-350, NENP-1-400 and NENP-1-450, respectively, (as against 840 m² g⁻¹ in NENP-1) (*Figure 4.18a*). It is important to note that there is almost no change in the S_ABET in the specimen NENP-1-300 and a marginal increase of <5% was observed in NENP-1-350. However, a decrease in the S_ABET was observed in the specimens heated at 400 and 450 °C as compared to the NENP-1. It is generally expected that on carbonization, the S_ABET increases. However, in the present example, the S_ABET decreases on carbonizing the NENP-1 above 400 °C. This may be attributed to the combined effect of increased PSD and collapse/degradation of the framework due to the depolymerisation of a part of the moieties (*Figure 4.18b*).

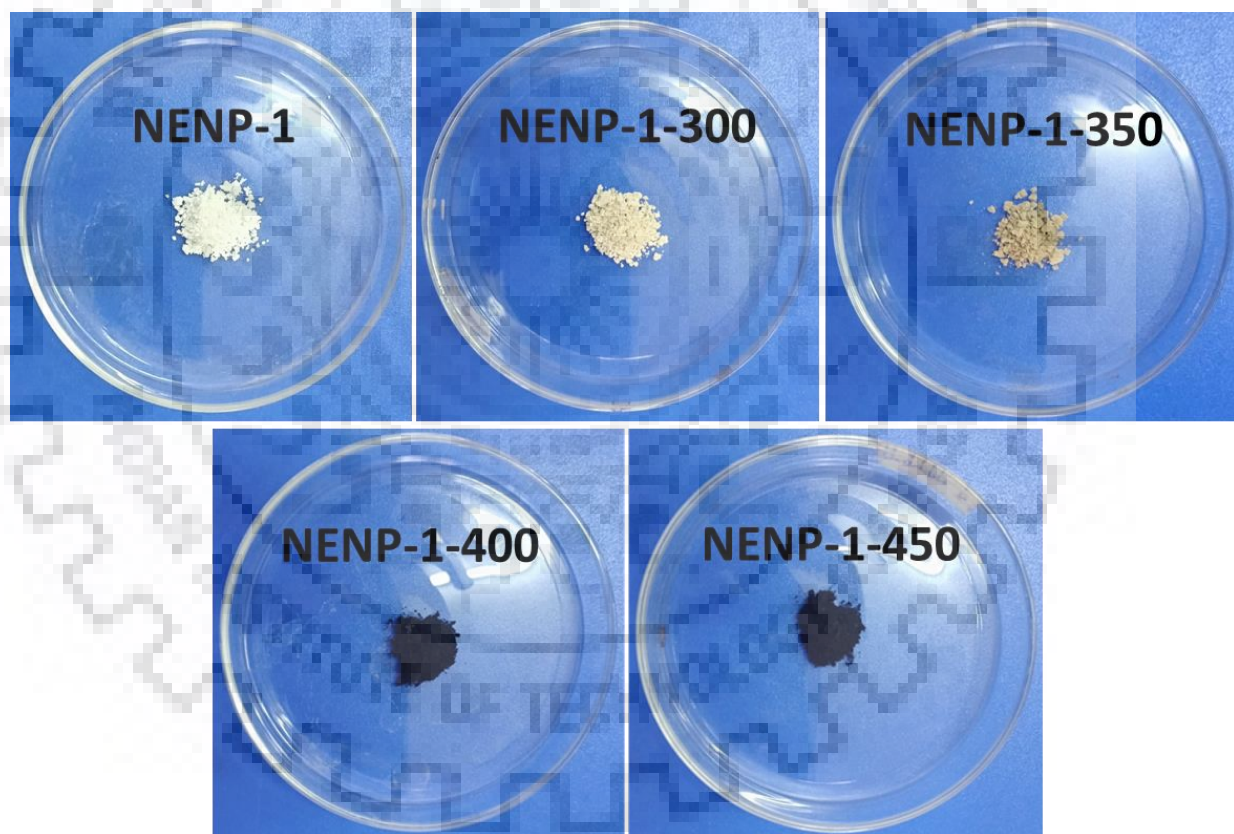


Figure 4.17. Photographs of pristine, pre-carbonized and carbonized NENPs.

It is important to note that there was a continuous increase in the mesopore contribution and was dominated in the specimens heated at 350 °C and above (*Table 4.6*). It can further be seen that although there was no change in the S_ABET of the specimen NENP-1-300 and a marginal increase in NENP-1-350, there was a substantial increase in the V_m from 0.71 cm³ g⁻¹ in NENP-1 to 0.92 and 1.10 cm³ g⁻¹ in NENP-1-300 and NENP-1-350, respectively (*Table 4.6*). This larger

V_m could be attributed to the dominance of the mesopores on heat treatment as well as removal of the trapped solvents, opening of the closed pores etc. In general, an increase in the PSD contributes towards a decreased S_{BET} . In the present case, as S_{BET} was not decreased rather a marginal increase was documented in the pre-carbonized specimens, it can be conceived that the large number of closed pores and trapped solvents are opened and get accessed for the textural properties investigation. Had the PSD not been increased towards the mesopore regime, the S_{BET} would have been increased to a greater extent.[38-49]

Table 4.5. Elemental analysis of pristine, pre-carbonized and carbonized specimens.

Sample ID	Elemental compositions (wt%)		
	N	C	H
Theoretical	62.6	35.8	1.4
NENP-1	50.0	37.9	2.4
NENP-1-300	50.4	37.5	2.4
NENP-1-350	52.1	36.2	1.9
NENP-1-400	48.5	38.0	1.4
NENP-1-450	45.0	41.4	1.1

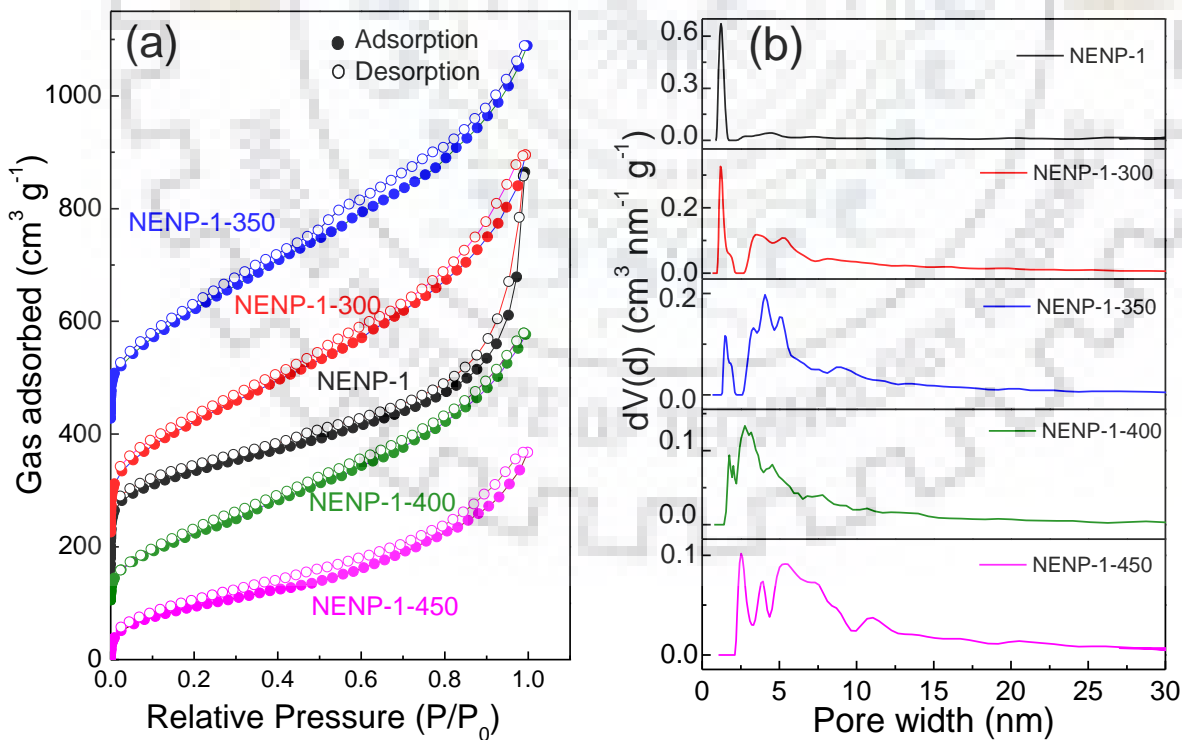


Figure 4.18. (a) N₂ sorption isotherms measured for NENP-1(+100), NENP-1-300 (+200), NENP-1-350 (+400), NENP-1-400 (+100) and NENP-1-450 at -196 °C and 1 bar, (b) PSD estimated using DFT model.

Table 4.6. Textural properties and CO₂ capture capacities of pristine, pre-carbonized and carbonized specimens.

Sample ID	Textural Properties			CO ₂ Capture (wt%)		CO ₂ @0 °C per m ² g ⁻¹
	S _A BET (m ² g ⁻¹)	V _m (cm ³ g ⁻¹)	PSD (nm)	0 °C	25 °C	
NENP-1	840	0.71	1.3	22.9	13.1	0.027
NENP-1-300	842	0.92	1.3	23.8	14.1	0.028
NENP-1-350	880	1.10	1.6	33.8	15.4	0.038
NENP-1-400	503	0.61	1.9	20.6	9.8	0.040
NENP-1-450	361	0.53	2.5	17.1	9.6	0.040

The marginal increase in the nitrogen content in the pre-carbonized specimens along with the increase in the PSD and V_m are expected to impact the CO₂ capture capacity positively. The CO₂ capture capacities of NENP-1-300, NENP-1-350, NENP-1-400 and NENP-1-450 are estimated to be 23.8, 33.8, 20.6, and 17.1 wt%, respectively, measured at 0 °C and 1 bar (*Figure 4.19a*). A similar trend in the CO₂ capture capacity was also observed when the measurement was carried out at 25 °C (*Figure 4.19b*). Moreover, Q_{st} estimated from the experimental CO₂ sorption data at 0 and 25 °C follows a similar trend (*Figure 4.19c*). Detailed textural and gas sorption properties of the pre-carbonized and carbonized specimens are compared in *Table 4.6*. The significance of increased CO₂ capture performance of about 148% in the NENP-1-350 as compared to NENP-1 could be strong deciding factor for practical applications. Increase in the V_m by 155% could be a deciding factor as only 5% increase of S_ABET could not have contributed substantially. Moreover, the dominance of mesopores in NENP-1-350 along with the micropores forming a hierarchical pore structure has worked positively in controlling the kinetics of the CO₂ sorption. The opening of closed pores, removal of trapped DMSO and TEA at high temperature are other factors that could contribute towards the higher CO₂ sorption capacity. Moreover, the surface architecture of the specimen that includes the nitrogen environment may have contributed positively for the CO₂ sorption.

The comparison of ¹³C CPMAS NMR of NENP-1, NENP-1-350 and NENP-1-450 has provided very important information on the N environment and surface functionality (*Figure 4.16b*). The signal at 166 ppm observed in the NENP-1 was attributed to the triazine carbon, which shifted to 165 and 164 ppm in the NENP-1-350 and NENP-1-450, respectively.[31] This signal is normally observed in polytriazine as well as carbon nitride obtained from triazine based precursors and polymers.[31-37] However, a new signal at 154 ppm in both NENP-1-350 and NENP-1-450 could be attributed to the stacking of triazine ring as reported earlier.[32-37] As

expected, the signals due to the trapped DMSO and TEA could no longer be seen in these specimens further support our claim of opening of the closed pores that increase the S_{ABET} although, there was a substantial increase in the PSD. The condensation of the frameworks could further help to increase PSD and V_m on heating. Thus, a combination of several factors have contributed to the net improvement of the textural properties of the NENP-1-350 resulted in the unprecedented CO_2 capture capacity. Further, increase in temperature triggered the framework decomposition as well as pore collapsing and triazine ring stacking become more prominent as supported by the ^{13}C CPMAS NMR.

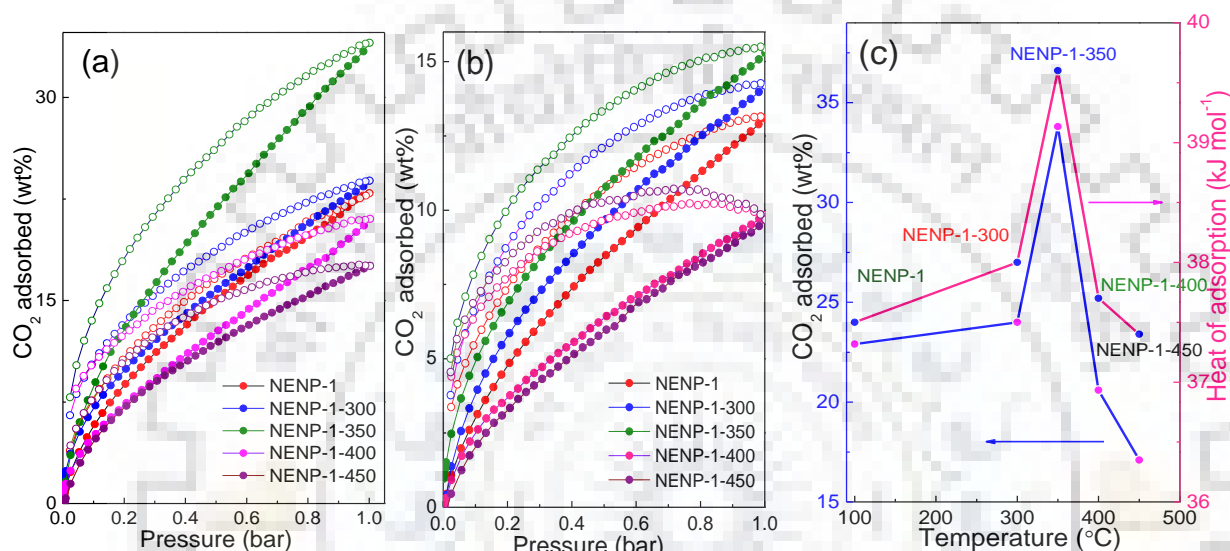


Fig 4.19. (a) and (b) CO_2 sorption isotherms measured at 0 and 25 °C (c) CO_2 sorption capacity (@0 °C and 1 bar) vs. temperature vs. heat adsorption capacity, respectively.

For practical application, not only the adsorption capacity but also the selectivity of CO_2 over N_2 and the reusability of the adsorbents are the major deciding factors. The selectivity of CO_2 over N_2 as estimated by initial slope method was 43 at 0 °C (Figure 4.20a). Furthermore, the CO_2 vs N_2 selectivity with binary gas composition of 15:85 ($\text{CO}_2:\text{N}_2$) at 0 °C and 1 bar was estimated to be 30 using IAST method. In addition to that, the retention of 89.6% of CO_2 capture capacity after five cycles even without any activation treatment further shows the potential of NENP-1-350 as a superior adsorbent for CO_2 capture application (Figure 4.20b).

Furthermore, NENP-1-350 was employed for the H_2 and CH_4 storage. The H_2 sorption isotherms (Figure 4.21a) was reversible with some hysteresis and the uptake was estimated to be 2.4 wt% at 77 K. It is further worth mentioning that the sorption isotherm was not saturated in the measured pressure range indicating a higher uptake could be achieved at higher pressure.[30] Although, the H_2 uptake is high considering its textural properties but is still way below the defined Department of Energy, USA target of 5.5 wt%. The CH_4 uptake for NENP-1-350 (Figure

4.21b) was observed to be 1.9 and 0.9 wt% at 0 and 25 °C, respectively. The selectivity of CO₂ over CH₄ as estimated by Henry constant method was 13 at 0 °C (Figure 4.20a).

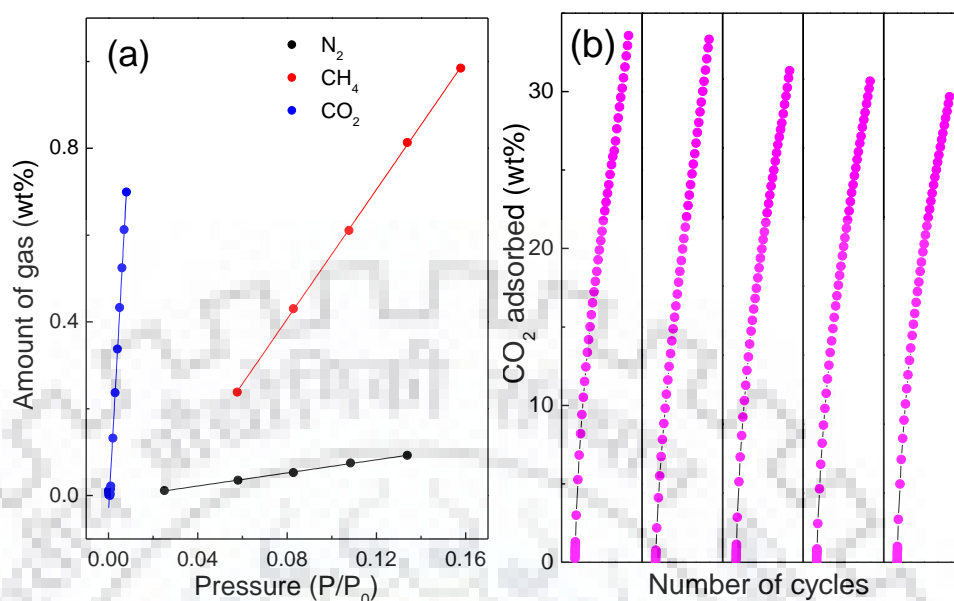


Figure 4.20. (a) Selectivity of CO₂ vs. N₂ vs. CH₄ (b) recyclability test of the specimen NENP-1-350 carried out at 0 °C and 1 bar.

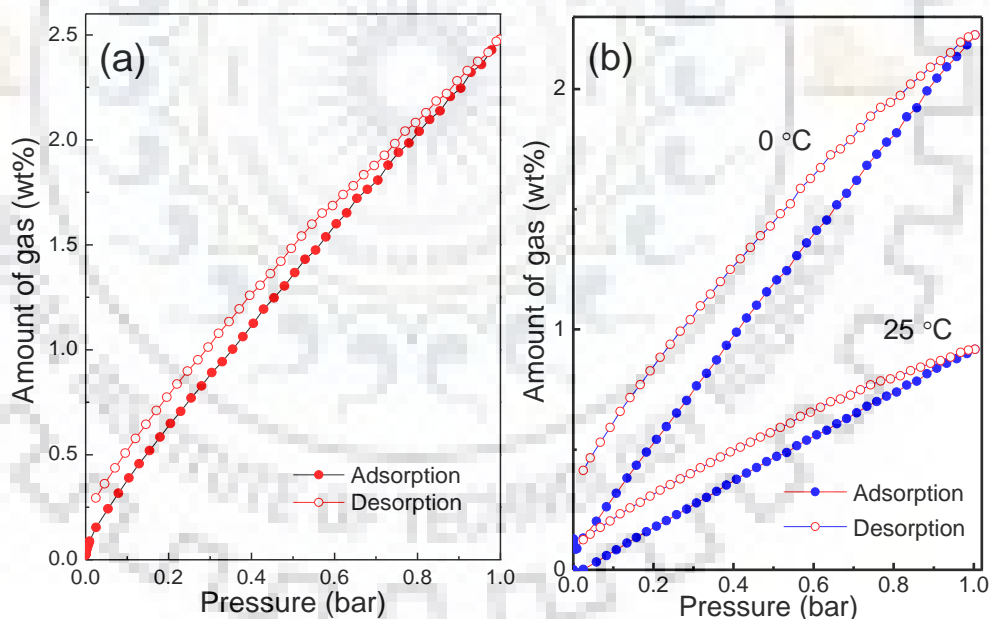


Figure 4.21. (a) H₂ sorption isotherm of NENP-1-350 estimated at -196 °C, (b) CH₄ sorption isotherms of NENP-1-350, estimated at 0 and 25 °C.

4.8. Summary

The textural analysis by N₂ sorption has provided useful information regarding the effective use of various experimental strategies for the synthesis nitrogen enriched nanoporous polytriazines (NENPs). Among all synthesized specimens, NENP-x *i.e.* synthesized by microwave assisted

method have shown best textural and gas sorption properties. Characterization of all the synthesized materials as discussed in *chapter-III* has revealed the usefulness of the microwave assisted methods as a complete condensation of framework was observed. The high N content of 50 wt% coupled with the hierarchical pore structure has helped NENPs to achieve CO₂ capture capacity of 22.9 wt% at 0 °C and 1 bar. The excellent recyclability with 96.2% retention even after 10 cycles without any activation and good CO₂ vs. N₂ selectivity of 111 in NENP-1 are considered as important milestones. Moreover, a new way of improving the CO₂ capture efficiency by pre-carbonizing NENP-1 that has shown the CO₂ capture capacity 33.8 wt% as against 22.9 wt% in the NENP-1 has further strengthen the research in this direction. This novel approach of improving the properties just by heating the specimens below their carbonization temperature could further be extended to other high surface area nanoporous polymeric materials.

References

1. K. Wang, H. Huang, D. Liu, C. Wang, J. Li and C. Zhong, Covalent triazine-based frameworks with ultramicropores and high nitrogen contents for highly selective CO₂ capture, *Environ. Sci. Technol.*, 2016, **50**, 4869-4876.
2. S. Hug, L. Stegbauer, H. Oh, M. Hirscher and B. V. Lotsch, Nitrogen-rich covalent triazine frameworks as high-performance platforms for selective carbon capture and storage, *Chem. Mater.*, 2015, **27**, 8001-8010.
3. G. Wang, K. Leus, S. Zhao and P. Van Der Voort, Newly designed covalent triazine framework based on novel heteroaromatic building blocks for efficient CO₂ and H₂ capture and storage, *ACS Appl. Mater. Interfaces*, 2018, **10**, 1244-1249.
4. Q. Dang, C. Y. Liu, X. M. Wang and X. M. Zhang, Novel covalent triazine framework for high-performance CO₂ capture and alkyne carboxylation reaction, *ACS Appl. Mater. Interfaces*, 2018, **10**, 27972-27978.
5. J. Yang, L. Yue, X. Hu, L. Wang, Y. Zhao, Y. Lin, Y. Sun, H. Da-Costa and L. Guo, Efficient CO₂ capture by porous carbons derived from coconut shell, *Energy Fuel*, 2017, **31**, 4287-4293.
6. R. Dawson, E. Stockel, J. R. Holst, D. J. Adams and A. I. Cooper, Microporous organic polymers for carbon dioxide capture, *Energy Environ. Sci.*, 2011, **4**, 4239-4245.
7. T. Ben, C. Pei, D. Zhang, J. Xu, F. Deng, X. Jing and S. Qiu, Gas storage in porous aromatic frameworks (PAFs), *Energy Environ. Sci.*, 2011, **4**, 3991-3999.
8. H. A. Patel, S. H. Je, J. Park, D. P. Chen, Y. Jung, C. T. Yavuz and A. Coskun, Unprecedented high-temperature CO₂ selectivity in N₂-phobic nanoporous covalent organic polymers, *Nat. Commun.*, 2013, **4**, 1357. DOI: 10.1038/ncomms2359.
9. W. C. Song, X. K. Xu, Q. Chen, Z. Z. Zhuang and X. H. Bu, Nitrogen-rich diaminotriazine-based porous organic polymers for small gas storage and selective uptake, *Polym. Chem.*, 2013, **4**, 4690-4696.
10. R. Muhammad and P. Mohanty, Cyclophosphazene-based hybrid nanoporous materials as superior metal-free adsorbents for gas sorption applications, *Langmuir*, 2018, **34**, 2926-2932.
11. P. Rekha, U. Sahoo and P. Mohanty, Click-based porous inorganic-organic hybrid material (PHM) containing cyclophosphazene unit and their application in carbon dioxide capture, *RSC Adv.*, 2014, **4**, 34860-34863.
12. R. Muhammad, M. Chaudhary and P. Mohanty, Harnessing electron-rich framework in cyclophosphazene derived hybrid nanoporous materials for organocatalytic C-C bond formation and gas sorption applications, *J. CO₂ Util.*, 2018, **25**, 302-309.

13. R. Muhammad, P. Rekha and P. Mohanty, Amino linked inorganic-organic hybrid nanoporous materials (HNMs) for CO₂ capture and H₂ storage applications, *RSC Adv.*, 2016, **6**, 17100-17105.
14. T. E. Reich, S. Behera, K. T. Jackson, P. Jena, H. M. El-Kaderi, Highly selective CO₂/CH₄ gas uptake by a halogen-decorated borazine-linked polymer, *J. Mater. Chem.*, 2012, **22**, 13524-13528.
15. D. E. Demirocak, M. K. Ram, S. S. Srinivasan, D. Y. Goswami and E. K. Stefanakos, A novel nitrogen rich porous aromatic framework for hydrogen and carbon dioxide storage, *J. Mater. Chem. A*, 2013, **1**, 13800-13806.
16. X. Zhu, C. Tian, G. M. Veith, C. W. Abney, J. Dehaut and S. Dai, In situ doping strategy for the preparation of conjugated triazine frameworks displaying efficient CO₂ capture performance, *J. Am. Chem. Soc.*, 2016, **138**, 11497-11500.
17. P. Puthiaraj, S. M. Cho, Y. R. Lee, and W. S. Ahn, Microporous covalent triazine polymers: efficient Friedel-Crafts synthesis and adsorption/storage of CO₂ and CH₄, *J. Mater. Chem. A*, 2015, **3**, 6792-6797.
18. Q. Y. Ma, B. X. Yang and J. Q. Li, Porous organic polymers derived from tetrahedral silicon-centered monomers and a stereocontorted spirobifluorene-based precursor: synthesis, porosity and carbon dioxide sorption, *RSC Adv.* 2015, **5**, 64163-64169.
19. P. Puthiaraj, S. M. Cho, Y. R. Lee, and W. S. Ahn, Covalent triazine polymers using a cyanuric chloride precursor via Friedel-Crafts reaction for CO₂ adsorption/separation, *Chem. Eng. J.*, 2016, **283**, 184-192.
20. M. G. Rabbani and H. M. El-Kaderi, Synthesis and characterization of porous benzimidazolelinked polymers and their performance in small gas storage and selective uptake, *Chem. Mater.*, 2012, **24**, 1511-1517.
21. P. Mohanty, L. D. Kull and K. Landskron, Porous covalent electron-rich organonitridic frameworks as highly selective sorbents for methane and carbon dioxide, *Nat. Commun.*, 2011, **2**, 401-406, DOI:10.1038/ncomms1405.
22. A. Bhunia, V. Vasylyeva and C. Janiak, From a supramolecular tetranitrile to a porous covalent triazine-based framework with high gas uptake capacities, *Chem. Commun.*, 2013, **49**, 3961-3963.
23. Y. Zhu, H. Long and W. Zhang, Imine-linked porous polymer frameworks with high small gas (H₂, CO₂, CH₄, C₂H₂) uptake and CO₂/N₂ selectivity, *Chem. Mater.*, 2013, **25**, 1630-1635.
24. Y. Liu, S. Wu, G. Wang, G. Yu, J. Guan, C. Pan and Z. Wang, Control of porosity of novel carbazole-modified polytriazine frameworks for highly selective separation of CO₂-N₂, *J. Mater. Chem. A*, 2014, **2**, 7795-7801.
25. Q. Chen, M. Luo, P. Hammersh, D. Zhou, Y. Han, B. W. Laursen, C. G. Yan and B. H. Han, Microporous polycarbazole with high specific surface area for gas storage and separation, *J. Am. Chem. Soc.*, 2012, **134**, 6084-6087.
26. Y. Zhao, K. X. Yao, B. Teng, T. Zhang and Y. Han, A perfluorinated covalent triazine-based framework for highly selective and water-tolerant CO₂ capture, *Energy Environ. Sci.*, 2013, **6**, 3684-3692.
27. J. Chen, J. Yang, G. S. Hu, X. Hu, Z. M. Li, S. W. Shen, M. Radosz and M. H. Fan, Enhanced CO₂ capture capacity of nitrogen-doped biomass-derived porous carbons, *ACS Sustainable Chem. Eng.*, 2016, **4**, 1439-1445.
28. L. Wang, L. Rao, B. Xia, L. Wang, L. Yue, Y. Liang, H. Da-Costa and X. Hu, Highly efficient CO₂ adsorption by nitrogen doped porous carbons synthesized with low-temperature sodium amide activation, *Carbon*, 2018, **130**, 31-40.
29. L. Yue, L. Rao, L. Wang, L. An, C. Hou, C. Ma, H. Da-Costa and X. Hu, Efficient CO₂ adsorption on nitrogen-doped porous carbons derived from d-glucose, *Energy Fuels*, 2018, **32**, 6955-6963.
30. L. Rao, S. Liu, L. Wang, C. Ma, J. Wu, L. An and X. Hu, N-doped porous carbons from low-temperature and single-step sodium amide activation of carbonized water chestnut shell with excellent CO₂ capture performance, *Chem. Eng. J.*, 2019, **359**, 428-435.

31. J. Zhang, Z. Wang, L. Li, J. Zhao, J. Zheng, H. Cui and Z. Zhu, Self-assembly of CNH nanocages with remarkable catalytic performance, *J. Mater. Chem. A*, 2014, **2**, 8179-8183.
32. J. Kou and L. B. Sun, Nitrogen-doped porous carbons derived from carbonization of a nitrogen-containing polymer: efficient adsorbents for selective CO₂ capture, *Ind. Eng. Chem. Res.*, 2016, **55**, 10916-10925.
33. L. Shao, Y. Li, J. Huang and Y. N. Liu, Synthesis of triazine-based porous organic polymers derived N-enriched porous carbons for CO₂ capture, *Ind. Eng. Chem. Res.*, 2018, **57**, 2856-2865.
34. L. Lin, H. Ou, Y. Zhang and X. Wang, Tri-s-triazine based crystalline graphitic carbon nitrides for highly efficient hydrogen evolution photocatalysis, *ACS. Catal.*, 2016, **6**, 3921-3931.
35. J. La-Manna, J. Braddock-Wilking, S. H. Lin and B. J. Feldman, ¹³C NMR spectroscopy of amorphous hydrogenated carbon nitride, *Solid State Comm.*, 1999, **109**, 573-576.
36. Y. Oh, J. O. Hwang, E. S. Lee, M. Yoon, V. D. Le, Y. H. Kim, D. H. Kim and S. O. Kim, Divalent Fe Atom Coordination in two-dimensional microporous graphitic carbon nitride, *ACS Appl. Mater. Interfaces*, 2016, **8**, 25438-25443.
37. Y. Hu, Y. Shim, J. Oh, S. Park, S. Park, and Y. Ishii, Synthesis of ¹³C, ¹⁵N-labeled graphitic carbon nitrides and NMR based evidence of hydrogen-bonding assisted two-dimensional assembly, *Chem. Mater.*, 2017, **29**, 5080-5089.
38. P. Arab, M. G. Rabbani, A. K. Sekizkardes, T. Islamoglu and H. M. El-Kaderi, Copper (I)-catalyzed synthesis of nanoporous azo-linked polymers: Impact of textural properties on gas storage and selective carbon dioxide capture, *Chem. Mater.*, 2014, **26**, 1385-1392.
39. L. Li, K. Cai, P. Wang, H. Ren and G. Zhu, Construction of sole benzene ring porous aromatic frameworks and their high adsorption properties, *ACS Appl. Mater. Interfaces*, 2015, **7**, 201-208.
40. X. Li, M. Zhou, J. Wang, F. Ge, Y. Zhao, S. Komarneni and Z. Cai, Flexible and internal series-connected supercapacitors with high working voltage using ultralight porous carbon nanofilms, *J. Power Sources*, 2017, **342**, 762-771.
41. S. Maiti, A. K. Das, S. K. Karan and B. B. Khatua, Carbon nanohorn-graphene nanoplate hybrid: An excellent electrode material for supercapacitor application, *J. Appl. Polym. Sci.*, 2015, **132**, 42118-42123.
42. A. K. Das, S. Maiti and B. B. Khatua, High performance electrode material prepared through *in-situ* polymerization of aniline in the presence of zinc acetate and graphene nanoplatelets for supercapacitor application, *J. Electroanalytical Chem.*, 2015, **739**, 10-19.
43. J. Cai, H. Niu, H. Wang, H. Shao, J. Fang, J. He, H. Xiong, C. Ma and T. Lin, High-performance supercapacitor electrode from cellulose-derived, inter-bonded carbon nanofibers, *J. Power Sources*, 2016, **324**, 302-308.
44. R. K. Sharma, A. C. Rastogi and S. B. Desu, Pulse polymerized polypyrrole electrodes for high energy density electrochemical supercapacitor, *Electrochem. Comm.*, 2008, **10**, 268-272.
45. L. Hao, J. Ning, B. Luo, B. Wang, Y. Zhang, Z. Tang, J. Yang, A. Thomas and L. Zhi, Structural evolution of 2D microporous covalent triazine-based framework toward the study of high-performance supercapacitors, *J. Am. Chem. Soc.*, 2015, **137**, 219-225.
46. A. Eftekhari, L. Li and Y. Yang, Polyaniline supercapacitors, *J. Power Sources*, 2017, **347**, 86-107.
47. A. Sumboja, C. Y. Foo, J. Yan, C. Yan, R. K. Gupta and P. S. Lee, Significant electrochemical stability of manganese dioxide/polyaniline coaxial nanowires by self-terminated double surfactant polymerization for pseudocapacitor electrode, *J. Mater. Chem.*, 2012, **22**, 23921-23928.
48. D. Mohapatra, S. Badranyana and S. Parida, Designing binder-free, flexible electrodes for high performance supercapacitors based on pristine carbon nano-onions and their composite with CuO, *RSC Adv.*, 2016, **6**, 14720-14729.
49. J. -W. Geng, Y. -J. Ye, D. Guo and X. -X. Liu, Concurrent electropolymerization of aniline and electrochemical deposition of tungsten oxide for supercapacitor, *J. Power Sources*, 2017, **342**, 980-989.



CHAPTER-V

**NENPs AS ELECTRODE MATERIALS
FOR SUPERCAPACITOR
APPLICATION**

5.1. Introduction

The presence of heteroatoms in the high surface area nanoporous polymeric frameworks have shown to improve the supercapacitor behaviour when used as active material for the electrode fabrication in the supercapacitor devices. Moreover, control over the pore size distribution and presence of both micropores and mesopores forming a hierarchical pore structure in the high surface area materials have added advantages. This has been discussed in detailed with the available literatures in *chapter-I*. As the synthesized material NENP-1 satisfy all the requirements to show high performance as an active material for the electrode of supercapacitor devices, it was planned to carry out the required experiments to test our hypothesis. This chapter deals with the detailed electrochemical investigations such as cyclic voltammetry (CV), galvanostatic charge discharge (GCD) and electrochemical impedance spectroscopy (EIS) of the fabricated electrodes in three electrodes set-up. Moreover, an asymmetric supercapacitor device (ASCD) was fabricated using NENP-1 as the active material that could deliver the energy density at par with commercial batteries and power density similar to supercapacitors. This, in fact could bridge the gap between the supercapacitors and batteries as evident from the Ragone's plot, which is very much required to justify its applicability in the industrial scale.

5.2. NENP-1 as an electrode material for supercapacitor application

The observation of large specific surface area of $840 \text{ m}^2 \text{ g}^{-1}$, narrow PSD and high N content (~50 wt%) in NENP-1, as discussed in previous chapter, has encouraged us to investigate the electrochemical supercapacitor application. It has already been documented in some of the recent reports that not only the superior textural properties but also the electrical conductivity of electrode material plays important role in tuning the electrochemical performance of supercapacitors.[1-4] The electrical conductivity of 0.95 S cm^{-1} at RT was estimated in the NENP-1 measured using a four point probe method. This value of conductivity is high considering the nature of the materials and the textural properties. In general, the electrical conductivity of some of the polymeric materials have value in the range of 10^4 to $10^{-7} \text{ S cm}^{-1}$. However, the introduction of nanopores in the material could substantially reduce the electrical conductivity.[1,4] Considering the high specific surface area and large pore volume, the estimated electrical conductivity for this nanoporous NENP-1 could be beneficial for enhancing the capacitance and charge storage capacity of the electrode.

The NENP-1 was subjected to CV and GCD measurements in a three electrodes configuration using $0.1 \text{ M H}_2\text{SO}_4$ as electrolyte as discussed in *chapter-II*. The specific

capacitance (C_{sp}) was calculated from CV curves measured at various scan rates using equation (5.1);[5-8]

$$C_{sp} = \frac{\int I \times dv}{m \times v \times \Delta V} \quad (5.1)$$

where, C_{sp} is specific capacitance ($F g^{-1}$), I is current (A), m is the mass of active material (g), v is the scan rate ($mV s^{-1}$), and ΔV is the potential window (V).

The C_{sp} from GCD curve was calculated using the below given equation (5.2);

$$C_{sp} = \frac{I \times \Delta t}{m \times \Delta V} \quad (5.2)$$

where, Δt signifies discharge time (s)

The energy density and power density was calculated using equation (5.3) and (5.4), respectively;[5-8]

$$E = \frac{1}{2} CV^2 \left(\frac{1000}{3600} \right) \quad (5.3)$$

$$P = \frac{E}{\Delta t} \left(\frac{1000}{3600} \right) \quad (5.4)$$

where, E is the energy density ($Wh kg^{-1}$) and P is power density ($kW kg^{-1}$).

The CV curves of NENP-1 (*Figure 5.1a*) measured at different scan rates in the range of 1 to $100 mV s^{-1}$ exhibited nearly rectangular profile with a pair of minor reversible humps, which remain similar even at high scan rate up to $100 mV s^{-1}$. Thus, the capacitive response for NENP-1 originates from the combination of electrical double layer (EDL) capacitance and pseudo-capacitance. The EDL feature is mainly due to the high S_{BET} of nanoporous polytriazine and the reversible redox transformation of N functionality of bridged amine and triazine ring contributed the pseudo-capacitance feature.[9] The C_{sp} of $1256 F g^{-1}$ at the scan rate of $1 mV s^{-1}$ estimated for NENP-1 is on the higher side. In order to further understand the electrochemical supercapacitor behaviour, the NENP-1 was further employed for GCD analysis. The GCD curves (*Figure 5.1b*) measured at different current densities between 1 to $8 A g^{-1}$ have exhibited regular triangular shapes with minor kink, which suggests reversible redox reaction during charging discharging processes. Almost inconspicuous IR drop was observed in GCD curve indicating a minute ohmic resistance and good capacitive performance. The maximum C_{sp} has been calculated to be $656 F g^{-1}$ at the current density of $1 A g^{-1}$ (*Figure 5.1c*). As expected, the drop in C_{sp} is not sharp on increasing the current density ($580 F g^{-1}$ @ $2 A g^{-1}$, $540 F g^{-1}$ @ $3 A g^{-1}$, $509 F g^{-1}$ @ $4 A g^{-1}$ and $362 F g^{-1}$ @ $8 A g^{-1}$), which could be attributed to the facile diffusion of proton, due to which most of the active sites on electrode surface are accessible to electrolyte.[10-12]

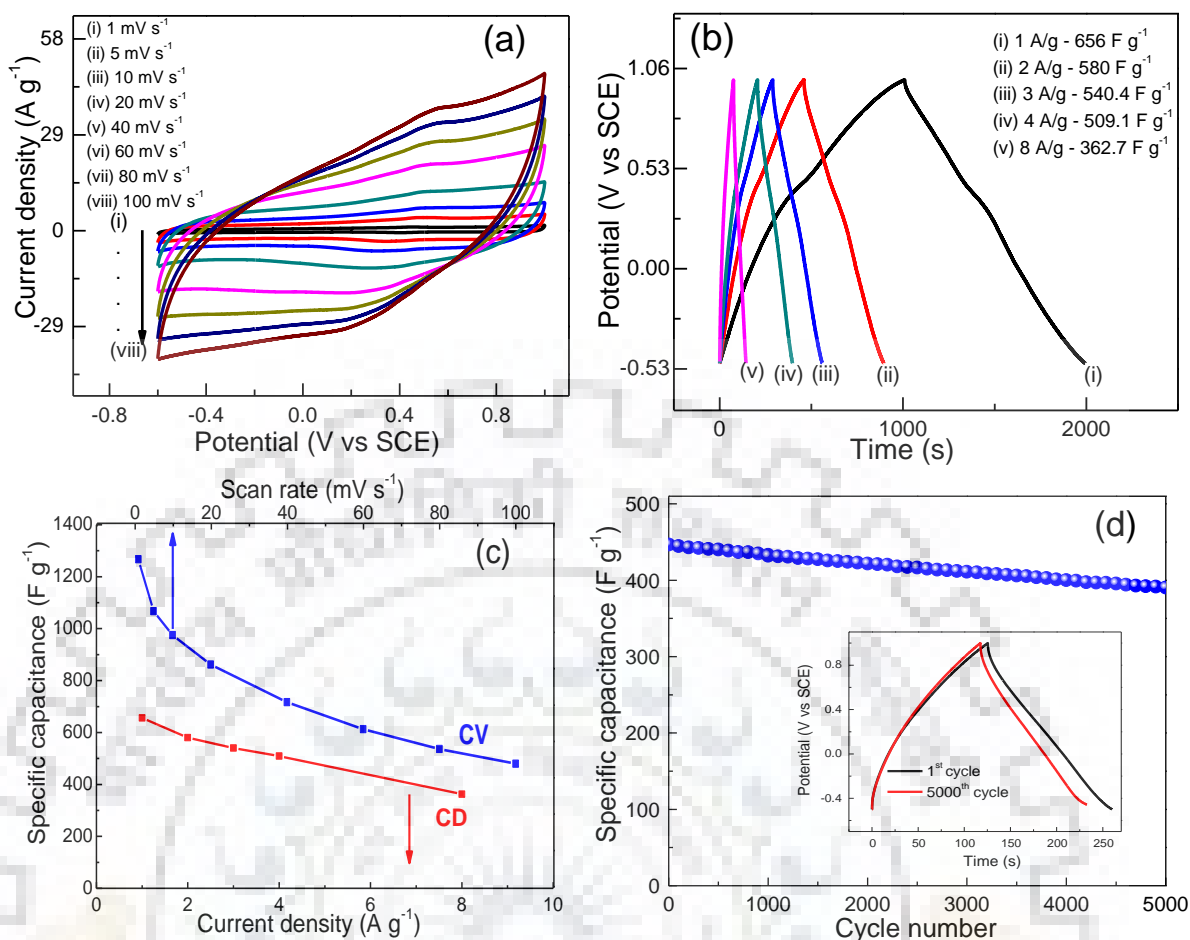


Figure 5.1. (a) CV curves at different scan rates, (b) GCD curves at various current densities, (c) specific capacitance vs scan rate/current density and (d) cyclic stability of NENP-1 tested using GCD.

It is worth mentioning that the C_{sp} of NENP-1 is comparable with many of the recently reported materials such as Aza-CMP@450 (946 F g⁻¹ @0.1 A g⁻¹), [13] and even better than TaPa-Py COF (102 F g⁻¹ @0.5 A g⁻¹) [14], DAAQ-TFP COF (48 ± 10 F g⁻¹ @0.1 A g⁻¹) [15] and TpDAB (432 F g⁻¹ @0.5 A g⁻¹), [16]. It is interesting to note that even at higher scan rate of 5, 10, 20, 80 and 100 mV s⁻¹, NENP-1 has exhibited C_{sp} of 1064, 975, 866, 625 and 497 F g⁻¹, respectively, (Figure 5.1c). A small decrease in the C_{sp} values with the increased scan rate is believed to be due to the hierarchical pore structure, which facilitates the smooth transfer of ions, at higher scan rates. Moreover, the smallest pores in the sample is also on the higher side of the micropore range that facilitates the ion transport. [17-20] The cyclic stability of the prepared electrode has been tested using GCD. Almost 87.4% of retention from its initial C_{sp} was observed even after 5000 cycles at a current density of 5 A g⁻¹ (Figure 5.1d), further reveals its importance as electrode material for supercapacitor application.

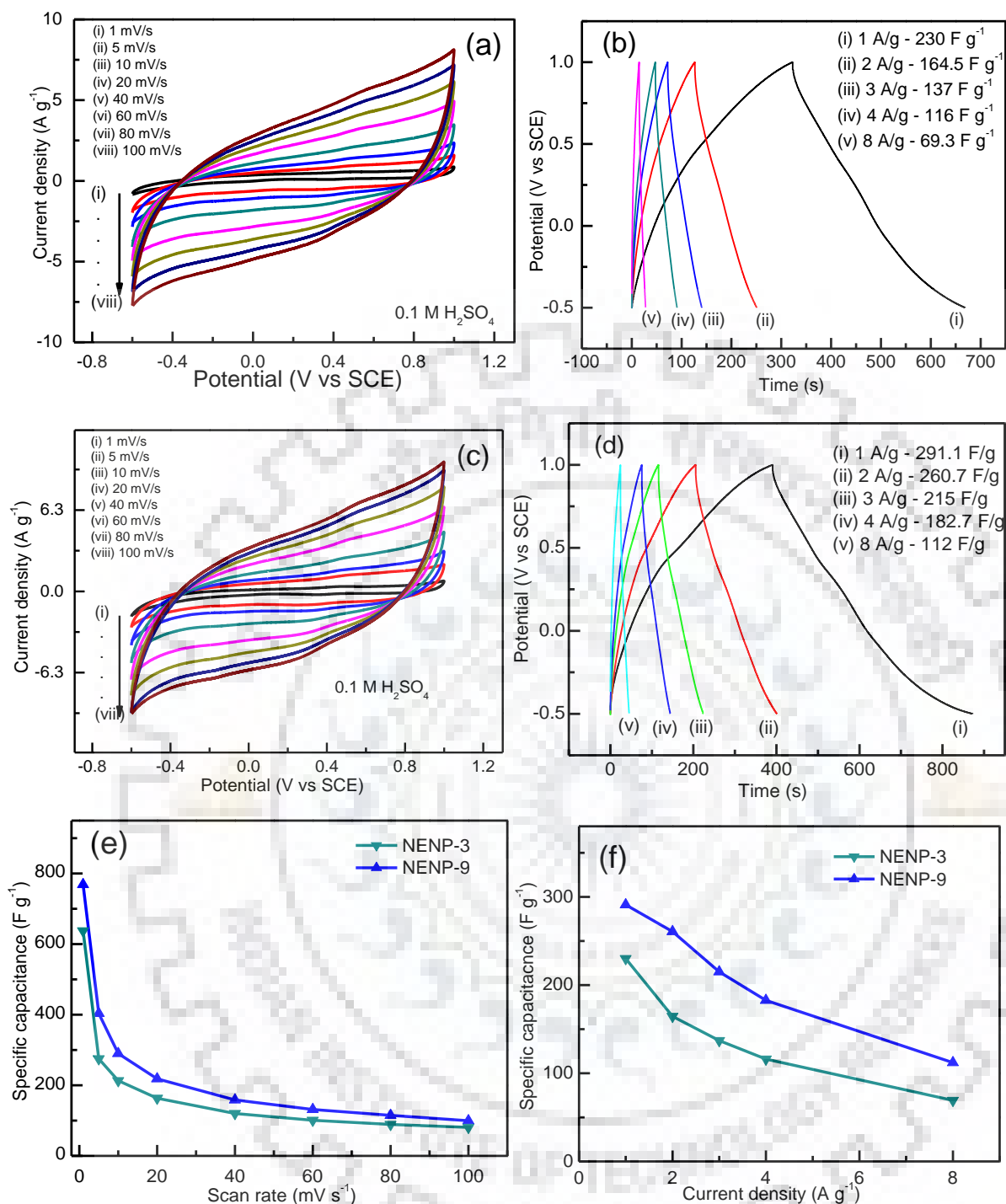


Figure 5.2. CV and GCD analysis of NENP-3 and NENP-9; (a) and (c) are CV curves of NENP-3 and NENP-9, respectively, (b) and (d) are GCD curves of NENP-3 and NENP-9, respectively, (e) specific capacitance vs scan rate and (f) specific capacitance vs current density.

Keeping in mind the large specific surface area and high N content, one more specimen NENP-3 with comparable S_{ABET} of $800 \text{ m}^2 \text{ g}^{-1}$, was selected from the series of samples synthesized in this work, for the investigation of electrochemical supercapacitor application. The specimens, NENP-3 was subjected to cyclic voltammetry CV and GCD measurements in a three

electrodes configuration using 0.1 M H₂SO₄ as electrolyte (*Figure 5.2a and 5.2b*). The CV curves of NENP-3 measured at different scan rates in the range of 1 to 100 mV s⁻¹ exhibited nearly rectangular profile. Although, NENP-1 and NENP-3 have comparable S_{ABET} but there was a large difference in their specific capacitance (C_{sp}) of 1256 F g⁻¹ and 637 F g⁻¹, respectively, at scan rate of 1 mV s⁻¹.

The observation of almost twice C_{sp} in NENP-1 as compared to NENP-3 could be ascribed to its wider pore size of 1.3 nm versus 1.0 nm. Due to small pore size, majority of the active sites may not be accessible to the electrolyte ions in NENP-3 resulting in a lower C_{sp}. Thus, the specific surface area is not the only parameter that contributes towards the C_{sp} but pore size also plays a significant role.[12] To further prove the observation to be correct, specimen NENP-9 having largest pore size (4.0 nm) among all the synthesized samples, was investigated for CV and GCD analysis (*Figure 5.2c and 5.2d*). The C_{sp} was estimated to be 768 F g⁻¹ with a scan rate of 1 mV s⁻¹. Although, the S_{ABET} of NENP-9 (313 m² g⁻¹) is only about 40% as compared to NENP-3 (800 m² g⁻¹), the C_{sp} is almost 120% (*Figure 5.2e and 5.2f*). However, the C_{sp} as well as the S_{ABET} of NENP-9 is lower than the NENP-1. It is worth mentioning that the PSD of NENP-1 (1.3 nm) is in between the NENP-3 (1.0 nm) and NENP-9 (4.0 nm). This indicates that the PSD cannot be the only deciding factor to choose the materials for electrode fabrication. Although the NENP-9 has wider pores still the contribution from the S_{ABET} has dominated in the NENP-1. Similar trend was also observed in the GCD analysis.

The high C_{sp} estimated both from the CV and GCD studies of the three electrodes configuration have encouraged us to further investigate the device behavior of NENP-1 in two electrodes asymmetric configuration. An ASCD was fabricated using NENP-1, as discussed in *chapter II*. The electrochemical performance of the ASCD was studied in 0.1 M H₂SO₄ as electrolyte. To observe the maximum performance of the NENP-1//AC based ASC device, mass ratio of negative to positive electrode was measured using the charge balance theory ($Q_+ = Q_-$).

According to charge balance theory,

$$Q_+ = Q_- \quad (5.5)$$

$$m_+ \times C_{sp+} \times \Delta V_+ = m_- \times C_{sp-} \times \Delta V_- \quad (5.6)$$

$$\frac{m_+}{m_-} = \frac{C_{sp-} \times \Delta V_-}{C_{sp+} \times \Delta V_+} \quad (5.7)$$

$$\frac{m_+}{m_-} = \frac{975 \times 1.6}{325 \times 1.6} = 3.00 \quad (5.8)$$

where, C_{sp} refers to the specific capacitance ($F g^{-1}$) at $10 mV s^{-1}$ scan rate, ΔV is the potential window (V), and m stands for mass of the electrode (g). From the CV profile (Figure 5.3a), the specific capacitance of NENP-1 and AC was calculated to be $975 F g^{-1}$ and $325 F g^{-1}$, respectively at $10 mV s^{-1}$. The mass ratio of NENP-1 and AC was 0.33 in the ASC device. Mass of NENP-1 and AC used in the fabrication of ASC device is 6.0 and 2.0 mg, respectively. Hence the total mass of the ASCD is 8 mg. The individual voltammograms of NENP-1 and AC was recorded (Figure 5.3a) by three electrode system at $10 mV s^{-1}$ in $0.1 M H_2SO_4$ electrolyte. The AC and NENP-1 has the potential window from -0.6 to 1.0 V. Thus, the total potential window was found to be 1.6 V in $0.1 M H_2SO_4$, suggesting that the operating cell voltage could be extended up to 1.6 V for two-electrode ASCD device.

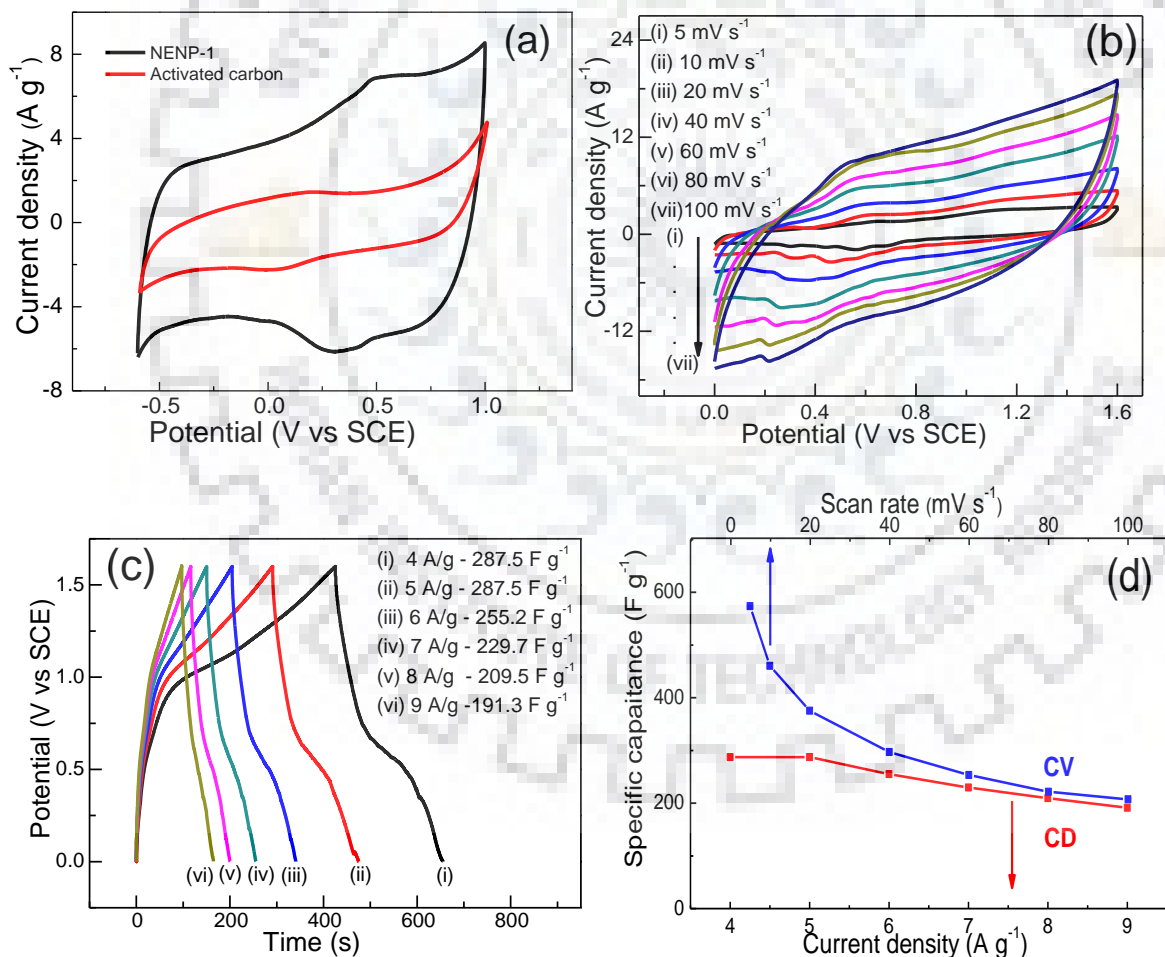


Figure 5.3. (a) CV of NENP-1 and activated carbon recorded using three electrode system at $10 mV s^{-1}$, (b) CV curves at different scan rates, (c) GCD curves at various current density, (d) specific capacitance vs. scan rate/current density of NENP-1 ASCD,

The CV (Figure 5.3b) and GCD (Figure 5.3c) profiles have shown a similar trend to three electrode configuration. The C_{sp} was estimated to be 567 F g^{-1} at 5 mV s^{-1} and 287 F g^{-1} at 4 A g^{-1} , from CV and GCD analysis, respectively (Figure 5.3d). As expected, the C_{sp} of the ASCD is lower compared to the three electrodes configuration. To the best of our knowledge, the calculated values of C_{sp} are much higher compared to many of the recently reported materials based ASCD such as SPANI/G-1 (157 F g^{-1} @ 1.5 A g^{-1}), [18] HFAC (114 F g^{-1} @ 0.5 A g^{-1}) [21] and also better than many of the metal oxide based ASCD such as $\text{Co}_3\text{O}_4/\text{carbon}$ (101 F g^{-1} @ 2 A g^{-1}), [22] $\text{Ni}(\text{OH})_2/\text{graphene}$ (218.4 F g^{-1} @ 1 mV s^{-1}), [23] $\text{Ni}(\text{OH})_2/\text{AC}$ (218.4 F g^{-1} @ 5 mV s^{-1}), [24] $\text{MnO}_2/\text{P-GA}$ (108.9 F g^{-1} @ 5 mV s^{-1}), [25] MWS/MWV (198 F g^{-1} @ 1 A g^{-1}). [26] Moreover, the ASCD shows remarkable energy efficiency with the maxima reaches as high as 71.4% at a current density of 8 A g^{-1} , further reveals that the applied potential window is efficient enough to provide good performance (Figure 5.4a). [27]

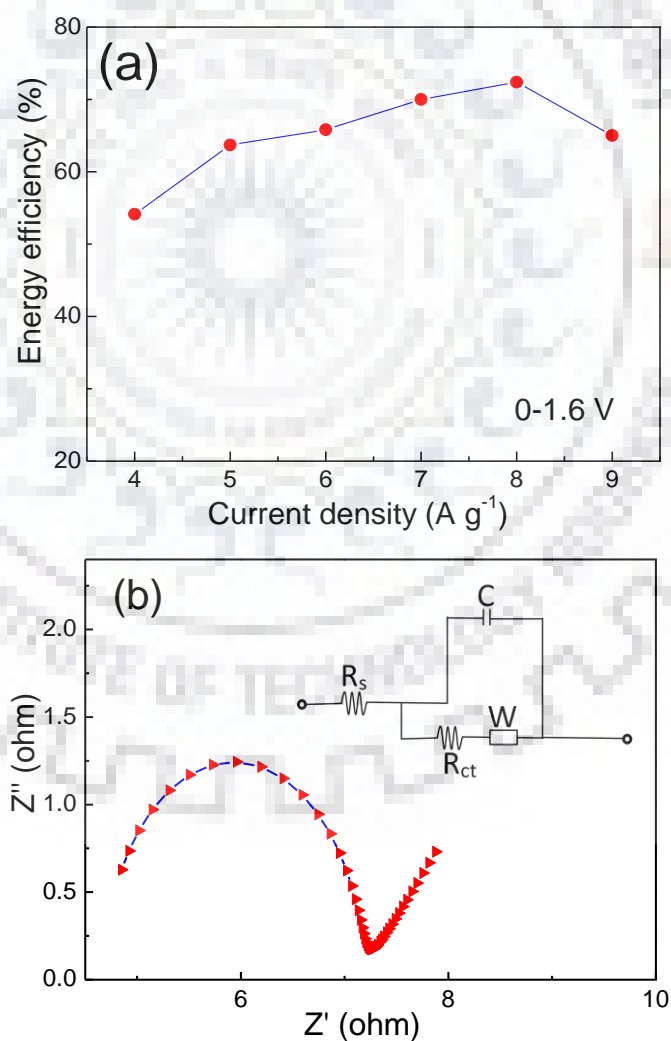


Figure 5.4. (a) Energy efficiency vs. current density and (b) Nyquist plot of NENP-1 (Inset: equivalent circuit diagram).

It is very important to note that the energy density of 102 Wh kg^{-1} calculated at the power density of 2.0 kW kg^{-1} in the ASCD was far better than the previously reported materials such as SPANI/G-1 (31.4 Wh kg^{-1} @ 14 kW kg^{-1}), [18] Ni(OH)₂/graphene (77.8 Wh kg^{-1} @ 0.174 kW kg^{-1}), [23] Ni(OH)₂/AC (12.6 Wh kg^{-1} @ 1.6 kW kg^{-1}), [24] RGO-MnO₂ (47.9 Wh kg^{-1} @ 0.270 kW kg^{-1}), [28] AC/MnO₂ (21 Wh kg^{-1} @ 0.300 kW kg^{-1}), [29] and lower than Li-ion battery (270 Wh kg^{-1}). [30] The remarkable energy density of 74 Wh kg^{-1} even at high power density of 3.6 kW kg^{-1} is estimated, further indicates its applicability as the future generation electrode materials for supercapacitor applications (*Table 5.1*).

To further understand the charge transfer behaviour and estimate the internal resistance, the EIS was measured in the frequency range of 1 Hz to 1 MHz and amplitude between 0.005 and 0.03 V (*Figure 5.4b*). An equivalent simulated circuit diagram of the experimental data consisting of solution resistance (R_s), charge transfer resistance (R_{ct}), Warburg element (W) and capacitor (C) was fitted. The obtained Nyquist plot has a semicircle in high frequency region and a straight line in the medium to low frequency region. The diameter of the semicircle provides the R_{ct} of electrode-electrolyte interface and the straight line is due to the diffusion of ions from the electrolyte to the electrode surface. The estimated R_{ct} value for NENP-1 electrode was 2.471Ω along with R_s of 4.679Ω obtained from the fitting of the equivalent circuit model as shown in the inset of *Figure 5.4b*. The low R_{ct} value is beneficial as it is responsible for the quick charge transfer and fast ions diffusion resulting in the improved electrochemical performance.

Table 5.1. Calculation of energy density and power density for two electrode configuration.

Sample ID	Energy density (Wh kg ⁻¹)	Power density (kW kg ⁻¹)	Current density (A g ⁻¹)
NENP-1	102	1.6	4
NENP-1	102	2.0	5
NENP-1	91	2.4	6
NENP-1	82	2.8	7
NENP-1	74	3.6	8

Further the Ragone plot compares the energy storage and power delivery rate of fabricated ASCD with reported energy storage devices as shown in *Figure 5.5a*. The Ragone plot indicates that the NENP based ASCD could store the energy comparable to batteries while keeping its power density performance comparable to supercapacitors. [23,24,30,31] The observation of the superior supercapacitive performance of the investigated material could be attributed to the high nitrogen content and hierarchical pore structure. The nitrogen functionality in the framework provides the active sites for the redox reaction, whereas the hierarchical pore

structure helps in the kinetics of the electrolytic ion movements. The ASCD was further tested as a power source to lit a 1.5 V red and green LEDs, and 3.0 V blue LED (*Figure 5.5b*). On charging for 30 s with an input potential of 3.0 V, the red, green and blue LEDs could be lit up to 11, 4 and 0.5 min, respectively.

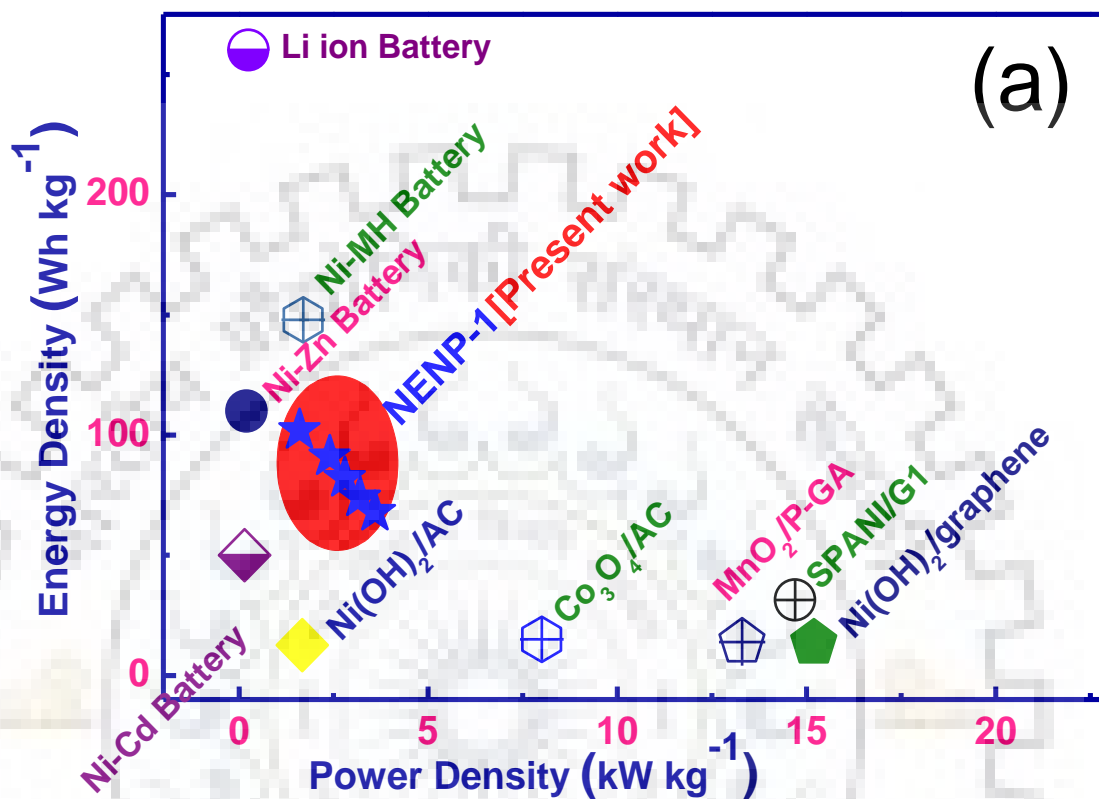


Figure 5.5. (a) Ragone plot of NENP-1 ASCD and its comparison with some reported energy storage devices, (b) snapshot of different LEDs.

5.3. Summary

Among the three best specimens, NENP-1 has been found to be performed best as an active electrode material for the supercapacitor applications. As expected the large nitrogen content, hierarchical pore structure, narrow pore size distribution and high specific surface area played significant role in the performance. The superior performance is found to be the combined contribution of all the above mentioned factors. Each of the factor could contribute to the better performance but was not the only parameters that decides it. Observation of high specific capacitance of 1256 F g^{-1} @ 1 mV sec^{-1} from the cyclic voltammogram in the three electrode system is in the higher side of the reported materials of similar type. The energy and power density of the device has provided hope for its application in the real scenario. The fabricated ASCD demonstrates excellent performance (567 F g^{-1} @ 5 mV sec^{-1}) and could deliver the energy density of 102 Wh kg^{-1} at 1.6 kW kg^{-1} . The energy density is much higher than the best reported supercapacitors and also close to the commercial batteries. This indicates the material could bridge the gap between the commercial batteries and supercapacitors. Superior capacitance retention of 87.4% of its initial C_{sp} was observed after 5000 cycles at a current density of 5 A g^{-1} demonstrates its potential as efficient electrode material for practical applications. All these above observed physicochemical properties make it a potential candidate for the future generation materials for energy storage applications.

References

1. D. H. Jurcakova, M. Kodama, S. Shiraishi, H. Hatori, Z. H. Zhu and G. Q. Lu, Nitrogen-enriched nonporous carbon electrodes with extraordinary supercapacitance, *Adv. Funct. Mater.*, 2009, **19**, 1800-1809.
2. Y. H. Lee, K. H. Chang and C. C. Hu, Differentiate the pseudocapacitance and double-layer capacitance contributions for nitrogen-doped reduced graphene oxide in acidic and alkaline electrolytes, *J. Power Sources*, 2013, **227**, 300-308.
3. M. R. Lukatskaya, B. Dunn and Y. Gogotsi, Multidimensional materials and device architectures for future hybrid energy storage, *Nat. Commun.*, 2016, **7**, DOI:10.1038/ncomms12647.
4. X. Zhan, Z. Chena and Q. Zhang, Recent progress in two-dimensional COFs for energy-related applications, *J. Mater. Chem. A*, 2017, **5**, 14463-14479.
5. W. G. Pell and B. E. Conway, Quantitative modeling of factors determining ragone plots for batteries and electrochemical capacitors, *J. Power Sources*, 1996, **63**, 255-266.
6. K. Lee, D. Kim, Y. Yoon, J. Yang, H. G. Yun, I. K. You and H. Lee, Fast diffusion supercapacitors via an ultra-high pore volume of crumpled 3D structure reduced graphene oxide activation, *RSC Adv.*, 2015, **5**, 60914-60919.
7. K. Lee, Y. Yoon, Y. Cho, S. M. Lee, Y. Shin and H. Lee, Tunable sub-nanopores of graphene flake interlayers with conductive molecular linkers for supercapacitors, *ACS Nano*, 2016, **10**, 6799-6807.
8. A. Zolfaghari, F. Ataherian, M. Ghaemi and A. Gholami, Capacitive behavior of nanostructured MnO_2 prepared by sonochemistry method, *Electrochim. Acta*, 2007, **52**, 2806-2814.
9. Y. F. Nie, Q. Wang, X. Y. Chen and Z. J. Zhang, Nitrogen and oxygen functionalized hollow carbon materials: The capacitive enhancement by simply incorporating novel redox additives into H_2SO_4 electrolyte, *J. Power Sources*, 2016, **320**, 140-152.

10. M. K. Bhunia, S. Melissen, M. R. Parida, P. Sarawade, J. M. Basset, D. H. Anjum, O. F. Mohammed, P. Sautet, T. L. Bahers and K. Takanahe, Dendritic tip-on polytriazine-based carbon nitride photocatalyst with high hydrogen evolution activity, *Chem. Mater.*, 2015, **27**, 8237-8247.
11. L. Lin, H. Ou, Y. Zhang and X. Wang, Tri-s-triazine based crystalline graphitic carbon nitrides for highly efficient hydrogen evolution photocatalysis, *ACS Catal.*, 2016, **6**, 3921-3931.
12. C. Largeot, C. Portet, J. Chmiola, P. L. Taberna, Y. Gogotsi and P. Simon, Relation between the ion size and pore size for an electric double-layer capacitor, *J. Am. Chem. Soc.*, 2008, **130**, 2730-2731.
13. Y. Kou, Y. Xu, Z. Guo and D. Jiang, Supercapacitive energy storage and electric power supply using an aza-fused P-conjugated microporous framework, *Angew. Chem. Int. Ed.*, 2011, **50**, 8753-8757.
14. M. Khattak, Z. A. Ghazi, B. Liang, N. A. Khan, A. Iqbal, L. Li and Z. Tang, A redox-active 2D covalent organic framework with pyridine moieties capable of faradaic energy storage, *J. Mater. Chem., A*, 2016, **4**, 16312-16317.
15. R. DeBlase, K. E. Silberstein, T. T. Truong, H. D. Abruna and W. R. Dichtel, β -Ketoenamine-linked covalent organic frameworks capable of pseudocapacitive energy storage, *J. Am. Chem. Soc.*, 2013, **135**, 16821-16824.
16. C. Patra, S. Khilari, L. Satyanarayan, D. Pradhan and A. Bhaumik, A new benzimidazole based covalent organic polymer having high energy storage capacity, *Chem. Commun.*, 2016, **52**, 7592-7595.
17. H. Wang, Z. Cheng, Y. Liao, J. Li, J. Weber, A. Thomas and C. F. J. Faul, Conjugated microporous polycarbazole networks as precursors for nitrogen-enriched microporous carbons for CO₂ storage and electrochemical capacitors, *Chem. Mater.*, 2017, **29**, 4885-4893.
18. P. Bandyopadhyay, T. Kuila, J. Balamurugan, T. T. Nguyen, N. H. Kim and J. H. Lee, Facile synthesis of novel sulfonated polyaniline functionalized graphene using m-aminobenzene sulfonic acid for asymmetric supercapacitor application, *Chem. Eng. J.*, 2017, **308**, 1174-1184.
19. C. Zhong, Y. Deng, W. Hu, J. Qiao and L. Zhang, A review of electrolyte materials and compositions for electrochemical supercapacitors, *Chem. Soc. Rev.*, 2015, **44**, 7484-7539.
20. M. Beidaghi and Y. Gogotsi, Capacitive energy storage in micro-scale devices: recent advances in design and fabrication of microsupercapacitors, *Energy Environ. Sci.*, 2014, **7**, 867-884.
21. Z. Li, Z. Xu, H. Wang, J. Ding, B. Zahiri, C. M. B. Holt, X. Tan and D. Mitlin, Colossal pseudocapacitance in a high functionality-high surface area carbon anode doubles the energy of an asymmetric supercapacitor, *Energy Environ. Sci.*, 2014, **7**, 1708-1718.
22. R. R. Salunkhe, J. Tang, Y. Kamachi, T. Nakato, J. H. Kim and Y. Yamauchi, Asymmetric supercapacitors using 3D nanoporous carbon and cobalt oxide electrodes synthesized from a single metal-organic framework, *ACS Nano*, 2015, **9**, 6288-6296.
23. J. Yan, Z. Fan, W. Sun, G. Ning, T. Wei, Q. Zhang, R. Zhang, L. Zhi and F. We, Advanced asymmetric supercapacitors based on Ni(OH)₂/graphene and porous graphene electrodes with high energy density, *Adv. Funct. Mater.*, 2012, **22**, 2632-2641.
24. H. B. Li, M. H. Yu, F. X. Wang, P. Liu, Y. Liang, J. Xiao, C. X. Wang, Y. X. Tong and G. W. Yang, Amorphous nickel hydroxide nanospheres with ultrahigh capacitance and energy density as electrochemical pseudocapacitor materials, *Nat. Commun.*, 2013, **4**, 1894, DOI: 10.1038/ncomms2932.
25. Z. Yu, M. McInnis, J. Calderon, S. Seal, L. Zhai and J. Thomas, Functionalized graphene aerogel composites for high-performance asymmetric supercapacitors, *Nano Energy*, 2015, **11**, 611-620.
26. A. Singh and A. Chandra, Significant performance enhancement in asymmetric supercapacitors based on metal oxides carbon nanotubes and neutral aqueous electrolyte, *Sci. Rep.*, 2015, **5**, DOI: 10.1038/srep15551.
27. X. N. Sun, W. Hu, D. Xu, X. Y. Chen, P. Cui, Integration of redox additive in H₂SO₄ solution and the adjustment of potential windows for improving the capacitive performances of supercapacitors, *Ind. Eng. Chem. Res.*, 2017, **56**, 2433-2443.
28. Y. Wang, W. Lai, N. Wang, Z. Jiang, X. Wang, P. Zou, Z. Lin, H. J. Fan, F. Kang, C. P. Wong, C. Yang, Graphene Oxide/Mixed-Valence Manganese oxide composite electrode for tailorable and surface mountable supercapacitors with high capacitance and super-long life, *Energy Environ. Sci.*, 2017, **10**, 941-949.

29. C. Xu, H. Du, B. Li, F. Kang and Y. Zeng, Asymmetric activated carbon-manganese dioxide capacitors in mild aqueous electrolytes containing alkaline-earth cations, *J. Electrochem. Soc.*, 2009, **156**, A435-A441.
30. J. Janek and W. G. Zeier, A solid future for battery development, *Nat. Energy*, 2016, DOI: 10.1038/NENERGY.2016.141.
31. C. Xu, J. Liao, C. Yang, R. Wang, D. Wu, P. Zou, Z. Lin, B. Li, F. Kang and C. P. Wong, An ultrafast, high capacity and superior longevity Ni/Zn battery constructed on nickel nanowire array film, *Nano Energy*, 2016, **30**, 900-908.





CHAPTER-VI

**NENP-1 AS AN ORGANOCATALYST
FOR KNOEVENAGEL REACTION**

6.1. Introduction

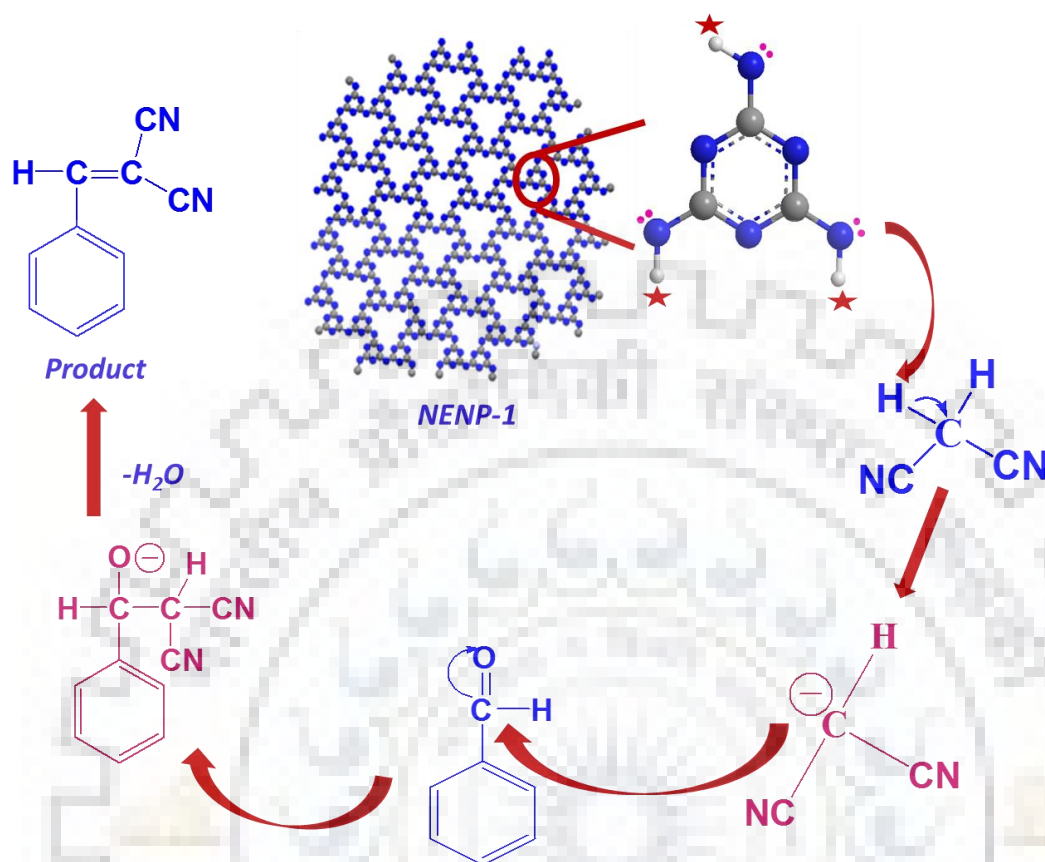
The impressive CO₂ sorption capacity of NENP-1 coupled with the superior electrochemical supercapacitor application have encouraged to use NENP-1 as electron rich entity. Base catalysed organocatalytic conversion of organic molecules using NENP-1 was presumed as one of the best choice and this chapter deals with the use of NENP-1 as an organocatalyst for the Knoevenagel reaction. This reaction deals with the reaction of malononitrile with aromatic aldehydes with high yield as high as ~98% in a very short reaction time of 30 min at room temperature. The mild experimental conditions and use of a number of aromatic aldehydes with a minimum of 85% yield have justified the choice of the catalyst.

6.2. Catalytic activity of NENP-1

Recently, various high surface area microporous materials have been explored as catalysts for different organic transformations.[1-15] The major advantages of these high surface area heterogeneous catalysts are; (i) metal free catalysts hence, no chance of leaching out of metals, and (ii) ease of separation from the product compared to the homogenous catalysts (both metal based catalysts and organocatalysts). The above advantages made these heterogeneous nanoporous polymeric catalysts as safe, green, environmental friendly and cost effective alternatives to produce high quality molecules of significant importance.[16-18] Further, the presence of nitrogen as electron rich entity in some of these materials have shown improved catalytic activities.[2-5] Here, in a model reaction, benzaldehyde (1 mmol) and malononitrile (1 mmol) were reacted in 1:1 volume ratio of dioxane-H₂O (total volume of the reaction mixture is 1 ml) at 25 °C in the presence of 5 mg of NENP-1 and the product was isolated after recrystallization with ethanol (*Scheme 6.1*).

Different experimental parameters such as reaction time, solvents and catalyst amount were varied to find out the optimum yield (*Table 6.1*). The reactions were carried out using tetrahydrofuran (THF), methanol, dioxane and H₂O as co-solvents. It has been observed that a high yield could be achieved in the mixtures of the solvents such as THF-H₂O, methanol-H₂O and dioxane-H₂O at the 1:1 volume ratio. This could be mainly attributed to the better solubility of the reactant molecules in these mixtures of solvents.[17] Moreover, the adsorption of water molecule on the N containing active sites further enhance the basicity of the system. Among these, a maximum yield was obtained in the dioxane-H₂O mixture and hence, used for further investigation. It was documented that a solvent mixture tunes the solubility of the reactants as well control the polarity, which in turn improve the reactivity and product yield by making

available of the active sites on removing the intermediates if any and the products formed.[4,16,18]



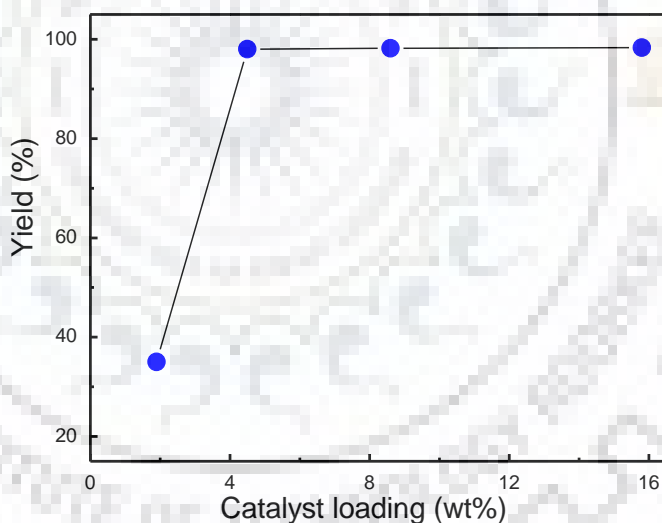
Scheme 6.1. Proposed reaction mechanism for Knoevenagel reaction catalyzed over the metal-free heterogeneous organocatalyst NENP-1.

Effect of catalyst loading is also investigated on the yield of product. It has been observed that a catalyst loading of 4.5 wt% in 1 ml of the dioxane-H₂O mixture (1:1) is ideal for the catalytic conversion of 1 mmol each of the reactants (*Figure 6.1*). A 98% yield could be achieved in a short reaction time of 30 min at 25 °C. To the best of our knowledge, the catalytic efficiency is the best among the reported literatures (*Table 6.2*). The reaction time was further increased to 60 min to check if the yield could be increased. However, there is almost no change in the yield. Moreover, the product yield of 45 and 60% could be achieved within short reaction time of 2 and 5 min, respectively. Thus, 30 min is considered as the ideal reaction time to have an optimum yield. No product formation could be observed in the absence of the catalyst, under the identical experimental condition. The progress of the reaction was continuously monitored by TLC at regular interval. After the completion of the reaction in 30 min the catalyst was separated by filtration and the product was recrystallized using ethanol.

Table 6.1. Catalytic data of the NENP-1 for the model Knoevenagel reaction at various reaction conditions.

Solvent	Volume (ml/ml)	Time (min)	Catalyst amount (wt%)	Yield (%)
THF	1.0/0	30	4.5	37
THF/H ₂ O	0.5/0.5	30	4.5	95
Methanol	1.0/0	30	4.5	85
Methanol/H ₂ O	0.5/0.5	30	4.5	94
Ethanol	1.0/0	30	4.5	87
Ethanol/H ₂ O	0.5/0.5	30	4.5	93
H ₂ O	1.0/0	30	4.5	48
Dioxane	1.0/0	30	4.5	41
Dioxane/H ₂ O	0.5/0.5	30	4.5	98
Dioxane/H ₂ O	0.5/0.5	30	1.9	35
Dioxane/H ₂ O	0.5/0.5	90	1.9	46
Dioxane/H ₂ O	0.5/0.5	30	8.6	98
Dioxane/H ₂ O	0.5/0.5	10	8.6	75
Dioxane/H ₂ O	0.5/0.5	02	4.5	45
Dioxane/H ₂ O	0.5/0.5	05	4.5	60
Dioxane/H ₂ O	0.5/0.5	10	4.5	71

General conditions: Benzaldehyde (1.0 mmol), Malononitrile (1.0 mmol) at 25 °C.

**Figure 6.1.** Effect of catalyst loading on yield (%) of benzyldinmalononitrile.

Spectroscopic investigations such as ¹H and ¹³C NMR, and FTIR confirm the successful conversion of benzaldehyde into α - β unsaturated product as proposed in scheme-1. Absence of the signals due to the carbonyl carbon of the benzaldehyde and CH₂ group of malononitrile in the ¹H and ¹³C NMR spectra [Figure 6.2a & 6.2b] indicate the complete condensation of the reactants to form α - β unsaturated product.[3,4] Moreover, the signal at 7.7(s) ppm in the ¹H NMR attributed to the benzylic hydrogen further confirm the product formation.[3,4]

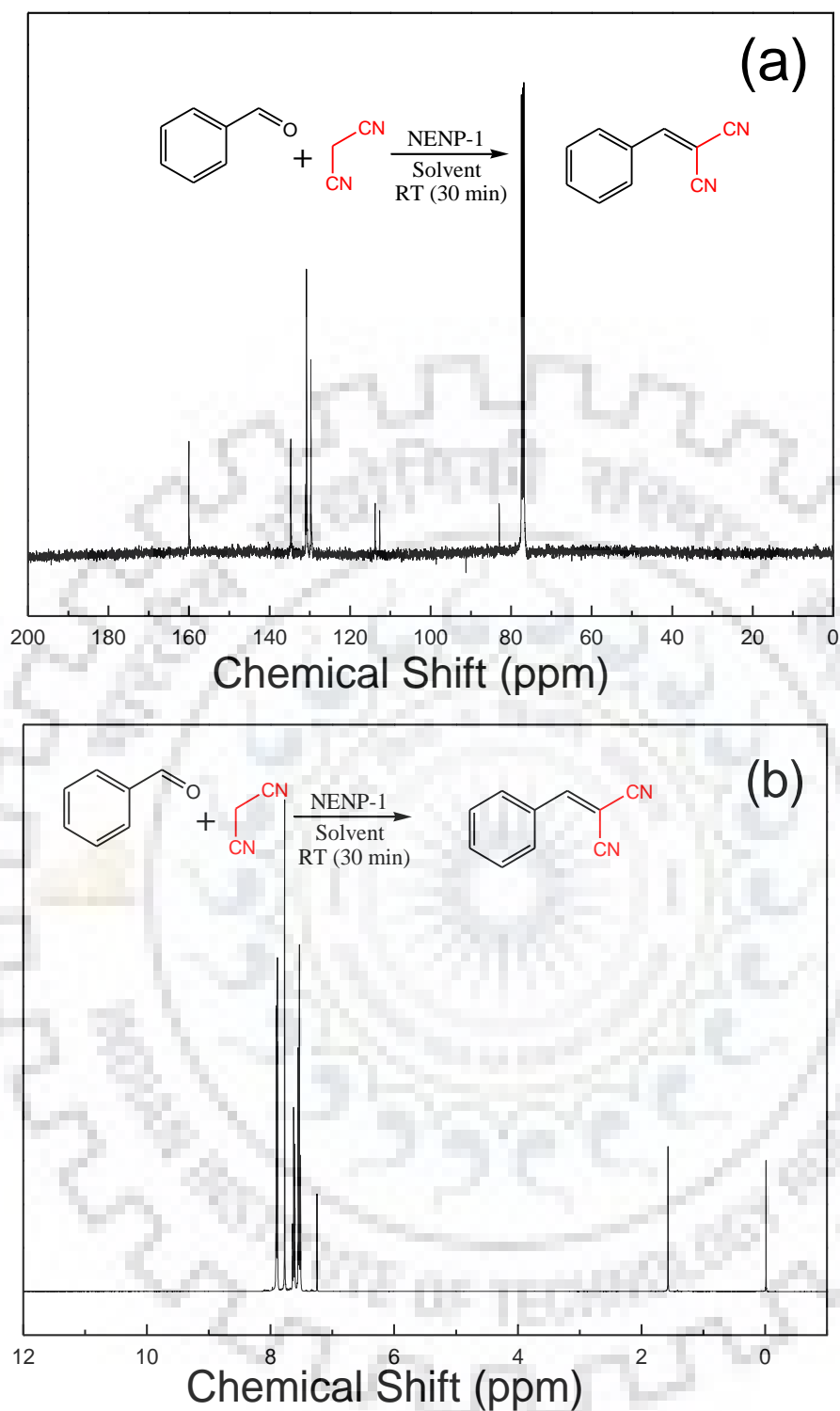


Figure 6.2. NMR spectra: (a) ^{13}C and (b) ^1H NMR spectra of benzylidinemalononitrile.

The FT-IR spectra further corroborate the results obtained from the NMR investigation. The band at 1700 cm^{-1} attributed to the carbonyl group was absent in the product, indicating the condensation of the aldehyde. Furthermore, a new band observed at 2270 cm^{-1} due to the CN stretching vibration confirms the formation of the product (Figure 6.3).[2-4]

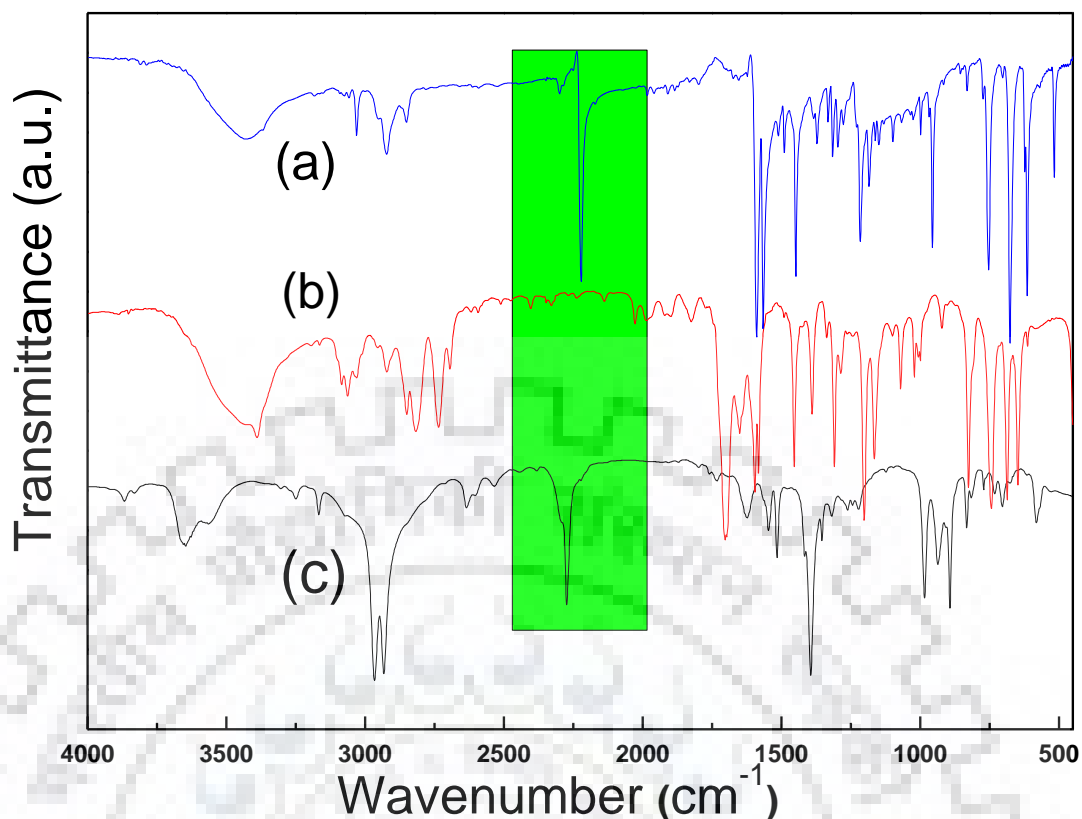


Figure 6.3. FT-IR spectra: (a) Benzyldinmalononitrile, (b) Benzaldehyde and (c) Malononitrile.

Further, the product purity was investigated by GC-MS. The GC chromatograph reveals a single peak at retention time of 15.03 min and the molecular ion peak at m/z of 154 in mass spectrum are in good agreement with molecular weight of product (*Figure 6.4a*). Systematic fragmentation pattern was observed in mass spectral analysis (*Figure 6.4b*). All of the spectral data fairly matched with the literatures.[3-5,14] Thus, the metal-free organocatalyst used in this investigation has shown good performance for the carbon-carbon bond formation using the Knoevenagel reaction.

In order to test the catalyst's activity for multiple cycles which is very much required for industrial scale use, the NENP-1 was employed for the recyclability test for eight consecutive cycles. It is important to note that no loss of activity was observed up to three consecutive cycles and a very minor loss of activity amounting to only ~2% could be seen even up to six cycles (*Figure 6.5*). The yield of 92% could be realized even after eight cycles. This further indicates the superiority of this metal-free catalyst as compared to the metal based catalysts, where leaching of the metal ions during the catalytic activity is a very common problem and a substantial loss of activity could be expected.[1-9]

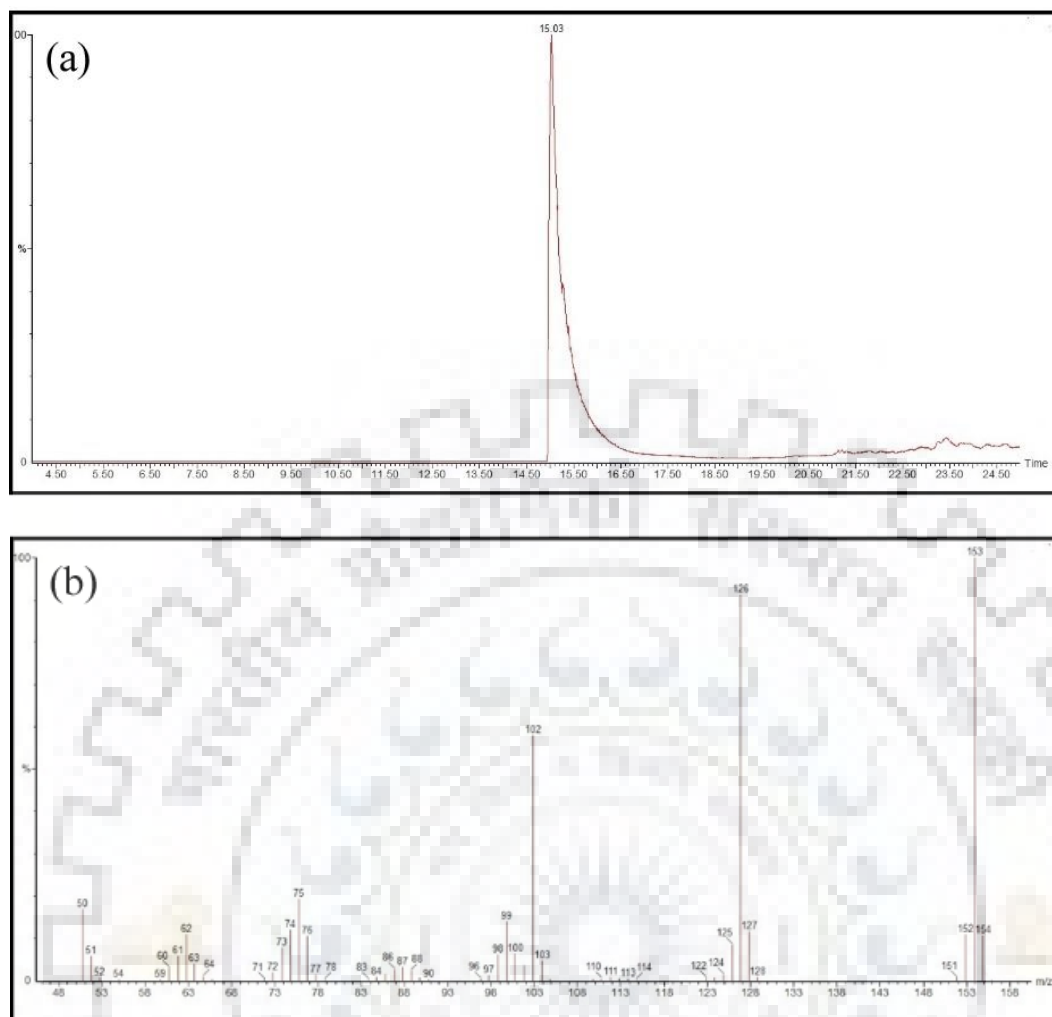


Figure 6.4. (a) GC and (b) MS spectrum of benzylidinemalononitrile.

Table 6.2. Comparison of experimental conditions for the synthesis of metal-free heterogeneous organocatalysts and their catalytic performance in Knoevenagel reaction.

Organocatalysts	Synthesis conditions			Catalysis conditions			Ref.
	Synthesis method	Temp (°C)	Time (h)	Temp. (°C)	Time (min)	Yield (%)	
ZIF-8	Solvothermal method	140	24	25	60	97	1
MCN	Carbonization	550	03	120	12	95	2
MFCMP-1	Oxidative coupling polymerization	60	72	25	240	99	3
MPU	Solvothermal synthesis	150	72	50	840	98	4
g-C ₃ N ₄	Condensation	550	08	40	120	98	10
JUC-Z12	Oxidative cyclodehydrogenation	130	72	25	1440	97	14
BF-COF-1	Schiff base condensation	120	120	25	600	96	19
NENP-1	MW-assisted condensation	140	0.5	25	30	98	Present work

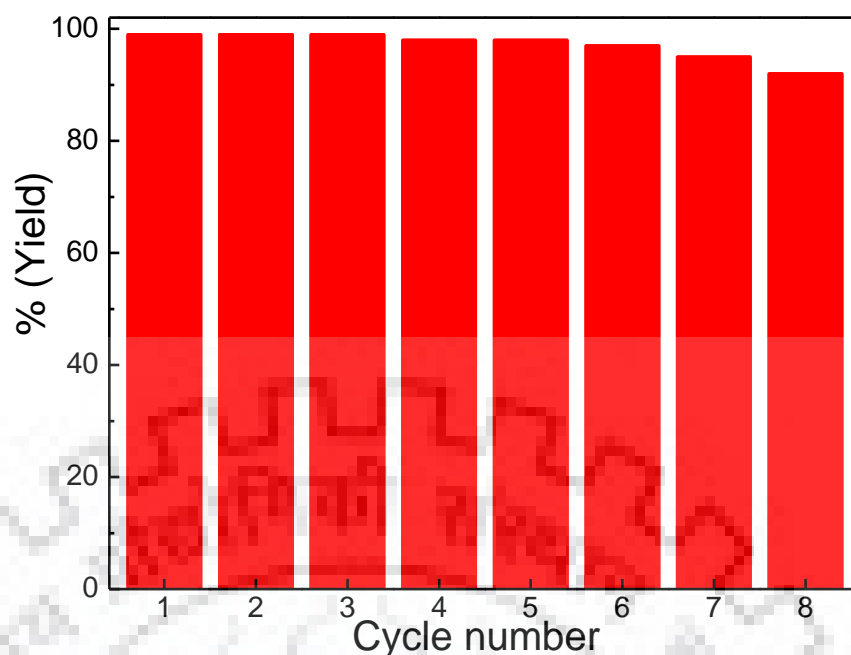


Figure 6.5. Reusability test of catalyst: General conditions; Aromatic aldehyde (1.0 mmol), malononitrile (1.0 mmol) in the presence of 5 mg of NENP-1 in dioxane-H₂O at 25 °C. (% Yield of the isolated product obtained after recrystallization with ethanol).

In order to further investigate if the catalyst could be generalized, various aromatic aldehydes were condensed with malononitrile (*Table 6.3*) and the products of all these reactions were characterized by ¹H NMR, ¹³C NMR and GC-MS (*Figure 6.6 to Figure 6.11*). The superior efficiency of the catalyst could be observed as the minimum 80% yield were realized in a short time span of 30 min for whatever aldehyde may be condensed.

Table 6.3. Catalytic data of the NENP-1 catalysed Knoevenagel reaction with different aromatic aldehydes.

Aldehyde	Active methylene compound	Time (min)	Yield (%)
Benzaldehyde	Malononitrile	30	98
4-Methoxy benzaldehyde	Malononitrile	30	95
3-Methoxy benzaldehyde	Malononitrile	30	92
2-Nitro benzaldehyde	Malononitrile	30	87
4-Nitro benzaldehyde	Malononitrile	30	86
α-Naphthaldehyde	Malononitrile	30	81
4-Bromo benzaldehyde	Malononitrile	30	97
2-Bromo benzaldehyde	Malononitrile	30	96

Reaction conditions: Aromatic aldehyde (1.0 mmol), malononitrile (1.0 mmol) in the presence of 5 mg of NENP-1 in dioxane-H₂O (1:1) at 25 °C.

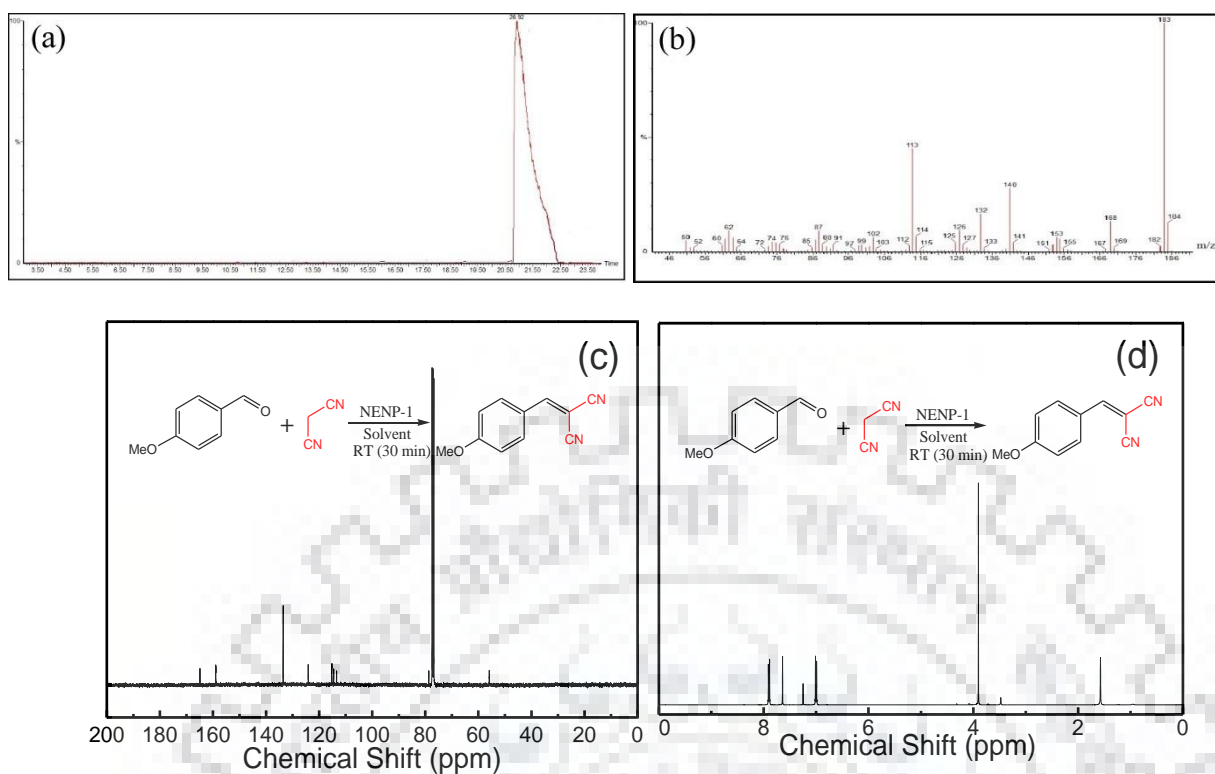


Figure 6.6. (a) GC and (b) MS spectra, (c) ^{13}C and (d) ^1H spectra NMR of 4-methoxybenzylidene malononitrile.

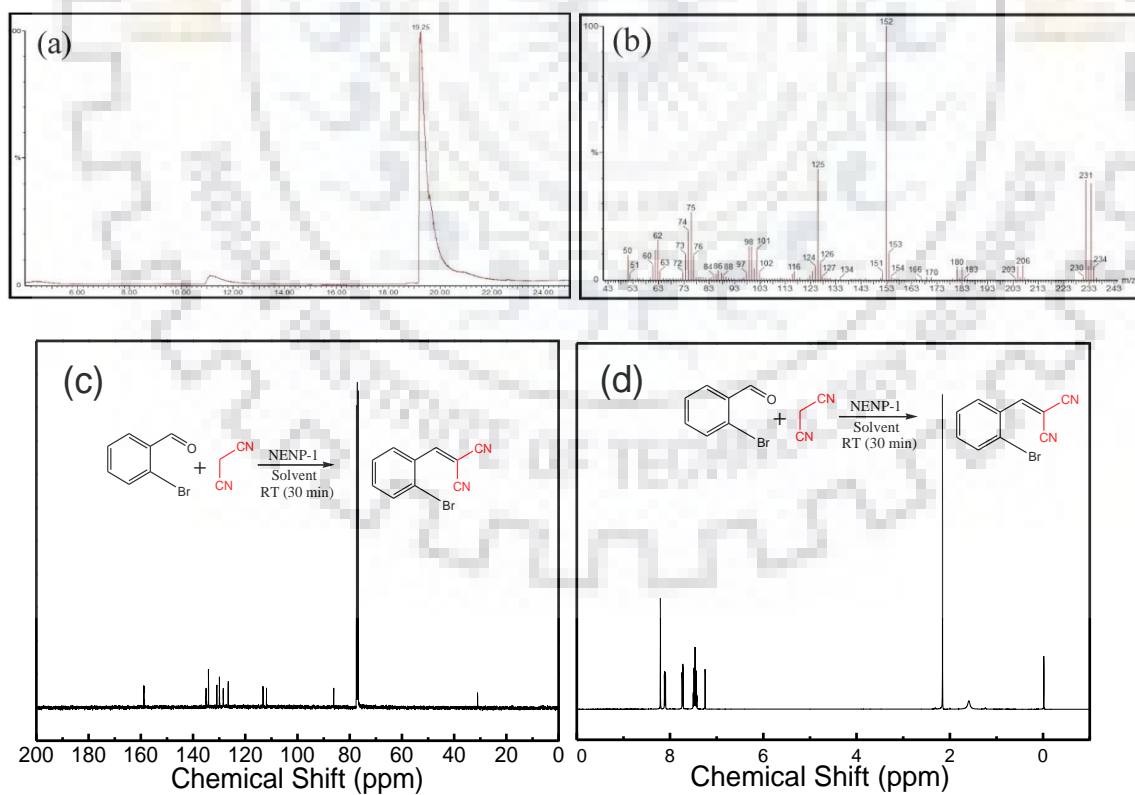


Figure 6.7. (a) GC and (b) MS (c) ^{13}C and (d) ^1H NMR spectra of 2-bromobenzylidene malononitrile.

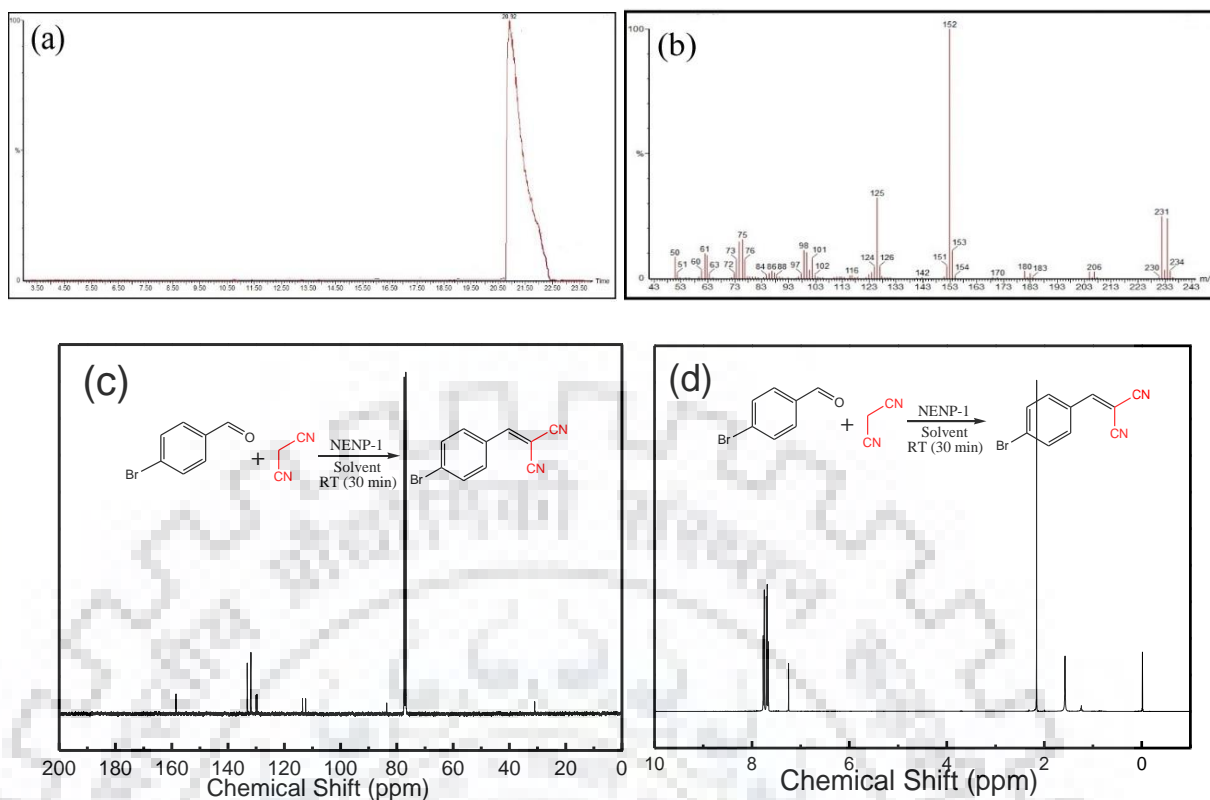


Figure 6.8. (a) GC (b) MS, (c) ¹³C and (d) ¹H NMR spectra of 4-bromobenzylidene malononitrile.

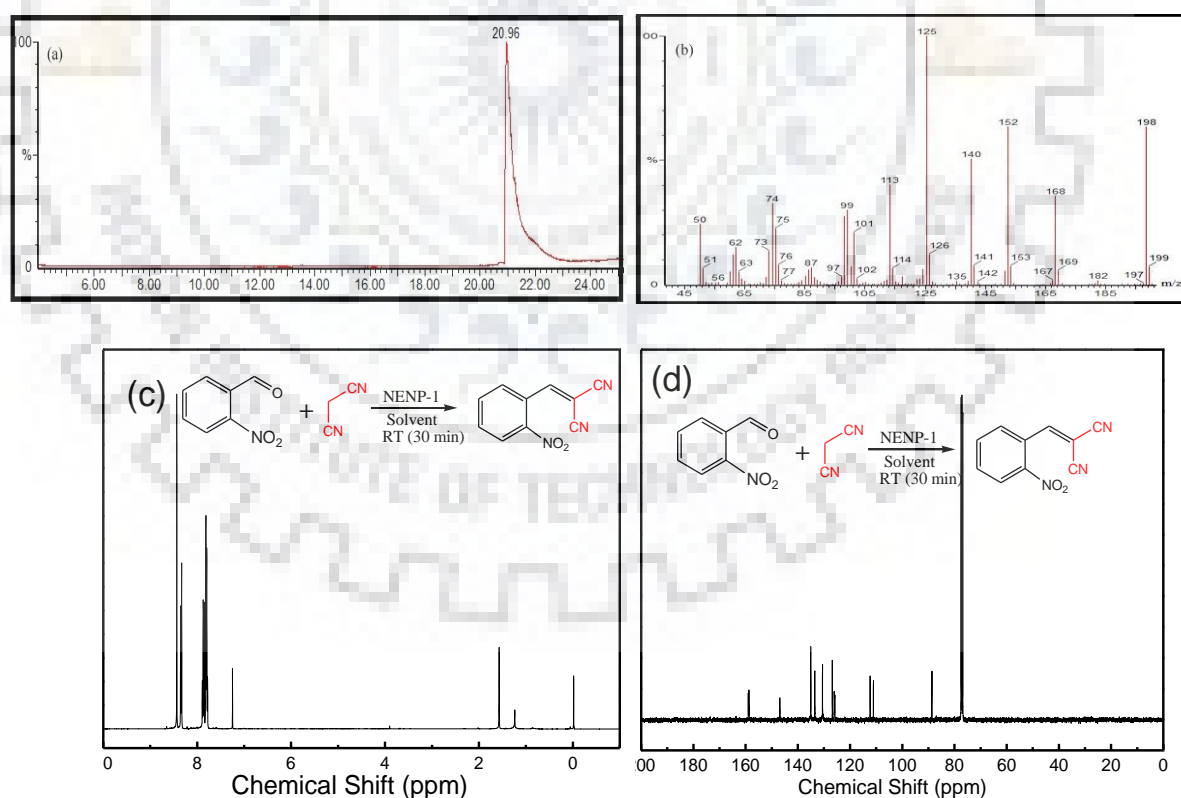


Figure 6.9. (a) GC and (b) MS spectra (c) ¹H and (d) ¹³C NMR spectra of 2-nitrobenzylidene malononitrile

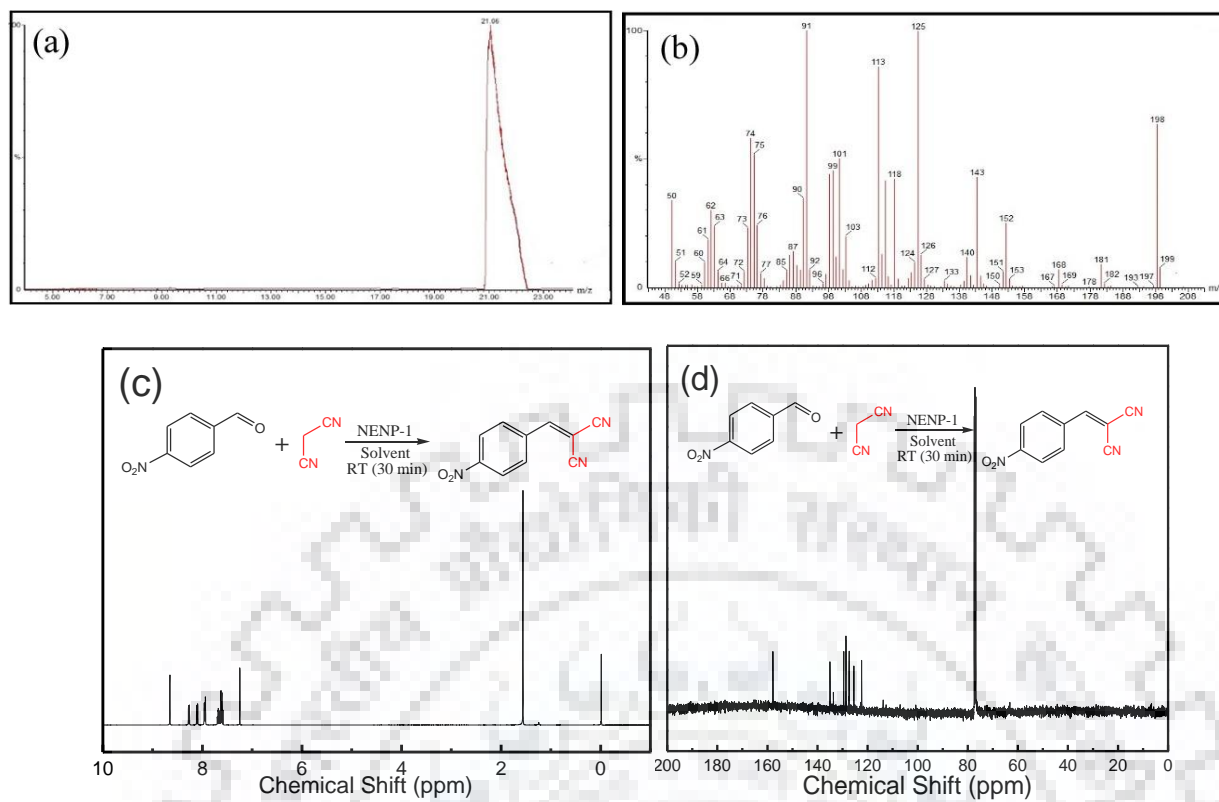


Figure 6.10 (a) GC and (b) MS spectra, (c) ^1H and (d) ^{13}C NMR spectra of 4-nitrobenzylidene malononitrile.

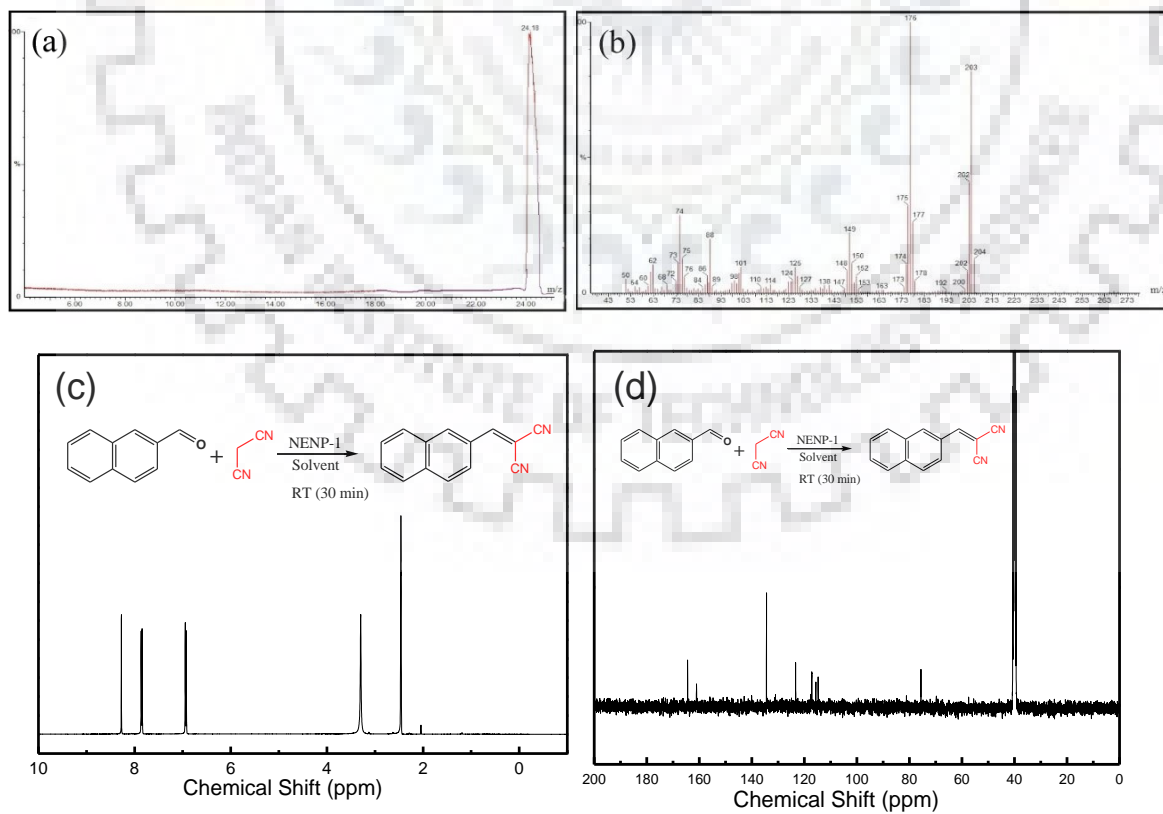


Figure 6.11. (a) GC and (b) MS, (c) ^1H and (d) ^{13}C NMR spectra of α -Naphthaldehyde.

6.3. Summary

In summary, NENP-1 as a high surface area metal-free nitrogen enriched catalyst was used that demonstrates a superior catalytic activity for the Knoevenagel reaction of aromatic aldehydes with malononitrile. The superior catalytic performance could be attributed to the large nitrogen content of 50 wt% in the framework coupled with the controlled textural properties. The formation of a single product with high yield (up to 98%) along with very minor loss on recyclability up to eight cycles, wide substrate adaptability and low cost, make this catalyst as a potential candidate for practical applications.

References

1. U. P. N. Tran, K. K. A. Le and N. T. S. Phan, Expanding applications of metal-organic frameworks: Zeolite imidazolate framework ZIF-8 as an efficient heterogeneous catalyst for the Knoevenagel reaction, *ACS Catal.*, 2011, **1**, 120.
2. M. B. Ansari, H. Jin, M. N. Parvin and S. Park, Mesoporous carbon nitride as a metal-free base catalyst in the microwave assisted Knoevenagel condensation of ethylcyanoacetate with aromatic aldehydes, *Catal. Today*, 2012, **185**, 211-216.
3. P. Puthiaraj, Y. Lee, S. Zhang and W. Ahn, Triazine-based covalent organic polymers: Design, synthesis and applications in heterogeneous catalysis, *J. Mater. Chem. A*, 2016, **4**, 16288-16311.
4. Y. Zhang, S. A. Y. Zou, X. Luo, Z. Li, H. Xia, X. Liu and Y. Mua, Gas uptake, molecular sensing and organocatalytic performances of a multifunctional carbazole-based conjugated microporous polymer, *J. Mater. Chem. A*, 2014, **2**, 13422-13430.
5. S. K. Dey, N. D. S. Amadeu and C. Janiak, Microporous polyurethane material for size selective heterogeneous catalysis of the Knoevenagel reaction, *Chem. Commun.*, 2016, **52**, 7834-7837.
6. R. Muhammad, M. Chaudhary and P. Mohanty, Harnessing electron-rich framework in cyclophosphazene derived hybrid nanoporous materials for organocatalytic C–C bond formation and gas sorption applications, *J. CO₂ Util.*, 2018, **25**, 302-309.
7. D. Elhamifar, S. Kazempoor and B. Karimi, Amine-functionalized ionic liquid-based mesoporous organosilica as a highly efficient nanocatalyst for the Knoevenagel condensation, *Catal. Sci. Technol.*, 2016, **6**, 4318-4326.
8. K. M. Parida, S. Mallick, P. C. Sahoo and S. K. A. Rana, Facile method for synthesis of amine-functionalized mesoporous zirconia and its catalytic evaluation in Knoevenagel condensation, *Appl. Catal., A*, 2010, **381**, 226-232.
9. S. Ren, R. Dawson, A. Laybourn, J. -X. Jiang, Y. Khimyak, D. J. Adams and A. I. Cooper, Functional conjugated microporous polymers: From 1,3,5-benzene to 1,3,5-triazine, *Polym. Chem.*, 2012, **3**, 928-934.
10. L. Zhang, H. Wang, W. Shen, Z. Qin, J. Wang and W. Fan, Controlled synthesis of graphitic carbon nitride and its catalytic properties in Knoevenagel condensations, *J. Catal.*, 2016, **344**, 293-302.
11. P. Puthiaraj, S. S. Kim and W. S. Ahn, Covalent triazine polymers using a cyanuric chloride precursor *via* Friedel-Crafts reaction for CO₂ adsorption/separation, *Chem. Eng. J.*, 2016, **283**, 184-192.
12. L. Jiao, Y. Hu, H. Ju, C. Wang, M. Gao, Q. Yang, J. Zhu, S. Yu and H. Jiang, From covalent triazine-based frameworks to N-doped porous carbon/reduced graphene oxide nanosheets: Efficient electrocatalysts for oxygen reduction, *J. Mater. Chem. A*, 2017, **5**, 23170-23178.

13. I. Janica, V. Patroniak, P. Samor and A. Ciesielski, Imine-based architectures at surfaces and interfaces: From self-assembly to dynamic covalent chemistry in 2D, *Chem. Asian J.*, 2018, **13**, 465-481.
14. B. Liu, T. Ben, J. Xu, F. Deng and S. Qiu, Hydrogen bonding controlled catalysis of a porous organic framework containing benzimidazole moieties, *New J. Chem.*, 2014, **38**, 2292-2299.
15. Y. Zhang and S. N. Riduan, Functional porous organic polymers for heterogeneous catalysis, *Chem. Soc. Rev.*, 2012, **41**, 2083-2094.
16. P. Pollet, E. A. Davey, E. E. U. Benavides, C. A. Eckert and C. L. Liotta, Solvents for sustainable chemical processes, *Green Chem.*, 2014, **16**, 1034-1055.
17. M. Taherimehr, B. V. de Voorde, L. H. Wee, J. A. Martens, D. D. Vos and P. P. Pescarmona, Strategies for enhancing the catalytic performance of metal-organic frameworks in the fixation of CO₂ into cyclic carbonates, *ChemSusChem*, 2017, **10**, 1283-1291.
18. S. K. Kundu and A. Bhaumik, A triazine-based porous organic polymer: A novel heterogeneous basic organocatalyst for facile one-pot synthesis of 2-amino-4H-chromenes, *RSC Adv.*, 2015, **5**, 32730-32739.
19. Q. Fang, S. Gu, J. Zheng, Z. Zhuang, S. Qiu, and Y. Yan, 3D microporous base-functionalized covalent organic frameworks for size-selective catalysis, *Angew. Chem. Int. Ed.*, 2014, **53**, 2878-2882.





CHAPTER-VII

**ADSORPTION OF URANIUM FROM
AQUEOUS SOLUTION AS WELL
AS SEAWATER CONDITIONS
USING NENP-1**

7.1. Introduction

This chapter deals with the discussion of utilizing NENP-1 as an efficient adsorbent for the adsorption of uranium from both aqueous solution and simulated seawater conditions. A maximum adsorption capacity of 489 mg g^{-1} with 97.8% adsorption efficiency was estimated at $25 \text{ }^\circ\text{C}$ and pH of 7 when the adsorption studies were performed in aqueous solution. The recyclability of the NENP-1 for 5 consecutive cycles with the retention of 93% activity was observed. Furthermore, the adsorbent NENP-1 have shown to achieve better than the permissible limits of the WHO (0.015 mg l^{-1}) and USEPA (0.03 mg l^{-1}). Moreover, effective enrichment of uranium from simulated seawater condition by NENP-1 has made this a potential adsorbent for industrial applications.

7.2. Uranium sorption in aqueous solution

Uranium sorption experiments were carried out using a stock solution of 1000 mg l^{-1} of uranium in de-ionized (DI) water [2.11 g of $\text{UO}_2(\text{NO}_3)_2 \cdot 6\text{H}_2\text{O}$ in 1000 ml of DI water]. The equilibrium adsorption capacity and adsorption efficiency were estimated using *equations 7.1 & 7.2* respectively, as given below;

$$q = \frac{(C_0 - C_e)V}{W} \quad (7.1)$$

$$\% E = \frac{(C_0 - C_e)}{C_0} \times 100 \quad (7.2)$$

where, q is the adsorption capacity (mg g^{-1}), C_0 and C_e are the initial and equilibrium concentration of adsorbate (mg l^{-1}), V is the volume of test solution (l), W is the weight of adsorbent (g) and E is the adsorption efficiency (%).

7.3. Uranium batch adsorption studies

Before starting the investigation on the uranium adsorption by the NENP-1, a thorough literature studies on the speciation of uranium ion as a function of pH in the aqueous solution was carried out. It was well documented by several reports that at lower pH of < 4 , UO_2^{2+} is the dominating species in the aqueous solution and its concentration becomes almost zero at a pH greater than 6.[1-6] At $pH \sim 7$, the dominating species is cationic $[(\text{UO}_2)_3(\text{OH})_5]^+$ species both at lower and higher uranium concentration. However, at a higher pH of 8 and above, the neutral species $\text{UO}_2(\text{OH})_2$, and anion species $[\text{UO}_2(\text{OH})_3]^-$ and $[(\text{UO}_2)_3(\text{OH})_7]^-$ are the dominating species.[2-9] Moreover, there may be slight deviation in the concentration of these species at different uranium concentration as reported by Huynh *et al.*[1] In order to understand the feasibility of the adsorbent for the uranium adsorption in aqueous solution, the surface charge of NENP-1 was investigated

by zeta potential measurements. As can be seen in *Figure 7.1a*, the zeta potential (ζ) values varies from positive to negative on increasing the pH values with the isoelectric point reached at the pH of 6.4. Thus, on comparing the speciation of uranium and the ζ -values, it can be expected that a lower pH may not be suitable for the adsorption of uranium by NENP-1 due to the positive charges both at the surface of the adsorbent as well as the dominating species UO_2^{2+} . However, at pH of 6 or 7 we can expect a better adsorption capacity due to the attractive interaction between the negatively charged adsorbent surface and the dominating ion $[(UO_2)_3(OH)_5]^+$. [6-28]

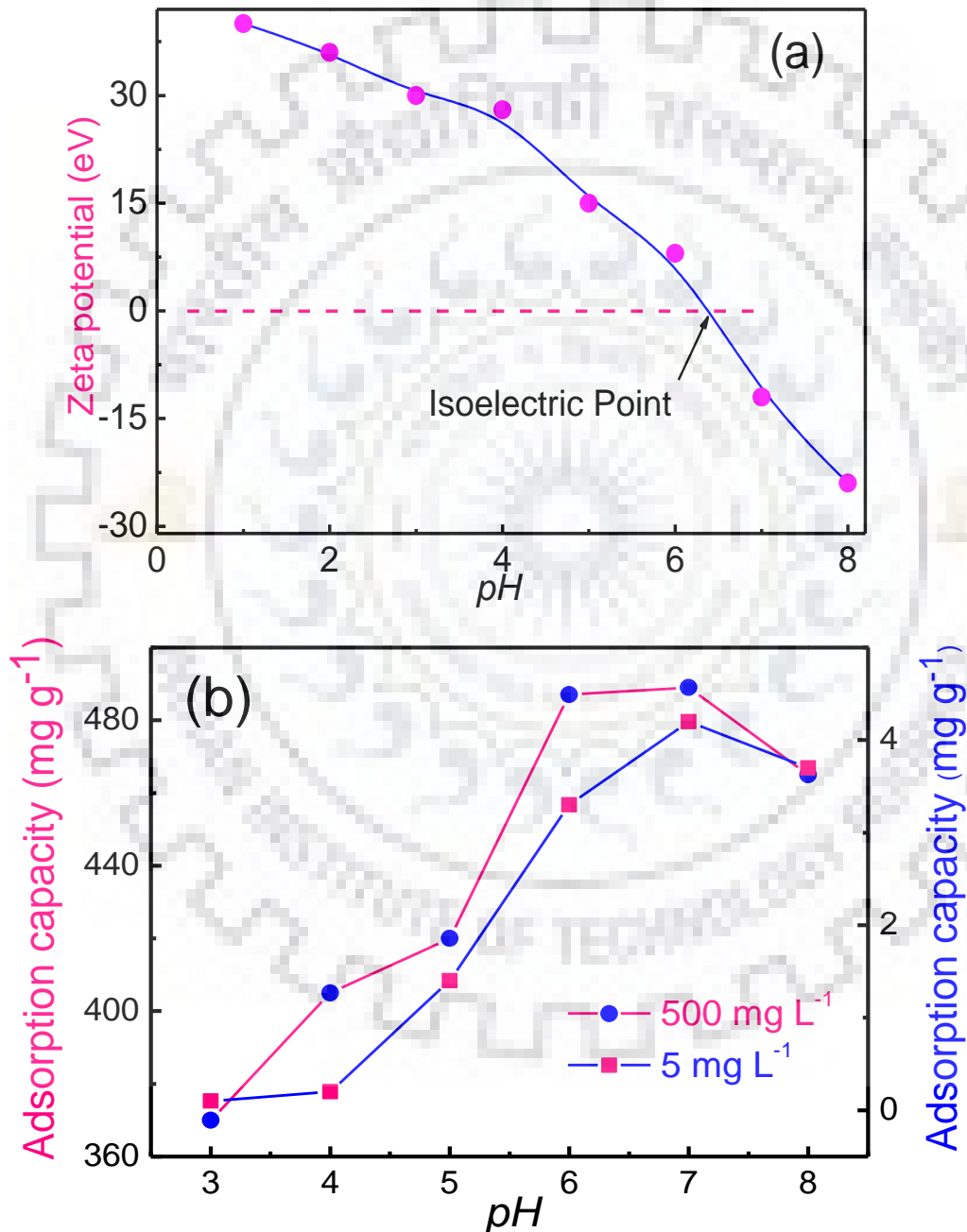


Figure 7.1. (a) Zeta potential of NENP-1 measured at different pH , (b) adsorption capacity vs pH .

In order to support the assumptions, the adsorption of uranium ion was performed at different *pH* values. Moreover, both lower and higher uranium concentrations of 5 and 500 mg l⁻¹ were employed to check the validity. As shown in *Figure 7.1b*, in both the lower and higher uranium concentration, as expected the maximum adsorption capacity was achieved at *pH* of 7 when 10 mg of the adsorbent was introduced to 10 ml of the adsorbate solution. Either increasing or decreasing the *pH* has adversely affected the adsorption capacity. A maximum adsorption capacity of 489 mg g⁻¹ was achieved when the initial concentration of the solution was 500 mg l⁻¹ with an adsorption efficiency of 97.8%. Similarly, at the lower concentration of 5 mg l⁻¹, an adsorption capacity of 4.7 mg g⁻¹ was recorded with the efficiency of 84%. These results indicate the effectiveness of the adsorbent for uranium removal in both lower and higher uranium concentration.

Further, in order to determine the adsorbent amount efficient for the removal of the uranium in the aqueous solution, the adsorption experiments were carried out by varying the adsorbent dosage of 5, 10, 20, 30, 40 and 50 mg with an initial adsorbate concentration of 500 mg l⁻¹. As shown in *Figure 7.2a*, although there was a marginal decrease in the adsorption capacity from 570 to 489 mg g⁻¹ on increasing the adsorbent from 5 to 10 mg, but the substantial increase in the adsorption efficiency from 57 to 97.8% has indicated that 10 mg of adsorbent is ideal for the adsorption experiments. Moreover, on further increasing the adsorbent amount up to 50 mg, no further increase in the adsorption efficiency was observed and rather a substantial decrease in the adsorption capacity could be seen. Thus, an adsorbent amount of 10 mg was chosen as optimum dose for subsequent experiments. The observed adsorption capacity of 489 mg g⁻¹ is better than some of reported porous adsorbents (*Table 7.1*).

The initial adsorbate concentration is another important parameter that determines the effectiveness of an adsorbent. In the present research, concentration of uranium was continuously varied from 5 to 1000 mg l⁻¹ keeping the adsorbent amount fixed at 10 mg. As shown in *Figure 7.2b*, there was a continuous increase in the adsorption capacity on increasing the molar concentration of uranium up to 500 mg l⁻¹, however, there was no appreciable change above this concentration. This indicates that the uranium concentration of 500 mg l⁻¹ is the equilibration concentration and was used to investigate the physical parameters. The effect of contact time on the adsorption capacity provides useful information on the adsorption kinetics. On varying the contact time from 5 to 120 min, a maximum adsorption capacity was achieved at the contact time of 60 min. Further increasing the contact time doesn't improve the adsorption capacity (*Figure 7.2c*). Therefore, 60 min was considered to be the optimum contact time for the efficient

adsorption. The effect of temperature on the adsorption capacity was further studied to estimate the thermodynamics parameters (Figure 7.2d). As expected, the adsorption capacity decreases on increasing the temperature which confirms the exothermic nature of the adsorption process.

Table 7.1. Comparison of adsorption capacities of some reported adsorbents for uranium adsorption from aqueous medium and seawater condition.

Adsorbent	Adsorption conditions	q_{\max} (mg g^{-1})	S_{ABET} ($\text{m}^2 \text{g}^{-1}$)	Ref.
Amino-functionalized SBA-15	$pH = 6$ Time = 30 min. Temp. = 20 °C	573	267	01
Functionalized graphene oxides	$pH = 4$ Time = 48 h Temp. = 20 °C	138	140.8	18
Glutamic acid grafted cellulose	$pH = 5$ Time = 3 h Temp. = 25 °C	168	-	24
Amino acid functionalized chitosan	$pH = 3.6$ Time = 2 h Temp. = 25 °C	116	-	05
Amine-functionalized graphene	$pH = 5.5$ Time = 4 h Temp. = 25 °C	215	-	25
Manganese oxide nanoparticles	$pH = 5.6$ Time = 24 h Temp. = 25 °C	600	-	12
Activated carbon (85c-AO)	Seawater, Time = 24 h Temp. = 25 °C	33	-	27
Activated carbon (85c-AO)	Seawater, Time = 24 h Temp. = 25 °C	29	103	27
Amino-functionalized MOF (1-NH ₂)	Seawater, $pH = 2.5$ Time = 2 h Temp. = 25 °C	0.3	-	6
Amino-functionalized MOF (1-NH ₂)	$pH = 2.5$, Time = 2 h Temp. = 25 °C	95	-	6
NO ₂ modified MOF (1-NO ₂)	$pH = 2.5$ Time = 2 h Temp. = 25 °C	165	-	6
mCMC-g-PANI	$pH = 4.5$ Time = 2 h Temp. = 25 °C	386	0.105	27
MA-TMA	$pH = 4.5$ Time = 2 h Temp. = 25 °C	1028	-	08
Amidoxime-functionalized PAF-1	$pH = 6$ Time = 90 min. Temp. = 25 °C	300	855	10
Amidoxime-functionalized COF material (COF-TpDb-AO)	$pH = 6$ Time = 12 h Temp. = 25 °C	408	826	28
PA/PANI/FeOOH	$pH = 8$ Time = 5 min Temp. = 25 °C	555.8	-	15
P1 zeolites	$pH = 2.5$ Time = 60 min Temp. = 20 °C	100	260	29
4A zeolites	$pH = 2$ Time = 60 min. Temp. = 20 °C	32	350	29
NENP-1	$pH = 6$ Time = 1 h Temp. = 25 °C	489	840	Present work

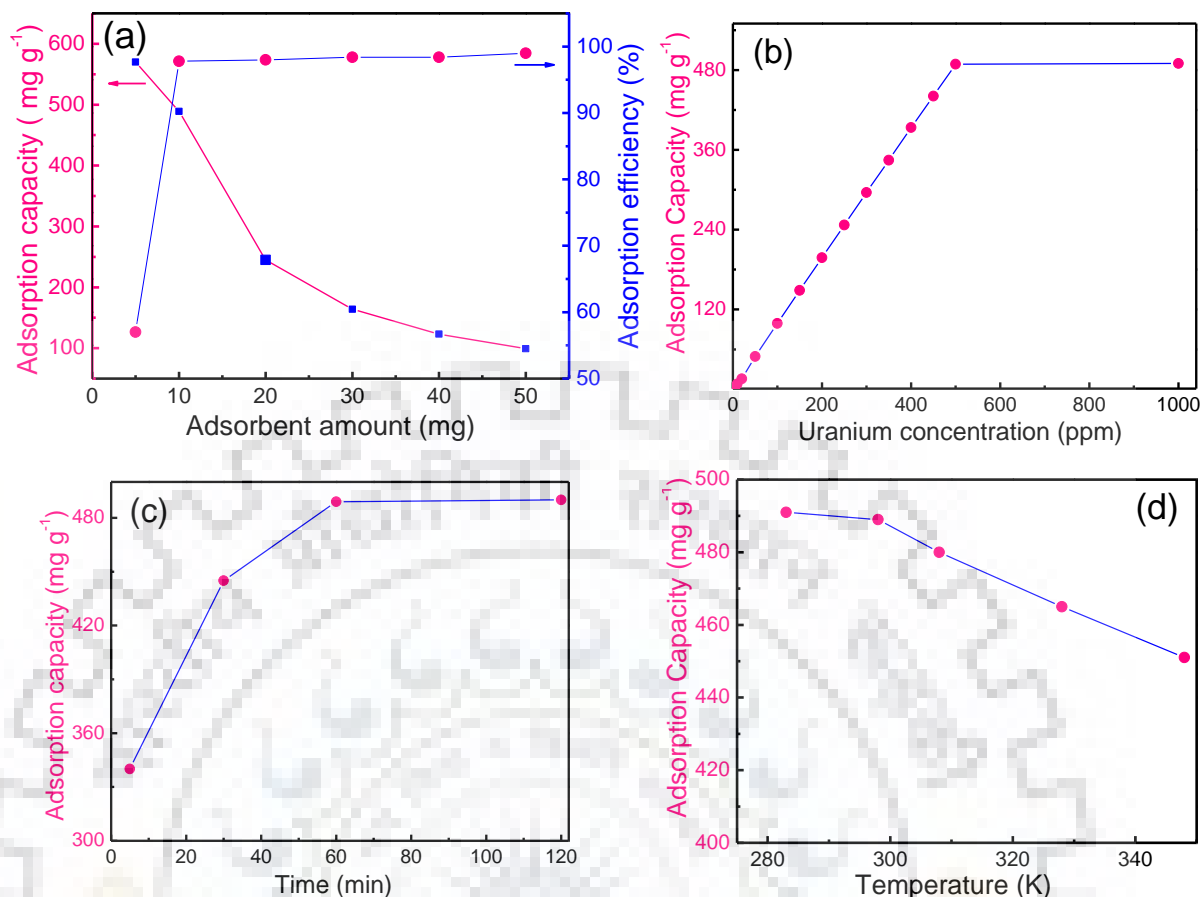


Figure 7.2. Effect on adsorption capacity of NENP-1 with (a) adsorbent amount (b) initial concentration, (c) contact time and (d) temperature.

7.4. Linear and nonlinear methods for equilibrium isotherm analyses and kinetic studies

The linear regression method is one of the most common methods to determine the best-fitted adsorption isotherms and kinetic model. However, the transformation of nonlinear equations to linear forms provide erroneous result in calculated parameters and hence, misrepresent the fit. On the other hand, the nonlinear method is rigorous method and comparatively more complex, and requires an error analysis to evaluate the fit of an equation to the given experimental data. In the present study, the linear and nonlinear regression methods have been compared for the determination of the best-fitted adsorption isotherms and kinetic models. Two isotherms (Langmuir and Freundlich) and two kinetic models (pseudo first order and pseudo second order) have been used. For nonlinear regression method, all the parameters of isotherms and kinetic models were determined using optimization procedure employed in MATLAB[®] software. Three error analysis methods were used in this optimization procedure as well as for comparison with linear method on the basis of goodness-of-fit: coefficient of determination (R^2), residual root mean square error (RMSE) and chi-square (χ^2).

$$R^2 = \frac{\sum (q_{\text{Pred}} - \bar{q}_{\text{exp}})^2}{\sum (q_{\text{Pred}} - \bar{q}_{\text{exp}})^2 + \sum (q_{\text{Pred}} - q_{\text{exp}})^2} \quad (7.3)$$

$$\text{RMSE} = \sqrt{\frac{1}{n-2} \sum_{i=1}^{i=n} (q_{\text{exp}} - q_{\text{pred}})^2} \quad (7.4)$$

$$\chi^2 = \sum \frac{(q_{\text{exp}} - q_{\text{pred}})^2}{q_{\text{exp}}} \quad (7.5)$$

where, q_{exp} is the adsorption capacity obtained from experiment, q_{pred} is the adsorption capacity predicted from the isotherms or kinetic models, \bar{q}_{exp} is the average of q_{exp} and n is the number of experimental observations. Higher R^2 and smaller values of standard errors (RMSE and χ^2) signify the better fitting of the data.

7.5. Adsorption isotherm studies: Among the various models used to study the adsorption isotherms, the Langmuir and Freundlich models were more acceptable and have been extensively used in the literatures.[15-18] Langmuir model assumes the monolayer adsorption while, the Freundlich model defines multilayer adsorption on a heterogeneous system.

The linear and nonlinear forms of Langmuir and Freundlich models are presented in the following equations.[19-21]

$$\text{Langmuir (Linear)} \quad \frac{C_e}{q_e} = \frac{C_e}{q_{\text{max}}} + \frac{1}{q_{\text{max}} b} \quad (7.6)$$

$$\text{Langmuir (Nonlinear)} \quad q_e = \frac{q_{\text{max}} b C_e}{1 + b C_e} \quad (7.7)$$

$$\text{Freundlich (Linear)} \quad \log q_e = \frac{\log C_e}{n} + \log \quad (7.8)$$

$$\text{Freundlich (Nonlinear)} \quad q_e = k_f C_e^{1/n} \quad (7.9)$$

where, q_{max} (mg g^{-1}) is the maximum monolayer adsorption capacity, b is a Langmuir equilibrium constant (l mg^{-1}) which is related to the energy of adsorption, K_f is a Freundlich constant [$\text{mg g}^{-1} (\text{l mg}^{-1})^{1/n}$], and n is the Freundlich exponent (dimensionless) indicating the extent of adsorption and degree of nonlinearity between solution concentration and adsorption.

Linear and nonlinear regression methods were employed for the fitting of linear (Equation 7.6 and 7.8) and nonlinear (Equation 7.7 and 7.9) forms of isotherms to the experimental data and the parameters were calculated (Table 7.2) using these equations. Figure

7.3 illustrates the fitting of different forms of above mentioned isotherms. Among these isotherms, higher R^2 and lower RMSE and χ^2 were observed for Langmuir model in comparison to Freundlich isotherm. When linear and nonlinear methods were compared for Langmuir model, the parameters values obtained by these methods were slightly different.

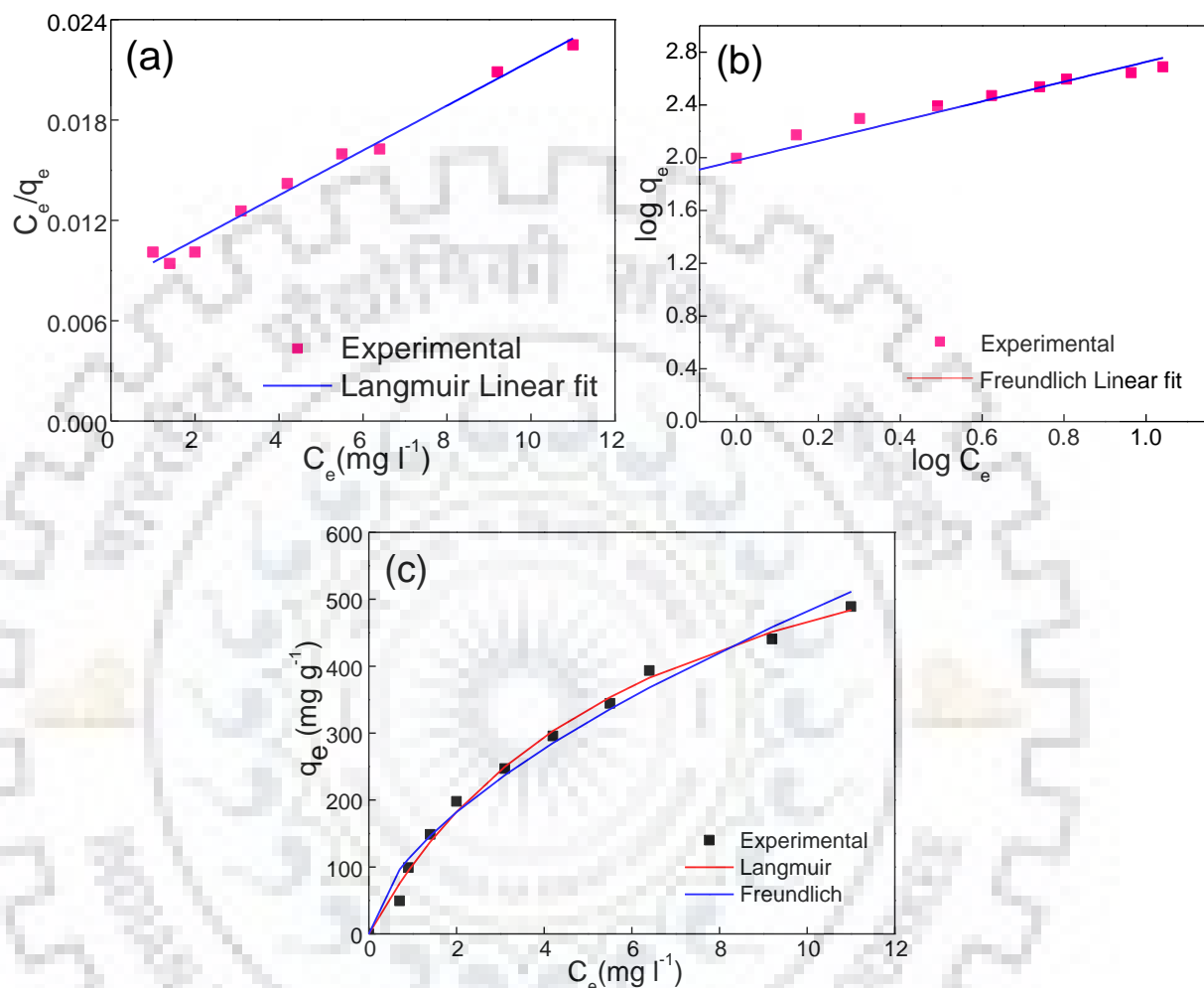


Figure 7.3. (a and b) Linear and (c) nonlinear fittings of Langmuir and Freundlich adsorption isotherms for NENP-1.

However, the error functions indicate a better fitting by non-linear regression method. On the other hand, the parameter values generated by linear and nonlinear methods were different for Freundlich isotherm. This could be attributed to difference in efficiency of both methods as well as limitations of linear regression method. The higher value of R^2 and lower values of RMSE and χ^2 were obtained for nonlinear method. These results show that nonlinear method provides better fitting and therefore better estimation of parameters. Similar result has also been reported by Parimal *et al.* in their study of comparison of linear and nonlinear methods for the fitting of different types of isotherms to experimental data. [22]

Table 7.2. Adsorption parameters and error functions for linear and nonlinear fittings of Langmuir and Freundlich isotherms for removal of uranium.

Models		Langmuir			Freundlich	
		Linear method	Nonlinear method		Linear method	Nonlinear method
Parameters	q_{\max} (mg g ⁻¹)	769.231	758.316	K_f	100.716	121.010
	b (L mg ⁻¹)	0.160	0.158	n	1.584	1.676
Error functions	R^2	0.990	0.994	R^2	0.970	0.980
	RMSE	13.806	12.856	RMSE	22.986	21.921
	χ^2	20.382	17.492	χ^2	48.692	46.525

7.6. Kinetics studies: To predict rate of the adsorption, the kinetic parameters have been calculated by plotting the linear and nonlinear form of pseudo first order and pseudo second order kinetic models as given in following equations.[19-21]

$$\text{Pseudo first order (linear)} \quad \ln(q_{\max} - q_t) = \ln q_{\max} - k_{ad} t \quad (7.10)$$

$$\text{Pseudo first order (nonlinear)} \quad q_t = q_{\max}(1 - e^{-k_{ad}t}) \quad (7.11)$$

$$\text{Pseudo second order (linear)} \quad \frac{t}{q_t} = \frac{1}{k_{ad}q_{\max}^2} + \frac{t}{q_{\max}} \quad (7.12)$$

$$\text{Pseudo second order (nonlinear)} \quad q_t = \frac{k_{ad} q_{\max}^2 t}{1 + k_{ad} q_{\max} t} \quad (7.13)$$

where, q_{\max} , q_t , and k_{ad} are maximum adsorption capacity, adsorption capacity at time t and adsorption rate constant, respectively.

Pseudo first order kinetics assumes that the rate of adsorption depends upon diffusion step. However, according to pseudo second order kinetics, the rate of adsorption depends upon the number of vacancies on adsorbent and mainly controlled by chemical adsorption mechanism.[22,23] *Figure 7.4* depicts the fitting of linear and nonlinear forms of kinetic models to given set of experimental data, and *Table 7.3* summarizes the values of kinetic parameters and error function corresponding to these fittings. Among different forms of kinetics models, the pseudo second order kinetic model exhibits higher R^2 and lower RMSE and χ^2 values as compared to the pseudo first order model. Therefore, the adsorption of uranium follows pseudo second order adsorption process. As observed during isotherms study, the higher value of R^2 and lower values of RMSE and χ^2 were obtained for nonlinear method in both types of kinetic models. Therefore, it can be concluded that nonlinear method provides better fitting and therefore better

estimation of parameters. All these observations support our assumption that the adsorption is mainly due to exchange of electrons between adsorbent and adsorbate.

Table 7.3. Kinetic parameters and error function for linear and nonlinear fitting of pseudo-first order and pseudo-second order kinetics for adsorption of uranium ions

Models	Pseudo first order			Pseudo second order		
		Linear method	Nonlinear method		Linear method	Nonlinear method
Parameters	q_{\max} (mg g ⁻¹)	443.774	468.170	q_{\max} (mg g ⁻¹)	500	491.007
	k_{ad} (min ⁻¹)	0.095	0.258	k_{ad} (g.mg ⁻¹ min ⁻¹)	0.001	0.0009
Error functions	R ²	0.838	0.973	R ²	0.988	0.992
	RMSE	82.607	23.482	RMSE	20.479	16.121
	χ^2	96.442	6.204	χ^2	5.049	2.972

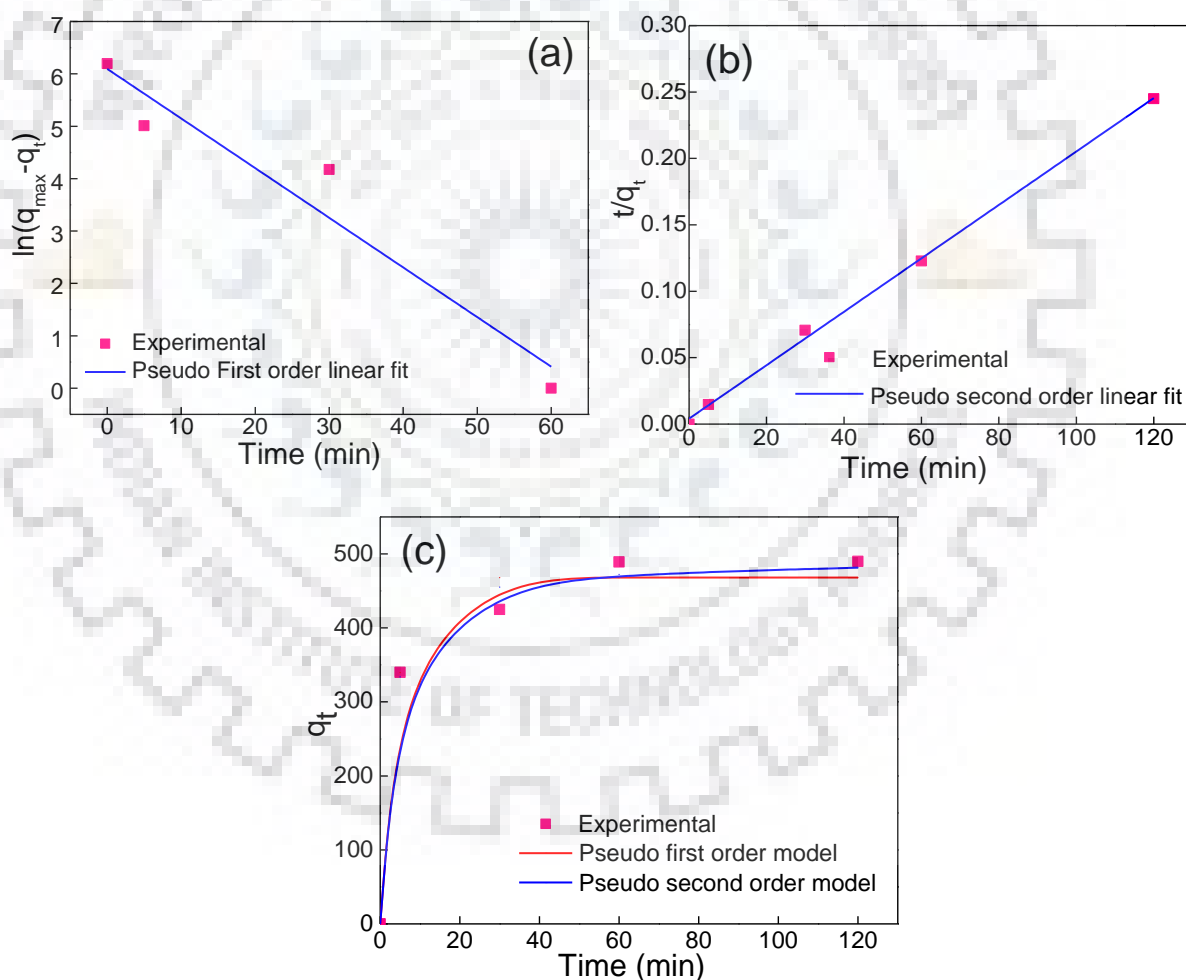


Figure 7.4. (a and b) Linear and (c) nonlinear fittings of pseudo first order and pseudo second order kinetics for the adsorption of uranium.

7.7. Thermodynamic studies: To get the better understanding of thermodynamics of the adsorption process, the thermodynamics parameters like ΔH and ΔS were calculated using the following equations; [15,17]

$$k_d = \frac{q_e}{C_e} \quad (7.14)$$

$$\ln(k_d) = \frac{\Delta S}{R} - \frac{\Delta H}{RT} \quad (7.15)$$

$$\Delta G = -RT\ln(k_d) \quad (7.16)$$

where, R , T and k_d are universal gas constant, temperature (K) and distribution coefficient, respectively (Figure 7.5). The values for ΔS and ΔH were estimated to be $-52.08 \text{ J mol}^{-1} \text{ K}^{-1}$ and $-24.37 \text{ kJ mol}^{-1}$, respectively. Negative ΔH value confirms the exothermic nature of adsorption process. Moreover, it is well known that for pure physical adsorption, the value of ΔH lies below -20 kJ mol^{-1} . [15] As the estimated ΔH value is marginally higher than the pure physisorption, the conclusion derived from the kinetic study was again supported by the thermodynamic investigation. Moreover, negative ΔS value specifies that randomness decreased at the adsorbent and adsorbate interface during the adsorption process. The ΔG values calculated by using Equation 9, were found to be -9.40 , -9.40 , -8.13 , -7.05 and $-6.35 \text{ kJ mol}^{-1}$ at 5 , 25 , 35 , 55 and 75 °C, respectively. The negative values indicate that the adsorption process is spontaneous in nature.

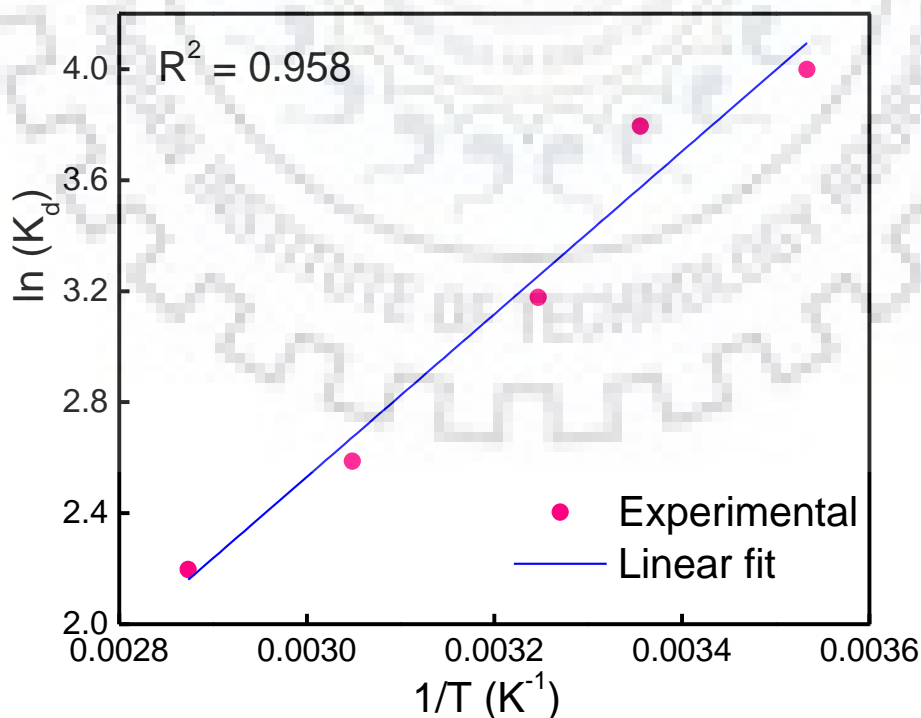
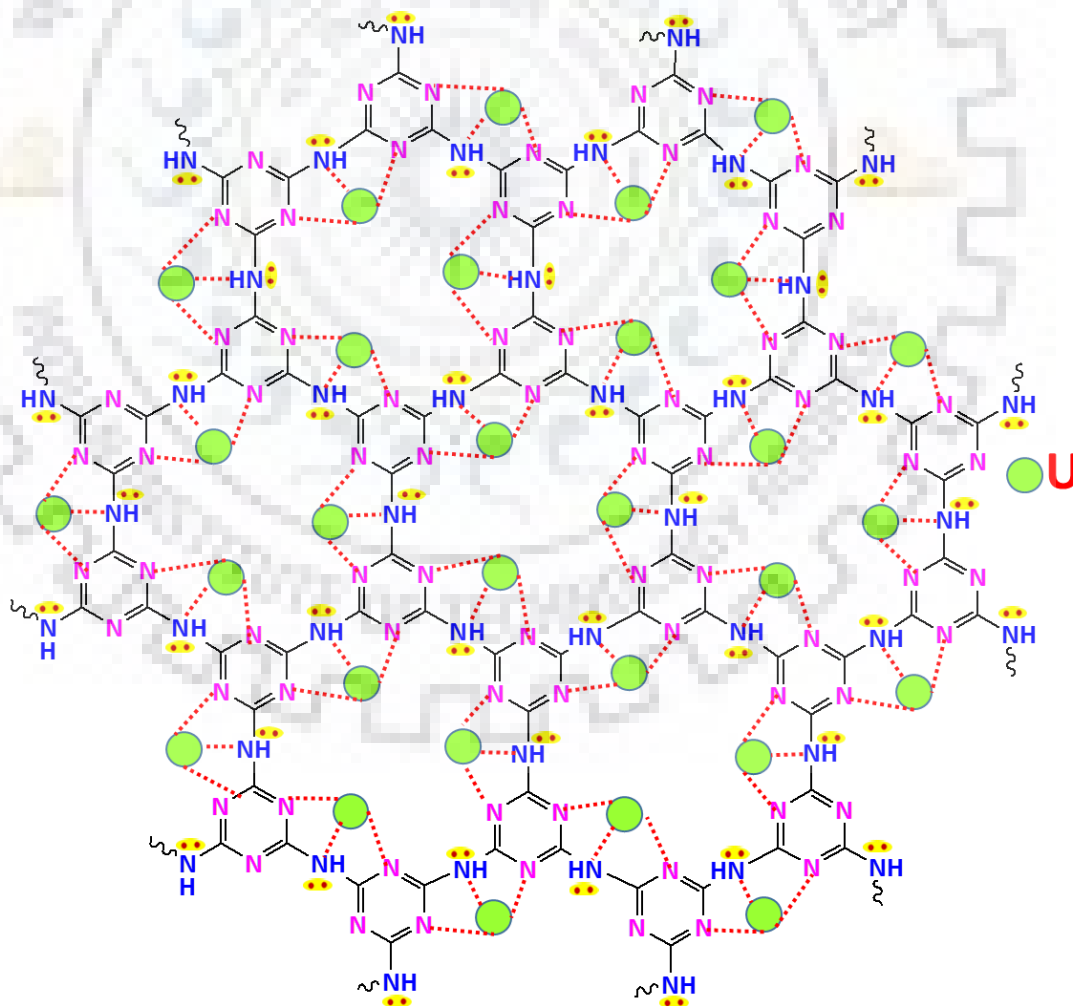


Figure 7.5. Plot of $\ln(k_d)$ v/s $1/T$ for adsorption of uranium.

7.8. Proposed mechanism

In order to understand the interaction that leads to a higher uranium adsorption, XPS analysis of the specimen after uranium adsorption (NENP-1U) was carried out and compared with the pristine sample (*Figure 7.6*). It can be seen from *Figure 7.6c* that the N 1s of the nitrogen from the triazine ring has shifted from 398.3 eV to a higher binding energy of 398.6 eV and the N 1s of the NH group has shifted from 399.6 to 400.1 eV. This indicates that the electron density of the electron rich NENP-1 has interacted with the positively charged uranium ion. This was further confirmed from the C 1s spectra, where a shift in the binding energy of the carbon in the triazine ring from 286.4 to 286.5 eV was recorded and leaving C1s peaks from other carbons unchanged (*Figure 7.6b*). Such shifts in the binding energy of different elements in the XPS spectra were also earlier reported by several research groups.[8,12,13,25] A schematic representation of the interaction of the uranium ion with the pore surface is proposed in *Scheme 7.1*. The quantitative EDAX analysis confirms the presence of uranium (*Table 7.4 & 7.5*). Further, the EDAX mapping indicates a uniform distribution of the uranium throughout the specimen as shown in *Figure 7.7*.



Scheme 7.1. Schematic presentation of interaction mechanism of uranium in the NENP-1.

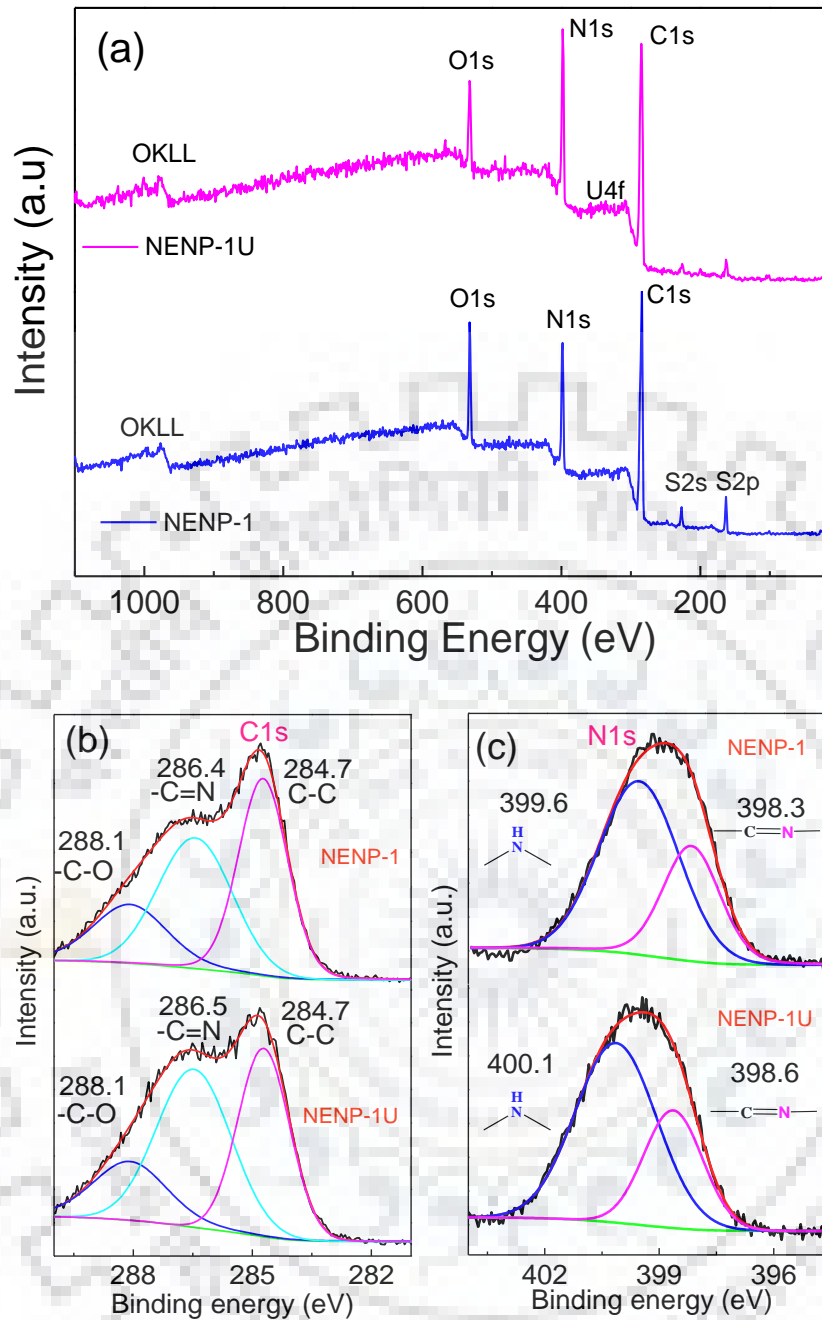


Figure 7.6. (a) Survey scan (Su 1s) XPS spectra of NENP-1 and NENP-1U (b) high resolution C 1s (b) N 1s XPS spectra, before and after uranium adsorption, respectively.

7.9. Reusability of the adsorbent

For practical application of the adsorbents, it is very much important to investigate the adsorption recyclability as it is significant for an effective and economical adsorption process. Here in, reusability of the adsorbent was investigated by performing five consecutive adsorption-desorption cycles (*Figure 7.8*). It is important to note that even after five consecutive cycles, the remarkable adsorption efficiency of 93% was retained, which further signifies its applicability as a superior adsorbent for uranium removal from industrial effluent.

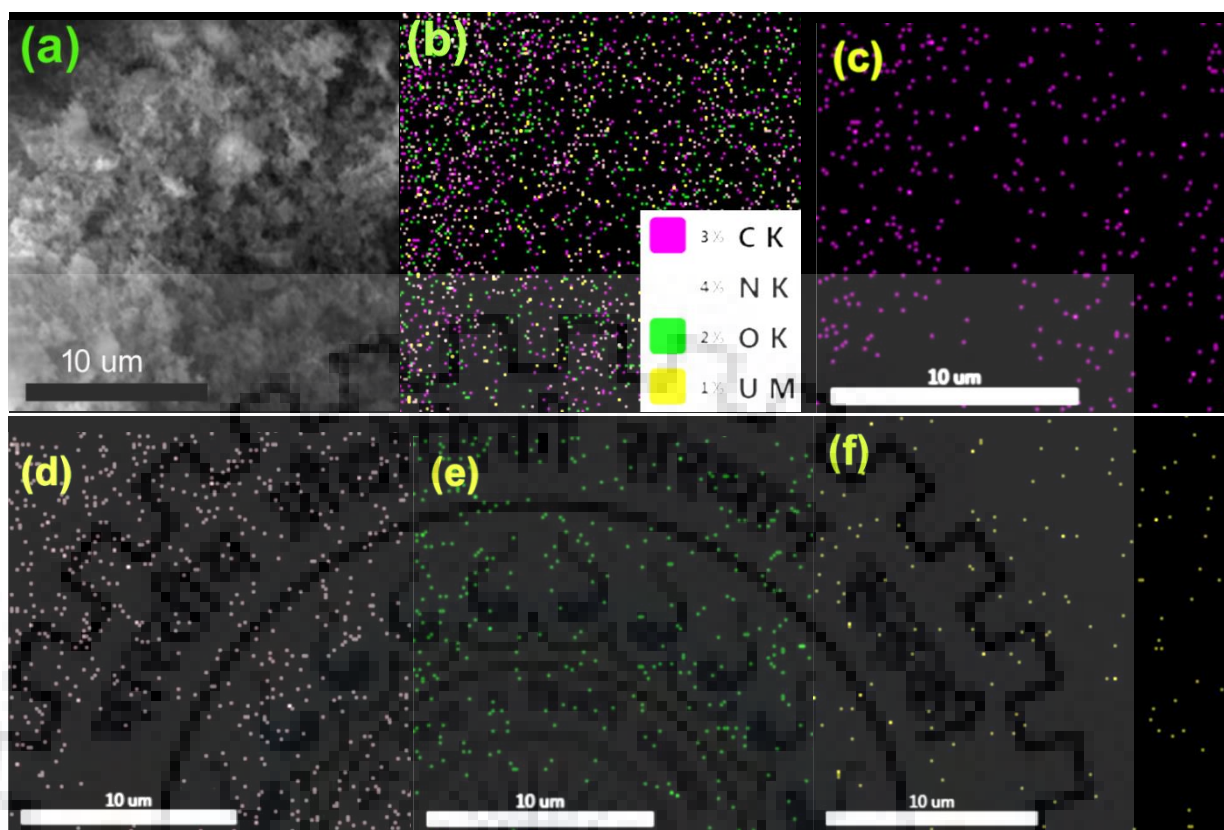


Figure 7.7. (a) FE-SEM (b) EDAX mapping and spatial distribution of (c) C (d) N (e) O (f) U after adsorption in NENP-1U, respectively.

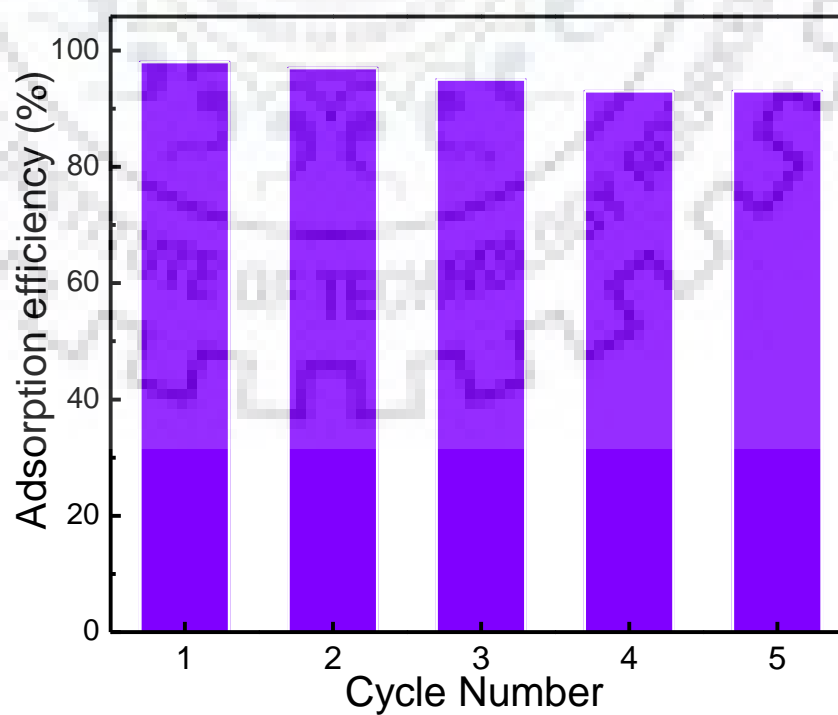


Figure 7.8. Recyclability test of NENP-1 for the adsorption of uranium.

7.10. Achieving the WHO and USEPA permissible limits

The high adsorption capacity and efficiency, along with the recyclability of the adsorbent is very important for practical applications. These have been achieved using the NENP-1 as adsorbent as discussed above. However, another important parameter that can be the bottleneck in using the adsorbent for practical applications is the effectiveness of the adsorbent for removing the uranium from the industrial effluent to an extent that satisfy the permissible limits of two of the major organizations, WHO and USEPA. As the uranium concentration in most of the effluents lies below 5 mg l^{-1} , a thorough investigation has been carried out at a lower uranium concentration of 5 mg l^{-1} . As expected, the isotherms (*Figure 7.9*) and kinetics (*Figure 7.10* and *Table 7.6*) of the adsorption followed the same trend also at a lower concentration of 5 mg l^{-1} . However, there was a substantial difference in the adsorption efficiency. Unlike for 500 mg l^{-1} solution where the maximum adsorption efficiency was achieved when 10 mg of the adsorbent was introduced, at a lower concentration of 5 mg l^{-1} as shown in *Figure 7.9*, there was a continuous increase in the adsorption efficiency recorded up to 99.8% for the 50 mg of the adsorbent. This leads to almost complete adsorption of the uranium leaving only 0.012 mg l^{-1} in the solution, which is below the WHO limit of 0.015 mg l^{-1} and USEPA limit of 0.03 mg l^{-1} .

Table 7.4. Elemental composition of NENP-1 observed by EDAX.

Element	Weight %	Atomic %	Net Int.	Net Int. Error
C K	23.36	26.23	66	0.03
N K	76.64	73.77	83.6	0.02

Table 7.5. Elemental composition of NENP-1U observed by EDAX.

Element	Weight %	Atomic %	Net Int.	Net Int. Error
C K	15.3	18.44	41.4	0.04
N K	46.16	47.7	71	0.03
O K	37.34	33.78	50.4	0.04
U M	1.19	0.07	5.2	0.03

Table 7.6. Kinetic parameters for pseudo-first order and pseudo-second order kinetics.

Pseudo-first order			Pseudo-second order		
R ²	k ₁ (min ⁻¹)	q _e (mg g ⁻¹)	R ²	k ₂ (g/(mg.min))	q _e (mg g ⁻¹)
0.886	0.0655	3.21	0.997	0.0432	4.44

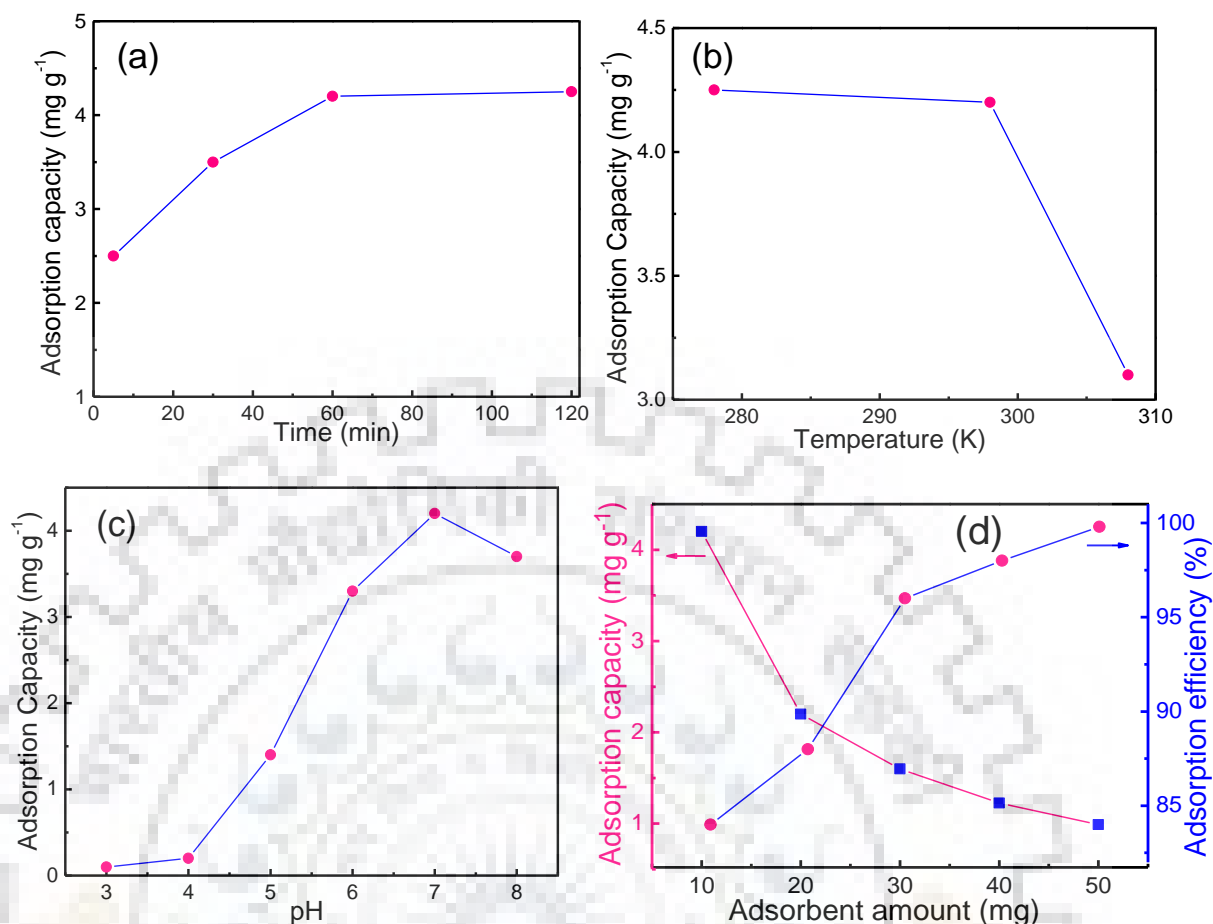


Figure 7.9. Variation of adsorption capacity as a function of (a) time, (b) temperature and (c) pH ($C_0 = 5 \text{ mg l}^{-1}$, adsorbent amount = 10 mg) and (d) adsorption capacity and adsorption efficiency of NENP-1 as a function of adsorbent amount at C_0 of 5 mg l^{-1} .

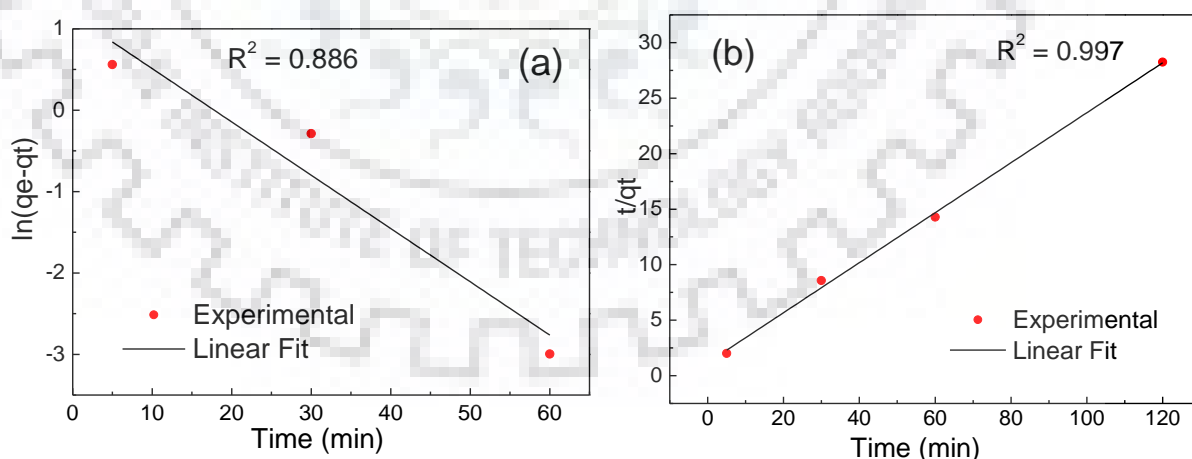


Figure 7.10. (a) Pseudo first order and (b) pseudo second order kinetics for the adsorption of uranium ($C_0 = 5 \text{ mg l}^{-1}$).

7.11. Adsorption studies in simulated seawater condition

Uranium enrichment from seawater using suitable adsorbent is of great significance for resource sustainability and environmental safety concerns. It has been observed that uranium adsorption capacity of 50 mg g^{-1} could be achieved using NENP-1 as an adsorbent under seawater conditions, when 50 mg of NENP-1 is introduced into 200 ml of simulated seawater with contact time of 24 h. Herein, high adsorption capacity and high affinity of NENP-1 towards uranium species makes the material an attractive adsorbent for uranium recovery in saline water conditions.

7.12. Summary

The NENP-1, a nitrogen enriched (N of ~50 wt%) polytriazine with S_{ABET} of $840 \text{ m}^2 \text{ g}^{-1}$ and hierarchical pore structure, has been used as an adsorbent for the removal of uranium from aqueous solution and simulated seawater. Remarkable adsorption capacity of 489 mg g^{-1} and adsorption efficiency of 97.8% were recorded at $25 \text{ }^\circ\text{C}$ and at a pH of 7 in aqueous medium. The recyclability up to five consecutive cycles has shown a remarkable retention of adsorption efficiency of 93%. The efficiency of the adsorbent both at higher and lower uranium concentration of 500 and 5 mg l^{-1} , respectively, have made this adsorbent a good candidate for practical applications. In this direction, the efficient adsorption of uranium at a lower initial concentration of 5 mg l^{-1} by the adsorbent NENP-1 leaving behind a concentration that is better than the permissible limits of the WHO and USEPA have made it stand out among its peer. Thus, based on the experimental outcome and thorough literature investigation, it can be concluded that the NENP-1 could be used as a superior adsorbent for removal of uranium from industrial effluents as well as seawater conditions leading to address the environmental concern of the nuclear power plant effluents as well as reusability of the collected uranium from seawater.

References

1. J. Huynh, R. Palacio, F. Safizadeh, G. Lefevre, M. Descostes, L. Eloy, N. Guignard, J. Rousseau, S. Royer, E. Tertre and I. Batonneau-Gener, Adsorption of uranium over NH_2 -functionalized ordered silica in aqueous solutions, *ACS Appl. Mater. Interfaces*, 2017, **9**, 15672-15684.
2. S. Verma and R. K. Dutta, A Facile method of synthesizing ammonia modified graphene oxide for efficient removal of uranyl ions from aqueous medium, *RSC Adv.*, 2015, **5**, 77192-77203.
3. X. Liu, J. Li, X. Wang, C. Chen and X. Wang, high performance of phosphate-functionalized graphene oxide for the selective adsorption of U(VI) from acidic solution, *J. Nucl. Mater.*, 2015, **466**, 56-64.
4. L. Chen, Z. Bai, L. Zhu, L. Zhang, Y. Cai, Y. Li, W. Liu, Y. Wang, L. Chen, J. Diwu, J. Wang, Z. Chai and S. Wang, Ultrafast and efficient extraction of uranium from seawater using an amidoxime appended metal-organic framework, *ACS Appl. Mater. Interfaces*, 2017, **9**, 32446-32451.

5. A. A. Galhoum, M. G. Mahfouz, A. A. Atia, S. T. Abdel-Rehem and N. A. Gomaa, T. Vincent and E. Guibal, Amino acid functionalized chitosan magnetic nanobased particles for uranyl sorption, *Ind. Eng. Chem. Res.*, 2015, **54**, 12374-12385.
6. L. L. Song, C. Chen, F. Luo, S. Y. Huang, L. L. Wang and N. Zhang, Isoreticular MOFs functionalized in the pore wall by different organic groups for high-performance removal of uranyl ions, *J. Radioanal. Nucl. Chem.*, 2016, **310**, 317-327.
7. L. Lin, H. Ou, Y. Zhang and X. Wang, Tri-s-triazine based crystalline graphitic carbon nitrides for highly efficient hydrogen evolution photocatalysis, *ACS. Catal.*, 2016, **6**, 3921-3931.
8. B. Li, C. Bai, S. Zhang, X. Zhao, Y. Li, L. Wang, K. Ding, X. Shu, S. Li and L. Ma, An adaptive supramolecular organic framework for highly efficient separation of uranium via an in situ induced fit mechanism, *J. Mater. Chem. A*, 2015, **3**, 23788-23798.
9. S. Yang, J. Qian, L. Kuang and D. Hua, Ion-imprinted mesoporous silica for selective removal of uranium from highly acidic and radioactive effluent, *ACS Appl. Mater. Interfaces*, 2017, **9** 29337-29344.
10. B. Li, Q. Sun, Y. Zhang, C. W. Abney, B. Aguila, W. Lin and S. Ma, Functionalized porous aromatic framework for efficient uranium adsorption from aqueous solutions, *ACS Appl. Mater. Interfaces*, 2017, **9**, 12511-12517.
11. S. Ma, L. Huang, L. Ma, Y. Shim, S. M. Islam, P. Wang, L. D. Zhao, S. Wang, G. Sun, X. Yang and M. G. Kanatzidis, efficient uranium capture by polysulfide/layered double hydroxide composites, *J. Am. Chem. Soc.*, 2015, **137**, 3670-3677.
12. S. S. Lee, W. Li, C. Kim, M. Cho, J. G. Catalano, B. J. Lafferty, P. Decuzzi and J. D. Fortner, Engineered manganese oxide nanocrystals for enhanced uranyl sorption and separation, *Environ. Sci.: Nano*, 2015, **2**, 500-508.
13. C. Gunathilake, J. Gorka, S. Dai and M. Jaroniec, Amidoxime-modified mesoporous silica for uranium adsorption under seawater conditions, *J. Mater. Chem. A*, 2015, **3**, 11650-11659.
14. P. Rekha, V. Sharma and P. Mohanty, Synthesis of cyclophosphazene bridged mesoporous organosilicas for CO₂ capture and Cr (VI) removal, *Microporous Mesoporous Mater.*, 2016, **219**, 93-102.
15. X. Wei, Q. Liu, H. Zhang, J. Liu, R. Chen, R. Li, Z. Li, P. Liu and J. Wang, Rapid and efficient uranium (VI) capture by phytic acid/polyaniline/FeOOH composites, *J. Colloid Interface Sci.*, 2018, **511**, 1-11.
16. P. Rekha, R. Muhammad and P. Mohanty, Sonochemical synthesis of cyclophosphazene bridged mesoporous organosilicas and their application in methyl orange, congo Red and Cr(VI) removal, *RSC Adv.*, 2015, **5**, 67690-67699.
17. V. Sharma, P. Rekha and P. Mohanty, Nanoporous hypercrosslinked polyaniline: An efficient adsorbent for the adsorptive removal of cationic and anionic dyes, *J. Mol. Liq.*, 2016, **222**, 1091-1100.
18. Y. Sun, S. Yang, Y. Chen, C. Ding, W. Cheng and X. Wang, Adsorption and desorption of u(vi) on functionalized graphene oxides: a combined experimental and theoretical study, *Environ. Sci. Technol.*, 2015, **49**, 4255-4262,
19. M. Sutton and S. R. Burastero, Uranium(VI) solubility and speciation in simulated elemental human biological fluids, *Chem. Res. Toxicol.*, 2004, **17**, 1468-1480,
20. H. P. Emerson, S. D. Pietro, Y. Katsenovich and J. Szecsody, Potential for U sequestration with select minerals and sediments via base treatment, *J. Environ. Manage.*, 2018, **223**, 108-114.
21. S. Parimal, M. Prasad and U. Bhaskar, Prediction of equilibrium sorption isotherm: comparison of linear and nonlinear methods, *Ind. Eng. Chem. Res.*, 2010, **49**, 2882-2888.
22. Y. S. Ho and G. McKay, Pseudo-second order model for sorption processes, *Process Biochem.*, 1999, **34**, 451-465.
23. P. Rekha, R. Muhammad, V. Sharma, M. Ramteke and P. Mohanty, Unprecedented adsorptive removal of Cr₂O₇²⁻ and methyl orange by using a low surface area organosilica, *J. Mater. Chem. A*, 2016, **4**, 17866-17874.

24. M. N. El-Bohy, Y. K. Abdel-Monem, K. A. Rabie, N. M. Farag, M. G. Mahfouz, A. A. Galhoum and E. Guibal, Grafting of arginine and glutamic acid onto cellulose for enhanced uranyl sorption, *Cellulose*, 2017, **24**, 1427-1443.
25. S. Liu, S. Li, H. Zhang, L. Wu, L. Sun and J. Ma, Removal of uranium(VI) from aqueous solution using graphene oxide and its amine-functionalized composite, *J. Radioanal. Nucl. Chem.*, 2016, **309**, 607-614.
26. R. T. Mayes, J. Gorka and S. Dai, Impact of pore size on the sorption of uranyl under seawater Conditions, *Ind. Eng. Chem. Res.*, 2016, **55**, 4339-4343.
27. M. Y. Arica and G. Bayramoglu, Polyaniline coated magnetic carboxymethylcellulose beads for selective removal of uranium ions from aqueous solution, *J. Radioanal. Nucl. Chem.*, 2016, **310**, 711-724.
28. Q. Sun, B. Aguila, L. D. Earl, C.W. Abney, L. Wojtas, P. K. Thallapally and S. Ma, Covalent organic frameworks as a decorating platform for utilization and affinity enhancement of chelating sites for radionuclide sequestration, *Adv. Mater.*, 2018, **30**, 1-9.
29. M. Barkat, D. Nibou, S. Amokrane, S. Chegrouche and A. Mellah, Uranium (VI) adsorption on synthesized 4A and P1 zeolites: Equilibrium, kinetic, and thermodynamic studies, *C. R. Chimie*, 2015, **18**, 261-269.





CHAPTER-VIII

**SUMMARY, CONCLUSIONS AND
DIRECTIONS FOR FUTURE
RESEARCH**

8.1. Summary and conclusions

This chapter deals with the overall summary of the research, how and to what extent the proposed objectives were achieved. This chapter further deals with the challenges faced during the research work and how these challenges were successfully overcome. The thesis concludes with a statement on the future prospects of the research. Nitrogen enriched nanoporous triazine based polymeric materials, an important class of functional polymers has attracted research community in recent times.[1-11] They possess intriguing properties owing to the presence of the electron rich moieties that help to achieve superior applications in energy and environmental fields such as adsorption, materials for energy storage and harvesting, catalysis, gas sorption and separation etc. Controlled textural properties are additional advantages of this class of materials. Their synthesis methodology varies depending up on the precursors used and the ease of condensation. These metal-free materials have mostly low density due to the presence of light weight elements, good thermal and chemical stabilities.[11-15] Based on the literature survey, the objectives of the research were drawn. Keeping in mind to synthesize nitrogen enriched materials with controlled textural properties made from inexpensive precursors, two precursors melamine and cyanuric chloride were chosen for the synthesis of polytriazines. The nitrogen enriched nanoporous polytriazines (NENPs) are expected to have high nitrogen content as the theoretical content of the fully condensed polytriazine made from these two precursors could reach 60 wt%.

To make the desired NENPs several experimental approaches such as conventional heating, solvothermal, sonochemical and microwave assisted methods have been explored. Complete condensation of the precursors, high nitrogen contents and the control of the textural properties are the major challenges that credited the microwave assisted method as the best method among all these explored approaches. All the synthesized specimens have been thoroughly characterized. Primarily, spectroscopic techniques such as ^{13}C CPMAS NMR, FTIR and XPS along with the XRD and TGA have been used to understand the extent of condensation. Moreover, FESEM and TEM were used for the microstructural analysis and CHNSO analyzer for the elemental composition studies. Based on the information derived from the above analytical techniques, it has been observed that a partial condensation could only be possible when the syntheses were carried out using conventional heating, solvothermal and sonochemical approaches although, all the experimental parameters have been varied to improve the extent of polymerization. Only the NENPs made using the microwave assisted method have much better polymerization, yielding the desired products as per the defined objectives.

The best material, NENP-1, among these was made at 140 °C with a microwave power of 400 W in a short experimental time of 30 min only, when the reactants were dissolved in 20 ml of DMSO. Almost complete condensation of the precursors was observed from the spectroscopic investigations and the NENP-1 has shown a high S_{BET} of 840 $\text{m}^2 \text{g}^{-1}$ and PSD centred 1.3 & 3.8 nm. Moreover, the N content of 50 wt% was highly encouraging, although, it didn't reach the theoretical value of ~60 wt%, which is common in high surface area materials due to the excess surface functionalities. As predicted expecting a stronger Lewis acid-Lewis base interactions between the electron rich nitrogen of the framework with the acidic gas CO_2 , the NENP-1 has shown a high CO_2 sorption capacity of 22.9 wt% at 0 °C and 1 bar. The H_2 and CH_4 storage capacities of 2.3 and 1.8 wt% were measured at -196 °C and 0 °C, respectively, at 1 bar. A new way to improve the CO_2 capture efficiency by pre-carbonizing (heating below carbonization temperature) the NENP-1 was explored, which shows an increased CO_2 capture capacity of 33.8 wt% as against 22.9 wt% in NENP-1. The H_2 storage capacity was marginally increased to 2.4 wt%.

The NENP-1 was further employed as the active material in fabricating electrodes for the electrochemical supercapacitor. It shows superior electrochemical supercapacitor performance with the specific capacitance reaching as high as 1256 F g^{-1} @ 1 mV sec^{-1} . An asymmetric supercapacitor device was fabricated and the energy and power densities are estimated to be 102 Wh kg^{-1} and 1.6 kW kg^{-1} , respectively. These values indicate that the NENP-1 could be the potential material to bridge the gap between supercapacitors and batteries. Moreover, on charging for 30 s with an input potential of 3.0 V, the red (1.5 V), green (1.5 V) and blue (3.0 V) LEDs could be lit up to 11, 4 and 0.5 min, respectively.

As an organocatalyst, the NENP-1 efficiently catalyses the Knoevenagel reaction for C-C bond formation with high yield of ~98% in a short reaction time of 30 min at room temperature. As an adsorbent, it further has a superior adsorption capacity of 489 mg g^{-1} with 97.8% adsorption efficiency for uranium removal at 25 °C and pH of 7 from aqueous solution. The NENP-1 has further shown to adsorb uranium ions in aqueous solution to an extent leaving behind the uranium concentration that is permissible in the WHO (0.015 mg l^{-1}) and USEPA (0.03 mg l^{-1}) limits. When used to enrich uranium from the seawater condition, an adsorption capacity of 50 mg g^{-1} was estimated.

In brief, the objectives of the present research were designed based on the extensive literature studies on the need of the hours largely directed towards the utilization of the materials in the energy and environmental applications. The planning of the research and its execution were done with great care using the state of the art facilities. As mentioned above, be it the adsorption of CO₂, performance as supercapacitors, metal-free organocatalysis or uranium removal from waste water and enrichment from seawater condition, always the NENP has shown superior performance which make this research quite successful.

8.2. New achievements

The major achievements of the present research are as follow;

- A novel approach of using microwave reactor for complete condensation of precursors, melamine and cyanuric chloride, otherwise most of the methods produce oligomers with a partial condensation
- Large N content which reaches as high as 52 wt% is quite phenomenal even when a high specific surface area of 840 m² g⁻¹ is realized. The narrow pore size distribution with hierarchical pore structure are instrumental in facilitating the kinetics of the adsorption process for achieving higher adsorption capacity.
- A maximum CO₂ capture capacity of 22.9 wt% and H₂ storage capacity of 2.3 wt% were achieved, that is among the best reported materials. Furthermore, a novel approach of pre-carbonization of the polytriazine below the carbonization temperature has substantially improved the CO₂ capture capacity to 33.8 wt%. This could further be extended to other polymeric high surface area materials. The stability of the materials is worth mentioning as no degradation of the CO₂ capture capacity was observed even after storing the materials in the ambient condition for two years. The excellent recyclability with 96.2% retention of CO₂ sorption capacity even after 10 cycles without activation and CO₂ vs. N₂, IAST selectivity of 111 are considered as important milestones, which could make a way for its application in industrial scale.
- Observation of high specific capacitance of 1256 F g⁻¹ @1 mV s⁻¹, high energy and power densities that lies in between the supercapacitors and batteries in the Ragone plot make it a potential futuristic energy storage material.
- The use of NENP-1 metal-free organocatalyst for the C-C bond formation in the Knoevenagel reaction is quite useful for its use to make molecules of industrial importance

- Achieving the WHO and USEPA limits by adsorbing uranium from the aqueous solution paved the way to its use in the nuclear power plant. Moreover, the enrichment of uranium from the simulated seawater makes it an energy material of the future.

8.3. Challenges

Although, all the objectives defined at the beginning of the research were achieved by synthesizing nitrogen enriched nanoporous polytriazine materials and investigating their applications for gas sorption and storage, supercapacitor, organocatalysis and uranium adsorption from aqueous and simulated seawater conditions, however, a significant number of hurdles were encountered during the course of the research. Some of the major challenges are as given below;

- Finding suitable precursors which can easily condense and are inexpensive
- Synthesis of fully condensed product, because most of the times formation of partially condensed oligomeric products are obtained
- Controlling the textural properties is one of the greatest challenge that was encountered. The template-free approach in most of the times resulted in the formation of porous materials with low specific surface area.
- Many other applications can be envisioned but due to the lack of accesses to the required instrumentation facilities is a major bottleneck

8.4. Directions for the future research work

Although, extensive research on the synthesis and characterization of the polytriazines were carried out in this research work along with several applications in energy and environmental fields, still few more avenues remain unexplored but are worth exploring as discussed below

- **Microstructure and morphology of the NENPs:** The microstructural investigations of the synthesized NENPs were carried out using FESEM and TEM. However, controlling the microstructure, especially, the shape and size of the nanoparticles can be an area of interest which may provide scope for its application as drug loading substrates. Moreover, only samples in the powder form were synthesized in this research. Preparation of monoliths and thin film morphologies can be another area of interest.
- **Drug delivery and bio-medical applications:** As mentioned above, the control of the particles size and shape could facilitate the drug delivery applications. Moreover, the control of the pore

functionalities either by choosing appropriate precursors or by post-synthesis functionalization could facilitates the loading of drug molecules of varied polarity. Creating hierarchical pore structure could further help in the use as tissue scaffold for the bio-medical applications.

- **Optical, electrical and sensing properties:** Presence of large amount of nitrogen with excess electrons in the form of lone pairs and conjugated double bonds could further provide interesting optical, electrical and sensing applications. These areas are worth exploring.
- **Water splitting applications:** Some of the recent reports suggest that presence of nitrogen in the carbonaceous materials have shown impressive hydrogen evolution and oxygen evolution reactions. Hence, the NENPs with large nitrogen content and high specific surface area could be explored for these applications.
- **Metal-free organocatalysis:** Although, NENP-1 was used as an organocatalyst for the C-C bond formation in the Knoevenagel reaction, many other base catalysed organic conversions can be explored. Moreover, the materials could be explored for the photo-reduction reactions.
- **Water purification:** The NENP-1 shown good uranium removal applications and could be extended to many other systems. Controlled textural properties by tuning the pore size distribution could facilitate the selective adsorptive removal of various organic and inorganic contaminants from the wastewater.

References

1. K. Wang, H. Huang, D. Liu, C. Wang, J. Li and C. Zhong, Covalent triazine-based frameworks with ultramicropores and high nitrogen contents for highly selective CO₂ capture. *Environ. Sci. Technol.*, 2016, **50**, 4869-4876.
2. S. Hug, L. Stegbauer, H. Oh, M. Hirscher and B. V. Lotsch, Nitrogen-rich covalent triazine frameworks as high-performance platforms for selective carbon capture and storage. *Chem. Mater.*, 2015, **27**, 8001-8010.
3. G. Wang, K. Leus, S. Zhao and P. V. D. Voort, Newly designed covalent triazine framework based on novel N-heteroaromatic building blocks for efficient CO₂ and H₂ capture and storage. *ACS Appl. Mater. Interfaces*, 2018, **10**, 1244-1249.
4. Q. Q. Dang, C. -Y. Liu, X. -M. Wang and X. -M. Zhang, Novel covalent triazine framework for high-performance CO₂ Capture and alkyne carboxylation reaction, *ACS Appl. Mater. Interfaces*, 2018, **10**, 27972-27978.
5. G. Sneddon, A. Greenaway and H. H. P. Yiu, The potential applications of nanoporous materials for the adsorption, separation, and catalytic conversion of carbon dioxide, *Adv. Energy Mater.*, 2014, **4**, 1301873-1301891.
6. W. -C. Song, X. -K. Xu, Q. Chen, Z. -Z. Zhuang and X. -H. Bu, Nitrogen-rich diaminotriazine-based porous organic polymers for small gas storage and selective uptake *Polym. Chem.*, 2013, **4**, 4690-4696.

7. S. Hug, L. Stegbauer, H. Oh, M. Hirscher and B. V. Lotsch, Nitrogen-rich covalent triazine frameworks as high-performance platforms for selective carbon capture and storage, *Chem. Mater.*, 2015, **27**, 8001-8010.
8. M. X. Tan, Y. N. Sum, J. Y. Ying and Y. Zhang, A mesoporous poly-melamine-formaldehyde polymer as a solid sorbent for toxic metal removal, *Energy Environ. Sci.*, 2013, **6**, 3254-3259.
9. P. Puthiaraj, Y. Lee, S. Zhang and W. Ahn, Triazine-based covalent organic polymers: design, synthesis and applications in heterogeneous catalysis, *J. Mater. Chem. A*, 2016, **4**, 16288-16311.
10. Y. Zhang, S. A. Y. Zou, X. Luo, Z. Li, H. Xi, X. Liu and Y. Mu, Gas uptake, molecular sensing and organocatalytic performances of a multifunctional carbazole-based conjugated microporous polymer, *J. Mater. Chem. A*, 2014, **2**, 13422-13430.
11. S. K. Dey, N. D. S. Amadeu and C. Janiak, Microporous polyurethane material for size selective heterogeneous catalysis of the Knoevenagel reaction, *Chem. Commun.*, 2016, **52**, 7834-7837.
12. Y. B. Zhou, Y. Q. Wang, L. C. Ning, Z. C. Ding, W. L. Wang, C. K. Ding, R. H. Li, J. J. Chen, X. Lu, Y. J. Ding and Z. P. Zhan, Conjugated microporous polymer as heterogeneous ligand for highly selective oxidative Heck reaction *J. Am. Chem. Soc.*, 2017, **139**, 3966-3969.
13. S. K. Kundu and A. Bhaumik, A triazine-based porous organic polymer: a novel heterogeneous basic organocatalyst for facile one-pot synthesis of 2-amino-4H-chromenes *RSC Adv.*, 2015, **5**, 32730-32739.
14. M. G. Schwab, B. H. Fassbender, W. Spiess, A. Thomas, X. Feng and K. Mullen, Catalyst-free preparation of melamine-based microporous polymer networks through Schiff base chemistry, *J. Am. Chem. Soc.*, 2009, **131**, 7216-7217.
15. O. Buyukcakir, S. H. Je, S. N. Talapaneni, D. Kim, and A. Coskun, Charged covalent triazine frameworks for CO₂ capture and conversion, *ACS Appl. Mater. Interfaces*, 2017, **9**, 7209-7216.